



HAL
open science

Modelling of masonry walls under seismic loadings

Michele Godio

► **To cite this version:**

Michele Godio. Modelling of masonry walls under seismic loadings. Materials. Université Paris-Est, 2015. English. NNT: 2015PESC1150 . tel-01305508

HAL Id: tel-01305508

<https://pastel.hal.science/tel-01305508>

Submitted on 21 Apr 2016

HAL is a multi-disciplinary open access archive for the deposit and dissemination of scientific research documents, whether they are published or not. The documents may come from teaching and research institutions in France or abroad, or from public or private research centers.

L'archive ouverte pluridisciplinaire **HAL**, est destinée au dépôt et à la diffusion de documents scientifiques de niveau recherche, publiés ou non, émanant des établissements d'enseignement et de recherche français ou étrangers, des laboratoires publics ou privés.



Thèse présentée pour l'obtention du grade de
Docteur de l'Université Paris-Est

Spécialité: Structures et Matériaux

**MODÉLISATION DES MURS EN MAÇONNERIE
SOUS SOLLICITATIONS SISMIQUES**
MODELLING OF MASONRY WALLS UNDER SEISMIC LOADS

Michele Godio

Thèse soutenue à l'Ecole des Ponts et Chaussées le 30 novembre 2015 devant:

M. Samuel FOREST	Professeur, MINES	<i>Rapporteur</i>
M. Alberto TALIERCIO	Professeur, POLIMI	<i>Rapporteur</i>
Mme. Katrin BEYER	Professeur, EPFL	<i>Examineur</i>
M. Claude BOUTIN	Professeur, ENTPE	<i>Examineur</i>
M. Seddik SAKJI	Ingénieur Recherche, CSTB	<i>Examineur</i>
M. Ioannis STEFANOU	Enseignant Chercheur, ENPC	<i>Examineur</i>
M. Jean SULEM	Professeur, ENPC	<i>Examineur</i>
M. Daniel BILLAUX	Président, Itasca S.A.S	<i>Invité</i>
M. Karam SAB	Professeur, ENPC	<i>Directeur de thèse</i>

Remerciements

Je tiens à remercier tout d'abord mon directeur de thèse, Karam Sab, pour l'honneur qu'il m'a fait de m'avoir accueilli dans le prestigieux laboratoire qu'il dirige. D'avoir cru en moi depuis la période de stage et puis tout le long de la thèse.

Je remercie ensuite Jean Sulem, qui a toujours montré un grand intérêt pour mes travaux, en s'associant au projet de thèse dès le début et en alimentant constamment mes recherches par des questions nouvelles.

Ioannis Stefanou a été celui qui m'a suivi de plus proche. Au bout de trois ans et un peu plus passés coude-à-coude avec lui, il est devenu pour moi un véritable interlocuteur. Avec lui j'ai le plaisir de partager cet intérêt tout particulier que j'ai pour la mécanique. Merci infiniment pour ton aide et tes enseignements.

Mes remerciements vont également à Seddik Sakji, pour le soutien qu'il m'a montré, de m'avoir souvent encouragé lorsque j'en avais besoin, et de m'avoir (encore plus souvent) interrogé, lorsque qu'il me voyait trop sûr de moi-même. Sa façon de mener son travail au quotidien au CSTB, avec tenace et modestie, reste pour moi exemplaire.

Je souhaite remercier les autres des membres du jury, pour l'honneur qu'ils m'ont fait de lire et juger cette thèse. M. Samuel Forest et M. Alberto Taliercio, d'avoir accepté de rapporter le manuscrit. Mme. Katrin Beyer et M. Claude Boutin, de l'avoir examiné. Vos questions et vos remarques ont été précieuses et constructives. Vos félicitations représentent pour moi une grande motivation qui me pousse à continuer dans le monde de la recherche.

Je dis merci aussi à Daniel Billaux, qui dirige 'ses' ingénieurs avec soin et simplicité, de m'avoir accepté dans le programme éducatif organisé par Itasca, de sa participation au jury et de la disponibilité montrée le long du projet.

Je remercie (et pas seulement) mes collègues de bureau aux Ponts. Achille, Bashar, Romain, Stefania, Grégoire. Avec vous j'ai partagé sans doute les moments les plus intenses et plus beaux de ses années passées au Labo. Votre bonne humeur, sympathie et générosité ont été pour moi le plus grand réconfort quotidien.

Je remercie de même mes collègues de l'Open Space du CSTB, où on picole du café pas cher et on discute. Toan, Romain, Medhi, Mathieu, Damien. Merci, vous avez été toujours accueillants et généraux vers moi malgré mes longues absences.

Merci Charisis. Sans toi je n'aurais jamais pensé entreprendre une thèse. Merci Dhionis. Sans toi je n'aurais jamais pensé pouvoir la terminer...

Si faire une thèse a été une petite entreprise, la faire sans jamais changer ses habitudes l'a été encore plus. Merci donc aux amis rencontrés à Paris, en particulier à Assad, Salvador, Carlos, Pablo et Andrea, pour tous les bons moments que j'ai passés avec vous et grâce à vous. Merci à Fabrizio, qui me soutient de loin et avec qui je continue partager tous mes centres d'intérêt et mes idées pour l'avenir. Merci à Marcello, excellent ami (et skieur) qui, désormais par tradition, participe à chaque soutenance.

J'aimerais enfin remercier ma famille du fond de mon cœur : maman papa et Ale. Et enfin Karin, un *grand* merci à toi, et bien plus encore...



Castello di Rivalta, Gazzola (Piacenza), Italie. Vue de l'escalier en colimaçon à l'intérieur du donjon. Détail sur la maçonnerie. (M.Godio 2015)

Résumé

La formulation de modèles sophistiqués et fiables pour l'évaluation du comportement sous sollicitations sismiques des structures de maçonnerie reste un vrai défi pour l'Ingénierie. Cette thèse contribue au développement et à l'utilisation de modèles continus pour la maçonnerie non renforcée et non chaînée.

Dans ce travail de doctorat, une méthode analytique pour l'estimation de la résistance globale de la maçonnerie est développée. La méthode s'appuie sur la théorie micropolaire (ou du milieu continu de Cosserat) et sur l'utilisation conjointe de l'approche cinématique de l'analyse limite et d'une technique d'homogénéisation. Dans un premier temps, la méthode est présentée pour le cas bidimensionnel. La méthode est introduite de manière générale, en ce qui concerne les milieux discrets périodiques. L'application à la maçonnerie est ensuite abordée. La résistance homogénéisée de colonnes et murs de maçonnerie est calculée en termes de contraintes et couples-contraintes généralisées du milieu continu de Cosserat. La formulation d'une méthode basée sur le milieu de Cosserat permet la prise en compte de l'influence de la rotation relative des particules du milieu discret. Cette influence est mise en évidence à travers l'application à la maçonnerie, en comparaison avec les autres méthodes présentes dans la littérature.

Dans un deuxième temps, la méthode est étendue au cas tridimensionnel. Des milieux discrets périodiques ayant leurs particules disposées le long de trois directions spatiales et montrant trois vecteurs de périodicité sont alors considérés. L'extension de la méthode s'inscrit dans le cadre de la théorie micropolaire tridimensionnelle. Cela permet la prise en compte des effets 3D de la translation et la rotation relative des particules. L'application aux colonnes et aux murs de maçonnerie montre comment la résistance dans le plan et hors-plan de la maçonnerie sont, par ces effets, couplées. La rotation relative des blocs accentue cette interaction, qui comporte une diminution de la résistance dans-le-plan précédemment calculée. Les murs de maçonnerie sont ici décrits par des modèles de plaque micropolaire.

Une formulation aux éléments finis pour des modèles de plaque micropolaire est ensuite développée. Dans un premier temps, la formulation est présentée pour l'élasticité et la dynamique. La validation d'un élément fini spécifique pour le calcul des structures est faite à l'aide d'exemples numériques. L'utilisation de cet élément sur des structures de maçonnerie est ensuite abordée, par l'implémentation d'un modèle d'homogénéisation déjà existant. Les fréquences fondamentales d'un mur maçonné sont ainsi calculées et comparées avec celle obtenues par un modèle aux éléments discrets. L'importance des rotations des blocs dans le plan du mur ainsi que leur participation dans la réponse inertielle du mur vis-à-vis des actions sismiques sont enfin investiguées.

Dans un deuxième temps, la formulation aux éléments finis est étendue à la plasticité, à travers l'implémentation de la théorie multi-critère pour les milieux de Cosserat. L'implémentation de cette théorie est basée sur un algorithme de projection, dont le schéma itératif de résolution est reporté. Les aspects numériques liés à l'implémentation de l'algorithme sont examinés. Une importante limitation de l'implémentation classique de l'algorithme est montrée et une nou-

velle stratégie de solution est proposée. L'élément fini de Cosserat est donc validé pour la plasticité à l'aide de nombreux exemples numériques.

En conclusion, trois approches de modélisation pour les structures de maçonnerie sont proposées et comparées. Un modèle continu d'homogénéisation basée sur le milieu de Cosserat est d'abord présenté. Le modèle est construit en introduisant les critères de ruptures homogénéisés calculés dans la première partie du travail dans l'élément fini développé dans la deuxième partie du travail. Un modèle continu basée sur le milieu de Cauchy est ensuite considéré. Ce dernier est construit à partir de modèles déjà présents dans la littérature. L'efficacité de ces deux modèles est examinée dans la représentation du comportement élastoplastique d'un mur de maçonnerie. Leur comparaison se base sur un troisième modèle, créé à l'aide des éléments discrets. La capacité des trois modèles de modéliser l'effet d'échelle dans la formation des mécanismes de ruine est enfin investiguée sur une application pratique aux structures de maçonnerie.

Mots-clés : Maçonnerie • Milieu de Cosserat • Homogénéisation • Analyse limite • Éléments finis • Théorie de la plasticité • Éléments discrets

Summary

The formulation of reliable and sophisticated models for the seismic assessment of masonry structures is a challenging task. This thesis contributes in this field to the development and the use of continuum models for unreinforced masonry.

An analytical method for the evaluation of the homogenised in-plane strength of masonry is first developed. The method is based on the two-dimensional micropolar continuum theory and makes use of the kinematic approach of limit analysis in conjunction with a rigorous homogenisation technique. The method is introduced in a general way, with regard to the generic class of discrete periodic media made of particles of the same type. The case of masonry is presented as application. The homogenised strength domains of masonry columns and walls are retrieved in terms of the generalized stresses and couple stresses of the Cosserat continuum. The formulation of the method based on the Cosserat continuum enables the investigation of the influence of the relative rotation of the particles on the strength of the discrete medium. This influence is illustrated by the application to masonry structures, in comparison with other methods presented in the literature.

The development of the homogenisation method continues with its extension to discrete periodic media made of particles disposed along three directions and showing three periodicity vectors. In this case, the approach relies on the three-dimensional micropolar theory. This enables to capture the three-dimensional effect of the relative translations and rotations of the particles constituting the discrete medium. The application to masonry columns and walls shows how the in-plane and out-of-plane actions result coupled in the assessment of masonry strength. The relative rotation of the blocks accentuates this effect, which consistently diminishes the in-plane strength. Masonry walls are finally ascribed to homogenised plates with Cosserat kinematics.

A finite element formulation for Cosserat plate models is next developed. The formulation is first presented for elasticity and dynamics. The validation of a specific finite element is made by means of numerical benchmarks and patch tests. The actual use of the element is presented in an application to masonry structures. The natural frequencies of a masonry panel modelled by discrete elements are computed and compared with those given by a homogenisation model implemented in the element. This allows to investigate the role of the in-plane rotations of the blocks and to show their implication towards seismic analyses of masonry structures.

The finite element formulation is next extended to the elastoplastic framework. The implementation of the multisurface plasticity theory into the Cosserat finite element is presented. The implementation of this theory is based on a projection algorithm. An important limitation of the classical implementation of this algorithm prevents its use in the framework of multisurface plasticity in efficient way. This limitation is discussed and a solution strategy is proposed. The finite element for Cosserat plate models is finally validated through numerous numerical benchmarks.

In conclusion, three different modelling approaches for masonry are proposed and com-

pared. A continuum model based on the Cosserat continuum is first presented. The model is constructed by implementing the homogenised yield criteria computed based on the proposed analytical method into the developed finite element. A homogenisation model based on Cauchy continuum is next introduced. This model is constructed by selecting appropriate constitutive laws and yield criteria from the literature. The performance of those homogenisation models in representing the elastoplastic response of a masonry panel is discussed, based on the comparison with a third analogue discrete elements model. The capability of the three models in predicting the scale effect in the formation of failure mechanisms is investigated in a practical application to masonry structures.

Keywords: Masonry • Cosserat continuum • Homogenisation • Limit analysis • Finite elements • Plasticity theory • Discrete elements

Contents

Motivation	1
1 Determination of the homogenised yield criteria for masonry: in-plane behaviour	9
1.1 Introduction	15
1.2 The Cosserat continuum: 2D statics and kinematics	18
1.3 The discrete medium: discrete variables and contact model	20
1.4 Homogenisation in limit analysis: average Cosserat variables and kinematic approach	23
1.4.1 Kinematic map	23
1.4.2 Average Cosserat variables	24
1.4.3 Homogenisation kinematic approach	25
1.4.4 Extension to generic periodic media	26
1.5 Application to masonry columns	27
1.5.1 Geometry	27
1.5.2 Average Cosserat variables	28
1.5.3 Homogenisation	30
1.5.4 Discussion	33
1.6 Application to masonry walls	35
1.6.1 Geometry	35
1.6.2 Average Cosserat variables	36
1.6.3 Homogenisation	40
1.7 Comparison with existing works	43
1.7.1 Comparison with de Buhan and de Felice (1997)	43
1.7.2 Comparison with Sulem and Mühlhaus (1997)	44
1.8 Conclusions	45
2 Determination of the homogenised yield criteria for masonry: in-plane and out-of-plane coupled behaviour	47
2.1 Introduction	53
2.2 The 3D Cosserat continuum	54
2.3 The 3D discrete medium	56
2.4 From the 3D discrete medium to the 3D Cosserat continuum: the homogenisation limit analysis kinematic approach	58
2.4.1 Kinematic map	58
2.4.2 Homogenisation kinematic approach	58
2.4.3 Average Cosserat variables	59
2.5 Application to masonry columns	60
2.5.1 Geometry	60

2.5.2	Average Cosserat variables	61
2.5.3	Homogenisation	63
2.6	Application to masonry walls	65
2.6.1	Geometry	65
2.6.2	Average Cosserat variables	66
2.6.3	Justification of the homogenisation procedure	70
2.6.4	Homogenisation	71
2.7	Conclusions	73
3	Finite element formulation for Cosserat plates: elasticity	75
3.1	Introduction	81
3.2	3D Cosserat dynamics prerequisites	82
3.3	Equations of motion for Cosserat elastic plates	84
3.4	Element formulation	86
3.4.1	Stiffness matrix	87
3.4.2	Mass matrix	89
3.4.3	Element motion	89
3.5	The COSS8R element	90
3.5.1	Choice of the polynomial order of interpolation	90
3.5.2	Zero-energy modes investigation	91
3.5.3	Consistent mass matrix	94
3.6	Element validation	94
3.6.1	Patch test	94
3.6.2	Shear locking investigation	96
3.6.3	Dispersion functions	97
3.7	Application to masonry structures	99
3.7.1	Comparison with Discrete Elements solution	101
3.7.2	The role of drilling rotations	101
3.8	Conclusions	102
4	Finite element formulation for Cosserat plates: plasticity	105
4.1	Introduction	111
4.2	The Cosserat (or micropolar) plate model	113
4.3	Multisurface plasticity theory for Cosserat materials	115
4.3.1	Further notations	117
4.4	Solution algorithm	118
4.4.1	Solution algorithm for multisurface plasticity	118
4.4.2	Implementation of the Newton-Raphson method in the CPP algorithm	119
4.5	Finite Element formulation	123
4.5.1	Element implementation	123
4.5.2	Derivation of the elastoplastic tangent stiffness matrix for multisurface plasticity	124
4.6	Element validation	126
4.6.1	The micropolar plate element COSS8R	127
4.6.2	Single element tests for multisurface plane plasticity	128
4.6.3	Structural benchmarks for micropolar plates	130
4.7	Conclusions	135

5	Scale effect in masonry failure: a numerical investigation by finite and discrete elements	143
5.1	Modelling strategies for masonry	149
5.2	The elastoplastic Cosserat continuum model	149
5.2.1	The Cosserat medium	149
5.2.2	A Cosserat model for masonry	151
5.3	The elastoplastic Cauchy continuum model	151
5.3.1	The Cauchy medium	151
5.3.2	A Cauchy model for masonry	152
5.4	The discrete elements model	152
5.4.1	A discrete elements model for masonry	153
5.5	Modelling of a simple shear wall	153
5.5.1	Geometry, material properties and boundary conditions	153
5.5.2	Scale effect	154
5.5.3	Prediction of the wall response	155
5.5.4	Failure mechanisms and local deformations	155
5.6	Conclusions	156
	Conclusions	163
	Appendices	169
A.1	Average Cosserat deformations of the discrete cell	171
A.2	Macroscopic relative deformations and curvatures on the elementary cell A	173
A.3	Macroscopic stresses and couple stresses on the elementary cell A	174
B.1	Out-of-plane components of the macroscopic Cosserat deformation measures of the cell \bar{A}	175
B.2	Out-of-plane components of the macroscopic Cosserat stresses and couple stresses of the cell \bar{A}	177
C.1	Stiffness matrix for materials with in-plane centro-symmetry	179
C.2	Coupling factor	180
C.3	Drilling rigidity	182
C.4	Patch test for anisotropic Cosserat materials	183
C.5	Advanced test to torsion for Cosserat plates	185
D.1	Implementation of the COSS8R element in Abaqus	187

List of Figures

1.1	The occurrence of blocks' rotation (in grey) in the formation of failure mechanisms in masonry shear walls. Reference to the shear walls modelled by Lourenço (1996).	16
1.2	Classes of continuum media according to Eringen (1999).	19
1.3	Stresses and couple stresses of a 2D Cosserat continuum (left). Its strength domain is formulated as the convex region of the generalized space $(T_{\alpha\beta}, M_\beta)$ enclosed by multiple plastic surfaces (right).	19
1.4	A periodic collection of discrete hexagonal blocks and the corresponding elementary cell. The elementary cell retained (right) is the parallelogram produced by the periodicity vectors.	21
1.5	Kinematics and statics of the contact model adopted for the discrete medium.	21
1.6	Relative translations $\llbracket v_\alpha^G \rrbracket^{IJ}$ and rotations $\llbracket \omega^G \rrbracket^{IJ}$ producing opening and sliding of the interface between two blocks. Both depicted mechanisms are related to interface failure.	23
1.7	Homogenisation based on the Cosserat continuum is carried out in the frame of limit analysis on a periodic collection of rigid particles. Starting from a failure criterion (left) expressed at the interfaces of the discrete medium (in red), it is possible to retrieve the homogenised yield criterion for the macroscopic Cosserat continuum (right). The resulting homogenised strength domain is the region of the generalized stress space $(T_{\alpha\beta}, M_\beta)$ enclosed by these yield criteria.	26
1.8	A periodic collection of beams disposed following a mono-atomic lattice (left), and the corresponding elementary cell (right).	27
1.9	Periodic masonry column (left) and the corresponding elementary cell (right).	28
1.10	Combinations of rigid-body motions of the blocks (translations and rotations) producing 1D Cosserat macroscopic deformation and curvature states on the elementary cell of a masonry column. Solid lines represent the deformed state of the discrete cell. Dotted lines represent its undeformed state. In grey: the deformed state of the elementary cell supposed as a continuum, undergoing 1D macroscopic Cosserat deformations.	29
1.11	Combinations of rigid-body motions of the blocks (translations and rotations) producing in-plane rigid-body translations V_α and Cosserat rotations Ω of the elementary cell of a masonry column.	30
1.12	Displacement jump across the interface of the periodic elementary cell of a masonry column, falling within the Coulomb friction cone. Condition for interface failure is that the displacement jump falls inside this cone.	31
1.13	Representation of the homogenised strength domain for the masonry column in the space of the generalized Cosserat deformations $(T_{\alpha 2}, K_2)$. In blue: the intersecting planes (Eq.(1.62)). In red: the vectors normal to the planes.	32

1.14	Representation of the homogenised strength domain for the masonry column in the space of the generalized Cosserat stresses $(T_{\alpha 2}, M_2)$. Intersecting plane (Eq.(1.67)).	33
1.15	Condition for failure of the elementary cell (macroscopic failure) of a masonry column. Representation of the homogenised strength criterion for $\zeta_1 = 0$ (Cauchy continuum) and for $\zeta_1 \neq 0$ (Cosserat continuum).	34
1.16	Periodic masonry column and corresponding elementary cells larger than B (left). Effect of the size of the cell on the computed strength (right).	35
1.17	Periodic masonry wall with generic running bond pattern (left) and the corresponding elementary cell (right).	36
1.18	Elementary cells for periodic masonry covered by the cell A . Left: the stack bond pattern, for $\eta = 0$. Right: the classical (1/2) running bond pattern, for $\eta = 1/2$	37
1.19	Rigid-body motions of the blocks (translations and rotations) producing 2D Cosserat macroscopic deformation and curvature states on the elementary cell of a periodic masonry wall (stack bond pattern). Solid lines represent the deformed state of the discrete cell. Dotted lines represent its undeformed state. In grey: the deformed state of the elementary cell supposed as a continuum, undergoing 2D macroscopic Cosserat deformations.	38
1.20	Rigid-body motions of the blocks (translations and rotations) producing in-plane rigid-body translations V_α and Cosserat rotations Ω^c of the elementary cell of a masonry wall.	39
1.21	Points of the elementary cell where the relevance condition needs to be verified.	41
1.22	Representation of the homogenised strength domain for the masonry wall (1/2 running bond pattern) in the space of Cosserat deformations. Intersections with $K_1 = K_2 = 0$ and $\Gamma_{12} = \Gamma_{21} = 0$ ($\Gamma_{11} = \Gamma_{22}$).	42
1.23	Representation of the homogenised strength domain for the masonry wall in the Cauchy stress space. The strength domains for the Cauchy continuum proposed by Sab et al. (2007) (stack bond) and de Buhan and de Felice (1997); Sab (2003) (1/2 running bond) are for $\beta = 0$ (in light red). The strength domains for the Cosserat continuum are for $\beta \neq 0$, here $\beta = 3$ (in dark red).	44
1.24	Comparison between the Cosserat strength domains for running bond pattern by Sulem and Mühlhaus (1997), Eq.(1.87)-(1.88) (in dark red), and the homogenised Cosserat strength domains from the present work (in light red). Intersections with $M_1 = M_2 = 0$ and $T_{12} = T_{21} = 0$ ($T_{11} = 0$).	45
2.1	Stresses and couple stresses of a 3D Cosserat continuum. Stresses (left) are represented by polar vectors. Couple stresses (right) are represented by spin vectors.	55
2.2	Examples of three-dimensional discrete periodic media with particles disposed following a mono-atomic lattice. Left: a periodic collection of beams. Right: a periodic collection of cubic blocks in contact. Both discrete media are based on the same elementary cell (in dotted line).	56
2.3	Periodic masonry column (left) and the corresponding 3D elementary cell \bar{B} (right).	60
2.4	Blocks' motions $(v_i^{GJ}, \omega_i^{GJ})$ producing 6 macroscopic Cosserat deformation modes of the discrete cell \bar{B} . Top: 3 displacement gradients D_{i2} . Bottom: 3 rotation gradients K_{i2}	62
2.5	Blocks' motions $(v_i^{GJ}, \omega_i^{GJ})$ producing 6 macroscopic rigid-body modes of the discrete cell \bar{B} . Top: 3 translations V_i . Bottom: 3 Cosserat rotations Ω_i^c	62
2.6	Periodic masonry platband (left) and the corresponding 3D elementary cell (right).	63

2.7	Coulomb slip criterion adopted at the interface level of the 3D cell \bar{B} . Cone of plastically admissible displacement jumps.	64
2.8	Points of the 3D elementary cell where the relevance condition (Eq.(2.44)) needs to be satisfied.	65
2.9	Representations of the cone of the plastically admissible homogenised Cosserat deformations for the masonry column.	65
2.10	Periodic masonry wall (left) and the corresponding 3D elementary cell \bar{A} (right).	66
2.11	Rigid-body motion of the blocks (translations and rotations) producing 6 out-of-plane Cosserat macroscopic deformations of the elementary cell \bar{A} of a periodic masonry wall (stack bond pattern). Top: 3 displacement gradients. Bottom: 3 rotation gradients.	68
2.12	Rigid-body motion of the blocks (v_i^{GJ}, ω_i^{GJ}) producing 3 macroscopic out-of-plane rigid-body modes of the discrete cell \bar{A} of a periodic masonry wall (stack bond pattern). Top: 1 rigid translation V_3 . Bottom: 3 Cosserat rotations (Ω_1^c, Ω_2^c).	69
2.13	Points of the 3D elementary cell where the relevance condition (Eq.(2.44)) needs to be satisfied.	72
3.1	Higher order continuum theories according to Germain (1973) terminology. Cosserat continuum is a special case of a micromorphic continuum of first order.	83
3.2	Stresses, couple stresses and degrees of freedom of a Cosserat plate: membrane (left) and flexural (right) behaviour.	85
3.3	The COSS8R element, with 4 Gauss points (X), 8 nodes and 6 DOF per node: translations (square) and rotations (circle).	90
3.4	Elements tested for zero-energy modes investigation: (A) Cosserat element, plate configuration; (B) Cosserat element, membrane configuration; (C) classical Cauchy element, membrane part.	91
3.5	(a) a highly rigid element resting upon a layer of flexible elements with reduced integration; (b) propagating spurious mode in an assembly of Cauchy (S8R) elements; (c) accurate results from a COSS8R subdivision.	92
3.6	Definition of the distortion δ of the rigid element.	93
3.7	Normalised distortion factor (left) and normalised vertical displacement (right) versus the coupling factor α . The classical Cauchy (S8R) element is retrieved for $\alpha = 0$. The COSS8R element is for $\alpha = 1$	94
3.8	Element discretisation employed for the patch test.	95
3.9	Bending-plate in two configurations: simply supported (left) and clamped edges (right).	96
3.10	Normalised central deflection versus length-to-thickness ratio for given meshes. Left: simply supported plate. Right: clamped-edge plate.	97
3.11	Dispersion relations for a one-dimensional Cosserat flexural problem: micro-rotation mode ν_1 and shear strain mode ν_2	99
3.12	Relative error committed in the evaluation of the first eleven flexural wave lengths.	100
3.13	The three simulated masonry panels modelled with DE and with equivalent Cosserat plates by the COSS8R element: notation, boundary conditions and aspect ratios $AR = B/A$	100
3.14	Modal frequencies of the masonry panel versus the number of building blocks composing the panel in both directions. Comparison between the results extracted by DE and by the use of the equivalent Cosserat plate model for masonry implemented in a COSS8R FE discretisation. Results for aspect ratio $AR = 0.50$	102

3.15	Modal frequencies of the masonry panel versus the number of building blocks composing the panel in both directions. Comparison between the results extracted by DE and by the use of the equivalent Cosserat plate model for masonry implemented in a COSS8R FE discretisation. Results for aspect ratio $AR = 1.00$.	103
3.16	Modal frequencies of the masonry panel versus the number of building blocks composing the panel in both directions. Comparison between the results extracted by DE and by the use of the equivalent Cosserat plate model for masonry implemented in a COSS8R FE discretisation. Results for aspect ratio $AR = 1.50$.	104
3.17	Percentage of modal effective masses and moment of inertia for the first in-plane mode of the masonry panel, versus the number of building blocks composing the panel in both directions. The modal masses \bar{M}_1 and \bar{M}_1 are associated to the horizontal and the vertical displacements. The modal moment of inertia \bar{J}_3 is associated to the drilling rotations.	104
4.1	Stresses and couple-stresses of a Cosserat plate.	114
4.2	Schematic representation of the elastic domain of a Cosserat continuum. According to the multisurface plasticity theory, it is a convex region in the generalised stress space $(\boldsymbol{\tau}, \boldsymbol{\mu}; \boldsymbol{q})$ defined by multiple yield criteria.	116
4.3	Illustration of the Closest-Point-Projection (CPP) algorithm adopted within the multisurface plasticity theory for Cosserat materials.	120
4.4	Two possible configurations for which Jacobian matrix is singular for perfect plasticity.	122
4.5	The quadratic micropolar plate element COSS8R (Godio et al., 2015a).	127
4.6	Configurations used for the single element tests in multisurface plasticity.	128
4.7	Element response to uni-axial cyclic loading. Elastic modulus $E = 10\text{MPa}$, hardening modulus $h = 10\text{MPa}$, yield stress $\tau_y = 5\text{MPa}$.	129
4.8	Element response to bi-axial test B1. Top: stress path in the $(\tau_{11} - \tau_{22})$ -plane. Bottom: stress-strain curve. In-plane elastic properties: $K = 5\text{MPa}$, $G = 5\text{MPa}$, $G_c = 0\text{MPa}$, $l_c = 0$. Hardening modulus $h = 10\text{MPa}$, yield stress $\tau_y = 5\text{MPa}$.	131
4.9	Element response to bi-axial test B2. Top: stress path in the $(\tau_{11} - \tau_{22})$ -plane. Bottom: stress-strain curve.	132
4.10	Element response to bi-axial test B3. Top: stress path in the $(\tau_{11} - \tau_{22})$ -plane. Bottom: stress-strain curve.	133
4.11	Element response to bi-axial test B4. Top: stress path in the $(\tau_{11} - \tau_{22})$ -plane. Center and bottom: stress-strain curve.	137
4.12	Element response to bi-axial test B5. Top: stress path in the $(\tau_{11} - \tau_{22})$ -plane. Center and bottom: stress-strain curve.	138
4.13	Hollow cylinder under axial rotation. Notations and boundary conditions.	139
4.14	Macroscopic behaviour of the hollow cylinder (left) and localisation of the in-plane shear strain γ_{12} (right) for different discretisations with the COSS8R finite element (FE).	139
4.15	Deformation pattern and iso-contour of in-plane shear strain distribution for different discretisations of the hollow cylinder: left 16×8 FE, centre 24×16 FE, right 32×24 FE. Values for the ultimate resulting moment beyond the peak level.	139
4.16	Square plate under torsion. Illustration of the boundary conditions and of the expected deformation pattern.	140
4.17	Macroscopic behaviour of the square plate under torsion for different finite element discretisations.	140

4.18	Deformation pattern and iso-contour of the number of activated plastic surfaces for different discretisations of the square plate: left 2×2 FE, centre 4×4 FE, right 8×8 FE.	140
4.19	Shallow foundation under distributed pressure supported by a soil with micropolar properties. Geometry and boundary conditions.	141
4.20	Illustration of the set of plastic surfaces describing the elastoplastic response of the soil.	141
4.21	Left: macroscopic response of the shallow foundation for soils with different internal lengths. Right: response for small internal lengths ($l_c = 0.00025\text{m}$) and comparison with finite elements based on the Cauchy continuum (Krabbenhøft et al., 2007b).	141
5.1	Notations used for the Cosserat medium (in-plane behaviour). Shear stresses and couple stresses (left) and elastic domain (right).	150
5.2	Two different elementary cells of a classical 1/2 running-bond masonry wall. Left: the cell with the form of a parallelogram considered for homogenisation in Chapter 1. Right: the diamond-shaped cell considered by Stefanou et al. (2008); de Buhan and de Felice (1997) and in the present Chapter.	151
5.3	Notations used for the Cauchy medium (in-plane behaviour). Shear stresses (left) and elastic domain (right).	152
5.4	Masonry shear wall. Illustration of the geometry and boundary conditions adopted for the discrete and the continuum models.	153
5.5	Set of homogenised yield criteria for 1/2 running-bond masonry, enclosing the elastic domains of the Cosserat (dark red) and the Cauchy (light red) elastoplastic continuum models (Table 5.1). Domains for non-symmetric (left) and symmetric (right) stress states.	154
5.6	Walls made up of different number of blocks considered for the study of the scale effect in masonry.	155
5.7	Scale effect in a confined masonry wall under shear. Normalized force-displacement diagrams from the discrete (top) and the homogenised continuum models (bottom), for walls composed by different number of blocks. The response given by the Cauchy model is invariant of the number of blocks.	156
5.8	Comparison between the discrete elements (DE) and the homogenised continuum finite element (FE) models in modelling a masonry shear wall, in terms of normalized force-displacement diagrams. Results are presented from the top to the bottom for walls composed by an increasing number of blocks.	158
5.9	Development of the inter-block slip in the discrete elements model when $\delta_1 \approx 0.05$ (top - red dots) versus activation of the multiple homogenised yield criteria in the Cauchy (red region - centre) and Cosserat continuum model (bottom). Wall made of 12×30 blocks.	159
5.10	Development of the inter-block slip in the discrete elements model when $\delta_1 \approx 0.1$ (top - red dots) versus activation of the multiple homogenised yield criteria in the Cauchy (red region - centre) and Cosserat continuum model (bottom). Wall made of 12×30 blocks.	160
5.11	Development of the inter-block slip in the discrete elements model when $\delta_1 \approx 0.2$ (top - red dots) versus activation of the multiple homogenised yield criteria in the Cauchy (red region - centre) and Cosserat continuum model (bottom). Wall made of 12×30 blocks.	161

C.1	Rhombic plate subjected to local out-of-plane force F_3 . Notations, boundary conditions and element discretisation.	185
C.2	Relative error committed in the evaluation of the out-of-plane displacement of point P of the plate. Top: response for isotropic plates. Bottom: comparison with anisotropic plates. Geometry: $A = 50\text{mm}$, $B = 45\text{mm}$, $F_3 = 1\text{N}$. Out-of-plane properties: $\alpha_4 = 1500\text{MPa}$, $\beta_1 = 2000\text{MPa} \times \text{mm}$, $\beta_2 = 0\text{MPa} \times \text{mm}$, $\beta_3 = 4000\text{MPa} \times \text{mm}$. Anisotropic plates are for $\delta = 0.5$	186
D.1	The algorithm through which Abaqus calls the user subroutine UEL and operates on the user-defined elements. CPP indicates the Closest-Point-Projection algorithm used for the solution of the elastoplastic problem (Chapter 4).	189

List of Tables

1.1	Coefficients used in Eqs.(1.81)-(1.83).	42
2.1	Coefficients used in Eqs.(2.63)-(2.65).	73
3.1	Field variables of the Cosserat plate-type model in matrix notation. Membrane and flexural behaviour. The components of the inertia tensor are represented in the principal basis.	86
3.2	Computed number of zero-energy modes other than those associated with rigid body modes.	92
3.3	Patch test for Cosserat plane elements: boundary conditions and expected solutions.	95
3.4	Results of patch tests at point P1. Exact results are reported in brackets.	96
4.1	Membrane and flexural static and kinematics of a Cosserat plate element.	127
5.1	Geometric and material properties of discrete and continuum models adopted for the masonry shear wall.	154
C.1	Results of patch tests for anisotropic Cosserat material. Stresses and couple stresses at point P1. Exact results are reported in brackets.	183
C.2	Generalization of the patch test of Providas and Kattis (2002) for anisotropic Cosserat materials: boundary conditions and expected solutions.	184

Motivation

Context

With the development in the 20th century of building materials such as steel and concrete, masonry was displaced in many important engineering applications. As a result, methods for the design and the assessment of the structural performance of masonry remained far behind those conceived for these newer materials (DeJong, 2009). Nonetheless, masonry remained of great relevance for the construction of load-bearing walls in low- and medium-rise buildings. It was also widely used for internal and infill walls in buildings where the primary structural function was covered by steel and concrete (Hendry, 2001).

Nowadays, masonry represents the majority of the built environment in the Mediterranean countries. These countries have the highest risk of damage from earthquakes in Europe, since most of the buildings do not benefit from modern engineering design concepts, but result instead from the use of empirical rules and expertise. In these countries, seismic loadings are certainly a major risk that causes the collapse of masonry buildings.

In this thesis we refer to traditional *unreinforced masonry*. This typology is comprehensive of a vast array of structures, ranging from those of historical dry-stone monuments to those of more recent mortar-brick buildings. The use of unreinforced masonry in these structures is almost always limited to components mainly subjected to compressive loads, that the material have to bear in the vertical direction (in the form of walls and pillars) or to span across distances (in the form of arches, vaults and domes) (Heyman, 1997; Como, 2013). Masonry has instead a limited load-bearing capacity to support horizontal loads acting in the out-of-plane direction and flexural moments (Doherty et al., 2002; Griffith et al., 2007). Therefore the design and modelling of masonry structures still remains an open task for civil engineers.

In modern constructions, traditional masonry is rarely used for the entire structure of the building. It is better employed in mixed structures. Unreinforced masonry panels are usually surrounded by reinforced-concrete or steel boundary frames. The fact that the panel is laid before or subsequently to the frame denotes two types of masonry (Hendry et al., 1997): the confined and the infill masonry. Compared to infill masonry, confined masonry provides better performance during earthquakes, by virtue of the effective connection established between the material and the surrounding frame. In this configuration, masonry has an enhanced shear strength and ductility (Tomazevic and Klemenc, 1997). Furthermore, it gains higher out-of-plane load-bearing capacity, due to the arching mechanisms that it develops within the frame (Tu et al., 2010). The study of the interaction between masonry and the surrounding frame is, however, outside of the scope of the present thesis. Herein, attention is focused on single unreinforced masonry elements and infill panels. The connection with the surrounding frame is in general less well established in these latter (the gap between the frame and masonry is usually poorly filled with mortar). This allows one to model the masonry separately from the rest of the structure, provided that correct boundary conditions are applied.

Today's Building Codes require the assessment of the seismic vulnerability of unreinforced masonry (Eurocode 8; Eurocode 6). In addition, they demand the estimation of the damage level and the residual load-bearing capacity after earthquake occurrence. This necessitates the use of *spatial models* for modelling buildings that include masonry elements, even in cases when the uniformity and symmetry of the building could suggest the choice of simplified two-dimensional models for the representation of its structural behaviour (Eurocode 8, Section 4).

According to Eurocode 8, models for masonry have to represent the correct distribution of mass and stiffness of the building. Masonry walls (confined or not) may contribute significantly to the lateral stiffness and resistance of the building and therefore they should be taken into account in the construction of the models. Moreover, particular attention should be given to infill panels and single masonry elements, since they are the most vulnerable to the seismic action

and, especially, to the out-of-plane failure. A number of uncertainties related to the behaviour of these elements should be considered in the construction of the models. For instance: the variability of their mechanical properties, the level of attachment to the surrounding frame, the possible modifications occurred during the use of the building (as the presence of openings), the non-uniform degree of damage suffered during earthquake events, the possibility of premature out-of-plane collapse of slender panels due to brittle failure, the torsional response of the building caused by the damage of the infill panels (Eurocode 8, Section 4, Section 9). These and further aspects may induce possible irregularities and non-uniformities in the building and therefore require spatial models to be captured.

In this context, the use of reliable and sophisticated models that correctly represent the mechanical behaviour of unreinforced masonry is a fundamental task. This certainly avoids premature decisions in masonry structural design that may prove overly conservative or, on the contrary, catastrophic. The formulation of these models requires, however, a higher degree of knowledge and education in the engineering practice, as well as the availability of adequate software.

This thesis contributes to the development and the use of continuum models for unreinforced masonry structures. Whether based on rigorous homogenisation methods (Anthoine, 1995; Cecchi and Sab, 2002b; Milani et al., 2006a; Stefanou et al., 2008) or on more phenomenological approaches (Casolo, 2004; Grande et al., 2011; Penna et al., 2014; Liberatore and Addessi, 2015), continuum (or macroscopic) models carry important advantages as compared to discrete (or microscopic) models (Lemos, 2007b; DeJong and Vibert, 2012; Simon and Bagi, 2014), in which masonry constituents are modelled separately. First, continuum models are computationally less demanding than the discrete ones (Lourenço et al., 2007). Second, these models are often based on numerical procedures as the Finite Elements Method that are common in today's engineering practice (Addessi et al., 2014). This enables to combine models for unreinforced masonry with existing models for concrete and steel. Finally, continuum models usually appeal to classical notions from the Continuum and Structural Mechanics (internal actions, moments, strains, etc.) that belong to engineering education and are recurrent in the Codes for masonry.

Research goals

As discussed in the previous Section, the assessment of the seismic performance of masonry structures is the research ground for the present thesis. Within this context, the primary objective is the development of an equivalent continuum model for the description of the mechanical behaviour of masonry. From a theoretical point of view the research focuses on:

- Masonry, studied at the microscopic scale as a discrete medium equipped with an apparent periodic micro-structure. This latter is provided by the brickwork, i.e. the shape, size and disposition of the building blocks. The bridge between the micro- and the macroscopic scale is assured by the use of homogenisation techniques.
- The three-dimensional behaviour of masonry, i.e. the determination of the in-plane and the out-of-plane macroscopic material response (internal actions and deformations). To this purpose, rectilinear and planar structural configurations such as masonry columns and walls are represented respectively by means of equivalent beam and equivalent plate models.
- The non-linear behaviour of masonry, i.e. the formation of macroscopic failure mechanisms as consequence of the plastic evolution of its micro-structure. In this (large) field, the research focuses on the determination of the strength capacities of the masonry, as function

of the mechanical and geometrical properties of the building blocks and of the mortar joints.

- The modal response of masonry, i.e. the study of the inertial effects of the micro-structure (blocks kinematics) and their participation to the overall structural behaviour.

Under these goals, several aspects related to the macroscopic modelling of masonry structures are more closely investigated in this thesis:

- The domain of applicability of the continuum model, i.e. the evaluation of the scale ratio for which the efficiency of the continuum model reaches its limits in representing the actual material response.
- The solution accuracy reached by the continuum within the limits imposed by the scale ratio.
- The capacity of the continuum model to capture the scale effect intrinsic to masonry.

Continuum choice

The formulation of continuum models for masonry leads us to consider the use of the Cosserat (or micropolar) continuous medium. It is well known from the literature that this particular higher order medium allows a more detailed and efficient description of the macroscopic behaviour of masonry as compared to the classical (or Cauchy) continuum (Mühlhaus et al., 1997; Masiani et al., 1995; Sulem and Mühlhaus, 1997; Trovalusci and Masiani, 1999, 2003, 2005; Stefanou et al., 2008; Salerno and de Felice, 2009; Addessi et al., 2010; de Bellis and Addessi, 2011; Addessi and Sacco, 2012; Pau and Trovalusci, 2012). Indeed, the absence of an internal length prevents the classical continuum to capture the scale effect, wave dispersion, and the influence that the relative rotations of the building blocks have on the overall structural response. This deficiency is known today (de Borst and Sluys, 1991; Lourenço, 1996; de Buhan and de Felice, 1997; de Felice et al., 2010) and motivates the development of alternative modelling approaches for masonry, which are based on the introduction of an internal length related to its micro-structure. It is worth noticing that all the higher order continuous media are equipped with an internal length (Mindlin, 1964; Germain, 1973; Eringen, 1999). Some of them have already been used for modelling masonry, see for instance the works of Stefanou et al. (2010); Stefanou and Sulem (2012); Bacigalupo and Gambarotta (2012); Trovalusci and Pau (2014). In this thesis, the Cosserat continuum is selected among the continuous media. As it will be shown, its formulation is relatively simple (limited number of variables and with clear physical meaning) and is flexible enough to accommodate pronounced micro-structural effects.

Modelling strategy

In order to achieve the research goals introduced above, a modelling strategy is followed in the present thesis. This consists in:

- (1) Formulating a continuum model for masonry, i.e. the constitutive laws and yield criteria that are capable of reproducing (on the average sense) the actual material response. The development and the use of homogenisation techniques is made. These techniques are referred to the Cosserat continuum.

- (2) Developing a numerical tool in order to implement the formulated continuum model and carry out simulations on more complex structural configurations. This new tool is based on the Finite Elements Method, herein formulated in the framework of the micropolar theory.
- (3) Validating the continuum model for masonry incorporated into the finite element procedure, by comparing its response with that of an analogue discrete model. The Discrete Elements Method is used for the construction of the analogue model.

Outline of the thesis

The structure of the thesis reflects the outlined modelling strategy. Its content is organized as follows:

- [Chapter 1](#) reports the development of an analytical homogenisation method for the evaluation of the in-plane strength of masonry. The method is presented as the extension to the Cosserat continuum of a procedure formulated in the literature for the Cauchy continuum. It is based on the two-dimensional micropolar continuum theory and makes use of the kinematic approach of limit analysis in conjunction with a rigorous homogenisation technique. The method is first presented with regard to a generic periodic collection of rigid blocks in contact. Next it is generalized to the whole class of discrete periodic media made of particles of the same type. The case of masonry is presented as application. The homogenised strength domains of masonry columns and walls are formulated in terms of the deformation measures of the Cosserat continuum. They are then projected into the space of the generalized stresses and couple stresses. This allows to retrieve the homogenised yield criteria for masonry. The formulation of the method based on the Cosserat continuum enables to investigate the influence of the relative rotation of the particles on the strength of the discrete medium. This influence is highlighted by the application to masonry, in comparison with the method based on the Cauchy continuum.
- [Chapter 2](#) continues the development of the method presented in the previous Chapter, by extending it to the evaluation of the coupled in-plane and out-of-plane strength of masonry. The method is illustrated first for discrete periodic media made of particles disposed along three directions and showing three periodicity vectors. It relies on the use of the kinematic approach of limit analysis, developed, in this case, within the framework of the three-dimensional micropolar theory. This enables to capture the three-dimensional effect of both the relative translations and the relative rotations of the particles constituting the discrete medium. The application to masonry columns and walls shows how the in-plane and out-of-plane actions are coupled in the assessment of masonry strength. The relative rotations of the blocks accentuate this effect, which reduces the in-plane strength and suggests the use of three-dimensional models for masonry. Masonry walls are ascribed at the end of this Chapter to homogenised plates with Cosserat kinematics.
- [Chapter 3](#) describes the formulation and the validation of a specific finite element for Cosserat plate models. The finite element formulation is given in detailed form for elasticity and dynamics. The validation of the element is made by means of numerical benchmarks and patch tests. The choice of the interpolation order and the degree of integration of the stiffness and the mass matrices are discussed. The possibility of numerical deficiencies accompanying the occurrence of hourglass modes and the assembly of shell structures is explored. The shear locking phenomenon is also investigated. The actual use of the

element is presented in an application to masonry structures, where the natural frequencies of a masonry panel modelled by discrete elements are computed and compared with those given by a homogenisation model implemented in the element. This allows also to investigate the role of the in-plane rotations of the blocks and its implication towards seismic analyses of masonry structures.

- [Chapter 4](#) reports the extension of the finite element presented in the previous Chapter to the elastoplastic framework. The implementation of the multisurface strain-hardening plasticity theory into the Cosserat finite element formulation is presented in extensive manner. The implementation of this theory is based on a projection algorithm, whose solution iterative scheme formulated for implicit time-integration procedures is described. Attention focuses on several numerical aspects concerning the element implementation. An important limitation of the classical implementation of the solution algorithm prevents its use in the framework of multisurface plasticity in an efficient way. This limitation is discussed and a solution strategy is proposed. The finite element for Cosserat plate models is next validated. Numerous numerical benchmarks show its performance in problems involving multiple plastic surfaces, perfect plasticity and strain localisation.
- [Chapter 5](#) concludes the thesis, by investigating the scale effect in the formation of failure mechanisms in masonry structures. Three different modelling strategies for masonry are proposed and compared. A homogenisation model based on the Cosserat continuum is first presented in the framework of the multisurface plasticity theory. The model is constructed by implementing the homogenised yield criteria computed in the previous Chapters into the developed Cosserat finite element. A second homogenisation model based on Cauchy continuum is introduced. This model is constructed by selecting appropriate constitutive laws and yield criteria from the literature. The performance of those homogenisation models in representing the elastoplastic response of a masonry panel is discussed, based on the comparison with a third analogue discrete elements model. The capability of the three models in predicting the scale effect in a practical application is investigated.

It is worth remarking that the analytical part of the work accomplished in this thesis is mainly concentrated in [Chapter 1](#) and [Chapter 2](#). The numerical part is principally given in [Chapter 3](#) and [Chapter 4](#). [Chapter 5](#) provides further developments to the analytical work and contains an application to masonry structures. Further applications to masonry are found in the final Sections of [Chapter 3](#).

The reader may notice that different areas of research are tackled throughout the thesis (Continuum Mechanics, Computational Mechanics, Plasticity and Limit Analysis Theory, Mechanics of Structures). Therefore, in order to gain clarity, a state-of-the art will be reported at the beginning of each Chapter. On the contrary, the Appendices mentioned in the text will be presented all together at the end of the report.

Acknowledgements

This research project has been supported financially by the École des Ponts Paris-Tech and the Centre Scientifique et Technique du Bâtiment (CSTB). The commercial code 3DEC was provided by Itasca Consulting Group (www.itascacg.com) within the framework of the participation to the Itasca Education Partnership program. The author would like to thank Daniel Billiaux and José Lemos for their technical support in the use of 3DEC.

Chapter 1

Determination of the homogenised yield criteria for masonry: in-plane behaviour

This Chapter reports the development of an analytical method for the evaluation of the homogenised in-plane strength of masonry. The method is based on the two-dimensional micropolar (or Cosserat) continuum theory and makes use of the kinematic approach of limit analysis in conjunction with a homogenisation technique. The formulation of the method based on the Cosserat continuum enables to investigate the influence of the relative rotation of the blocks on the masonry strength. This influence is highlighted in view of the comparison with the method based on the Cauchy continuum.

This Chapter is a submitted paper. Its reference is [Godio et al. \(2015d\)](#).

Contents

1.1	Introduction	15
1.2	The Cosserat continuum: 2D statics and kinematics	18
1.3	The discrete medium: discrete variables and contact model	20
1.4	Homogenisation in limit analysis: average Cosserat variables and kinematic approach	23
1.4.1	Kinematic map	23
1.4.2	Average Cosserat variables	24
1.4.3	Homogenisation kinematic approach	25
1.4.4	Extension to generic periodic media	26
1.5	Application to masonry columns	27
1.5.1	Geometry	27
1.5.2	Average Cosserat variables	28
1.5.3	Homogenisation	30
1.5.4	Discussion	33
1.6	Application to masonry walls	35
1.6.1	Geometry	35
1.6.2	Average Cosserat variables	36
1.6.3	Homogenisation	40
1.7	Comparison with existing works	43
1.7.1	Comparison with de Buhan and de Felice (1997)	43
1.7.2	Comparison with Sulem and Mühlhaus (1997)	44
1.8	Conclusions	45

Summary

In the frame of Cosserat continuum theory, a homogenisation procedure for the assessment of the in-plane strength of discrete media is developed in this paper. The procedure is the extension to the Cosserat continuum of a procedure initially formulated for the Cauchy continuum, based on the kinematic approach of limit analysis and the classical homogenisation theory. The extension to the Cosserat continuum is made in order to take into account the effect of particles' rotation on the strength of the discrete medium. The procedure is illustrated with regard to periodic assemblies of blocks in contact, and then generalized to the whole class of discrete periodic media with particles of the same type. The case of masonry is considered as application. Homogenised strength criteria of columns and walls are formulated in terms of non-symmetric stresses and in-plane couples. The procedure allows to show how the in-plane strength of masonry is reduced, as a result of blocks' rotation on the material.

1.1 Introduction

In the last three decades, a renewed interest towards the Cosserat (or micropolar) continuum has driven researchers to the development of specific models for masonry. Since the original works of Besdo (1985); Mühlhaus (1989); Masiani et al. (1995); Dai et al. (1996); Mühlhaus et al. (1997); Sulem and Mühlhaus (1997) up to the more recent of Stefanou et al. (2008); Addessi et al. (2010); Addessi and Sacco (2012), the resort to the Cosserat continuum has seemed motivated by the advantages enclosed in its enhanced kinematics and the non-symmetry of the stress tensor. Indeed, when used for the formulation of continuum equivalent models for masonry, Cosserat continuum allows to efficiently take into account high deformation gradients (Trovalusci and Masiani, 2005), relative blocks' rotation (Pau and Trovalusci, 2012) and scale effects (Salerno and de Felice, 2009; Godio et al., 2015a). Moreover, Cosserat continuum enables the investigation of the phenomenon of wave dispersion, which governs the dynamic response of periodic media such as masonry (Pain, 2005; Mühlhaus et al., 1997; Sulem and Mühlhaus, 1997; Stefanou et al., 2008). Those aspects makes Cosserat-continuum-based models particularly well suited for the description of the mechanical behaviour of masonry structures and preferable, in this sense, with respect to models based on the Cauchy continuum (Salerno and de Felice, 2009) or the second gradient continuum (Trovalusci and Pau, 2014).

The aforementioned features of the Cosserat continuum are strictly related to rotations. Contrary to the Cauchy continuum, rotations in micropolar continua are inherent to the medium, i.e. attached to the material particle (Germain, 1973; Vardoulakis and Sulem, 1995). Many works have shown how, aiming at representing masonry as an equivalent Cosserat continuum, these rotations are actually representative of blocks' rotations. They enable a continuum description of the medium which is capable to capture not only the relative rotations occurring between the blocks, but also their relative rotations with respect to the local rigid rotation of masonry considered as a whole (Pau and Trovalusci, 2012). The role of rotations is even more apparent in the dynamic regime. Whether regarding the in-plane (Mühlhaus et al., 1997; Sulem and Mühlhaus, 1997) or the out-of-plane behaviour (Stefanou et al., 2008), the mechanical response of masonry is governed by translational and rotational waves. Only their superposition gives the complete structural response. Therefore, blocks' rotations can have a significant participation in the inertial response of masonry, for instance when this latter is subjected to in-plane seismic excitations (Godio et al., 2015a).

On the other hand, the effect of blocks' rotations on masonry behaviour is not always apparent. In general, blocks' rotations account for the overall deformation of masonry for as little as their relative size with the structure (scale effect). Hence, when blocks are small as compared to the size of the whole structure, the effect of their rotation tends to vanish (Trovalusci and Masiani, 1999, 2005; Salerno and de Felice, 2009).

Nevertheless, the influence of blocks' rotations on the performance of masonry can be far more important than this proportion indicates. Indeed, the rotation of the blocks contributes to the relative displacements across the joints, which, in many cases, are the main responsible for the deformation of masonry. This may promote the formation of irreversible inelastic deformations within masonry and lead, consequently, to the premature development of macroscopic failure mechanisms. Even though this aspect is visible in the majority of the experimental tests carried out on masonry structures (see the recent tests by Petry and Beyer (2014a)), it has been seldom explored in the corresponding literature, see for instance Besdo (1985); Sulem and Mühlhaus (1997); Trovalusci and Masiani (2003, 2005); Addessi and Sacco (2012).

By way of example, we refer to classical full-scale tests made on masonry shear walls, as those reported and modelled by Lourenço (1996), see Figure 1.1. Regarding the test on the shear wall without opening (Figure 1.1-left), consequent to the increasing of the horizontal displacement,

deformation tends to concentrate within masonry in a band of finite size. As observed by [Lourenço \(1996\)](#), this band goes from one corner of the wall to the other, and leads, at failure, to the formation of two distinct regions under compression (struts). Band formation is initiated by blocks' slip, which is mainly due to joints' sliding. This is formerly limited to the central region of the wall. Upon load increase, however, the band tends to cover a larger region of wall and to propagate progressively towards the wall corners. This is accompanied by the rotation of groups of blocks (highlighted in [Figure 1.1](#)) that are closed to the wall corners. On the one hand, their rotation promotes the formation of gaps between the blocks, due to joints' opening and blocks' cracking, and allows the diagonal band to propagate. On the other hand, it leads to the compression failure of the blocks positioned at the corners (toe crushing). This phenomena are even more accentuated if one regards the shear wall with opening ([Figure 1.1-right](#)). Therein, the same mechanisms are responsible for the deformation of the wall. Moreover, the presence of the opening leads to a failure mechanism with two groups of blocks undergoing an apparent rigid-body rotation ([Lourenço, 1996](#)).

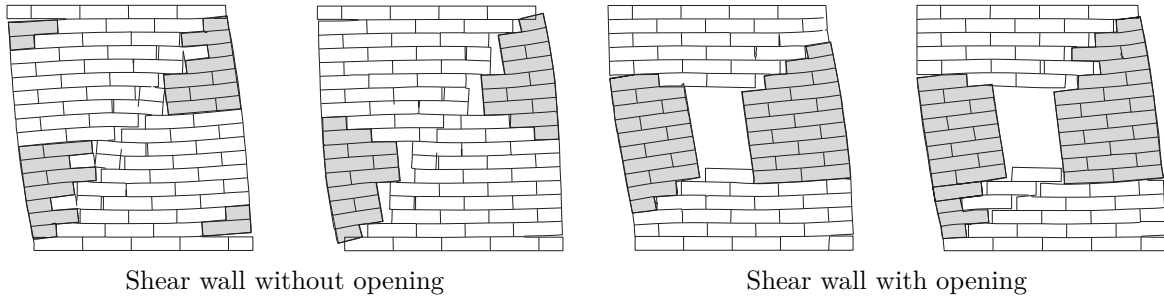


Figure 1.1: The occurrence of blocks' rotation (in grey) in the formation of failure mechanisms in masonry shear walls. Reference to the shear walls modelled by [Lourenço \(1996\)](#).

The problem of the influence of blocks' rotations on the strength capacity of masonry is addressed in this paper. Herein, the purpose is to determine the overall in-plane strength of masonry, by means of a rigorous homogenisation procedure specifically developed in the frame of Cosserat continuum theory. At the microscopic level, masonry is regarded as a discrete medium, i.e. an assemblage of rigid blocks. The blocks interact with each other through Coulomb interfaces, representing the masonry joints. Failure corresponds to the use of the strength capacities of the joints only, and not of the blocks, which are considered infinitely resistant. In particular, whether engendered by the relative blocks' translation or by the relative blocks' rotation, joints' failure is accounted for by a unique Coulomb slip criterion. At the macroscopic level, masonry is ascribed to a 2D Cosserat continuum. The determination of its overall strength is made with reference to the kinematic approach of limit analysis and homogenisation. Originally developed for classical continua ([Suquet, 1983](#)) the approach is here extended to the micropolar continua.

It is to note that a considerable amount of literature is devoted to the modelling of the in-plane strength of masonry. For instance, one may mention the works of [Baggio and Trovalusci \(1998\)](#); [Pietruszczak and Ushaksaraei \(2003\)](#); [Mojsilović \(2011\)](#). Concerning the use of homogenisation models, other than the aforementioned works, one may cite [de Buhan and de Felice \(1997\)](#); [Sab \(2003\)](#); [Massart et al. \(2004\)](#); [Milani et al. \(2006a,b\)](#); [Sab et al. \(2007\)](#); [Chettah et al. \(2013\)](#); [Stefanou et al. \(2015\)](#); [Milani and Taliervo \(2015\)](#). However, a very limited number of works have shown the use of Cosserat medium for the evaluation of masonry strength. [Sulem and Mühlhaus \(1997\)](#) proposed strength criteria for masonry in the framework of plasticity theory formulated for Cosserat materials (see also [Besdo \(1985\)](#); [Mühlhaus \(1989\)](#); [Dai et al. \(1996\)](#)). In their work, masonry was regarded as an assemblage of blocks. The criteria were

constructed by considering relevant failure mechanisms at the blocks' level, and formulated at the macroscopic level by adopting a micropolar continuum. On the same assumption of masonry as a discrete medium were based the works of [Trovalusci and Masiani \(2003, 2005\)](#). However, in that case the strength criteria were not computed explicitly. Failure mechanisms at the joints were formulated and integrated in a numerical procedure for the assessment of masonry overall behaviour. The procedure was based on the identification of the contact stresses exchanged by the blocks with the stress measures of the Cosserat continuum. [Addessi et al. \(2010\)](#) and [Addessi and Sacco \(2012\)](#) developed a sophisticated numerical homogenisation procedure, based on the Transformation Field Analysis technique. Masonry was assumed as a composite Cauchy material at the microscopic level. The transition to the Cosserat continuum at the macroscopic level was made by means of a specific kinematic map ([Forest and Sab, 1998](#)). The same map was employed in the work of [de Bellis and Addessi \(2011\)](#).

The present work represents somehow the extension of the homogenisation procedure proposed by [de Buhan and de Felice \(1997\)](#) based on the Cauchy continuum, to the Cosserat continuum. [de Buhan and de Felice \(1997\)](#) made use of the kinematic limit analysis approach ([Suquet, 1983](#)) in order to derive the homogenised strength of masonry. Since the strength properties of the joints were considered significantly lower than those of the blocks, the implementation of the kinematic approach required the use of failure mechanisms involving the relative displacements across the joints. In the frame of a Cauchy continuum, this amounted to consider the relative blocks' translations only, and neglect the relative blocks' rotations. In that case, the resulting yield criteria gave an upper bound of the researched strength domain, and were formulated in terms of symmetric macroscopic in-plane stresses. In this paper, the work of [de Buhan and de Felice \(1997\)](#) is extended and generalized in order to take into account both relative blocks' translation and relative blocks' rotation. This is made by adopting a Cosserat continuum at the macroscopic scale. Hence, the resulting yield criteria are expressed in terms of non-symmetric in-plane stresses and couple stresses. It is worth noticing that the resort to the micropolar theory for the assessment of masonry in-plane strength was indicated by [de Buhan and de Felice \(1997\)](#) as crucial for capturing the scale effect observed in the failure mechanisms resulted from full-scale tests. Therefore, although the yield criteria computed for the Cosserat continuum may always give upper bounds of the researched strength domain, they are supposed to be better estimates of the *actual* strength capacity of the material, as compared to those computed for the Cauchy continuum by [de Buhan and de Felice \(1997\)](#). The reason may be found, once again, in the enhanced kinematics of the adopted continuum. On the one hand, they provide an improved estimation of the dissipated power. On the other hand, they allow a finer reproduction of the deformation modes and failure mechanisms of the medium (see the upper bound theorem of limit analysis).

At present, very few works have shown the use of the Cosserat medium in problems related to limit analysis and homogenisation. Concerning reinforced soils and rocks mechanics, one can mention [de Buhan et al. \(1998\)](#) and [de Buhan et al. \(2002\)](#). Herein, the extension of the classical homogenisation theory to the Cosserat continuum is made in a rigorous, extensive and general way, with regard to discrete periodic media having particles of the same type (*mono-atomic* pattern). The resulting homogenisation procedure is thus general, and may apply to the whole class of materials with periodic inner micro-structure ([Eringen, 1999](#)), to which also masonry belongs.

The paper has the following structure. The first part is devoted to the extension of the kinematic limit analysis homogenisation approach to the Cosserat continuum. A brief summary of the equations governing the micropolar medium is first given in [Section 1.2](#). The contact model adopted for the discrete media and on which homogenisation is illustrated, is presented next in [Section 1.3](#). Cosserat macroscopic variables are then computed as average values of

the discrete ones. The homogenisation procedure is presented for the contact model first and it is then generalized for generic discrete media (Section 1.4). Further in Section 1.5 and Section 1.6, two applications are described. In Section 1.5 homogenisation is carried on the illustrative example of a simple masonry column. In Section 1.6, homogenisation is performed on a masonry wall, with building blocks arranged following a generic periodic pattern and interface joints showing different dissipative properties depending on their orientation. In each case, the expression of the homogenised strength domain is derived, as function of the geometry of the blocks, the distance at which blocks of alternate courses are laid, and the mobilized joints friction angle and cohesion. Comparisons with existing works are made in Section 1.7, allowing to show the advantages of the presented homogenisation procedure and to highlight the role of relative blocks' rotations in the evaluation of masonry in-plane strength.

Indicial notation is adopted throughout the paper, with Greek indices $\alpha, \beta, \gamma, \dots$ ranging between 1 and 2. Einstein summation applies for repeated indices. Lower case letters denote variables referring to the discrete medium, while upper case letters refer to the macroscopic variables of the Cosserat continuum. Partial differentiation with respect to orthogonal coordinates is denoted with $[\]_{\alpha, \beta}$, while $\partial_{X_\beta} [\]_\alpha$ designates tensor derivative. Time derivative $[\]_{\alpha, t}$ is indicated with $[\]_{\alpha, \dot{}}$.

1.2 The Cosserat continuum: 2D statics and kinematics

Cosserat (or micropolar) continuum is a special case of a micromorphic continuum of first order (Eringen, 1999; Germain, 1973; Godio et al., 2015a). In this case, the material particle is associated with a rigid oriented triad (Figure 1.2) which, when the medium undergoes deformation, experiences displacement velocities V_α (or translations), and angular displacement velocities Ω^c (or rotations). The rate of the linear deformation measures of the medium, is given by two second order tensors (Schaefer, 1967; Germain, 1973; Vardoulakis and Sulem, 1995). The first deformation tensor, denoted by $\Gamma_{\alpha\beta}$, accounts for the relative deformation occurring between the rate of the displacement gradient $D_{\alpha\beta}$ and the Cosserat (or particle) rotation Ω^c :

$$\Gamma_{\alpha\beta} = D_{\alpha\beta} + e_{\alpha\beta}\Omega^c, \quad (1.1)$$

with:

$$D_{\alpha\beta} = V_{\alpha, \beta}, \quad (1.2)$$

and $e_{\alpha\beta}$ the 2D Levi-Civita's symbol. $\Gamma_{\alpha\beta}$ is a non-symmetric tensor, and is decomposed into its symmetric $\Gamma_{(\alpha\beta)}$ and skew-symmetric $\Gamma_{[\alpha\beta]}$ parts as follows:

$$\Gamma_{\alpha\beta} = \Gamma_{(\alpha\beta)} + \Gamma_{[\alpha\beta]}, \quad (1.3)$$

reading:

$$\Gamma_{(\alpha\beta)} = D_{(\alpha\beta)}, \quad \Gamma_{[\alpha\beta]} = D_{[\alpha\beta]} + e_{\alpha\beta}\Omega^c. \quad (1.4)$$

The second deformation tensor, denoted with K_β , accounts for the rate of the rotation gradient (or curvature) of the medium. In the two-dimensional case, where only the in-plane rotations Ω^c are considered, it reduces to:

$$K_\beta = \Omega^c_{, \beta}. \quad (1.5)$$

In the Cauchy continuum the rigid triad is non-oriented (Figure 1.2), and the kinematics of the material particle, considered as a point, is described by the translations V_α only. The

deformation measures of the medium reduce then to the symmetric tensor $D_{(\alpha\beta)}$ (Eq.(1.4)-1), contrary to the Cosserat continuum, where the skew-symmetric part of the relative deformations $D_{[\alpha\beta]}$ is non-null and related to the particle rotations (Eq.(1.4)-2). The microstretch continuum is a first generalization of the Cosserat continuum (Eringen, 1999). In that case, in addition to the translations and rotations, the material particle experiences also volume changes, i.e. micro-contractions and expansions (Figure 1.2). In the micromorphic continuum the material particle is considered as fully-deformable, carrying an oriented triad and undergoing any kind of micro-deformation.

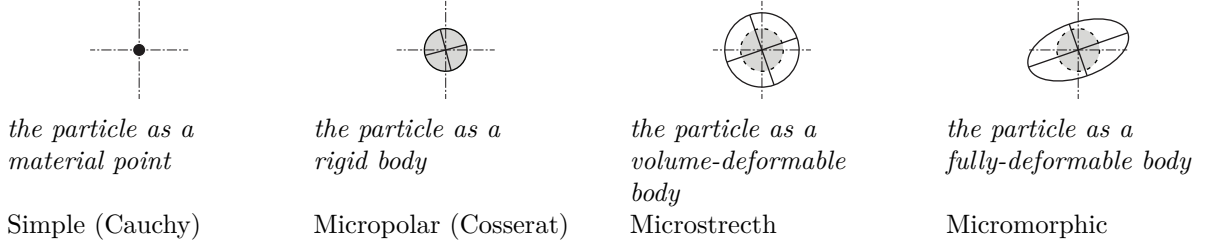


Figure 1.2: Classes of continuum media according to Eringen (1999).

Three balance equations govern the in-plane (or membrane) dynamic behaviour of a Cosserat continuum (Eringen, 1999):

$$\begin{aligned} T_{\alpha\beta,\beta} + \rho (B_\alpha - \dot{V}_\alpha) &= 0 \\ M_{\beta,\beta} - e_{\alpha\beta} T_{\alpha\beta} + \rho (L - I\dot{\Omega}^c) &= 0, \end{aligned} \quad (1.6)$$

where B_α and L are respectively the intensity of the external in-plane body forces and body couples acting on the medium, ρ the mass density of the medium, and I its micro-inertia, which represents the rotary inertia of the particle. $T_{\alpha\beta}$ and M_β denote respectively the in-plane components of the non-symmetric stress tensor and of the couple stress tensor. The convention used for those tensors follows Vardoulakis and Sulem (1995): the first index gives the direction of the component and the second index the oriented face where this component is applied (see Figure 1.3-left). With this notation, the internal power density of the Cosserat continuum reads:

$$P^c = T_{\alpha\beta} \Gamma_{\alpha\beta} + M_\beta K_\beta. \quad (1.7)$$

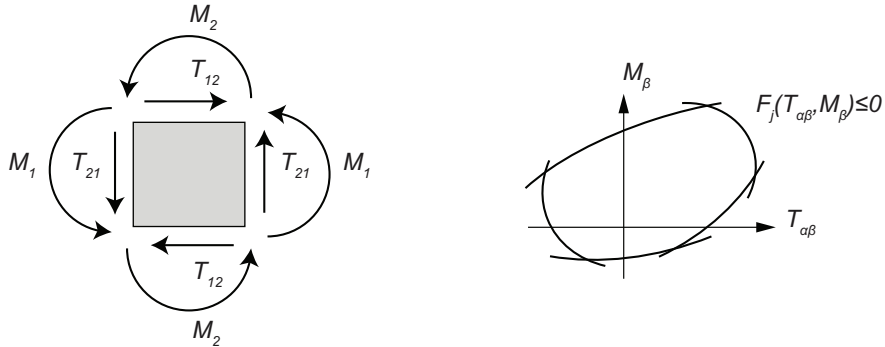


Figure 1.3: Stresses and couple stresses of a 2D Cosserat continuum (left). Its strength domain is formulated as the convex region of the generalized space $(T_{\alpha\beta}, M_\beta)$ enclosed by multiple plastic surfaces (right).

As in the Cauchy continuum, the rate of deformation is split to an elastic and plastic part:

$$\Gamma_{\alpha\beta} = \Gamma_{\alpha\beta}^e + \Gamma_{\alpha\beta}^p, \quad K_\beta = K_\beta^e + K_\beta^p. \quad (1.8)$$

A general linear constitutive law may be introduced, relating the stresses and couple stresses to the rate of the elastic deformations $(\Gamma_{\alpha\beta}^e, K_\beta^e)$. The definition of plastic potentials P_j allows to derive the plastic deformations, as in the classical plastic flow theory developed for the Cauchy continuum (Vermeer and de Borst, 1984). In the frame of Cosserat continua, those potentials are functions of both the stress and the couple stress tensors (de Borst, 1991; de Borst and Sluys, 1991): $P_j = P_j(T_{\alpha\beta}, M_\beta)$. Admitting that P_j are differentiable with respect to $T_{\alpha\beta}$ and M_β , the expression of the plastic deformation takes the following form:

$$\Gamma_{\alpha\beta}^p = \sum_{j=1}^{N_F} \lambda_j \partial_{T_{\alpha\beta}} P_j, \quad K_\beta^p = \sum_{j=1}^{N_F} \lambda_j \partial_{M_\beta} P_j, \quad (1.9)$$

with $\lambda_j \geq 0$ the consistency parameters.

In this paper we focus on the formulation of a homogenised strength domain for masonry, considered as a Cosserat equivalent continuum at the macroscopic scale. The strength domain in a Cosserat material is defined as the convex region of the generalized stress space $(T_{\alpha\beta}, M_\beta)$ which is bounded by multiple N_F and intersecting plastic surfaces $F_j = F_j(T_{\alpha\beta}, M_\beta)$, representing the yield criteria:

$$G^c = \{(T_{\alpha\beta}, M_\beta) | F_j(T_{\alpha\beta}, M_\beta) \leq 0, \forall j = 1, \dots, N_F\}. \quad (1.10)$$

Another definition of the strength domain alternative to the *direct* (Salençon, 2013) definition (1.10) follows from the expression of the maximum dissipation principle. This principle states that, during the deformation, the plastic dissipation, herein denoted with $\Pi^c = \Pi^c(\Gamma_{\alpha\beta}^p, K_\beta^p)$, attains its maximum for the actual stress tensor (Simo and Hughes, 1998). In a Cosserat medium and in the case of perfect plasticity (no hardening), the principle reads:

$$\Pi^c = \sup_{(T_{\alpha\beta}, M_\beta) \in G^c} \{T_{\alpha\beta} \Gamma_{\alpha\beta}^p + M_\beta K_\beta^p\}. \quad (1.11)$$

One recognizes in Π^c the support function of G^c . Eq.(1.11) then leads to the second, referred to as *kinematic* (Salençon, 2013), definition of the strength domain, which writes:

$$G^c = \{(T_{\alpha\beta}, M_\beta) | T_{\alpha\beta} \Gamma_{\alpha\beta}^p + M_\beta K_\beta^p \leq \Pi^c, \forall (\Gamma_{\alpha\beta}^p, K_\beta^p)\}. \quad (1.12)$$

1.3 The discrete medium: discrete variables and contact model

The structure considered for homogenisation consists of a discrete collection of rigid interacting bodies (or blocks) that translate and rotate in space. Arranged following a periodic lattice, the blocks form elementary cells in the form of geometrical figures, like rectangles, hexagons, etc. All blocks share the same shape and size. Their position within the lattice is marked in a global reference system (OY_1Y_2) by two periodicity vectors α^i ($i = 1, 2$), and reads:

$$\mathbf{Y}^{GJ} = \mathbf{Y}^{G0} + n\alpha^1 + m\alpha^2 \quad (1.13)$$

where GJ represent the centre of mass G of the block B^J , with $J = 1, \dots, N$ and $(n, m) \in \mathbb{Z}^2$. This configuration is often referred to as *mono-atomic* lattice (Kittel, 1996).

We focus on D , the elementary cell repeated in the lattice. A straightforward way to find D is to consider as lattice points of the structure, the centres of mass of the blocks GJ , and

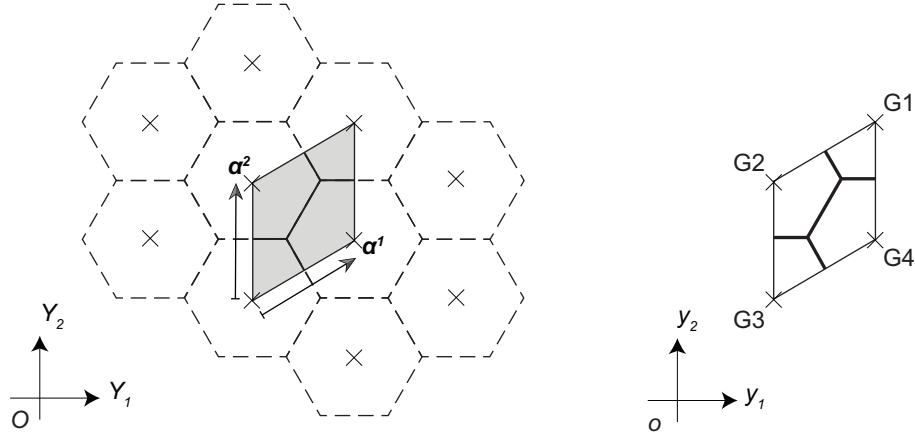


Figure 1.4: A periodic collection of discrete hexagonal blocks and the corresponding elementary cell. The elementary cell retained (right) is the parallelogram produced by the periodicity vectors.

as basis, the periodicity vectors α^i (Figure 1.4). In this way, the lattice points are kept only at the corners of the cell and the periodicity vectors coincide with the primitive basis of the lattice. This cell represents for the discrete medium the structural unit with the *smallest* surface (Kittel, 1996):

$$|D| = |\alpha^1 \times \alpha^2|. \quad (1.14)$$

A local reference system (oy_1y_2) is attached to D , and N_D denotes the number of blocks J that compose this cell (in this case $J = 1, \dots, N_D$). For rigid blocks, the kinematics of the whole cell is described by piece-wise linear distributions of the displacement and the angular displacement velocity fields v_α and ω , of the form:

$$\begin{aligned} v_\alpha^J(\mathbf{y}) &= v_\alpha^{GJ} - e_{\alpha\beta} \omega^{GJ} (y_\beta - y_\beta^{GJ}) \\ \omega^J(\mathbf{y}) &= \omega^{GJ}, \forall \mathbf{y} \in B^J, \end{aligned} \quad (1.15)$$

with v_α^{GJ} and ω^{GJ} respectively the translational and the rotational velocities of the centre of mass G of the block B^J (Figure 1.5-left):

$$\begin{aligned} v_\alpha^{GJ} &= v_\alpha(\mathbf{y}^{GJ}) \\ \omega^{GJ} &= \omega(\mathbf{y}^{GJ}). \end{aligned}$$

These kinematics represent the degrees of freedom of the discrete cell.

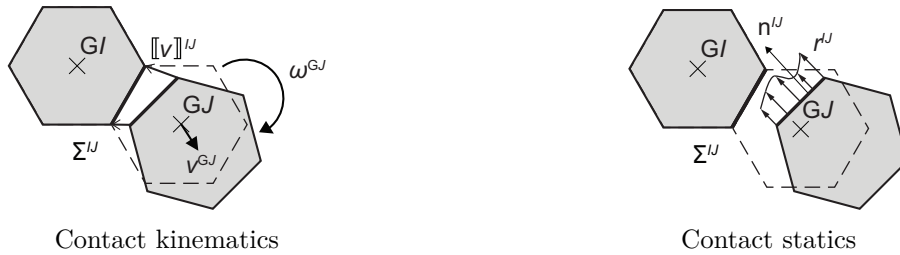


Figure 1.5: Kinematics and statics of the contact model adopted for the discrete medium.

Blocks may have arbitrary shape and their external surface may be in contact only with the surface of neighbouring blocks. In particular, the block I interacts with the adjacent block J through contact stresses r_α^{IJ} , at every point of the interface Σ^{IJ} (Figure 1.5-right). Contact stresses are associated to the displacement velocity jumps (or relative displacements) occurring across the interfaces shared by the blocks:

$$\llbracket v_\alpha \rrbracket^{IJ} = v_\alpha^I(\mathbf{y}) - v_\alpha^J(\mathbf{y}), \forall \mathbf{y} \in \Sigma^{IJ}. \quad (1.16)$$

The internal power density of the cell is then:

$$p^D = \frac{1}{|D|} \left(\sum_{IJ} \int_{\Sigma^{IJ}} r_\alpha^{IJ} \llbracket v_\alpha \rrbracket^{IJ} dL \right), \quad (1.17)$$

where the sum is made over all the interfaces of the cell.

The relative displacements (1.16) produce both gaps and slips between the blocks (see Figure 1.6). Those two basic mechanisms are due respectively to the opening (Figure 1.6-left) and the sliding (Figure 1.6-right) of the interfaces. They are described by the normal $[\]^\sigma$ and tangential $[\]^\tau$ components of the relative displacements:

$$\llbracket v_\alpha \rrbracket^\sigma = \llbracket v_\beta \rrbracket^{IJ} n_\beta^{IJ} n_\alpha^{IJ}, \quad \llbracket v_\alpha \rrbracket^\tau = \llbracket v_\alpha \rrbracket^{IJ} - \llbracket v_\alpha \rrbracket^\sigma. \quad (1.18)$$

These components are conjugate in energy to respectively the normal and tangential components of the contact stresses, reading:

$$r_\alpha^\sigma = r_\beta^{IJ} n_\beta^{IJ} n_\alpha^{IJ}, \quad r_\alpha^\tau = r_\alpha^{IJ} - r_\alpha^\sigma, \quad (1.19)$$

with n_α^{IJ} the unit vector normal to the interface Σ^{IJ} (Figure 1.5). No contact moments are considered at each point of the common interfaces. This is a reasonable assumption for the applications considered herein. Nevertheless, a transfert of moments is always possible between two adjacent blocks, as the distribution of the stresses is not necessarily constant. Resultant contact moments (or couples) are in fact those generated by first order moments of r_α^σ (Bardet and Vardoulakis, 2001). These are associated to the angular displacement velocity jumps:

$$\llbracket \omega \rrbracket^{IJ} = \omega^I - \omega^J, \quad (1.20)$$

which coincide with the rigid-body rotation jumps (relative blocks' rotations):

$$\llbracket \omega^G \rrbracket^{IJ} = \omega^{GI} - \omega^{GJ}. \quad (1.21)$$

Resultant contact forces, in turn, are generated by r_α^σ and r_α^τ , and are associated to the rigid-body displacement jumps (relative blocks' translations):

$$\llbracket v_\alpha^G \rrbracket^{IJ} = v_\alpha^{GI} - v_\alpha^{GJ}. \quad (1.22)$$

It is apparent how the relative rotations and relative translations are both related to interface failure (Figure 1.6).

The strength capacity of each interface is described by g^{IJ} , a convex domain characterised by multiple N_f yield criteria $f_j = f_j(r_\alpha^{IJ})$:

$$g^{IJ} = \{ (r_\alpha^{IJ}) \mid f_j(r_\alpha^{IJ}) \leq 0, \forall j = 1, \dots, N_f \}. \quad (1.23)$$

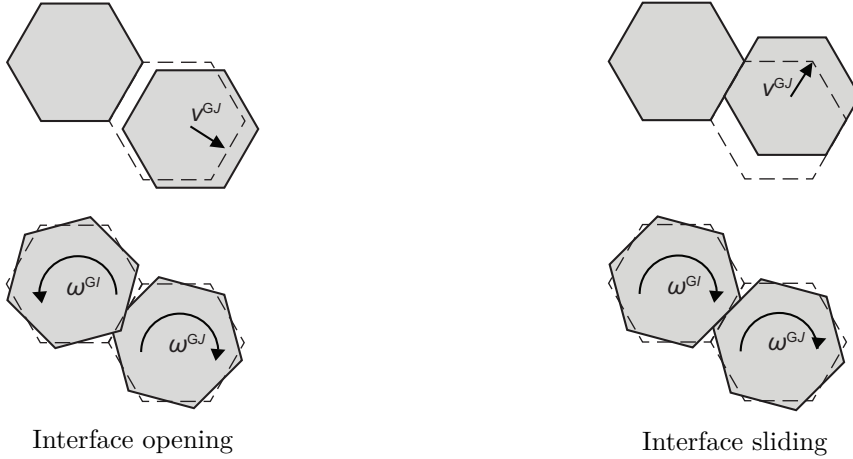


Figure 1.6: Relative translations $\llbracket v_\alpha^G \rrbracket^{IJ}$ and rotations $\llbracket \omega^G \rrbracket^{IJ}$ producing opening and sliding of the interface between two blocks. Both depicted mechanisms are related to interface failure.

A kinematic condition for the interface failure is then:

$$r_\alpha^{IJ} \in g^{IJ} \Leftrightarrow r_\alpha^{IJ} \llbracket v_\alpha \rrbracket^{IJ} \leq \pi^{IJ}, \forall \llbracket v_\alpha \rrbracket^{IJ}. \quad (1.24)$$

where the support function $\pi^{IJ} = \pi^{IJ}(\llbracket v_\alpha \rrbracket^{IJ})$ represents the maximum plastic dissipation at the interface. Its definition is as follows (Salençon, 2013):

$$\pi^{IJ} = \text{Sup}_{r_\alpha^{IJ} \in g^{IJ}} \left\{ r_\alpha^{IJ} \llbracket v_\alpha \rrbracket^{IJ} \right\}. \quad (1.25)$$

Admitting that all interfaces attain failure simultaneously and a (periodic) failure mechanism is produced within the discrete cell, the amount of plastic dissipation in D is then:

$$\pi^D(v_\alpha^{GJ}, \omega^{GJ}) = \frac{1}{|D|} \left(\sum_{IJ} \int_{\Sigma^{IJ}} \pi^{IJ}(\llbracket v_\alpha \rrbracket^{IJ}) dL \right). \quad (1.26)$$

1.4 Homogenisation in limit analysis: average Cosserat variables and kinematic approach

The purpose of homogenisation is to replace the discrete medium by a continuum homogeneous medium that has the same shape and shares the same mechanical properties with the discrete ones. What is obtained from homogenisation is therefore an equivalent material, which can be used further, for instance when implemented in appropriate finite element codes (de Felice et al., 2010; Godio et al., 2014, 2015a), for the analysis of structures. Here the discrete medium is replaced by the continuum at the cell level, by means of a kinematic map.

1.4.1 Kinematic map

We focus on the elementary cell D , and we define with $KA(\Gamma_{\alpha\beta}, K_\beta)$ the set of kinematically admissible (or compatible, Eq.(1.1)) translations and rotations $(v_\alpha^{GJ}, \omega^{GJ})$ of the cell as follows:

$$KA(\Gamma_{\alpha\beta}, K_\beta) = \left\{ (v_\alpha^{GJ}, \omega^{GJ}) \mid v_\alpha^{GJ} = D_{\alpha\beta} y_\beta^{GJ} + V_\alpha, \omega^{GJ} = K_\beta y_\beta^{GJ} + \Omega^c, \forall J = 1, \dots, N_D \right\}. \quad (1.27)$$

From a mechanical point of view, Eq.(1.27) gives the map between the kinematics of the discrete medium that we intend to homogenize, and the macroscopic deformation measures of the homogenised Cosserat continuum. Such map is linear and is defined on the elementary cell of the discrete medium. It is a special case of the map proposed by Pradel and Sab (1998), adapted for discrete media with mono-atomic pattern, i.e. composed by particles of the same size and shape.

Using the map (1.27), the displacement and angular displacement velocity fields (1.15) become:

$$\begin{aligned} v_\alpha^J(\mathbf{y}) &= (D_{\alpha\beta} + e_{\alpha\beta}\Omega^c) y_\beta^{GJ} + V_\alpha - e_{\alpha\beta} \left[K_\gamma y_\gamma^{GJ} (y_\beta - y_\beta^{GJ}) + \Omega^c y_\beta \right] \\ \omega^J(\mathbf{y}) &= K_\beta y_\beta^{GJ} + \Omega^c, \forall \mathbf{y} \in B^J. \end{aligned} \quad (1.28)$$

Eq.(1.28) constitutes an alternative definition to (1.27) of kinematically admissible displacement and angular displacement velocity fields obeying Eq.(1.15). This definition can be used for homogenisation, as illustrated next for the presented contact model.

1.4.2 Average Cosserat variables

In Eq.(1.28) one recognizes the rate of macroscopic relative deformation of the Cosserat continuum $\Gamma_{\alpha\beta}$, as defined by Eq.(1.1), together with the macroscopic curvature K_β , Eq.(1.5). Here $\Gamma_{\alpha\beta}$ and K_β have a precise physical meaning, as they represent the average Cosserat deformation measures of the discrete cell. Their expression follows straightforwardly from the map (1.27), and depends on the selected cell D . When the cell is constructed as illustrated in Section 1.3 and the local reference system is attached to the centre of mass of the cell, $\Gamma_{\alpha\beta}$ and K_β write:

$$\Gamma_{\alpha\beta} = \frac{1}{|D|} \left(\sum_{IJ} \int_{\Sigma^{IJ}} \llbracket v_\alpha \rrbracket^{IJ} n_\beta^{IJ} dL \right) \quad (1.29)$$

$$K_\beta = \frac{1}{|D|} \left(\sum_{IJ} \int_{\Sigma^{IJ}} \llbracket \omega \rrbracket^{IJ} n_\beta^{IJ} dL \right), \quad (1.30)$$

with the relative displacement and rotations from Eqs.(1.16) and (1.20). By definition, $\Gamma_{\alpha\beta}$ gather the displacement gradient $D_{\alpha\beta}$ and the Cosserat rotation Ω^c . The former is identified with the average value of the relative blocks' translations (1.22), i.e.:

$$D_{\alpha\beta} = \frac{1}{|D|} \left(\sum_{IJ} \int_{\Sigma^{IJ}} \llbracket v_\alpha^G \rrbracket^{IJ} n_\beta^{IJ} dL \right). \quad (1.31)$$

The latter, Ω^c , is the average rigid-body cell rotation:

$$\Omega^c = \frac{1}{|D|} \left(\sum_{J=1}^{N_D} \int_{B^J} \omega^J dS \right). \quad (1.32)$$

Similarly, V_α is the average rigid-body cell translation:

$$V_\alpha = \frac{1}{|D|} \left(\sum_{J=1}^{N_D} \int_{B^J} v_\alpha^J dS \right). \quad (1.33)$$

For the demonstration of Eqs.(1.29)-(1.33) the reader is referred to Appendix A.1. It is also worth pointing out that, for the Cauchy continuum, the only average deformation measure would be (de Buhan and de Felice, 1997):

$$D_{(\alpha\beta)} = \frac{1}{|D|} \left(\sum_{IJ} \frac{1}{2} \int_{\Sigma^{IJ}} \left(\llbracket v_\alpha^G \rrbracket^{IJ} n_\beta^{IJ} + \llbracket v_\beta^G \rrbracket^{IJ} n_\alpha^{IJ} \right) dL \right). \quad (1.34)$$

By substituting Eq.(1.28) into the expression of the internal power density of the cell p^D (Eq.(1.17)), one retrieves:

$$p^D = T_{\alpha\beta} \Gamma_{\alpha\beta} + M_\beta K_\beta, \quad (1.35)$$

where the non-symmetric macroscopic stresses:

$$T_{\alpha\beta} = \frac{1}{|D|} \left(\sum_{IJ} \int_{\Sigma^{IJ}} r_\alpha^{IJ} l_\beta^{IJ} dL \right) \quad (1.36)$$

and the macroscopic couple stresses:

$$M_\beta = \frac{1}{|D|} \left(\sum_{IJ} \int_{\Sigma^{IJ}} -e_{\alpha\gamma} r_\alpha^{IJ} \left(y_\gamma l_\beta^{IJ} - y_\gamma^{GI} y_\beta^{GI} + y_\gamma^{GJ} y_\beta^{GJ} \right) dL \right) \quad (1.37)$$

are found to be the average values of the contact stress distributions exchanged between the blocks of the cell. In the above, l_β^{IJ} is the vector connecting the centre of mass of two adjacent blocks I and J : $l_\beta^{IJ} = y_\beta^{GI} - y_\beta^{GJ}$. The physical meaning of the deformation and stress measures of the Cosserat continuum with respect to those of the presented contact model is clear from the above equations.

1.4.3 Homogenisation kinematic approach

In the present paper, homogenisation is carried out in the framework of limit analysis. In this case, one aims at substituting the discrete by a continuum medium that has similar deformation modes (Eqs.(1.29)-(1.33)) and equivalent dissipation properties. In such context, the principle of maximum plastic dissipation expressed for the Cosserat (Eq.(1.11)) and the discrete medium (Eq.(1.25)) plays a fundamental role. This principle has, as main implications (Simo and Hughes, 1998): a) the condition for the plastic potentials of being associative, and b) the convexity of the strength domain in the stress space. The same results hold true when the plasticity theory is formulated in the space of the deformations, for materials with elastic-perfectly plastic behaviour (Naghdi and Trapp, 1975). Under these assumptions the two fundamental theorems of limit analysis are applicable.

The homogenisation procedure followed in this paper is the extension to the Cosserat continuum of a procedure initially formulated for the Cauchy continua (Suquet, 1983). This procedure is based on the upper bound theorem of limit analysis, and therefore is called *kinematic approach* within the framework of the yield design theory, see also Salençon (2013). Formulated for the Cosserat continuum, the homogenisation kinematic approach consists in finding among the established displacement and angular displacement velocity fields (in this case Eq.(1.28)), the sets of kinematically admissible blocks' translations and rotations $(v_\alpha^{GJ}, \omega^{GJ}) \in KA(\Gamma_{\alpha\beta}, K_\beta)$ that solves the following problem:

$$\Pi^{c,hom}(\Gamma_{\alpha\beta}^p, K_\beta^p) = \pi^D(v_\alpha^{GJ}, \omega^{GJ}). \quad (1.38)$$

The above equation equates the maximum plastic dissipation density produced by the discrete cell π^D (Eq.(1.26)) with $\Pi^{c,hom}$, representing the maximum plastic dissipation of the *homogenised* Cosserat continuum (Eq.(1.11)). It should be mentioned that the choice of compatible $KA(\Gamma_{\alpha\beta}, K_\beta)$ sets of translations and rotations is not arbitrary. Solution to the above problem is found only when the kinematics of the discrete medium obey the map (1.27), and generate on the elementary cell plastic dissipation of finite value, i.e.:

$$\pi^D(v_\alpha^{GJ}, \omega^{GJ}) < \infty. \quad (1.39)$$

This condition is essential in the construction of compatible sets of kinematics, and homogenisation may be carried out only when Eq.(1.38) is used in conjunction with it.

The kinematic definition of the Cosserat homogenised strength domain $G^{c,hom}$ follows immediately from the expression of $\Pi^{c,hom}$. This latter is identified as the support function of $G^{c,hom}$ (Eq.(1.12)):

$$G^{c,hom} = \{(T_{\alpha\beta}, M_\beta) | T_{\alpha\beta} \Gamma_{\alpha\beta}^p + M_\beta K_\beta^p \leq \Pi^{c,hom}, \forall (\Gamma_{\alpha\beta}^p, K_\beta^p)\}. \quad (1.40)$$

The resulting homogenisation procedure is illustrated in Figure 1.7. It is worth emphasizing that, as a result of the kinematic approach, Eq.(1.40) provides upper bound estimates of the actual strength capacity of the discrete medium.

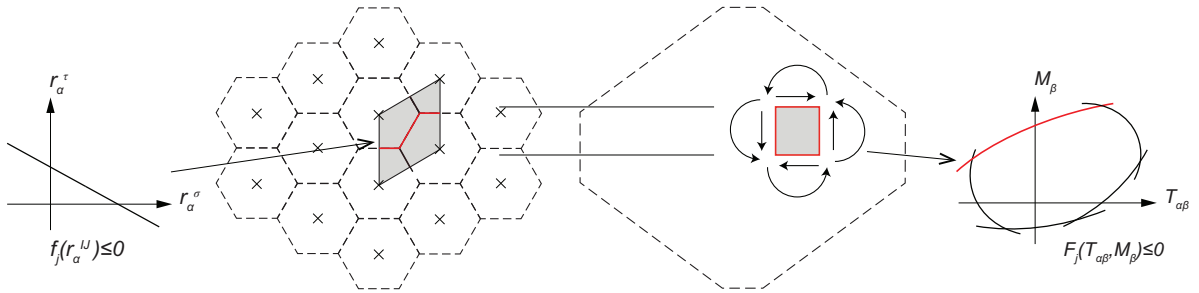


Figure 1.7: Homogenisation based on the Cosserat continuum is carried out in the frame of limit analysis on a periodic collection of rigid particles. Starting from a failure criterion (left) expressed at the interfaces of the discrete medium (in red), it is possible to retrieve the homogenised yield criterion for the macroscopic Cosserat continuum (right). The resulting homogenised strength domain is the region of the generalized stress space $(T_{\alpha\beta}, M_\beta)$ enclosed by these yield criteria.

1.4.4 Extension to generic periodic media

The homogenisation procedure has been illustrated according to the contact model presented in Section 1.3, see Figure 1.7. Such model is representative of a class of media, like soils, fractured rock masses, masonry structures, etc. Nevertheless, the proposed procedure can cover the whole class of discrete periodic media with mono-atomic pattern. An example of application is given in Figure 1.8, where a grid-work is represented, based on the same mono-atomic lattice used for the contact model (Figure 1.4). In this case, the lattice points represent the nodes of the grid-work. It is clear that, when these latter are considered rigid, the kinematic description of the whole medium reduces to the degrees of freedom of the nodes, and a micropolar description of the medium can be then attempted (Kumar and McDowell, 2004).

The same considerations apply for generic discrete media, where translations and rotations may always be attached to the distinct interacting particles. Therefore, starting from the

kinematics $(v_\alpha^{GJ}, \omega^{GJ})$ of a pair of particles I and J , it is possible to define in a general way the following generalized deformation measures (Florence and Sab, 2006):

$$\begin{aligned} d_\alpha^{IJ} &= \llbracket v_\alpha^G \rrbracket^{IJ} + e_{\alpha\beta} l_\beta^{IJ} \frac{\omega^{GI} + \omega^{GJ}}{2} \\ \delta^{IJ} &= \llbracket \omega^G \rrbracket^{IJ}. \end{aligned} \quad (1.41)$$

Without the need of specifying the power-conjugate variables, the power dissipated by the pair of particles is function of the above deformations: $\hat{\pi}^{IJ} = \hat{\pi}^{IJ}(d_\alpha^{IJ}, \delta^{IJ})$. Hence, the amount of plastic dissipation density on the cell writes:

$$\pi^D(v_\alpha^{GJ}, \omega^{GJ}) = \frac{1}{|D|} \left(\sum_{IJ} \hat{\pi}^{IJ}(d_\alpha^{IJ}, \delta^{IJ}) \right). \quad (1.42)$$

where, in this case, the sum is made over all the particle pairs of the cell, see Eq.(1.26). Notice that the particle pairs shared by adjacent cells will be accounted by half of their power. homogenisation is made over the discrete medium as illustrated in the previous sections. The map (1.27) allows to substitute the Cosserat continuum into the generic discrete medium, by reproducing its kinematics and deformation modes (Eqs.(1.29)-(1.33)). Eq.(1.38) then assures that the two media have equivalent plastic dissipation.

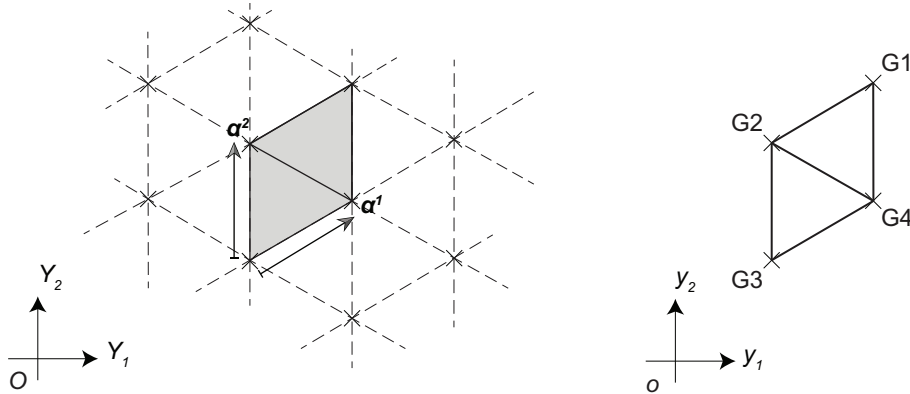


Figure 1.8: A periodic collection of beams disposed following a mono-atomic lattice (left), and the corresponding elementary cell (right).

1.5 Application to masonry columns

The method illustrated in Section 1.4 is herein applied to the case of masonry columns made of distinct blocks of the same type. For simplicity, the superscript p will be neglected next. The rate of plastic deformations to which the continuum undergoes, will be noted generally as a total rate of (irreversible) deformation. Consistently, but not restrictively, we are assuming that blocks' interaction in masonry has a rigid-plastic behaviour.

1.5.1 Geometry

Masonry columns are quasi periodic assemblages of rectangular blocks (Figure 1.9). Here the blocks are stacked in the vertical (y_2) direction following a regular pattern. The height and the

width of each block are denoted respectively with a and b . In such situation, a single vector describes the period of the structure, that is:

$$\boldsymbol{\alpha}^1 = 0\mathbf{e}_1 + a\mathbf{e}_2.$$

The elementary cell of Figure 1.9 is considered. It consists of two adjacent half-blocks B^J (the block B^1 and the block B^2) sharing a single interface, Σ^{12} . Denoted with B , and referred to a specific local coordinate system (oy_1y_2) attached to its center, the elementary cell is defined as:

$$B = \left[-\frac{b}{2}, +\frac{b}{2}\right] \times \left[-\frac{a}{2}, +\frac{a}{2}\right].$$

The position of the centre of mass of each block is then:

$$\begin{aligned} \mathbf{y}^{\mathbf{G}1} &= 0\mathbf{e}_1 + \frac{a}{2}\mathbf{e}_2 \\ \mathbf{y}^{\mathbf{G}2} &= 0\mathbf{e}_1 - \frac{a}{2}\mathbf{e}_2. \end{aligned}$$

The interface between the blocks is located at:

$$\mathbf{y}^{\Sigma^{12}} = y_1\mathbf{e}_1 + 0\mathbf{e}_2, \forall y_1 \in \left[-\frac{b}{2}, +\frac{b}{2}\right]$$

and its unit normal vector is $\mathbf{n}^{12} = \mathbf{e}_2$.

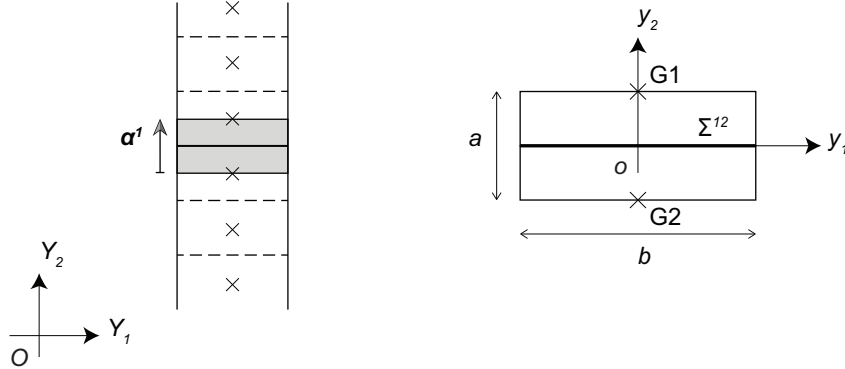


Figure 1.9: Periodic masonry column (left) and the corresponding elementary cell (right).

1.5.2 Average Cosserat variables

We assume that each block B^J is a rigid body. Consequently, the kinematics of the masonry column is described by piece-wise linear distributions of the displacement and angular displacement velocity fields of the form (1.15). In this case, and for the elementary cell considered, the map (1.27) giving the kinematically admissible sets $(v_\alpha^{\mathbf{G}J}, \omega^{\mathbf{G}J}) \in KA(\Gamma_{\alpha\beta}, K_\beta)$ yields:

$$\begin{aligned} &KA(\Gamma_{\alpha 2}, K_2) = \\ &\left\{ \left(v_\alpha^{\mathbf{G}J}, \omega^{\mathbf{G}J} \right) \mid v_\alpha^{\mathbf{G}J} = D_{\alpha 2} y_2^{\mathbf{G}J} + V_\alpha, \omega^{\mathbf{G}J} = K_2 y_2^{\mathbf{G}J} + \Omega^c, \forall J = 1, 2 \right\}, \end{aligned} \quad (1.43)$$

with $\alpha = 1, 2$. Similarly, the resulting displacement and angular displacement field distributions (Eq.(1.28)) read:

$$\begin{aligned} v_\alpha^J(\mathbf{y}) &= \Gamma_{\alpha 2} y_2^{\mathbf{G}J} + V_\alpha - e_{\alpha\beta} \left[K_2 y_2^{\mathbf{G}J} (y_\beta - y_\beta^{\mathbf{G}J}) + \Omega^c y_\beta \right] \\ \omega^J(\mathbf{y}) &= K_2 y_2^{\mathbf{G}J} + \Omega^c, \forall \mathbf{y} \in B^J. \end{aligned} \quad (1.44)$$

The above equations consist in a limited number of terms of macroscopic deformation. With respect to the general form (1.28), where all the Cosserat deformation measures ($\Gamma_{\alpha\beta}, K_\beta$) are present, the only available deformation measures in Eq.(1.44) are $\Gamma_{\alpha 2}$ and K_2 . This results from the geometry of the discrete structure considered. Here, the blocks are arranged following a periodic lattice that is developed along one periodicity vector α^1 . The orientation of the interface is perpendicular to this vector. For such configuration, replacing the general form (1.28) into Eqs.(1.29)-(1.30) leads to:

$$\Gamma_{\alpha 1} = 0, \quad K_1 = 0. \quad (1.45)$$

The remaining macroscopic deformation measures ($\Gamma_{\alpha 2}, K_2$) presented in Eq.(1.44) are produced by combinations of in-plane rigid-body motions (i.e. translations and rotations) of the blocks that compose the cell (see Figure 1.10). Their expression reads from Eqs.(1.29)-(1.30) as follows:

$$\Gamma_{\alpha 2} = D_{\alpha 2} + e_{\alpha 2} \Omega^c, \quad K_2 = \frac{\omega^{G1} - \omega^{G2}}{a}, \quad (1.46)$$

where:

$$D_{\alpha 2} = \frac{v_\alpha^{G1} - v_\alpha^{G2}}{a}. \quad (1.47)$$

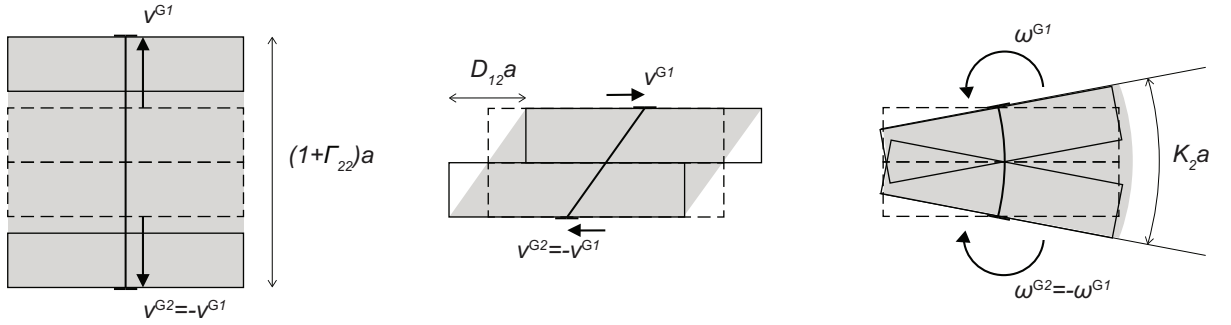


Figure 1.10: Combinations of rigid-body motions of the blocks (translations and rotations) producing 1D Cosserat macroscopic deformation and curvature states on the elementary cell of a masonry column. Solid lines represent the deformed state of the discrete cell. Dotted lines represent its undeformed state. In grey: the deformed state of the elementary cell supposed as a continuum, undergoing 1D macroscopic Cosserat deformations.

The Cosserat deformations reproduce then the deformation modes of the discrete cell. In particular, blocks' rotations with opposite direction induce the opening of the interface and, consequently, generate macroscopic curvatures on the cell (Figure 1.10). On the contrary, the terms V_α and Ω^c denote rigid-body motions of B (see Eqs.(1.33)-(1.32)). As shown in Figure 1.11, they are provided by combinations of in-plane blocks' motions producing no average deformation on the elementary cell. The first term (Figure 1.11-left) designates the average rigid-body translations of the cell and is generated by uniform blocks' translations:

$$V_\alpha = \frac{v_\alpha^{G1} + v_\alpha^{G2}}{2}. \quad (1.48)$$

The second term (Figure 1.11-right) defines the average rigid-body rotation of the cell. It is generated by blocks' rotations having the same direction, which induce the sliding but not the opening of the common interface:

$$\Omega^c = \frac{\omega^{G1} + \omega^{G2}}{2}. \quad (1.49)$$

In the framework of Cosserat continuum, Ω^c has a specific physical meaning, since it represents the average Cosserat rotation of the cell (Eq.(1.32)).

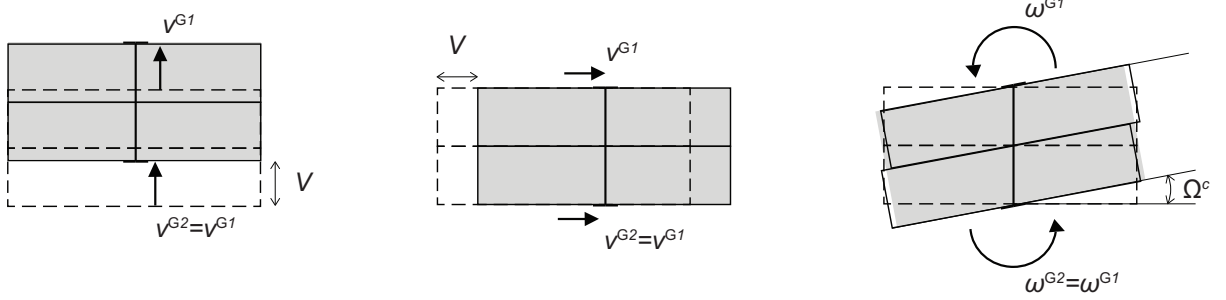


Figure 1.11: Combinations of rigid-body motions of the blocks (translations and rotations) producing in-plane rigid-body translations V_α and Cosserat rotations Ω of the elementary cell of a masonry column.

The conjugate Cosserat static quantities are then necessarily $T_{\alpha 2}$ and M_2 . These forces and couples are provided by distributions of contact stresses r_α^{IJ} along the interface Σ^{12} . The use of the Eqs.(1.36)-(1.37) gives directly:

$$T_{\alpha 1} = 0, \quad M_1 = 0, \quad (1.50)$$

and:

$$T_{\alpha 2} = \frac{1}{b} \int_{-\frac{b}{2}}^{\frac{b}{2}} r_\alpha^{IJ} dL, \quad M_2 = \frac{1}{b} \int_{-\frac{b}{2}}^{\frac{b}{2}} r_2^{IJ} y_1 dL. \quad (1.51)$$

Eq.(1.50) is a condition for the external facets of the masonry column (for $y_1 = \pm b/2$) to be stress- and couple stress-free. Eq.(1.51) gives then the overall forces $T_{\alpha 2}$ and the overall couple M_2 of what can be considered a Timoshenko beam model (Mühlhaus et al., 1997).

In view of the homogenisation, we compute the displacement and angular displacement velocity jumps, Eqs.(1.16),(1.20). These jumps may occur within the elementary cell, at the interface between the blocks, which represents a discontinuity line with respect to the velocity field distributions (1.44). Given (1.43), these jumps read:

$$[[\mathbf{v}]]^{12} = a \begin{bmatrix} \Gamma_{12} \\ \Gamma_{22} + y_1 K_2 \end{bmatrix} \quad (1.52)$$

or:

$$[[\omega]]^{12} = a K_2, \quad (1.53)$$

and:

$$[[\mathbf{v}^G]]^{12} = a \begin{bmatrix} \Gamma_{12} \\ \Gamma_{22} \end{bmatrix}. \quad (1.54)$$

1.5.3 Homogenisation

We assume that the strength of the blocks (masonry units) that compose the column is very large compared to that of the interfaces (masonry joints). Failure may then take place within the elementary cell only on these latter. The effect of the finite strength of the blocks in the frame of homogenisation of a Cauchy continuum is presented by Stefanou et al. (2015).

For the interface we make use of a Coulomb slip failure criterion. This criterion is classically expressed in the following form:

$$f(r_\alpha^{IJ}) = |r_\alpha^r| - c + r^\sigma \text{Tan}[\phi] \leq 0. \quad (1.55)$$

with $r^\sigma = r_\alpha^\sigma n_\alpha^{IJ}$, c the joint cohesion and ϕ the joint friction angle. Its support function is given in terms of the displacement velocity jumps $\llbracket v_\alpha \rrbracket^{IJ}$ and reads (Salençon, 2013):

$$\pi^{IJ}(\llbracket v_\alpha \rrbracket^{IJ}) = \pi^{IJ}(\llbracket v_\alpha \rrbracket^{IJ}; \mathbf{n}_\alpha^{IJ}) = \frac{c}{\text{Tan}[\phi]} \llbracket v_\alpha \rrbracket^{IJ} n_\alpha^{IJ}, \quad (1.56)$$

with $\pi^{IJ} < \infty$ if:

$$\llbracket v_\alpha \rrbracket^{IJ} n_\alpha^{IJ} \geq |\llbracket v_\alpha \rrbracket^{IJ}| \text{Sin}[\phi], \quad (1.57)$$

and \mathbf{n}_α^{IJ} the unit vector normal to the interface considered. Eq.(1.57) is called *relevance condition* (Salençon, 2013). From a physical point of view, this is a kinematic condition establishing the impenetrability between the blocks (see Figure 1.12). From a mechanical point of view, it assures that the plastic dissipation is finite at every point of the interface, see Eq.(1.39).

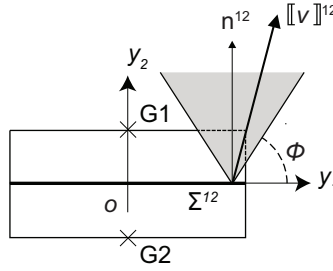


Figure 1.12: Displacement jump across the interface of the periodic elementary cell of a masonry column, falling within the Coulomb friction cone. Condition for interface failure is that the displacement jump falls inside this cone.

With these definitions, Eqs.(1.38) and (1.40) yields:

$$T_{22}G_{22} + T_{12}G_{12} + M_2K_2 \leq \frac{1}{ab} \int_{-\frac{b}{2}}^{+\frac{b}{2}} \pi^{12}(\llbracket \mathbf{v} \rrbracket^{12}; \mathbf{n}^{12}) dy_1. \quad (1.58)$$

Using Eq.(1.52), we obtain:

$$\pi^{12}(\llbracket \mathbf{v} \rrbracket^{12}; \mathbf{n}^{12}) = \frac{c}{\text{Tan}[\phi]} a (G_{22} + y_1 K_2). \quad (1.59)$$

Integrating over the interface, Eq.(1.58) then becomes:

$$\left(T_{22} - \frac{c}{\text{Tan}[\phi]} \right) G_{22} + T_{12}G_{12} + M_2K_2 \leq 0. \quad (1.60)$$

It is worth pointing out that, at this stage, no failure condition has been explicitly formulated in terms of the angular displacement velocity jumps $\llbracket \omega \rrbracket^{IJ}$ (cf. Trovalusci and Masiani (2003)). The Coulomb slip criterion is expressed only in terms of the displacement jumps $\llbracket v_\alpha \rrbracket^{IJ}$. It is the same criterion with the one originally considered by de Buhan and de Felice (1997) for the homogenisation of masonry panels, with the important exception that now $\llbracket v_\alpha \rrbracket^{IJ}$ is produced by

both the relative translations and the relative rotations occurring between the blocks (Eq.(1.52)). On the contrary, in the case of the Cauchy continuum, Eq.(1.54) would be used instead of Eq.(1.52) (see also Section 1.4). Therefore, in the frame of the Cosserat continuum, the use of a Coulomb slip criterion at the interfaces level leads to a form of plastic dissipation (Eq.(1.59)) that contains not only the macroscopic relative deformations Γ_{22} , coincident with D_{22} , but also an additional term depending on the average curvature K_2 . This additional term, is related through Eq.(1.53) to the relative blocks' rotations, and can only be seized by the enhanced kinematics of a Cosserat continuum.

The consequences of this change emerge in the formulation of the homogenised strength criterion. In fact, looking at Eq.(1.60), one can state that the homogenised failure criterion is calculated among *all* the $KA(\Gamma_{\alpha 2}, K_2)$ set of kinematics, associated to the following macroscopic stresses and couples:

$$T'_{\alpha 2} = \left(T_{\alpha 2} - \frac{c}{\text{Tan}[\phi]} \delta_{\alpha 2} \right), \quad M'_2 = M_2$$

These kinematics, in order to be relevant in the formulation of the maximum plastic dissipation (1.59), must respect condition (1.57), reading in this case:

$$-G_{22} + \text{Tan}[\phi] |\Gamma_{12}| - y_1 K_2 \leq 0, \forall y_1 \in \left[-\frac{b}{2}, +\frac{b}{2} \right]. \quad (1.61)$$

As Eq.(1.61) is linear, it needs to be verified only at the extreme points of the cell's interface, i.e. at $y_1 = \pm b/2$. This leads to the following four distinct inequalities:

$$H_{1-4}(\Gamma_{\alpha 2}, K_2) = -G_{22} \pm \text{Tan}[\phi] \Gamma_{12} \pm \frac{b}{2} K_2 \leq 0. \quad (1.62)$$

Eq.(1.62) gives directly the researched homogenised strength domain for the masonry column, in the space of the generalized Cosserat deformations. This forms a conical region, that is bounded by four intersecting planes of equation $H_{1-4} = 0$ and with the apex in the origin of the axes, see Figure 1.13. Condition for failure of the cell (macroscopic failure) is then that the macroscopic deformation state falls inside the depicted domain.

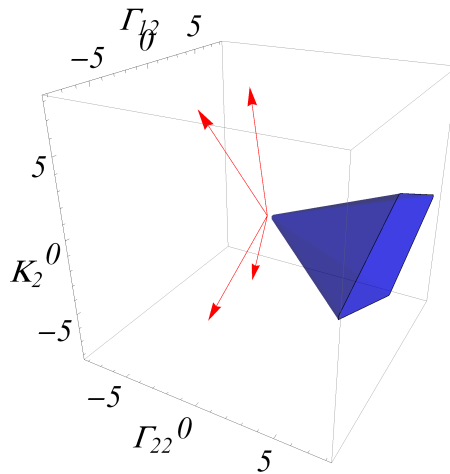


Figure 1.13: Representation of the homogenised strength domain for the masonry column in the space of the generalized Cosserat deformations $(\Gamma_{\alpha 2}, K_2)$. In blue: the intersecting planes (Eq.(1.62)). In red: the vectors normal to the planes.

The set of stresses and couple stresses for which cell failure may occur (macroscopic yield criterion), is also a cone. This cone is generated in the Cosserat generalized stress space $(T_{\alpha 2}, M_2)$ by the normality rule (Naghdi and Trapp (1975); Lee (1995)) applied at the apex of (1.62) (see also de Buhan and de Felice (1997)):

$$T'_{\alpha 2} = \sum_{j=1}^4 \lambda_j \partial_{T_{\alpha 2}} H_j, \quad M'_2 = \sum_{j=1}^4 \lambda_j \partial_{M_2} H_j. \quad (1.63)$$

The resulting homogenised strength domain $G^{c, hom}$ is then the convex hull of the normal vectors produced by (1.63), see Figure 1.13. In this case, it is given by the following four surfaces, which correspond to the homogenised yield criteria:

$$\begin{aligned} F_{1,2}(T_{\alpha 2}, M_2) &= \pm T_{12} + \text{Tan}[\phi] \left(T_{22} - \frac{c}{\text{Tan}[\phi]} \right) \leq 0 \\ F_{3,4}(T_{\alpha 2}, M_2) &= \pm \frac{2}{b} M_2 + \left(T_{22} - \frac{c}{\text{Tan}[\phi]} \right) \leq 0 \end{aligned} \quad (1.64)$$

The strength domain is plotted in Figure 1.14.

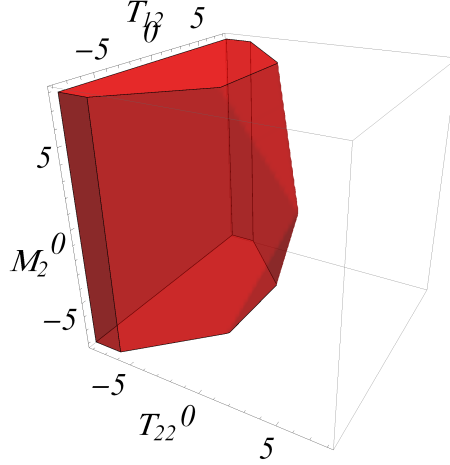


Figure 1.14: Representation of the homogenised strength domain for the masonry column in the space of the generalized Cosserat stresses $(T_{\alpha 2}, M_2)$. Intersecting plane (Eq.(1.67)).

1.5.4 Discussion

In this paragraph, we focus on: a) the contribution of the Cosserat model in the determination of the homogenised strength criterion of the masonry column, and b) the effect of the choice of the cell on the computed strength domain.

For the first purpose, it is useful to express the macroscopic couple stress M_2 as an eccentric macroscopic stress T_{22} , situated along y_1 at the normalized distance ζ_1 from the center of the column cross section:

$$M_2 = \frac{b}{2} \zeta_1 T_{22}. \quad (1.65)$$

Consequently, the homogenised strength criterion (1.67) takes the following alternative form:

$$\begin{aligned} F_{1,2}(T_{\alpha 2}, \zeta_1) &= \pm T_{12} + \text{Tan}[\phi] \left(T_{22} - \frac{c}{\text{Tan}[\phi]} \right) \leq 0 \\ F_{3,4}(T_{\alpha 2}, \zeta_1) &= \pm \zeta_1 T_{22} + \left(T_{22} - \frac{c}{\text{Tan}[\phi]} \right) \leq 0, \end{aligned} \quad (1.66)$$

with $\zeta_1 \leq |1|$ when T_{22} falls into the section, and $\zeta_1 > |1|$ otherwise. The resulting domain is plotted in [Figure 1.15](#), in the $(T_{12} - T_{22})$ -stress space and for different values of eccentricity ζ_1 . It is worth emphasizing the fact that the Coulomb slip criterion (1.56) considered as failure condition at the interfaces level (masonry joints), is retrieved at the macroscopic scale, as a failure condition for the whole cell (masonry column). This condition is described by Eq.(1.66)-1, and a similar expression can be recovered also when homogenisation is carried out with the use of a simple Cauchy continuum, i.e. for $\zeta_1 = 0$ ([Figure 1.15-left](#)). The expression has the same form, but it is expressed in terms of the macroscopic deformation $D_{(\alpha 2)}$ instead of $\Gamma_{\alpha 2}$. On the contrary, the effects of considering a Cosserat continuum are visible when also the second condition (Eq.(1.66)-2) is involved, i.e. for $\zeta_1 \neq 0$. In such case ([Figure 1.15-right](#)), the presence of moments M_2 (visible when blocks rotate) limits considerably the tensile (T_{22}) and shear (T_{12}) strength. Consistently, the overall strength capacity of the column is reduced.

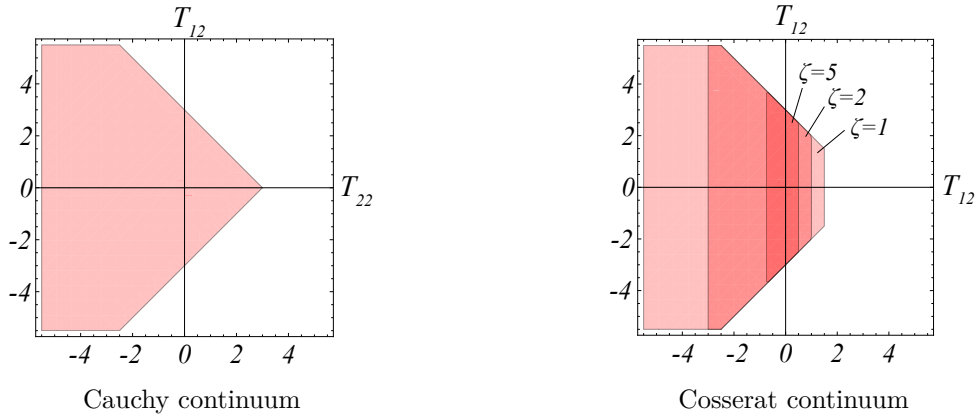


Figure 1.15: Condition for failure of the elementary cell (macroscopic failure) of a masonry column. Representation of the homogenised strength criterion for $\zeta_1 = 0$ (Cauchy continuum) and for $\zeta_1 \neq 0$ (Cosserat continuum).

The elementary cell B considered for the masonry column is the cell with the smallest surface (see [Section 1.4](#)). However, in the frame of the Cosserat continuum, the choice of the cell is not arbitrary. Therefore, in order to justify our choice and show the effect of the cell's size on the computed homogenised strength, we consider elementary cells larger than B . By following the procedure described in the previous section, homogenisation is carried out on a cell containing a generic number of interfaces $N_\Sigma \geq 1$ ([Figure 1.16-left](#)). For this cell, the resulting homogenised yield criteria are:

$$\begin{aligned}
 F_{1,2}(T_{\alpha 2}, M_2, N_\Sigma) &= \pm T_{12} + \text{Tan}[\phi] \left(T_{22} - \frac{c}{\text{Tan}[\phi]} \right) \leq 0 \\
 F_{3,4}(T_{\alpha 2}, M_2, N_\Sigma) &= \pm \frac{2}{b} \frac{1}{1 + m} M_2 + \left(T_{22} - \frac{c}{\text{Tan}[\phi]} \right) \leq 0,
 \end{aligned} \tag{1.67}$$

where $m = (N_\Sigma - 1)a/b$, N_Σ is the number of interfaces enclosed within the cell and a/b is the block aspect ratio. The expressions above are the generalization of Eqs.(1.67) for the generic cell. The yield criteria for the cell B are retrieved for $N_\Sigma = 1$, whereas for $N_\Sigma > 1$ the cell considered is larger than B . [Figure 1.16](#) shows the effect of choosing a cell larger than the minimum one, B , on the overall strength of the masonry column. In general, the fact of considering a larger cell leads to an expansion of the homogenised domain. In the frame of the kinematic limit analysis approach, where upper bounds of $G^{c,hom}$ are researched, this results in a worse estimation of the masonry strength capacity. This is an interesting but not

unexpected result, if one considers the upper bound theorem of limit analysis, and the fact that the kinematics of the Cosserat continuum capture the kinematics of the larger cells only in an average sense (Eqs.(1.29)-(1.33)). It is also worth noticing that the increase of strength due to the cell's size is only related to the couple stress M_2 (Eq.(1.67)-2). On the contrary, the terms related to the tensile and shear forces are not affected by the choice of the cell. Hence the cell with the smallest surface must always be considered, as a rule of thumb, in the frame of the Cosserat continuum.

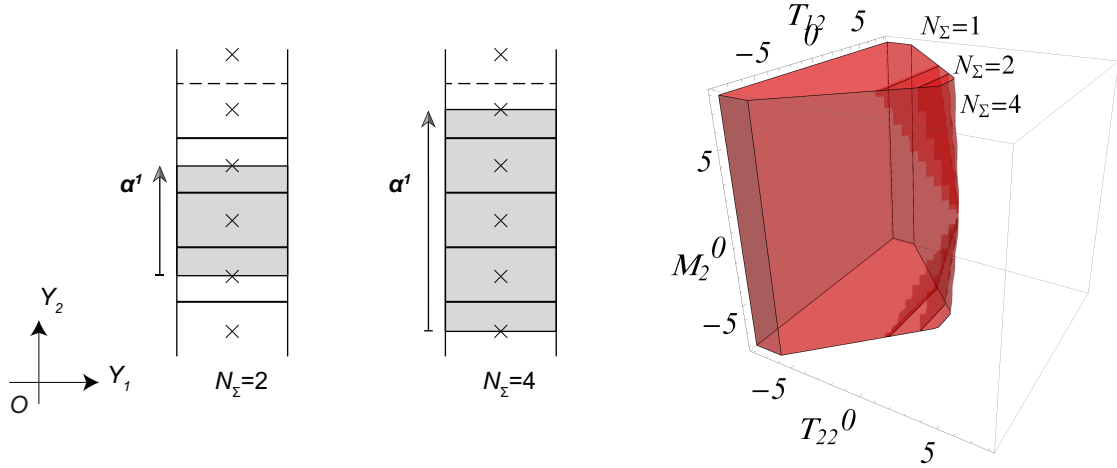


Figure 1.16: Periodic masonry column and corresponding elementary cells larger than B (left). Effect of the size of the cell on the computed strength (right).

1.6 Application to masonry walls

1.6.1 Geometry

We consider a masonry wall in which rectangular blocks are disposed according to a generic running bond periodic pattern (Figure 1.17), i.e. alternate courses of blocks are laid with a generic overlap with respect to the neighbouring courses. In such configuration, the periodicity is described by the following vectors:

$$\begin{aligned}\alpha^1 &= b\mathbf{e}_1 + 0\mathbf{e}_2 \\ \alpha^2 &= \eta b\mathbf{e}_1 + a\mathbf{e}_2,\end{aligned}$$

and the resulting elementary cell, denoted with A , is defined as:

$$A = \alpha^1 \times \alpha^2.$$

The area of the cell is $|A| = |\alpha^1 \times \alpha^2| = ab$, where a and b designate respectively the height and the width of the blocks (see Section 1.5). The overlap between the blocks is generic and described by ηb , with the parameter $\eta \in [0, 1/2]$. The stack bond and the classic $(1/2)$ running bond patterns are special cases of the considered pattern. They are retrieved respectively for $\eta = 0$ and for $\eta = 1/2$ (Figure 1.18).

The cell consists of 4 blocks. The position of the centre of mass of each block is expressed

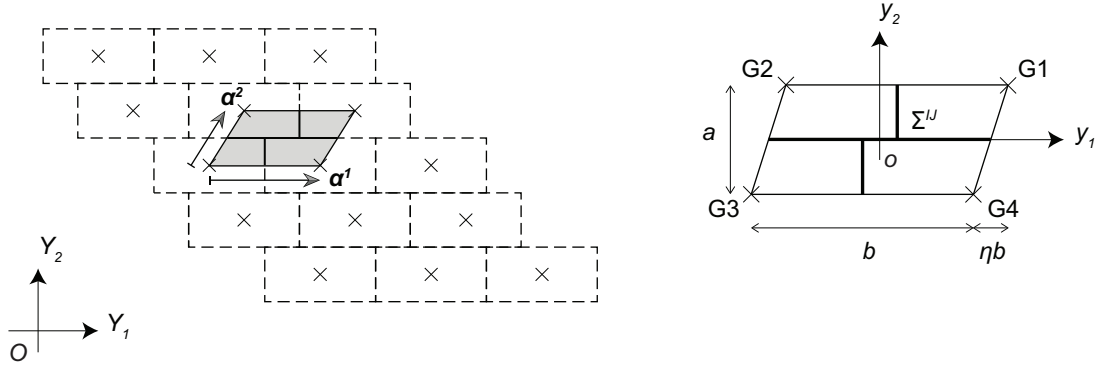


Figure 1.17: Periodic masonry wall with generic running bond pattern (left) and the corresponding elementary cell (right).

with respect to a local reference system (oy_1y_2) , attached to the centre of the cell (Figure 1.17):

$$\begin{aligned} \mathbf{y}^{G1} &= (1 + \eta) \frac{b}{2} \mathbf{e}_1 + \frac{a}{2} \mathbf{e}_2 \\ \mathbf{y}^{G2} &= -(1 - \eta) \frac{b}{2} \mathbf{e}_1 + \frac{a}{2} \mathbf{e}_2 \\ \mathbf{y}^{G3} &= -(1 + \eta) \frac{b}{2} \mathbf{e}_1 - \frac{a}{2} \mathbf{e}_2 \\ \mathbf{y}^{G4} &= (1 - \eta) \frac{b}{2} \mathbf{e}_1 - \frac{a}{2} \mathbf{e}_2. \end{aligned}$$

The interfaces shared by the blocks are situated and oriented as follows:

$$\begin{aligned} \mathbf{y}^{\Sigma^{14}} &= y_1 \mathbf{e}_1 + 0 \mathbf{e}_2, \forall y_1 \in \left[\frac{\eta}{2} b, +\frac{b}{2} \right], \quad \mathbf{n}^{14} = \mathbf{e}_2 \\ \mathbf{y}^{\Sigma^{23}} &= y_1 \mathbf{e}_1 + 0 \mathbf{e}_2, \forall y_1 \in \left[-\frac{b}{2}, -\frac{\eta}{2} b \right], \quad \mathbf{n}^{23} = \mathbf{e}_2 \\ \mathbf{y}^{\Sigma^{24}} &= y_1 \mathbf{e}_1 + 0 \mathbf{e}_2, \forall y_2 \in \left[-\frac{\eta}{2} b, +\frac{\eta}{2} b \right], \quad \mathbf{n}^{24} = \mathbf{e}_2 \\ \mathbf{y}^{\Sigma^{12}} &= \frac{\eta}{2} b \mathbf{e}_1 + y_2 \mathbf{e}_2, \forall y_2 \in \left[0, +\frac{a}{2} \right], \quad \mathbf{n}^{12} = \mathbf{e}_1 \\ \mathbf{y}^{\Sigma^{43}} &= -\frac{\eta}{2} b \mathbf{e}_1 + y_2 \mathbf{e}_2, \forall y_2 \in \left[-\frac{a}{2}, 0 \right], \quad \mathbf{n}^{43} = \mathbf{e}_1. \end{aligned}$$

It is worth noticing that, in the limit for $\eta \rightarrow 0$ (stack bond pattern), the interface between the block 2 and the block 4 degenerates into a point: $|\Sigma^{24}| \rightarrow 0$. In this case, Σ^{24} must be excluded from the computations.

1.6.2 Average Cosserat variables

The elementary cell A is periodic in both the local directions $(y_1 - y_2)$. Consequently, the kinematically admissible sets of displacement and angular displacement velocity fields $(v_\alpha^{GJ}, \omega^{GJ}) \in KA(\Gamma_{\alpha\beta}, K_\beta)$ follow the general form (1.27), with $\alpha, \beta = 1, 2$ and $J = 1, \dots, 4$. Similarly to the previous sections, the blocks undergo rigid-body motions. The velocity field distributions are then of the form (1.28).

The macroscopic deformations $(\Gamma_{\alpha\beta}, K_\beta)$ contained in Eq.(1.28) are produced by combinations of translations and rotations of the blocks that compose the elementary cell. However, with

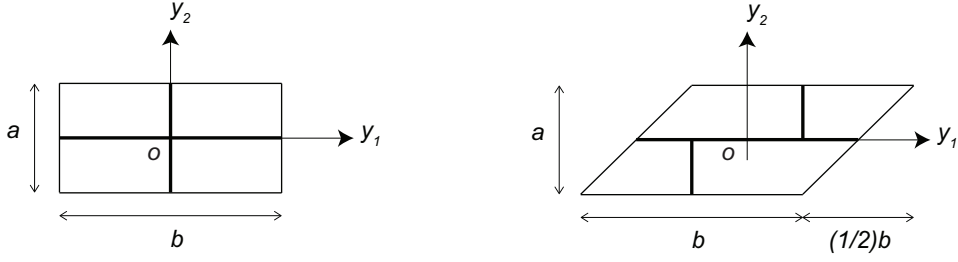


Figure 1.18: Elementary cells for periodic masonry covered by the cell A . Left: the stack bond pattern, for $\eta = 0$. Right: the classical $(1/2)$ running bond pattern, for $\eta = 1/2$.

respect to the cell B of Section 1.5, on the cell A no in-plane Cosserat deformation measures vanish. The relative deformations are, after Eq.(1.29):

$$\begin{aligned}
 \Gamma_{11} &= \frac{v_1^{G1} - v_1^{G2} - v_1^{G3} + v_1^{G4}}{2b} + \frac{a(\omega^{G1} - \omega^{G2} + \omega^{G3} - \omega^{G4})}{8b} \\
 \Gamma_{12} &= \frac{(1-\eta)v_1^{G1} + (1+\eta)v_1^{G2} - (1-\eta)v_1^{G3} - (1+\eta)v_1^{G4}}{2a} + \frac{\eta(\omega^{G1} - \omega^{G2} + \omega^{G3} - \omega^{G4})}{4} + \Omega^c \\
 \Gamma_{21} &= \frac{v_2^{G1} - v_2^{G2} - v_2^{G3} + v_2^{G4}}{2b} - \Omega^c \\
 \Gamma_{22} &= \frac{(1-\eta)v_2^{G1} + (1+\eta)v_2^{G2} - (1-\eta)v_2^{G3} - (1+\eta)v_2^{G4}}{2a} + \frac{(1-\eta^2)b(\omega^{G1} - \omega^{G2} + \omega^{G3} - \omega^{G4})}{8a}. \tag{1.68}
 \end{aligned}$$

The in-plane curvatures write (Eq.(1.30)):

$$\begin{aligned}
 K_1 &= \frac{\omega^{G1} - \omega^{G2} - \omega^{G3} + \omega^{G4}}{2b} \\
 K_2 &= \frac{(1-\eta)\omega^{G1} + (1+\eta)\omega^{G2} - (1-\eta)\omega^{G3} - (1+\eta)\omega^{G4}}{2a}. \tag{1.69}
 \end{aligned}$$

Eqs.(1.68)-(1.69) are detailed in A.2, in the case of the stack bond and the $1/2$ running bond patterns. Regarding the stack bond pattern ($\eta = 0$), an illustration of the Cosserat deformation measures and their connection to the discrete kinematic variables is given in Figure 1.19. It is worth noticing that the blocks' rotations do not appear only in the expression of the macroscopic curvatures, but also in that of the macroscopic deformations. In fact, following simple rotations, the blocks can be arranged to form specific geometric configurations that involve the opening of the interfaces and induce average elongations and contractions (Γ_{11}, Γ_{22}) of the cell, see Eq.(1.68)-1,4. These configurations can take the shape of an hourglass (Figure 1.19), and cannot be represented by a simple Cauchy continuum, since in that case the macroscopic deformation would only be generated by blocks' translations (see Eq.(1.31)). The contribution of blocks' rotations in the definition of the macroscopic relative deformations of the Cosserat continuum is even more apparent when the blocks' overlap is marked, i.e. for increasing η . In such case, blocks' rotations produce also shear deformations (Γ_{12}), see Eq.(1.68)-2.

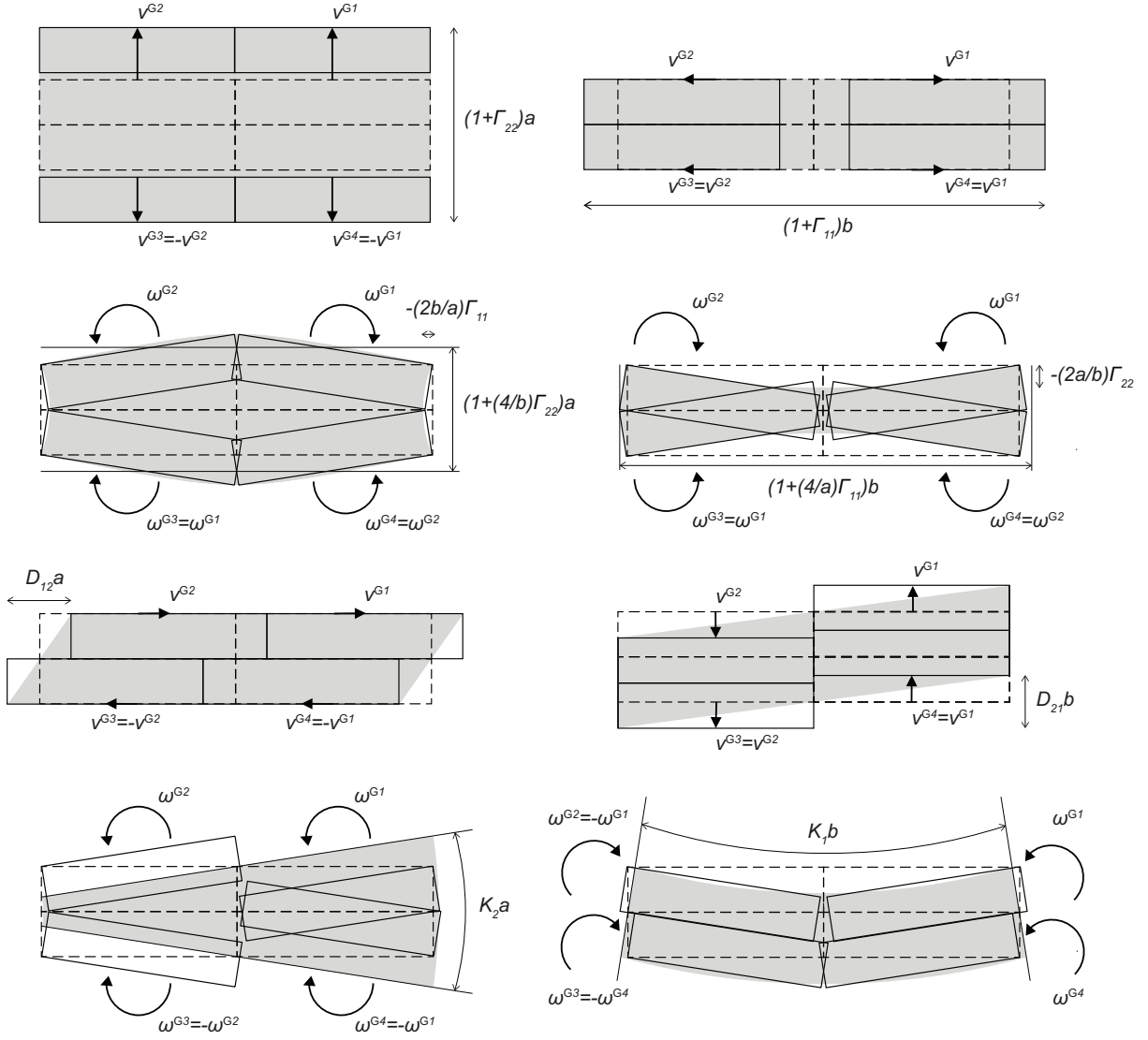


Figure 1.19: Rigid-body motions of the blocks (translations and rotations) producing 2D Cosserat macroscopic deformation and curvature states on the elementary cell of a periodic masonry wall (stack bond pattern). Solid lines represent the deformed state of the discrete cell. Dotted lines represent its undeformed state. In grey: the deformed state of the elementary cell supposed as a continuum, undergoing 2D macroscopic Cosserat deformations.

The terms V_α and Ω^c represent, as in the case of the column, the average rigid-body kinematics of the cell (Eqs.(1.33)-(1.32)). V_α indicates the average rigid-body cell translations (Figure 1.20-left):

$$V_\alpha = \frac{v_\alpha^{G1} + v_\alpha^{G2} + v_\alpha^{G3} + v_\alpha^{G4}}{4}. \quad (1.70)$$

Ω^c equals the average rotation of the blocks of the cell (Figure 1.20-right):

$$\Omega^c = \frac{\omega^{G1} + \omega^{G2} + \omega^{G3} + \omega^{G4}}{4}. \quad (1.71)$$

The macroscopic stresses $T_{\alpha\beta}$ and couple stresses M_β are computed by using Eq.(1.36) and

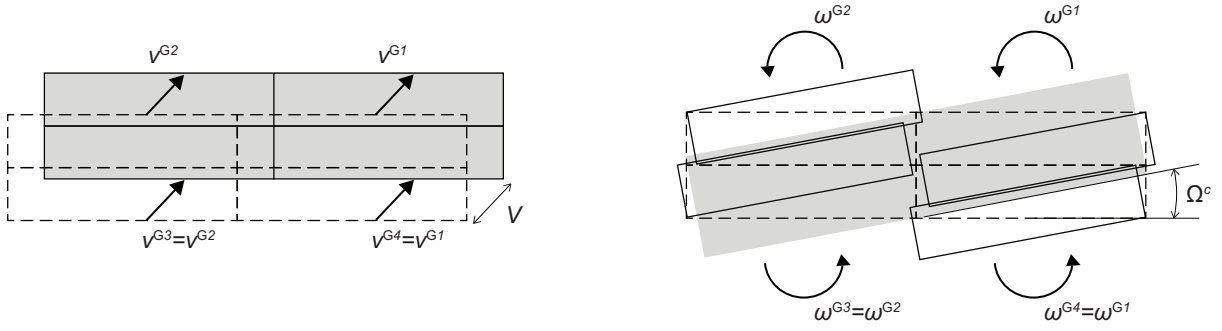


Figure 1.20: Rigid-body motions of the blocks (translations and rotations) producing in-plane rigid-body translations V_α and Cosserat rotations Ω^c of the elementary cell of a masonry wall.

(1.37). They read, respectively:

$$\begin{aligned}
T_{\alpha 1} &= \frac{1}{a} \left(\int_0^{\frac{a}{2}} r_\alpha^{12} dy_2 + \int_{-\frac{a}{2}}^0 r_\alpha^{43} dy_2 \right. \\
&\quad \left. + \int_{\frac{b}{2}}^b \eta r_\alpha^{14} dy_1 + \int_{-\frac{b}{2}}^{-\eta \frac{b}{2}} \eta r_\alpha^{23} dy_1 - \int_{-\eta \frac{b}{2}}^{\eta \frac{b}{2}} (1-\eta) r_\alpha^{24} dy_1 \right) \\
T_{\alpha 2} &= \frac{1}{b} \left(\int_{\frac{b}{2}}^b r_\alpha^{14} dy_1 + \int_{-\frac{b}{2}}^{-\eta \frac{b}{2}} r_\alpha^{23} dy_1 + \int_{-\eta \frac{b}{2}}^{\eta \frac{b}{2}} r_\alpha^{24} dy_1 \right), \tag{1.72}
\end{aligned}$$

and:

$$\begin{aligned}
M_1 &= \frac{1}{a} \left(\int_0^{\frac{a}{2}} \frac{1}{2} (-2r_1^{12} y_2 + \eta b r_2^{12}) dy_2 + \int_{-\frac{a}{2}}^0 -\frac{1}{2} (2r_1^{43} y_2 + \eta b r_2^{43}) dy_2 \right. \\
&\quad \left. + \int_{\frac{b}{2}}^b \eta r_2^{14} y_1 dy_1 + \int_{-\frac{b}{2}}^{-\eta \frac{b}{2}} \eta r_2^{23} y_1 dy_1 - \int_{-\eta \frac{b}{2}}^{\eta \frac{b}{2}} (1-\eta) r_2^{24} y_1 dy_1 \right) \\
M_2 &= \frac{1}{b} \left(\int_{\frac{b}{2}}^b r_2^{14} y_1 dy_1 + \int_{-\frac{b}{2}}^{-\eta \frac{b}{2}} r_2^{23} y_1 dy_1 + \int_{-\eta \frac{b}{2}}^{\eta \frac{b}{2}} r_2^{24} y_1 dy_1 \right). \tag{1.73}
\end{aligned}$$

Their expression for the stack bond and the classical running bond patterns is given in A.3.

The displacement and angular displacement velocity jumps across all the interfaces of the cell A read:

$$\begin{aligned}
\llbracket \mathbf{v} \rrbracket^{14} &= \begin{bmatrix} \eta b \Gamma_{11} + a \left(\Gamma_{12} + \frac{b}{2} K_1 \right) \\ \eta b \left(\Gamma_{21} + (-b + y_1) K_1 \right) + a \left(\Gamma_{22} - \frac{b}{2} K_2 + y_1 K_2 \right) \end{bmatrix} \\
\llbracket \mathbf{v} \rrbracket^{23} &= \begin{bmatrix} \eta b \Gamma_{11} + a \left(\Gamma_{12} - \frac{b}{2} K_1 \right) \\ \eta b \left(\Gamma_{21} + (b + y_1) K_1 \right) + a \left(\Gamma_{22} + \frac{b}{2} K_2 + y_1 K_2 \right) \end{bmatrix} \\
\llbracket \mathbf{v} \rrbracket^{24} &= \begin{bmatrix} (-1 + \eta) b \Gamma_{11} + a \Gamma_{12} \\ (-1 + \eta) b \left(\Gamma_{21} + y_1 K_1 \right) + a \left(\Gamma_{22} + y_1 K_2 \right) \end{bmatrix} \\
\llbracket \mathbf{v} \rrbracket^{12} &= \frac{1}{2} b \begin{bmatrix} 2\Gamma_{11} + (a - 2y_2) K_1 \\ 2\Gamma_{21} - \eta b K_1 - a K_2 \end{bmatrix} \\
\llbracket \mathbf{v} \rrbracket^{43} &= \frac{1}{2} b \begin{bmatrix} 2\Gamma_{11} - (a + 2y_2) K_1 \\ 2\Gamma_{21} + \eta b K_1 + a K_2 \end{bmatrix}, \tag{1.74}
\end{aligned}$$

and:

$$\begin{aligned}
\llbracket \omega \rrbracket^{14} &= \eta b K_1 + a K_2 \\
\llbracket \omega \rrbracket^{23} &= \eta b K_1 + a K_2 \\
\llbracket \omega \rrbracket^{24} &= (-1 + \eta) b K_1 + a K_2 \\
\llbracket \omega \rrbracket^{12} &= b K_1 \\
\llbracket \omega \rrbracket^{43} &= b K_1.
\end{aligned} \tag{1.75}$$

It is worth noticing that Eq.(1.74) is more general and covers the expression used by [Cecchi and Sab \(2002b\)](#); [Sab \(2003\)](#); [Sab et al. \(2007\)](#) in the formulation of the in-plane kinematics of their plate models for masonry. In particular, the kinematics considered in the above works are retrieved as special cases of Eq.(1.74), when the curvatures are neglected. The introduction of the curvatures in the description of the in-plane kinematic jumps of the discrete cell is legitimate only in the frame of Cosserat ([Stefanou et al., 2008](#); [Salerno and de Felice, 2009](#)) and micromorphic ([Stefanou et al., 2010](#); [Stefanou and Sulem, 2012](#)) continua. In those cases blocks' rotations are appropriately seized by additional macroscopic deformation measures that are absent in a simple Cauchy continuum.

1.6.3 Homogenisation

The blocks are considered infinitely resistant, whereas the account of interfaces' failure to shear r_α^τ and to tension r_α^σ is made with reference to a Coulomb slip failure criterion of the form (1.55). To this purpose, distinction is made between the horizontal interfaces of the cell, representing the masonry bed joints, and the vertical interfaces, representing the masonry head joints. For those two sets of joints, failure results in the use of different values of cohesion and friction, and the plastic dissipation at the corresponding interfaces reads (Eq.(1.56)):

$$\pi^{IJ} \left(\llbracket v_\alpha \rrbracket^{IJ}; \mathbf{n}_\alpha^{IJ} \right) = \frac{c}{\text{Tan}[\phi]} \llbracket v_\alpha \rrbracket^{IJ} \mathbf{n}_\alpha^{IJ}, \text{ with } \begin{cases} (c, \phi) = (c^h, \phi^h), & \text{for } \Sigma^{14}, \Sigma^{23}, \Sigma^{24} \\ (c, \phi) = (c^v, \phi^v), & \text{for } \Sigma^{12}, \Sigma^{43}, \end{cases} \tag{1.76}$$

with $\pi^{IJ} < \infty$ if:

$$\begin{cases} \llbracket v_\alpha \rrbracket^{IJ} \mathbf{n}_\alpha^{IJ} \geq \left| \llbracket v_\alpha \rrbracket^{IJ} \right| \text{Sin}[\phi^h], & \text{for } \Sigma^{14}, \Sigma^{23}, \Sigma^{24} \\ \llbracket v_\alpha \rrbracket^{IJ} \mathbf{n}_\alpha^{IJ} \geq \left| \llbracket v_\alpha \rrbracket^{IJ} \right| \text{Sin}[\phi^v], & \text{for } \Sigma^{12}, \Sigma^{43}. \end{cases} \tag{1.77}$$

In the above the superscripts h and v refer respectively to the horizontal (bed joints) and vertical (head joints) interfaces. The adoption of distinct interface properties between the bed and the head joints corresponds to the use, in practical applications, of joints with different thickness and strength. In general, the bed joints are thicker than the head joints, and, in many cases, these latter are left unfilled ([Beall, 2000](#)). It is known that this results in an overall reduction of the in-plane strength capacity of masonry ([Barth and Marti, 1997](#); [Mojsilović, 2011](#)), and therefore it must be taken into account in the computations.

The plastic dissipation on the whole cell is then:

$$\begin{aligned}
\pi^D(v_\alpha^{\text{GJ}}, \omega^{\text{GJ}}) &= \frac{1}{ab} \left(\int_{\eta \frac{b}{2}}^{\frac{b}{2}} \pi^{14} \left(\llbracket \mathbf{v} \rrbracket^{14}; \mathbf{n}^{14} \right) dy_1 \right. \\
&+ \int_{-\frac{b}{2}}^{-\eta \frac{b}{2}} \pi^{23} \left(\llbracket \mathbf{v} \rrbracket^{23}; \mathbf{n}^{23} \right) dy_1 + \int_{-\eta \frac{b}{2}}^{\eta \frac{b}{2}} \pi^{24} \left(\llbracket \mathbf{v} \rrbracket^{24}; \mathbf{n}^{24} \right) dy_1 \\
&\left. + \int_0^{\frac{a}{2}} \pi^{12} \left(\llbracket \mathbf{v} \rrbracket^{12}; \mathbf{n}^{12} \right) dy_2 + \int_{-\frac{a}{2}}^0 \pi^{43} \left(\llbracket \mathbf{v} \rrbracket^{43}; \mathbf{n}^{43} \right) dy_2 \right), \tag{1.78}
\end{aligned}$$

where the displacement jumps $[[v_\alpha]]^{IJ}$ follow Eq.(1.74). Equations (1.38) and (1.40) then yield:

$$T_{11}\Gamma_{11} + T_{12}\Gamma_{12} + T_{21}\Gamma_{21} + T_{22}\Gamma_{22} + M_1K_1 + M_2K_2 \leq \pi^D (v_\alpha^{GJ}, \omega^{GJ}). \quad (1.79)$$

Using Eq.(1.76), Eq.(1.79) reduces to:

$$T'_{11}\Gamma_{11} + T'_{12}\Gamma_{12} + T'_{21}\Gamma_{21} + T'_{22}\Gamma_{22} + M'_1K_1 + M'_2K_2 \leq 0, \quad (1.80)$$

where we set:

$$\begin{aligned} T'_{11} &= \left(T_{11} - \frac{c^v}{\text{Tan}[\phi^v]} \right), & T'_{22} &= \left(T_{22} - \frac{c^h}{\text{Tan}[\phi^h]} \right) \\ T'_{12} &= T_{12}, & T'_{21} &= T_{21} \\ M'_\beta &= M_\beta. \end{aligned}$$

The homogenised strength criterion is calculated among *all* the $KA(\Gamma_{\alpha\beta}, K_\beta)$ set of kinematics (1.28), associated to the Cosserat deformations defined above. This, under the relevance conditions (1.77). Similarly to the case of the masonry column (Section 1.5), conditions (1.77) need to be verified at every end point of each interface (see Figure 1.21). Notice that in absence of blocks' rotations, it would be sufficient to verify the relevance condition only at the extreme points of the cell A , i.e. at points P1, ..., P4 (Sab, 2003; Sab et al., 2007).

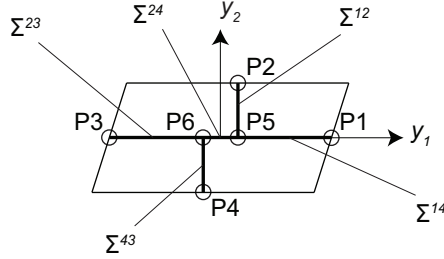


Figure 1.21: Points of the elementary cell where the relevance condition needs to be verified.

At the points belonging to the horizontal interfaces (bed joints) the relevance condition results in the following 12 conditions:

$$\begin{aligned} H_{1-8}(\Gamma_{\alpha\beta}, K_\beta) &= -a \left(\Gamma_{22} - \epsilon_1 (1 - \epsilon_2) \frac{b}{2} K_2 \right) \\ &+ \eta b \left(-\Gamma_{21} + \epsilon_1 \left(1 - \frac{\epsilon_2}{2} \right) b K_1 \right) + \epsilon_0 \text{Tan}[\phi^h] \left[\eta b \Gamma_{11} + a \left(\Gamma_{12} + \epsilon_1 \frac{b}{2} K_1 \right) \right] \leq 0 \end{aligned} \quad (1.81)$$

$$\begin{aligned} H_{9-12}(\Gamma_{\alpha\beta}, K_\beta) &= -a \left(\Gamma_{22} + \epsilon_3 \frac{\eta b}{2} K_2 \right) \\ &+ (1 - \eta) b \left(\Gamma_{21} + \epsilon_3 \frac{\eta b}{2} K_1 \right) + \epsilon_0 \text{Tan}[\phi^h] \left[-(1 - \eta) b \Gamma_{11} + a \Gamma_{12} \right] \leq 0. \end{aligned} \quad (1.82)$$

At the points belonging to the vertical interfaces (head joints) the relevance condition leads to the following 8 conditions:

$$H_{13-20}(\Gamma_{\alpha\beta}, K_\beta) = - \left(\Gamma_{11} + \epsilon_4 \frac{a}{2} K_1 \right) + \epsilon_0 \text{Tan}[\phi^v] \left[\epsilon_5 \Gamma_{21} + \frac{\eta b}{2} K_1 + \frac{a}{2} K_2 \right] \leq 0. \quad (1.83)$$

The coefficients $\epsilon_0, \epsilon_1, \dots, \epsilon_5$ take the value -1,0,+1, η according to Table 1.1.

	Σ^{14}		Σ^{23}		Σ^{24}		Σ^{12}		Σ^{43}	
	P1	P5	P3	P6	P5	P6	P2	P5	P4	P6
ϵ_0	± 1	± 1								
ϵ_1	1	1	-1	-1						
ϵ_2	1	η	1	η						
ϵ_3					1	-1				
ϵ_4							0	1	0	-1
ϵ_5							-1	-1	1	1

Table 1.1: Coefficients used in Eqs.(1.81)-(1.83).

The inequalities contained in Eqs.(1.81)-(1.83) give the strength domain for the masonry wall with a generic running bond pattern. This domain is a convex cone formulated in the space of the generalized Cosserat deformations $(\Gamma_{\alpha\beta}, K_\beta)$, given by the intersection of the planes of equation $H_{1-20} = 0$, and with its apex falling at the origin of the axes. Intersections of the resulting domain in the space of the Cosserat deformations are illustrated in Figure 1.22.

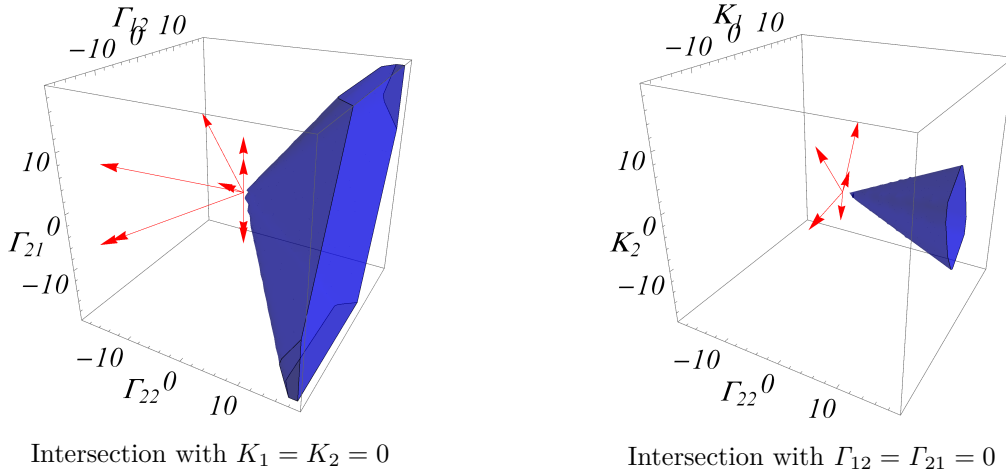


Figure 1.22: Representation of the homogenised strength domain for the masonry wall (1/2 running bond pattern) in the space of Cosserat deformations. Intersections with $K_1 = K_2 = 0$ and $\Gamma_{12} = \Gamma_{21} = 0$ ($\Gamma_{11} = \Gamma_{22}$).

Based on the aforementioned domain, it is possible to retrieve the homogenised strength domain $G^{c,hom}$. As in the case of the column, the procedure is justified by the use of the flow rule (see Eq.(1.63)), which yields:

$$T'_{\alpha\beta} = \sum_{j=1}^{10} \lambda_j \partial_{\Gamma_{\alpha\beta}} H_j, \quad M'_\beta = \sum_{j=1}^{10} \lambda_j \partial_{K_\beta} H_j. \quad (1.84)$$

Eq.(1.84) generates a set of normal vectors (highlighted in red in Figure 1.22). The resulting homogenised strength domain $G^{c,hom}$ is then the region of the generalized Cosserat stresses $(T_{\alpha\beta}, M_\beta)$ enclosed by the convex hull formed by these vectors. Notice that the research of the convex hull gives automatically, and for any given set of deformations, the failure mechanisms producing the minimum plastic dissipation on the discrete cell (upper bound theorem). However,

with respect to [Section 1.5](#), the corresponding yield surfaces are here computed semi-analytically. This is due to the large number of equations and variables.

1.7 Comparison with existing works

In this section, we show the contribution of the present Cosserat continuum model in the evaluation of the homogenised in-plane strength of masonry, with respect to other existing works. The works considered in the comparison are those of [de Buhan and de Felice \(1997\)](#) and [Sulem and Mühlhaus \(1997\)](#). The first work is considered since, as shown in the previous sections, it gives the theoretical basis for the formulation of the homogenised strength domain of masonry in the frame of the Cauchy continuum. The present work represents its extension to the Cosserat continuum. The second work is considered since it contains the first (and only) example of strength domain for masonry formulated in the frame of Cosserat continuum.

1.7.1 Comparison with [de Buhan and de Felice \(1997\)](#)

First, the comparison is carried between the strength domain resulting from the present work and the strength domain obtained within the framework of the Cauchy continuum by [de Buhan and de Felice \(1997\)](#). In particular we refer to [de Buhan and de Felice \(1997\)](#); [Sab \(2003\)](#) regarding the classical (1/2) running bond pattern, and to [Sab et al. \(2007\)](#) regarding the stack bond pattern.

The aforementioned homogenised domains are represented in the space of the in-plane stresses of the Cauchy continuum, i.e. $(T_{11}, T_{(12)}, T_{22})$. In order to highlight the contribution of the Cosserat continuum model within the stress space considered, a parameter β is introduced. Defined as $\beta = T_{[12]}/T_{(12)}$, this parameter allows to control simultaneously all the remaining stress measures contained in the Cosserat medium, namely $(T_{[12]}, M_1, M_2)$. By means of β , the macroscopic in-plane stresses $T_{\alpha\beta}$ are separated into the symmetric and the skew-symmetric parts ([Eq.\(1.3\)](#)) and they are expressed as follows:

$$T_{12} = (1 + \beta)T_{(12)}, \quad T_{21} = (1 - \beta)T_{(12)}. \quad (1.85)$$

The macroscopic couple stresses are given in the form:

$$M_1 = M_2 = \frac{ab}{a+b}\beta T_{(12)}. \quad (1.86)$$

By using the above transformations it is possible to express the domain resulting from [Eq.\(1.84\)](#) in function of the Cauchy stresses only, and to trace the Cosserat's terms through the parameter β . The expressions for the stack bond and the running bond patterns are then obtained by imposing $\eta = 0$ and $\eta = 1/2$, respectively. Moreover, for $\eta = 0$ one has to neglect [Eq.\(1.82\)](#) in the computation of the convex hull (see [Section 1.6](#)).

In view of the comparison, we consider the same friction angle ϕ and cohesion c for both the head and the bed joints. [Figure 1.23](#) shows the comparison between the homogenised strength domain resulting from the present work (Cosserat continuum) and the in-plane strength domains obtained by [de Buhan and de Felice \(1997\)](#); [Sab \(2003\)](#) and [Sab et al. \(2007\)](#) (Cauchy continuum). It is worth pointing out that these latter are retrieved starting from [Eqs.\(1.81\)-\(1.83\)](#), by computing the convex hull through [Eq.\(1.84\)](#), by applying the transformations [\(1.85\)-\(1.86\)](#), and by imposing $\beta = 0$. The so-obtained homogenised Cauchy strength domain is then a special case of the present homogenised Cosserat strength domain. In particular, the homogenised domain based on Cosserat continuum is contained for the greatest part into the

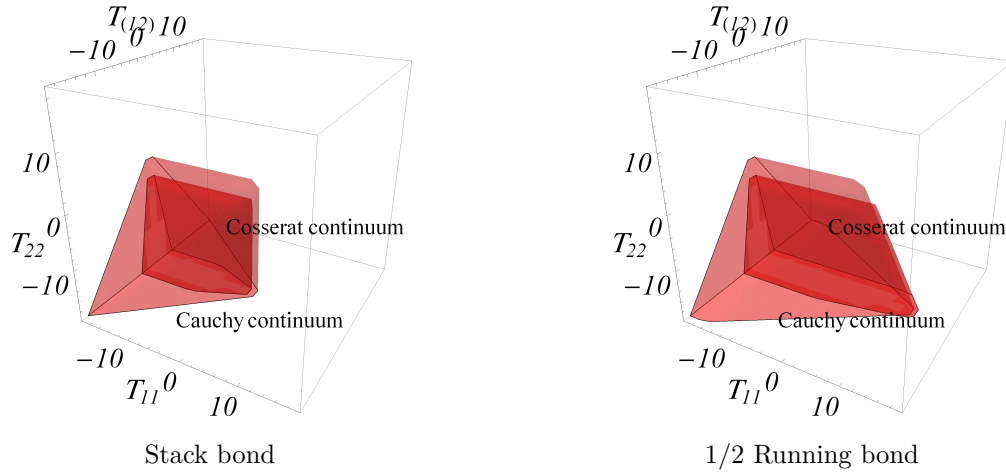


Figure 1.23: Representation of the homogenised strength domain for the masonry wall in the Cauchy stress space. The strength domains for the Cauchy continuum proposed by Sab et al. (2007) (stack bond) and de Buhan and de Felice (1997); Sab (2003) (1/2 running bond) are for $\beta = 0$ (in light red). The strength domains for the Cosserat continuum are for $\beta \neq 0$, here $\beta = 3$ (in dark red).

domain referred to the Cauchy continuum. Only a small portion of the Cosserat strength domain falls outside the Cauchy strength domain, as it is visible in the case of the running bond pattern (Figure 1.23-right). This occurs specifically for $T_{11} > 0$. The role of the terms related to the Cosserat continuum, i.e. the in-plane couples (M_1, M_2) and the non-symmetric stress $T_{[12]}$, is apparent from the comparison. These terms lead to an overall reduction of the masonry strength domain. It is worth noticing that these terms are related to the relative blocks' rotations.

1.7.2 Comparison with Sulem and Mühlhaus (1997)

Sulem and Mühlhaus (1997) gave yield criteria for masonry within the framework of a 2D Cosserat continuum theory. Those criteria were constructed by starting from geometrical and physical considerations made directly on the elementary cell. It resulted in two sets of conditions, representative of both failure mechanisms discussed in Section 1.3 (Figure 1.6). The first set was formulated for representing the interface opening mechanism, due to blocks' tilting. Adopting the present notation, it resulted in the following 4 conditions (Sulem and Mühlhaus, 1997):

$$T_{22} \pm \frac{2a}{b} T_{21} - \frac{4}{b} \left| \frac{2a}{b} M_1 \pm M_2 \right| \leq 0. \quad (1.87)$$

The second set was a cohesion-less Coulomb slip criterion, capable to capture the interface sliding mechanism due to blocks' slip at the bed joints only. It resulted in the following 2 conditions (Sulem and Mühlhaus, 1997):

$$\pm T_{12} + \text{Tan}[\phi] T_{22} \leq 0. \quad (1.88)$$

The strength domain for masonry proposed by Sulem and Mühlhaus (1997) is then the region of the generalized Cosserat stress space enclosed by the hyperplanes of equation (1.87)-(1.88). In Figure 1.24 we show the comparison between this strength domain and the homogenised domain obtained from the present work. The comparison is carried out after having imposed zero joints' cohesion ($c^h = c^v = 0$) and the same friction angle for the head and the bead joints. Two intersections of the strength domains are plotted, one for $M_1 = M_2 = 0$ and one for

$T_{12} = T_{21} = 0$. Moreover, for the comparison we impose $T_{11} = 0$ in the homogenised domain. Concerning the intersection with $M_1 = M_2 = 0$ (Figure 1.24-left), the depicted Cosserat strength domains are relatively close, with exception to the fact that the homogenised domain exhibits a more pronounced anisotropy. Regarding the intersection with $T_{12} = T_{21} = 0$ (Figure 1.24-right), the Cosserat strength domain proposed by Sulem and Mühlhaus (1997) is enclosed by the homogenised domain obtained here. This is probably due to the limited number of variables used for the description of the tilting mechanism and present in Eqs.(1.87)-(1.88).

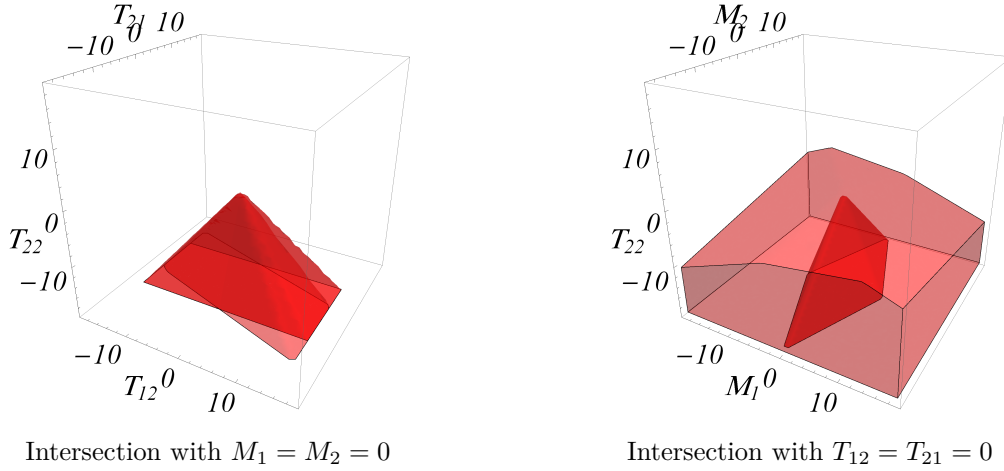


Figure 1.24: Comparison between the Cosserat strength domains for running bond pattern by Sulem and Mühlhaus (1997), Eq.(1.87)-(1.88) (in dark red), and the homogenised Cosserat strength domains from the present work (in light red). Intersections with $M_1 = M_2 = 0$ and $T_{12} = T_{21} = 0$ ($T_{11} = 0$).

1.8 Conclusions

homogenisation models based on Cosserat (or micropolar) continuum allow to model the mechanical behaviour of discrete media, by incorporating the dominant length scales of the micro-structure. In other words, they permit to take into account not only the geometrical configuration of the inner structure, but also its size and its detailed kinematics. The advantages of micropolar continua are well known nowadays (Germain (1973); Mindlin (1964); Vardoulakis and Sulem (1995); de Borst and Sluys (1991)). However, determining the constitutive parameters for a given micro-structure remains still an open research topic. Various approaches have been proposed in the literature for modelling discrete media in the frame of micropolar elasticity, but only few works for plasticity.

In this paper, we developed a consistent homogenisation procedure for the assessment of the in-plane strength domain of discrete periodic media. The procedure followed was the extension to the Cosserat continuum of the procedure initially formulated for the Cauchy continuum (Suquet, 1983; de Buhan and de Felice, 1997; Sab, 2003). The strength domain was derived by application of the kinematic approach of limit analysis. In this way, the relative rotation of the particles and the non-vanishing curvatures of the medium are adequately taken into account.

The extension to the Cosserat continuum was made in a rigorous, extensive and general way. As shown in Section 1.4, the presented homogenisation procedure is applicable to the whole class of discrete media with periodic inner micro-structure (Eringen, 1999). To this class belong, for instance, natural materials as rock assemblies, soils and solid crystals, but also man-made materials as fiber composites, beam lattices, and layered structures. It is worth

noticing that the proposed procedure was limited to 2D periodic media. However, it could be easily extended to media with 3D periodic patterns. In that case, the resort to a 3D Cosserat continuum could be envisaged.

The homogenisation procedure was illustrated with regard to a periodic collection of rigid bodies (or blocks). The interaction between the blocks was established at their interfaces by contact. As result of homogenisation, the macroscopic Cosserat relative deformations and curvatures were produced by combinations of the rigid-body motion of the blocks that composed the discrete medium (see [Section 1.4](#)). Similarly, the macroscopic stresses and couple stresses were computed as the average values of the contact stress distributions exchanged by the blocks along their interfaces. Due to periodicity, all the computations were made on a preselected elementary cell. It was noticed that, with respect to the Cauchy continuum, the use of a Cosserat continuum allowed to capture a richer number of deformation modes of the cell. In particular, the extension to the Cosserat continuum allowed to take into account the effect of blocks' rotation and blocks' relative rotation on the discrete medium. Besides the kinematics, the difference with the Cauchy continuum arose also in the expression of the dissipated power density of the cell, which was better estimated by the Cosserat continuum.

The homogenisation procedure was applied to the case of masonry, which is an interesting example due to the presence of interfaces. homogenised yield criteria were obtained by way of the following assumptions made on masonry: a) the strength capacities of the joints were considered far lower than those of the building blocks, regarded as infinitely resistant, and b) masonry joints were considered as interfaces with Coulomb dissipative properties, given by the joint cohesion and friction angle. Under these assumptions masonry was studied as a discrete assemblage of blocks, which exchange contact stresses and experience rigid-body translations and rotations when masonry undergoes deformation. The homogenised in-plane strength of masonry was determined then by deriving an equivalent Cosserat continuum at the macroscopic scale. Even though it was used the same Coulomb failure criterion than that considered for the Cauchy continuum ([de Buhan and de Felice, 1997](#)), the expression of the dissipated power retrieved for the Cosserat continuum was different. This change, which held true both for the masonry column ([Section 1.5](#)) and the masonry wall ([Section 1.6](#)), was due to the different kinematics of the two media and led to a different form of the computed strength domain.

The application to masonry allowed to highlight the role of particles' rotations on the strength of a discrete medium. Both the example of the column and of the wall showed that the overall strength capacity of masonry was reduced due to the relative blocks' rotations. The Cosserat continuum correctly captured these effects, in contrast with the Cauchy continuum which did not cover them (see [Section 1.5](#) and [Section 1.7](#)). Indeed, relative blocks' rotations were related by means of a kinematic map of the macroscopic in-plane curvatures and the non symmetric part of the macroscopic deformation. These deformation measures were conjugate in energy respectively to the in-plane couples (or moments) and the non symmetric part of the stress tensor of the Cosserat continuum. It is worth noticing that the presence of moments acting in the plane of the walls is intrinsic in structural problems related to masonry ([Petry and Beyer, 2014b](#)). Consequently, in view of practical applications, the use of the homogenised strength domain obtained for the Cosserat continuum would be on the safe side with respect to that computed for the Cauchy continuum.

Chapter 2

Determination of the homogenised yield criteria for masonry: in-plane and out-of-plane coupled behaviour

This Chapter continues the development of the method presented in the previous Chapter. The method relies on the use of the kinematic approach of limit analysis developed, in this case, within the framework of the three-dimensional micropolar (or Cosserat) continuum theory. This further development enables to capture the interaction between the in-plane and out-of-plane actions in the assessment of masonry strength. The relative rotations of the blocks accentuate this interaction, which reduces the in-plane strength and suggests the use of three-dimensional models for masonry. At the end of this Chapter, masonry walls are ascribed to homogenised plates with Cosserat kinematics.

This Chapter is a paper under preparation.

Contents

2.1	Introduction	53
2.2	The 3D Cosserat continuum	54
2.3	The 3D discrete medium	56
2.4	From the 3D discrete medium to the 3D Cosserat continuum: the homogenisation limit analysis kinematic approach	58
2.4.1	Kinematic map	58
2.4.2	Homogenisation kinematic approach	58
2.4.3	Average Cosserat variables	59
2.5	Application to masonry columns	60
2.5.1	Geometry	60
2.5.2	Average Cosserat variables	61
2.5.3	Homogenisation	63
2.6	Application to masonry walls	65
2.6.1	Geometry	65
2.6.2	Average Cosserat variables	66
2.6.3	Justification of the homogenisation procedure	70
2.6.4	Homogenisation	71
2.7	Conclusions	73

Summary

Discrete media may exhibit very complex particle arrangements, that may affect the macroscopic behaviour and place a limit to the use of two-dimensional (or plane) models for the assessment of their strength. In this paper, a method for the evaluation of the homogenised strength of discrete media with three-dimensional periodic micro-structure is developed. The method relies on the use of a three-dimensional Cosserat continuum within the framework of the limit analysis theory. The homogenised strength domain is obtained by application of the kinematic approach. This enables to seize the three-dimensional effect of both the relative translations and the relative rotations of the particles constituting the discrete medium. Two applications to masonry highlight this effect. The homogenised strength of masonry columns and walls is herein retrieved as function of the stresses and couple-stresses of the Cosserat continuum. As a result of the proposed method, the in-plane and out-of-plane actions result coupled in the assessment of masonry strength. It is found that blocks' relative rotation accentuates this interaction, which diminishes the in-plane strength of the medium and justifies the use of three-dimensional with respect to two-dimensional models for masonry.

2.1 Introduction

In a previous work (Godio et al., 2015d), the authors presented a procedure for the assessment of the homogenised strength of discrete media with 2D periodic particle arrangement. In this paper, the homogenisation procedure formulated by Godio et al. (2015d) is properly extended to media with particles disposed along three directions and having three periodicity vectors. This procedure is based on the kinematic approach of limit analysis. Formulated for the most general case of a 3D Cosserat continuum, the homogenisation kinematic approach mainly consists in two steps. First, the discrete medium is replaced by the 3D Cosserat continuum. This is made at cell level, by means of a map that relates the kinematics of the discrete medium to the macroscopic deformation measures of the Cosserat continuum. Second, the macroscopic continuum is constructed by setting the same plastic dissipation with that produced by the discrete medium. By application of the kinematic approach provided by homogenisation theory, an upper bound of the researched strength domain is then retrieved.

The case of masonry is considered as application. The aim of the paper is not to investigate the limits of the assumption of two-dimensional (or plane) behaviour often taken for this material (Anthoine, 1997; Massart et al., 2005) - herein blocks are considered rigid with deformable interfaces. It is to extend the in-plane description made by Godio et al. (2015d) in order to capture the out-of-plane effect of blocks' translations and rotations. Indeed, except when building blocks are disposed following curved structural configurations (Milani et al., 2008), the action of membrane and flexural contact stresses between the blocks, respectively related to their in-plane and out-of-plane kinematics, are uncoupled in the elastic range of masonry (Zucchini and Lourenço, 2002; Mistler et al., 2007; Stefanou et al., 2008). In the non-linear range, the outset and the evolution of irreversible deformations within the material lead inevitably to stresses redistribution. This gives rise to the interaction between the membrane and the flexural actions and ultimately affects masonry strength. This aspect is apparent in media such as soils, and other particulate solids, where discrete particles' interaction is mainly controlled by friction and expressed by laws which are pressure-dependent (Vardoulakis and Sulem, 1995).

In this paper the problem of the coupled in-plane and out-plane behaviour of masonry, i.e. the interaction between the membrane and flexural actions in the assessment of masonry strength, is addressed. This is made by avoiding any a priori assumptions, but is the result of the homogenisation procedure herein developed. The procedure considers the complete 3D kinematics of the blocks, including blocks' rotations, and the finite thickness of the medium. It is worth noticing that the study of masonry strength has been treated by many researchers. However, the interaction between the in-plane and the out-of-plane actions of masonry due to the actual geometry, kinematics and properties of the blocks are considered in few works only. The problem was studied, for instance, by Sab (2003), who proposed a homogenisation method for the assessment of masonry strength within the framework of the limit analysis theory. In that work, masonry was regarded as a periodic assemblage of blocks in contact. Blocks were disposed into a specific pattern and formed a single-leaf wall with finite thickness and two in-plane periodicity directions. Moreover, blocks' strength was considered much larger than that of the interfaces. This further assumption allowed the use of the homogenisation kinematic approach (Suquet, 1983; de Buhan and de Felice, 1997) in analytical form. The homogenised strength of masonry was retrieved according to a Love-Kirchhoff plate model at the macroscopic level. In the same spirit were the works of Sab et al. (2007); Cecchi et al. (2007); Cecchi and Milani (2008). In those case, masonry was ascribed to a plate with Reissner-Mindlin kinematics, in order to take into account the effects of moderate wall thickness. The work of Milani et al. (2006c) was also based in the framework of homogenisation and limit analysis theory. In that work, a numerical procedure based on Linear Programming was proposed for the estimation of

the homogenised masonry strength. The main difference with the aforementioned works (and the present one), was that masonry was considered as a composite material and not as a discrete medium. The finite strength of blocks and mortar layers was taken into account by including polynomial approximations of the stress fields in the resulting homogenisation limit analysis problem. In that case, a plate model with Love-Kirchhoff kinematics was assigned to masonry at the macroscopic level.

The paper is organized as follows. In [Section 2.2](#) we briefly review the basic equations of the 3D Cosserat continuum theory. Basic notations are given in elasticity and the notion of strength for the micropolar medium is presented in the framework of the multisurface plasticity theory. [Section 2.3](#) provides details and extend to 3D the contact model adopted for the description of the discrete medium. The geometric description of its particle arrangement, the choice of the elementary cell and the contact kinematics and statics are discussed. The homogenisation method is presented in [Section 2.4](#) with respect to the presented contact model and then it is applied to the case of masonry columns ([Section 2.5](#)) and walls ([Section 2.6](#)). In the applications, attention is focused on the out-of-plane effect of the relative translations and rotations of the blocks and in the resulting interaction between the in-plane and out-of-plane actions in the evaluation of masonry strength.

Indicial notation is used in this paper, with indices $i, j, k = 1, 2, 3, \dots$. Lower case letters denote variables referring to the discrete medium, while upper case letters refer to the macroscopic variables of the 3D Cosserat continuum. Partial differentiation with respect to orthogonal coordinates is denoted with $[\]_{i,j}$, while $\partial_{Y_j} [\]_i$ designates tensor derivative. Time derivative is indicated with $[\]_{\dot{}}$.

2.2 The 3D Cosserat continuum

The main feature of the Cosserat (or micropolar) continuum is that not only the displacement velocity V_i , but also the angular displacement velocity Ω_i^c of the particles (or *micro-elements* ([Eringen, 1999](#))) that compose the medium contribute to its macroscopic deformation. The rate of linear deformation of the medium is given by two tensors. The first tensor is denoted with Γ_{ij} and describes the relative deformation of the medium:

$$\Gamma_{ij} = D_{ij} + \Theta_{ij}, \quad (2.1)$$

where:

$$D_{ij} = V_{i,j} \quad (2.2)$$

is the gradient of the displacement velocity field of the medium, and:

$$\Theta_{ij} = e_{ijk} \Omega_k^c \quad (2.3)$$

is the micro-spin tensor. The symbol e_{ijk} denotes the third-order permutation tensor. The second tensor is denoted by K_{ij} and contains the gradient of the angular displacement velocity field (or curvature) of the medium:

$$K_{ij} = \Omega_{i,j}^c. \quad (2.4)$$

Tensors D_{ij} , Γ_{ij} and K_{ij} are not necessarily symmetric. Tensor Θ_{ij} is, by construction for a Cosserat continuum, skew-symmetric. In the most general case, a three-dimensional (3D) micropolar medium is then fully described by 18 independent deformation measures.

The static variables associated to Γ_{ij} and K_{ij} are respectively the stress and the couple stress tensors, T_{ij} and M_{ij} . The notations used for these tensors are illustrated in Figure 2.1. Based on these notations, the momentum and angular momentum balance equations are expressed in the following form:

$$\begin{aligned} T_{ij,j} + \rho (B_i - \dot{V}_i) &= 0 \\ M_{ij,j} - e_{ijk} T_{jk} + \rho (L_i - I_{ij} \dot{\Omega}_j^c) &= 0, \end{aligned} \quad (2.5)$$

where B_i and L_i are respectively the intensity of external actions, i.e. body forces and body couples acting on the medium, ρ is the mass density of the medium and I_{ij} is the micro-inertia tensor, containing the moments of inertia of the particles. The internal power density for the Cosserat continuum is then:

$$P^c = T_{ij} \Gamma_{ij} + M_{ij} K_{ij} \quad (2.6)$$



Figure 2.1: Stresses and couple stresses of a 3D Cosserat continuum. Stresses (left) are represented by polar vectors. Couple stresses (right) are represented by spin vectors.

The strength capacities of the Cosserat continuum are expressed in a fashion similar to that used for the Cauchy continuum. The strength (or elastic) domain G^c is the convex region of the generalized stress space (T_{ij}, M_{ij}) , enclosed by a set of N_F plastic surfaces F^β :

$$G^c = \{(T_{ij}, M_{ij}) | F^\beta \leq 0, \forall \beta = 1, \dots, N_F\}. \quad (2.7)$$

The plastic surfaces are implicit functions of the stress and couple stress tensors (Lippmann, 1969; Steinmann, 1994): $F^\beta = F^\beta(T_{ij}, M_{ij})$. They are smooth functions, but according to Eq.(2.7) they may intersect with corners. In this case, the normal to G^c is given by application of the Koiter's rule. For a medium with associative properties, this rule defines the rate of plastic deformation $[\]^p$ of the Cosserat continuum as follows:

$$\Gamma_{ij}^p = \sum_{\beta=1}^{N_F} \lambda^\beta \partial_{T_{ij}} F^\beta, \quad K_{ij}^p = \sum_{\beta=1}^{N_F} \lambda^\beta \partial_{M_{ij}} F^\beta, \quad (2.8)$$

where scalars $\lambda^\beta \geq 0$ are the consistency parameters. The plastic dissipation function (or plastic power) is indicated with Π^c , and for the 3D Cosserat continuum it writes:

$$\Pi^c = \text{Sup}_{(T_{ij}, M_{ij}) \in G^c} \{T_{ij} \Gamma_{ij}^p + M_{ij} K_{ij}^p\}. \quad (2.9)$$

The dissipation function proves essential in the homogenisation procedure proposed in this paper, since it defines the support function of the strength domain, and gives the kinematic definition of G^c (Salençon, 2013):

$$G^c = \{(T_{ij}, M_{ij}) | T_{ij} \Gamma_{ij}^p + M_{ij} K_{ij}^p \leq \Pi^c, \forall (\Gamma_{ij}^p, K_{ij}^p)\}. \quad (2.10)$$

The plastic surfaces and the plastic dissipation are therefore *dual* (or conjugate) functions, in the sense of convex analysis (Hiriart-Urruty and Lemaréchal, 1993; Salençon, 2013).

2.3 The 3D discrete medium

Three key features of the contact model described by Godio et al. (2015d) are briefly outlined in this Section. In Godio et al. (2015d) the description was limited to discrete media with particles arranged in 2D periodic structural configurations. Herein the description is extended to media with particles disposed along 3 directions, and having 3 periodicity vectors.

The first feature concerns the geometric description of the discrete inner structure of the medium. The constituent particles (or blocks) of the discrete medium repeat periodically and regularly in space and share the same size and shape. In this structural configuration, which in crystallographic science is referred to as *mono-atomic* lattice (Kittel, 1996), the relative distance between two generic blocks B^I and B^J is given by:

$$\mathbf{Y}^{GJ} - \mathbf{Y}^{GI} = n\boldsymbol{\alpha}^1 + m\boldsymbol{\alpha}^2 + k\boldsymbol{\alpha}^3 \quad (2.11)$$

where GJ is a specific point of the block B^J (the same for all blocks), \mathbf{Y}^{GJ} is its coordinate vector in a 3D global reference system $(OY_1Y_2Y_3)$, and $(n, m, k) \in \mathbb{Z}^3$. Since particles are equally spaced, it's always possible to choose the periodicity vectors $\boldsymbol{\alpha}^i$ so that: $|\boldsymbol{\alpha}^1| = |\boldsymbol{\alpha}^2| = |\boldsymbol{\alpha}^3| = l_c$, where l_c represents the characteristic length inner to the medium (Figure 2.2).

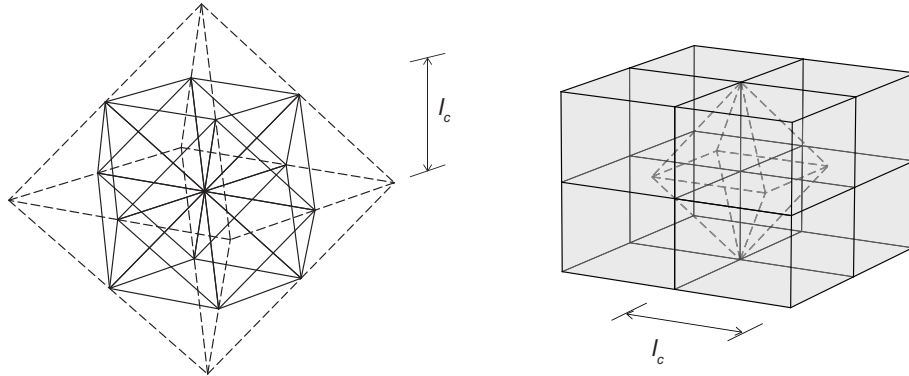


Figure 2.2: Examples of three-dimensional discrete periodic media with particles disposed following a mono-atomic lattice. Left: a periodic collection of beams. Right: a periodic collection of cubic blocks in contact. Both discrete media are based on the same elementary cell (in dotted line).

The second feature to be considered, is the choice of the elementary (or unit) cell, herein denoted with \bar{D} . Of particular interest in the context of homogenisation is the primitive cell, i.e. the cell with the smallest volume: $|\bar{D}| \propto l_c^3$. Indeed, studies have shown how this cell could lead to better estimations of the homogenised properties of the medium (Godio et al., 2015d). For this reason, homogenisation will be carried out on this specific cell.

The third feature consists in the definition of the particles' interaction within the elementary cell, by means of constitutive laws. Constitutive laws are usually comprehensive of: a) moduli controlling the elastic behaviour of the medium, b) yield criteria prescribing the strength capacity of the medium, and c) evolution laws describing the non-linear material response. In the present case, particles are rigid blocks in contact, which interact by exchanging contact stresses r_i^{IJ} at every point of the oriented interfaces Σ^{IJ} (Figure 2.2). Contact stresses are conjugate in

energy to the displacement velocity jumps $\llbracket v_i \rrbracket^{IJ}$ across the interfaces. These latter are defined as:

$$\llbracket v_i \rrbracket^{IJ} = v_i^I(\mathbf{y}) - v_i^J(\mathbf{y}), \forall \mathbf{y} \in \Sigma^{IJ}, \quad (2.12)$$

where \mathbf{y} is the coordinate vector in a 3D local reference system $(oy_1y_2y_3)$ attached to the discrete cell. In the assumption that cell's deformation takes place only at the interface of the blocks, the internal power density of the whole cell writes:

$$p^D = \frac{1}{|\bar{D}|} \left(\sum_{IJ} \int_{\Sigma^{IJ}} r_i^{IJ} \llbracket v_i \rrbracket^{IJ} dS \right), \quad (2.13)$$

where the sum is made over all the interfaces of the cell. In this paper we are interested in the strength capacities of the discrete medium. Consequently, neither linear elastic nor evolution laws of contact are here explicitly formulated. Moreover, for the assessment of the homogenised strength of the discrete medium we make use of the kinematic approach of limit analysis. Therefore, it is handy to introduce $\pi^{IJ} = \pi^{IJ}(\llbracket v_i \rrbracket^{IJ})$, the plastic dissipation function of the interface, defined as:

$$\pi^{IJ} = \text{Sup}_{r_i^{IJ} \in g^{IJ}} \left\{ r_i^{IJ} \llbracket v_i \rrbracket^{IJ} \right\}, \quad (2.14)$$

with g^{IJ} the interface's yield criterion. Provided that:

$$\pi^{IJ} \leq \infty, \quad (2.15)$$

function π^{IJ} gives the amount of maximum plastic dissipation for the discrete cell \bar{D} , reading (Godio et al., 2015d):

$$\pi^D(v_i^{GJ}, \omega_i^{GJ}) = \frac{1}{|\bar{D}|} \left(\sum_{IJ} \int_{\Sigma^{IJ}} \pi^{IJ} dL \right). \quad (2.16)$$

It is worth mentioning that only a limited set of displacement velocity jumps respect Eq.(2.15). These kinematics are those for which the *relevance condition* associated to the interface's yield criterion is respected (Salençon, 2013).

For the sequel, the local reference system is attached to the centre of the cell. The blocks in the discrete cell will undergo 3D rigid-body kinematics of the form:

$$\begin{aligned} v_i^J(\mathbf{y}) &= v_i^{GJ} - e_{ijk} \omega_k^{GJ} (y_j - y_j^{GJ}) \\ \omega_i^J(\mathbf{y}) &= \omega_i^{GJ}, \forall \mathbf{y} \in B^J, \end{aligned} \quad (2.17)$$

where:

$$\begin{aligned} v_i^{GJ} &= v_i(\mathbf{y}^{GJ}) \\ \omega_i^{GJ} &= \omega_i(\mathbf{y}^{GJ}), \end{aligned} \quad (2.18)$$

are the kinematics of the discrete medium (translations and rotations). In addition, it is useful to distinguish the rigid-body displacement jumps, i.e. the relative blocks' translations:

$$\llbracket v_i^G \rrbracket^{IJ} = v_i^{GI} - v_i^{GJ}, \quad (2.19)$$

from the rigid-body rotation jumps, i.e. the relative blocks' rotations, which write:

$$\llbracket \omega_i^G \rrbracket^{IJ} = \omega_i^{GI} - \omega_i^{GJ}. \quad (2.20)$$

In the framework of the Cosserat continuum theory, both relative kinematics contribute to the cell's failure and affect the homogenised strength of the discrete medium (Godio et al., 2015d).

2.4 From the 3D discrete medium to the 3D Cosserat continuum: the homogenisation limit analysis kinematic approach

The purpose of homogenisation in limit analysis is to replace the discrete medium by an equivalent continuum that has the same shape and size, and shares the same dissipation properties with the discrete one. The homogenisation procedure followed in this paper is the extension to 3D of a procedure initially formulated for 2D Cosserat continua (Godio et al., 2015d). This procedure is based on the kinematic approach, i.e. the use of upper bound theorem of limit analysis. Formulated for the most general case of a 3D Cosserat continuum, the homogenisation kinematic approach consists in two fundamental steps. These steps are briefly described below.

2.4.1 Kinematic map

The first step of the homogenisation procedure consists in expressing the discrete medium kinematics in terms of Cosserat deformation measures. This is made at the cell level, by considering the following set of *kinematically admissible* translations and rotations $(v_i^{GJ}, \omega_i^{GJ}) \in KA(\Gamma_{ij}, K_{ij})$ of the 3D discrete cell:

$$KA(\Gamma_{ij}, K_{ij}) = \left\{ (v_i^{GJ}, \omega_i^{GJ}) \mid v_i^{GJ} = D_{ij}y_j^{GJ} + V_i, \omega_i^{GJ} = K_{ij}y_j^{GJ} + \Omega_i^c, \forall J = 1, \dots, N_{\bar{D}} \right\}. \quad (2.21)$$

This set contains virtual variations (herein reported in the form of velocities v_i^{GJ} and microspins ω_i^{GJ}) of the displacements and angular displacements of the discrete medium (Eq.(2.18)), as function of the (rate of) macroscopic deformations of the 3D Cosserat continuum (Eqs.(2.1)-(2.4)). This set is the generalization of that proposed by Godio et al. (2015d) to media with 3D mono-atomic structural configurations, i.e. composed by particles of the same type.

Eq.(2.21) may also be expressed according to the contact model presented in Section 2.3, where blocks undergo rigid-body kinematics (Eq.(2.17)). An alternative form of Eq.(2.21) is then:

$$\begin{aligned} v_i^J(\mathbf{y}) &= \Gamma_{ij}y_j^{GJ} + V_i - e_{ijk} \left[K_{kl}y_l^{GJ} (y_j - y_j^{GJ}) + \Omega_k^c y_j \right] \\ \omega_i^J(\mathbf{y}) &= K_{ij}y_j^{GJ} + \Omega_i^c, \forall \mathbf{y} \in B^J. \end{aligned} \quad (2.22)$$

This definition will be used next, in the application to masonry.

2.4.2 Homogenisation kinematic approach

The second step of the homogenisation procedure followed here consists in setting $\Pi^{c,hom}$, i.e. the plastic power of the homogenised Cosserat continuum (Eq.(2.9)), equal to π^D , the density of plastic dissipation produced by the cell of the discrete medium (Eq.(2.16)):

$$\Pi^{c,hom}(\Gamma_{ij}^p, K_{ij}^p) = \pi^D(v_i^{GJ}, \omega_i^{GJ}). \quad (2.23)$$

It is worth mentioning that, with respect to the homogenisation procedures followed for the Cauchy continuum (Suquet, 1983; de Buhan and de Felice, 1997; Sab, 2003), no optimization is involved in Eq.(2.23). The relative rotations of the discrete medium are directly related to the macroscopic curvature of the continuum through Eq.(2.21).

An upper bound to the homogenised strength of the discrete medium is then found, based on the kinematic definition of the strength domain, here defined as $G^{c,hom}$ (Eq.(2.10)), and the dual properties of the dissipation function $\Pi^{c,hom}$:

$$G^{c,hom} = \{(T_{ij}, M_{ij}) \mid T_{ij}\Gamma_{ij}^p + M_{ij}K_{ij}^p \leq \Pi^{c,hom}, \forall (\Gamma_{ij}^p, K_{ij}^p)\}. \quad (2.24)$$

In the kinematic approach, the choice of compatible $KA(\Gamma_{ij}, K_{ij})$ sets of discrete kinematics $(v_i^{GJ}, \omega_i^{GJ})$ is crucial in order to obtain a good estimation of the homogenised strength. In particular, an upper bound is found only when the kinematics of the discrete medium generate on the elementary cell plastic dissipation of finite value (Eq.(2.15)). The kinematics obeying Eq.(2.15) are said *plastically admissible* (Suquet, 1983), and so are the macroscopic deformations resulting from the presented homogenisation procedure.

2.4.3 Average Cosserat variables

In light of the homogenisation procedure, the macroscopic deformations of the 3D Cosserat continuum have a precise physical meaning, as they represent the average deformation modes of the cell. Similar to Godio et al. (2015d), it can be shown that the average values of the macroscopic displacement velocity gradient, relative deformation and curvature tensors are:

$$D_{ij} = \frac{1}{|\bar{D}|} \left(\sum_{IJ} \int_{\Sigma^{IJ}} \llbracket v_i^G \rrbracket^{IJ} n_j^{IJ} dS \right), \quad (2.25)$$

$$\Gamma_{ij} = \frac{1}{|\bar{D}|} \left(\sum_{IJ} \int_{\Sigma^{IJ}} \llbracket v_i \rrbracket^{IJ} n_j^{IJ} dS \right), \quad (2.26)$$

$$K_{ij} = \frac{1}{|\bar{D}|} \left(\sum_{IJ} \int_{\Sigma^{IJ}} \llbracket \omega_i \rrbracket^{IJ} n_j^{IJ} dS \right). \quad (2.27)$$

Notice that the deformation measures above can always be split in their elastic and plastic parts. For brevity, the superscript p that distinguishes the plastic from the elastic part of the deformation measures is omitted. Similarly, the values of V_i and Ω_i^c , representing the average rigid-body translations and rotations of the discrete cell, are:

$$V_i = \frac{1}{|\bar{D}|} \left(\sum_{J=1}^{N_{\bar{D}}} \int_{B^J} v_i^J dV \right). \quad (2.28)$$

$$\Omega_i^c = \frac{1}{|\bar{D}|} \left(\sum_{J=1}^{N_{\bar{D}}} \int_{B^J} \omega_i^J dV \right). \quad (2.29)$$

The associated average static variable are retrieved by equating the power density of the cell \bar{D} with that of the homogenised Cosserat continuum:

$$p^D = T_{ij} \Gamma_{ij} + M_{ij} K_{ij}, \quad (2.30)$$

and by expressing the discrete kinematics through the kinematic map (2.21). The resultant non-symmetric macroscopic stresses are:

$$T_{ij} = \frac{1}{|\bar{D}|} \left(\sum_{IJ} \int_{\Sigma^{IJ}} r_i^{IJ} l_j^{IJ} dS \right), \quad (2.31)$$

and the resultant macroscopic couple stresses are:

$$M_{ij} = \frac{1}{|\bar{D}|} \left(\sum_{IJ} \int_{\Sigma^{IJ}} -e_{kji} r_k^{IJ} (y_l^{IJ} - y_l^{GI} y_j^{GI} + y_l^{GJ} y_j^{GJ}) dS \right). \quad (2.32)$$

It is worth remarking that the above expressions are the same with those found by [Bardet and Vardoulakis \(2001\)](#).

2.5 Application to masonry columns

2.5.1 Geometry

We consider a simple masonry column (or pillar), with rectangular building blocks arranged periodically in the vertical direction y_2 ([Figure 2.3](#)). The dimensions of each block in the local directions (y_1, y_2, y_3) are denoted respectively with a, b and t . In particular, t is the block thickness. The column has a periodic micro-structure, which is organized along a single periodicity vector $\boldsymbol{\alpha}^1$:

$$\boldsymbol{\alpha}^1 = 0\mathbf{e}_1 + a\mathbf{e}_2 + 0\mathbf{e}_3.$$

The elementary cell chosen here consists of two adjacent half-blocks, sharing a single interface Σ^{12} ([Figure 2.3](#)). It is denoted with \bar{B} and defined as:

$$\bar{B} = \left[-\frac{b}{2}, +\frac{b}{2}\right] \times \left[-\frac{a}{2}, +\frac{a}{2}\right] \times \left[-\frac{t}{2}, +\frac{t}{2}\right].$$

The position of the centre of mass of each block in the cell is:

$$\begin{aligned} \mathbf{y}^{\mathbf{G}1} &= 0\mathbf{e}_1 + \frac{a}{2}\mathbf{e}_2 + 0\mathbf{e}_3 \\ \mathbf{y}^{\mathbf{G}2} &= 0\mathbf{e}_1 - \frac{a}{2}\mathbf{e}_2 + 0\mathbf{e}_3. \end{aligned}$$

The interface between the blocks is located at:

$$\mathbf{y}^{\Sigma^{12}} = y_1\mathbf{e}_1 + 0\mathbf{e}_2 + y_3\mathbf{e}_3, \forall (y_1, y_3) \in \left[-\frac{b}{2}, +\frac{b}{2}\right] \times \left[-\frac{t}{2}, +\frac{t}{2}\right]$$

and its unit normal vector is $\mathbf{n}^{12} = \mathbf{e}_2$.

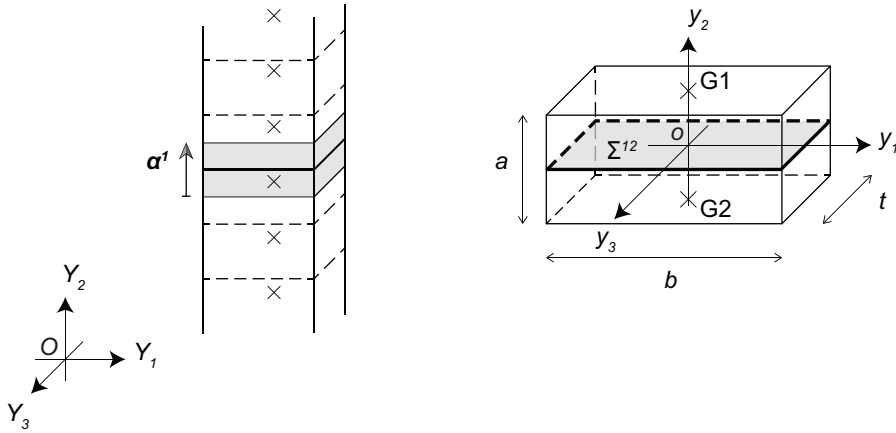


Figure 2.3: Periodic masonry column (left) and the corresponding 3D elementary cell \bar{B} (right).

2.5.2 Average Cosserat variables

The kinematics of the column is described by piece-wise linear distributions of the displacement and angular displacement velocity fields of the form (2.17) (rigid-body kinematics). However, the kinematically admissible sets $(v_i^{GJ}, \omega_i^{GJ}) \in KA(\Gamma_{ij}, K_{ij})$ differ from the general form (2.21) by the absence of the terms (Γ_{i1}, K_{i1}) , and write:

$$KA(\Gamma_{i2}, K_{i2}) = \left\{ (v_i^{GJ}, \omega_i^{GJ}) \mid v_i^{GJ} = D_{i2}y_2^{GJ} + V_i, \omega_i^{GJ} = K_{i2}y_2^{GJ} + \Omega_i^c, \forall J = 1, 2 \right\}, \quad (2.33)$$

with $i = 1, 2, 3$. In similar way, the displacement and angular displacement field distributions (Eq.(2.22)) result in the following simplified expressions:

$$\begin{aligned} v_i^J(\mathbf{y}) &= \Gamma_{i2}y_2^{GJ} + V_i - e_{ijk} \left[K_{i2}y_2^{GJ} (y_j - y_j^{GJ}) + \Omega_k^c y_j \right] \\ \omega_i^J(\mathbf{y}) &= K_{i2}y_2^{GJ} + \Omega_i^c, \forall \mathbf{y} \in B^J. \end{aligned} \quad (2.34)$$

In Eqs.(2.33)-(2.34), the macroscopic deformation measures (Γ_{i2}, K_{i2}) capture the 3D average deformation modes of the discrete cell. In fact, according to Eqs.(2.27)-(2.26), the macroscopic relative deformations and curvatures of the 3D Cosserat continuum are generated by specific combinations of translations and rotations of the blocks that compose the cell (Figure 2.4). On the contrary, the terms V_i and Ω_i^c describe the 3D rigid-body modes of the cell (Figure 2.5). These terms are in fact provided by blocks' motions producing, in an average sense, zero deformation energy on the cell (Eqs.(2.29)-(2.28)). In the case of the column, the resulting relative deformations and curvatures are:

$$\Gamma_{i2} = D_{i2} + e_{i2k}\Omega_k^c, \quad K_{i2} = \frac{\omega_i^{G1} - \omega_i^{G2}}{a}, \quad (2.35)$$

with:

$$D_{i2} = \frac{v_i^{G1} - v_i^{G2}}{a} \quad (2.36)$$

the 3D average displacement gradient, and:

$$\Omega_k^c = \frac{\omega_k^{G1} + \omega_k^{G2}}{2} \quad (2.37)$$

the 3D average Cosserat rotations. The cell translations are:

$$V_i = \frac{v_i^{G1} + v_i^{G2}}{2}. \quad (2.38)$$

The static variables conjugate to (Γ_{i2}, K_{i2}) are (T_{i2}, M_{i2}) . These quantities are computed as the average values of the contact stress distributions exchanged between the blocks of the cell. By application of Eqs.(2.31)-(2.32), they read:

$$T_{i2} = \frac{1}{bt} \int_{-\frac{b}{2}}^{\frac{b}{2}} \int_{-\frac{t}{2}}^{\frac{t}{2}} r_i^{IJ} dy_3 dy_1, \quad M_{i2} = -\frac{1}{bt} \int_{-\frac{b}{2}}^{\frac{b}{2}} \int_{-\frac{t}{2}}^{\frac{t}{2}} e_{kti} r_k^{IJ} y_l dy_3 dy_1. \quad (2.39)$$

In particular, Eq.(2.39)-2 yields:

$$\begin{aligned} M_{12} &= -\frac{1}{bt} \int_{-\frac{b}{2}}^{\frac{b}{2}} \int_{-\frac{t}{2}}^{\frac{t}{2}} r_2^{IJ} y_3 dy_3 dy_1 \\ M_{22} &= \frac{1}{bt} \int_{-\frac{b}{2}}^{\frac{b}{2}} \int_{-\frac{t}{2}}^{\frac{t}{2}} (r_1^{IJ} y_3 - r_3^{IJ} y_1) dy_3 dy_1 \\ M_{32} &= \frac{1}{bt} \int_{-\frac{b}{2}}^{\frac{b}{2}} \int_{-\frac{t}{2}}^{\frac{t}{2}} r_2^{IJ} y_1 dy_3 dy_1. \end{aligned} \quad (2.40)$$

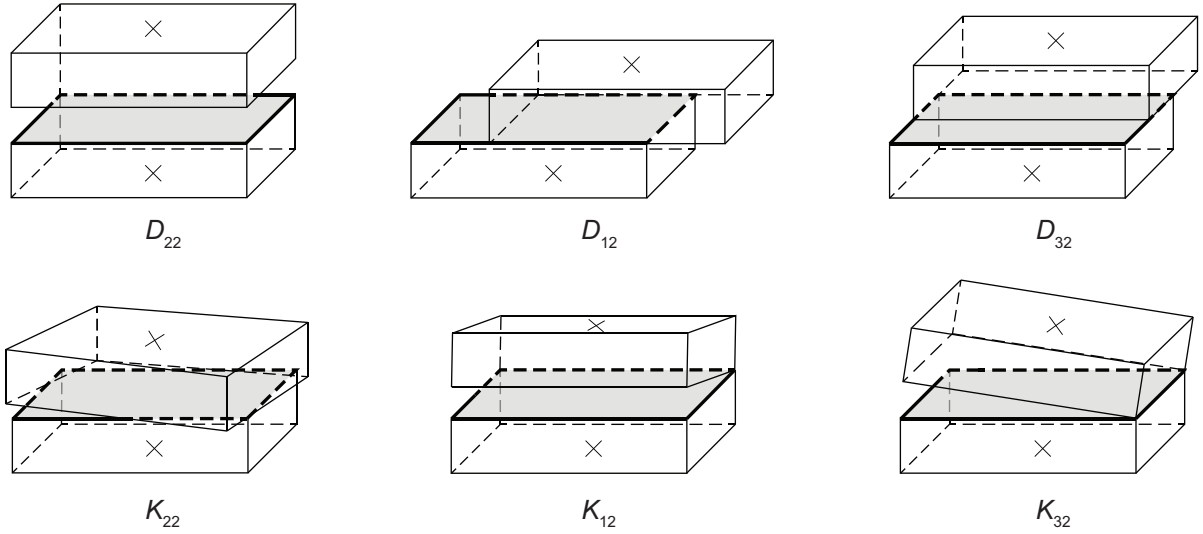


Figure 2.4: Blocks' motions $(v_i^{GJ}, \omega_i^{GJ})$ producing 6 macroscopic Cosserat deformation modes of the discrete cell \bar{B} . Top: 3 displacement gradients D_{i2} . Bottom: 3 rotation gradients K_{i2} .

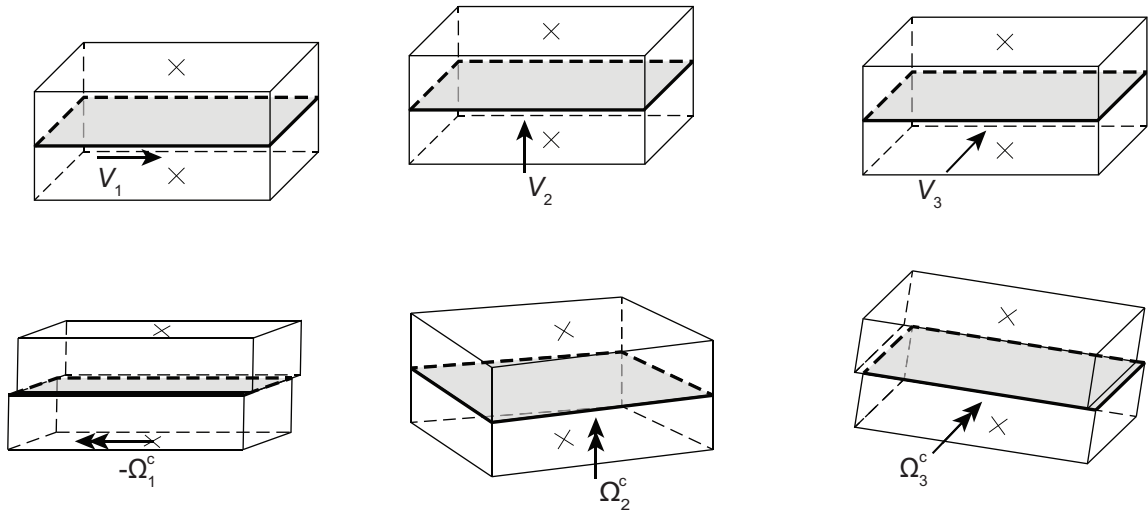


Figure 2.5: Blocks' motions $(v_i^{GJ}, \omega_i^{GJ})$ producing 6 macroscopic rigid-body modes of the discrete cell \bar{B} . Top: 3 translations V_i . Bottom: 3 Cosserat rotations Ω_i^c .

The remaining static variables (T_{i1}, M_{i1}) , together with (Γ_{i1}, K_{i1}) , are null (Eqs.(2.31)-(2.32)):

$$T_{i1} = 0, \quad M_{i1} = 0. \quad (2.41)$$

The external boundaries of the column are then free faces.

Therefore, at the macroscopic scale, the masonry column can be ascribed to a 3D Cosserat (or Timoshenko) beam model, showing 3 macroscopic stresses T_{i2} (or forces), 3 macroscopic couple stresses M_{i2} (or moments), together with 6 associated deformation variables. It is worth pointing out that the reduction of the problem (from 18 deformation measures to 6, Eq.(2.33)) in the case of the column is not an a priori assumption, but is a result of the adopted homogenisation procedure. Eqs.(2.26)-(2.27),(2.31)-(2.32) are general and apply for every periodic medium with 3D mono-atomic pattern. The average Cosserat variables resulting from these equations depend on the periodicity of the discrete medium, and the geometry of the elementary cell. Namely,

they depend on the disposition of the blocks within the cell and the relative orientation of the interfaces. In many cases, this can lead to a possible reduction of the kinematic map (2.21). Taking, for instance, the case of a platband with $\mathbf{n}^{12} = -\mathbf{e}_1 + \mathbf{e}_2$ (Figure 2.6), Eq.(2.21) would produce the additional macroscopic deformation measures:

$$\Gamma_{i1} = -\Gamma_{i2}, \quad K_{i1} = -K_{i2}$$

but still:

$$T_{i1} = 0, \quad M_{i1} = 0$$

with (Γ_{i2}, K_{i2}) and (T_{i2}, M_{i2}) given respectively by Eq.(2.35) and (2.39).

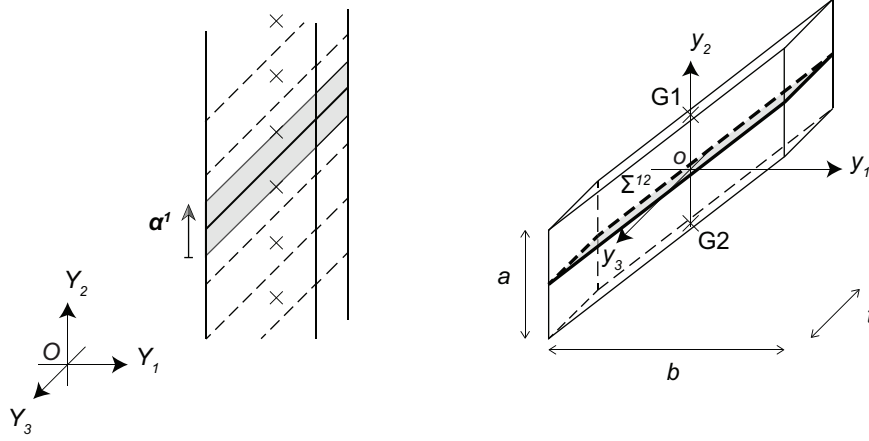


Figure 2.6: Periodic masonry platband (left) and the corresponding 3D elementary cell (right).

The displacement velocity jumps across the interface Σ^{12} needed for homogenisation read, according to Eq.(2.33):

$$\llbracket \mathbf{v} \rrbracket^{12} = a \begin{bmatrix} \Gamma_{12} + y_3 K_{22} \\ \Gamma_{22} + y_1 K_{32} - y_3 K_{12} \\ \Gamma_{32} - y_1 K_{22} \end{bmatrix}. \quad (2.42)$$

2.5.3 Homogenisation

Blocks are considered infinitely resistant, while interfaces obey to a Coulomb slip failure criterion. For such criterion, the dissipation function is (Salençon, 2013):

$$\pi^{IJ} (\llbracket v_i \rrbracket^{IJ}) = \pi^{IJ} (\llbracket v_i \rrbracket^{IJ}; \mathbf{n}_i^{IJ}) = \frac{c}{\tan[\phi]} \llbracket v_i \rrbracket^{IJ} \mathbf{n}_i^{IJ}, \quad (2.43)$$

where c is the cohesion and ϕ is friction angle of the interface. The relevance condition for which $\pi^{IJ} < \infty$ is:

$$\llbracket v_i \rrbracket^{IJ} \mathbf{n}_i^{IJ} \geq \left| \llbracket v_i \rrbracket^{IJ} \right| \sin[\phi]. \quad (2.44)$$

A geometric interpretation of condition (2.44) is given in Figure 2.7, with reference to the present cell \bar{B} . The 3D displacement velocity jump $\llbracket v_i \rrbracket^{12}$ is considered plastically admissible when it falls inside the depicted cone. Displacement jumps leading the interface Σ^{12} to failure (according to a Coulomb slip criterion) are then those which promote opening and sliding

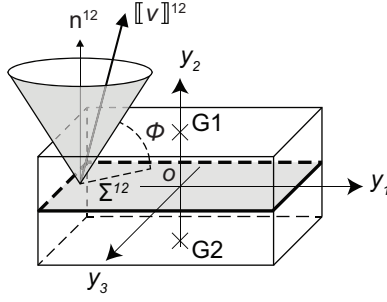


Figure 2.7: Coulomb slip criterion adopted at the interface level of the 3D cell \bar{B} . Cone of plastically admissible displacement jumps.

mechanisms across the interface. On the contrary, failure will not occur for kinematics that involve compression between the blocks. In the instance of masonry columns this remains a reasonable assumption.

Eq.(2.43) gives the plastic dissipation at every point of the interface Σ^{12} . Using Eq.(2.42), this can be expressed as function of the 3D macroscopic Cosserat deformation measures:

$$\pi^{12} \left(\llbracket \mathbf{v} \rrbracket^{12}; \mathbf{n}^{12} \right) = \frac{c}{\text{Tan}[\phi]} a (\Gamma_{22} - y_3 K_{12} + y_1 K_{32}). \quad (2.45)$$

Integrating the above expression over the interface Σ^{12} , we obtain then the plastic dissipation on the discrete cell \bar{B} :

$$\pi^D = \frac{1}{abt} \int_{-\frac{b}{2}}^{\frac{b}{2}} \int_{-\frac{t}{2}}^{\frac{t}{2}} \pi^{12} \left(\llbracket \mathbf{v} \rrbracket^{12}; \mathbf{n}^{12} \right) dy_3 dy_1 = \frac{c}{\text{Tan}[\phi]} \Gamma_{22}. \quad (2.46)$$

Setting then:

$$\Pi^{c,hom} = \pi^D,$$

the kinematic definition of $G^{c,hom}$ (Eq. (2.24)) yields for the column :

$$\begin{aligned} G^{c,hom} = \{ (T_{i2}, M_{i2}) \mid & T_{12} \Gamma_{12} + \left(T_{22} - \frac{c}{\text{Tan}[\phi]} \right) \Gamma_{22} + T_{32} \Gamma_{32} \\ & + M_{12} K_{12} + M_{22} K_{22} + M_{32} K_{32} \leq 0, \forall (\Gamma_{i2}, K_{i2}) \}. \end{aligned} \quad (2.47)$$

According to the Coulomb criterion, the following relevance condition must be satisfied at every point of the interface (Eq.(2.44)):

$$- (\Gamma_{22} - y_3 K_{12} + y_1 K_{32}) + \text{Tan}[\phi] \sqrt{(\Gamma_{32} - y_1 K_{22})^2 + (\Gamma_{12} + y_3 K_{22})^2} \leq 0. \quad (2.48)$$

Due to the convexity of the strength domain, it is necessary to satisfy the above condition only at the corners of the cell's interface (Figure 2.8). This generates the following four inequalities:

$$\begin{aligned} H^{1-4}(T_{i2}, M_{i2}) = & - \left(\Gamma_{22} - \epsilon_2 \frac{t}{2} K_{12} + \epsilon_1 \frac{b}{2} K_{32} \right) \\ & + \text{Tan}[\phi] \sqrt{\left(\Gamma_{32} - \epsilon_1 \frac{b}{2} K_{22} \right)^2 + \left(\Gamma_{12} + \epsilon_2 \frac{t}{2} K_{22} \right)^2} \leq 0, \end{aligned} \quad (2.49)$$

with $\epsilon_1, \epsilon_2 = \pm 1$. These inequalities give the domain of plastically admissible kinematics $(v_i^{GJ}, \omega_i^{GJ}) \in KA(\Gamma_{i2}, K_{i2})$ for the periodic masonry column. This domain is a conical region of the space of the generalized Cosserat deformations enclosed by multiple surfaces. Its

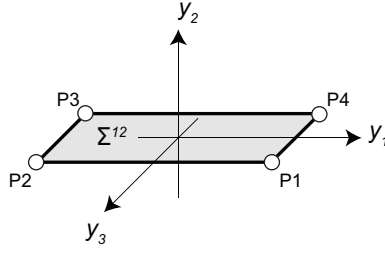


Figure 2.8: Points of the 3D elementary cell where the relevance condition (Eq.(2.44)) needs to be satisfied.

intersection in the space of different Cosserat deformations is given in Figure 2.9 for different values of the curvature K_{22} .

Notice that the expressions obtained by Godio et al. (2015d) for the in-plane behaviour of the column are retrieved by imposing $\Gamma_{32} = K_{12} = K_{22} = 0$ in Eq.(2.49). However, with respect to the in-plane case, the expressions herein retrieved are non-linear. This makes problematic the computation of the homogenised strength domain in the space of the generalized Cosserat stresses, by means of algorithms based on the convex hull research (Godio et al., 2015d).

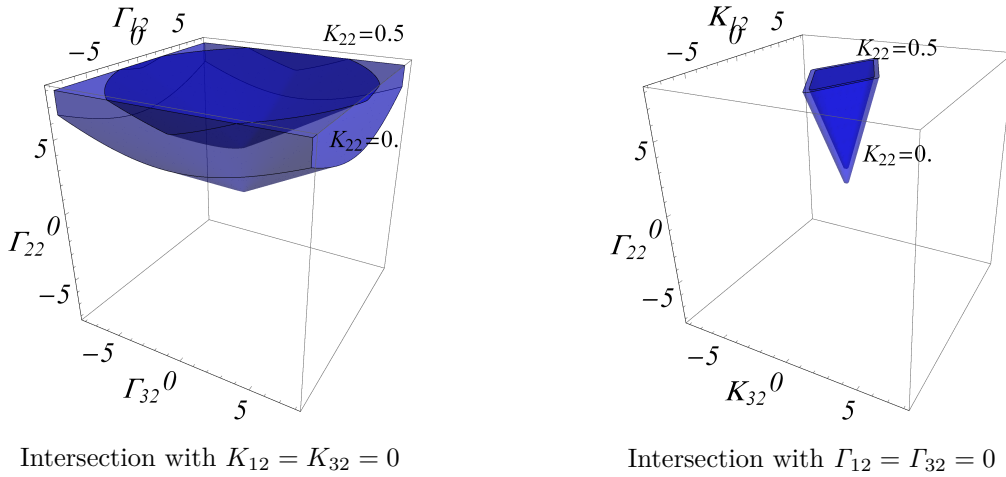


Figure 2.9: Representations of the cone of the plastically admissible homogenised Cosserat deformations for the masonry column.

2.6 Application to masonry walls

2.6.1 Geometry

Two periodicity vectors generate the elementary cell \bar{A} of a single-leaf masonry wall (Figure 2.10):

$$\begin{aligned}\alpha^1 &= b\mathbf{e}_1 + 0\mathbf{e}_2 + 0\mathbf{e}_3 \\ \alpha^2 &= \eta b\mathbf{e}_1 + a\mathbf{e}_2 + 0\mathbf{e}_3,\end{aligned}$$

This cell has the form of a parallelogram. Its volume is $|\bar{A}| = |\alpha^1 \times \alpha^2|t = abt$, where a , b and t are respectively the width, height and thickness of a each block. Following Godio et al. (2015d), the parameter $\eta \in [0, 1/2]$ is introduced in order to control the shape of the cell. In

this way, computations are made on an arbitrary cell corresponding to a generic running bond pattern. Results relative to particular patterns are then produced for different values of η . The cells for the stack bond pattern and the classical (1/2) running bond pattern are respectively for $\eta = 0$ and $\eta = 1/2$.

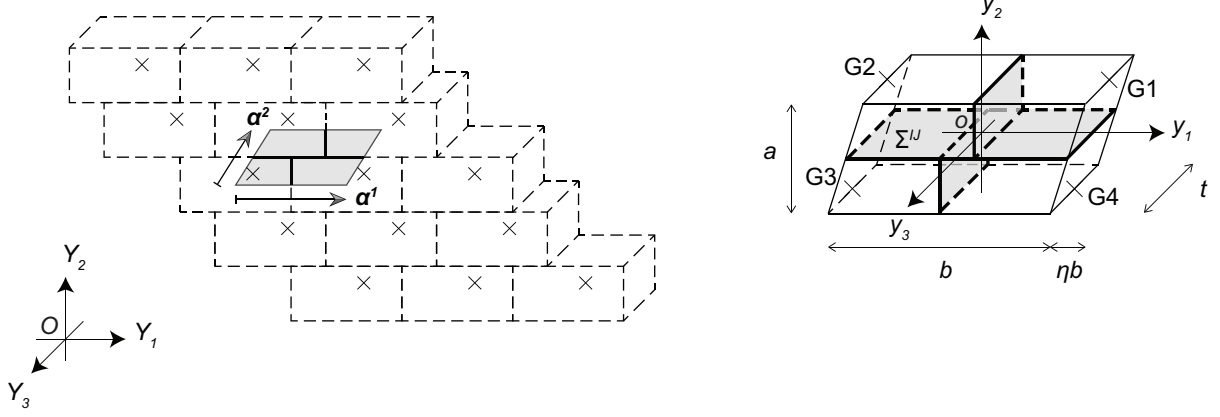


Figure 2.10: Periodic masonry wall (left) and the corresponding 3D elementary cell \bar{A} (right).

A 3D local coordinate system $(oy_1y_2y_3)$ is attached to the center of the cell, and $(\mathbf{e}_1, \mathbf{e}_2, \mathbf{e}_3)$ are the rectangular unit base vectors. The centres of mass of the blocks are denoted with GJ and are situated at the boundary of the primitive cell \bar{A} :

$$\begin{aligned} \mathbf{y}^{\mathbf{G1}} &= (1 + \eta) \frac{b}{2} \mathbf{e}_1 + \frac{a}{2} \mathbf{e}_2 + 0\mathbf{e}_3 \\ \mathbf{y}^{\mathbf{G2}} &= -(1 - \eta) \frac{b}{2} \mathbf{e}_1 + \frac{a}{2} \mathbf{e}_2 + 0\mathbf{e}_3 \\ \mathbf{y}^{\mathbf{G3}} &= -(1 + \eta) \frac{b}{2} \mathbf{e}_1 - \frac{a}{2} \mathbf{e}_2 + 0\mathbf{e}_3 \\ \mathbf{y}^{\mathbf{G4}} &= (1 - \eta) \frac{b}{2} \mathbf{e}_1 - \frac{a}{2} \mathbf{e}_2 + 0\mathbf{e}_3. \end{aligned}$$

Blocks' interfaces are situated across the thickness of the cell and are oriented as follows:

$$\begin{aligned} \mathbf{y}^{\Sigma^{14}} &= y_1 \mathbf{e}_1 + 0\mathbf{e}_2 + y_3 \mathbf{e}_3, \forall (y_1, y_3) \in \left[\frac{\eta}{2}b, \frac{b}{2} \right] \times \left[-\frac{t}{2}, \frac{t}{2} \right], \quad \mathbf{n}^{14} = \mathbf{e}_2 \\ \mathbf{y}^{\Sigma^{23}} &= y_1 \mathbf{e}_1 + 0\mathbf{e}_2 + y_3 \mathbf{e}_3, \forall (y_1, y_3) \in \left[-\frac{b}{2}, -\frac{\eta}{2}b \right] \times \left[-\frac{t}{2}, \frac{t}{2} \right], \quad \mathbf{n}^{23} = \mathbf{e}_2 \\ \mathbf{y}^{\Sigma^{24}} &= y_1 \mathbf{e}_1 + 0\mathbf{e}_2 + y_3 \mathbf{e}_3, \forall (y_2, y_3) \in \left[-\frac{\eta}{2}b, \frac{\eta}{2}b \right] \times \left[-\frac{t}{2}, \frac{t}{2} \right], \quad \mathbf{n}^{24} = \mathbf{e}_2 \\ \mathbf{y}^{\Sigma^{12}} &= \frac{\eta}{2}b \mathbf{e}_1 + y_2 \mathbf{e}_2 + y_3 \mathbf{e}_3, \forall (y_2, y_3) \in \left[0, \frac{a}{2} \right] \times \left[-\frac{t}{2}, \frac{t}{2} \right], \quad \mathbf{n}^{12} = \mathbf{e}_1 \\ \mathbf{y}^{\Sigma^{43}} &= -\frac{\eta}{2}b \mathbf{e}_1 + y_2 \mathbf{e}_2 + y_3 \mathbf{e}_3, \forall (y_2, y_3) \in \left[-\frac{a}{2}, 0 \right] \times \left[-\frac{t}{2}, \frac{t}{2} \right], \quad \mathbf{n}^{43} = \mathbf{e}_1. \end{aligned}$$

In the limit of $\eta \rightarrow 0$ (stack bond pattern), the interface Σ^{24} degenerates into a point. In that case it is not considered in the homogenisation process.

2.6.2 Average Cosserat variables

Masonry walls are three-dimensional discrete media, with two in-plane $(y_1 - y_2)$ periodicity directions and finite thickness (Figure 2.10). Their geometry leads to consider the following set

of admissible kinematics:

$$KA(\Gamma_{i\alpha}, K_{i\alpha}) = \left\{ \left(v_i^{GJ}, \omega_i^{GJ} \right) \mid v_\alpha^{GJ} = D_{\alpha\beta} y_\beta^{GJ} + V_\alpha, \omega_3^{GJ} = K_{3\beta} y_\beta^{GJ} + \Omega_3^c, \right. \\ \left. v_3^{GJ} = D_{3\beta} y_\beta^{GJ} + V_3, \omega_\alpha^{GJ} = K_{\alpha\beta} y_\beta^{GJ} + \Omega_\alpha^c, \forall J = 1, \dots, 4 \right\}, \quad (2.50)$$

with $(i, j) = 1, 2, 3$ and $(\alpha, \beta) = 1, 2$. The above are reduced expressions of the general form (2.21). As in the case of the column, this simplification is dictated by: a) the periodicity of the discrete medium (there are 2 periodicity vectors belonging to the plane of the wall), b) the geometry of the selected cell (wall thickness is finite), and c) the 3D kinematics of the blocks. More particularly, Eq.(2.50) is the extension of the map proposed by Godio et al. (2015d), that takes into account both the in-plane $(v_\alpha^{GJ}, \omega_3^{GJ})$ and the out-of-plane $(v_3^{GJ}, \omega_\alpha^{GJ})$ translations and rotations of the blocks, relative to the wall's mid-plane (at $y_3 = 0$). Indeed, the application of Eqs.(2.26)-(2.27) gives:

$$\Gamma_{i3} = 0, \quad K_{i3} = 0, \quad (2.51)$$

whereas the remaining average deformation measures of the cell are non-null. In particular, the in-plane components of the macroscopic relative deformations and curvatures $(\Gamma_{\alpha\beta}, K_{3\beta})$ are the same than those found by Godio et al. (2015d). For brevity, they are not reported here. Attention is focused on the out-of-plane components $(\Gamma_{3\beta}, K_{\alpha\beta})$, which read respectively:

$$\Gamma_{31} = \frac{v_3^{G1} - v_3^{G2} - v_3^{G3} + v_3^{G4}}{2b} + \\ - \frac{a \left(\omega_3^{G1} - \omega_3^{G2} + \omega_3^{G3} - \omega_3^{G4} \right)}{8b} + \Omega_2^c \\ \Gamma_{32} = \frac{(1 - \eta) v_3^{G1} + (1 + \eta) v_3^{G2} - (1 - \eta) v_3^{G3} - (1 + \eta) v_3^{G4}}{2a} + \\ \frac{(1 - \eta^2) b \left(\omega_2^{G1} - \omega_2^{G2} + \omega_2^{G3} - \omega_2^{G4} \right)}{8a} + \frac{\eta \left(\omega_1^{G1} - \omega_1^{G2} + \omega_1^{G3} - \omega_1^{G4} \right)}{4} - \Omega_1^c, \quad (2.52)$$

and:

$$K_{11} = \frac{\omega_1^{G1} - \omega_1^{G2} - \omega_1^{G3} + \omega_1^{G4}}{2b} \\ K_{12} = \frac{(1 - \eta) \omega_1^{G1} + (1 + \eta) \omega_1^{G2} - (1 - \eta) \omega_1^{G3} - (1 + \eta) \omega_1^{G4}}{2a} \\ K_{21} = \frac{\omega_2^{G1} - \omega_2^{G2} - \omega_2^{G3} + \omega_2^{G4}}{2b} \\ K_{22} = \frac{(1 - \eta) \omega_2^{G1} + (1 + \eta) \omega_2^{G2} - (1 - \eta) \omega_2^{G3} - (1 + \eta) \omega_2^{G4}}{2a}. \quad (2.53)$$

For the expressions of the macroscopic Cosserat out-of-plane deformation measures in the case of the stack bond and the 1/2 running bond patterns, the reader is referred to Appendix B.1. Figure 2.11 gives an illustration of the deformation modes of the cell A for the stack bond pattern, in relation with those of the Cosserat continuum. It is worth noticing that the small overlaps visible along the blocks' interface are absent in real structures, by virtue of distributed local deformations, as blocks are not perfectly rigid.

The terms V_3 and Ω_α^c represent the average out-of-plane rigid-body kinematics of the cell

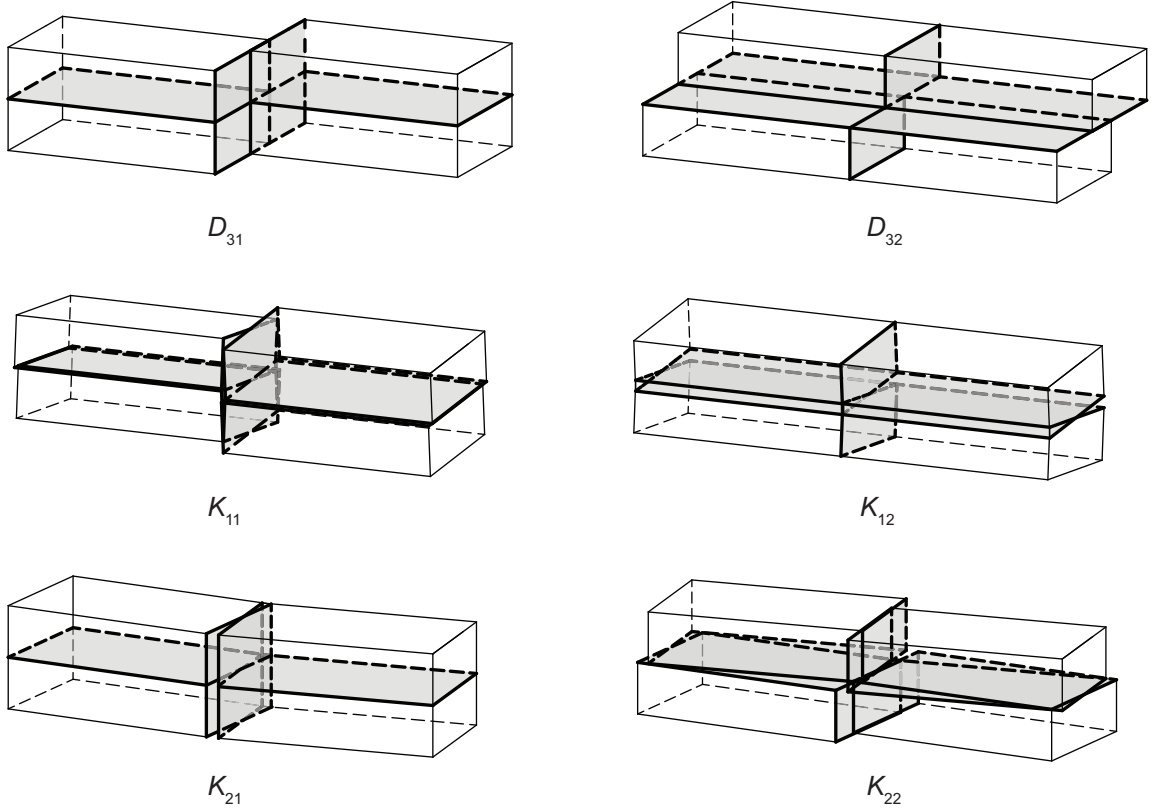


Figure 2.11: Rigid-body motion of the blocks (translations and rotations) producing 6 out-of-plane Cosserat macroscopic deformations of the elementary cell \bar{A} of a periodic masonry wall (stack bond pattern). Top: 3 displacement gradients. Bottom: 3 rotation gradients.

(Figure 2.12). Their expression is (Eqs.(2.29)-(2.28)):

$$\begin{aligned}
 V_3 &= \frac{v_3^{G1} + v_3^{G2} + v_3^{G3} + v_3^{G4}}{4} \\
 \Omega_\alpha^c &= \frac{\omega_\alpha^{G1} + \omega_\alpha^{G2} + \omega_\alpha^{G3} + \omega_\alpha^{G4}}{4}.
 \end{aligned} \tag{2.54}$$

As far as it concerns the average Cosserat static variables, by using Eqs.(2.31)-(2.32) one obtains:

$$T_{i3} = 0, \quad M_{i3} = 0. \tag{2.55}$$

The in-plane components $(T_{\alpha\beta}, M_{3\beta})$ differ slightly from those of Godio et al. (2015d) since, in the present case, average is computed on the volume (and not the surface) of the cell \bar{A} , and integration is made also over the thickness of the interfaces Σ^{IJ} . The out-of-plane components $(T_{3\beta}, M_{\alpha\beta})$ are, referring to the contact model described in Section 2.3:

$$\begin{aligned}
 T_{31} &= \frac{1}{at} \left(\int_{-\frac{t}{2}}^{\frac{t}{2}} \int_0^{\frac{a}{2}} r_3^{12} dy_2 dy_3 + \int_{-\frac{t}{2}}^{\frac{t}{2}} \int_{-\frac{a}{2}}^0 r_3^{43} dy_2 dy_3 \right. \\
 &\quad \left. + \int_{-\frac{t}{2}}^{\frac{t}{2}} \int_{\eta\frac{b}{2}}^{\frac{b}{2}} \eta r_3^{14} dy_1 dy_3 + \int_{-\frac{t}{2}}^{\frac{t}{2}} \int_{-\frac{b}{2}}^{-\eta\frac{b}{2}} \eta r_3^{23} dy_1 dy_3 - \int_{-\frac{t}{2}}^{\frac{t}{2}} \int_{-\eta\frac{b}{2}}^{\eta\frac{b}{2}} (1-\eta) r_3^{24} dy_1 dy_3 \right) \\
 T_{32} &= \frac{1}{bt} \left(\int_{-\frac{t}{2}}^{\frac{t}{2}} \int_{\eta\frac{b}{2}}^{\frac{b}{2}} r_3^{14} dy_1 dy_3 + \int_{-\frac{t}{2}}^{\frac{t}{2}} \int_{-\frac{b}{2}}^{-\eta\frac{b}{2}} r_3^{23} dy_1 dy_3 + \int_{-\frac{t}{2}}^{\frac{t}{2}} \int_{-\eta\frac{b}{2}}^{\eta\frac{b}{2}} r_3^{24} dy_1 dy_3 \right),
 \end{aligned} \tag{2.56}$$

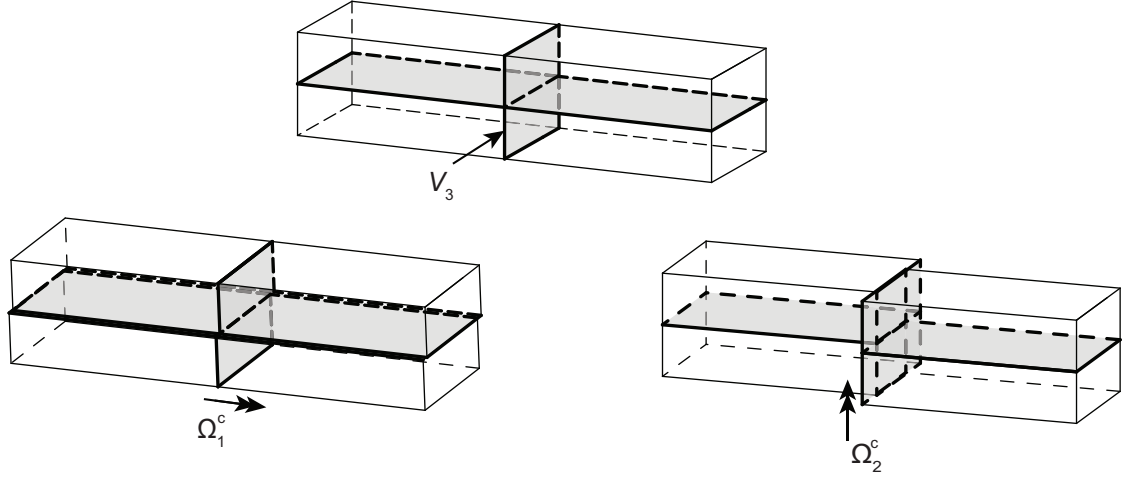


Figure 2.12: Rigid-body motion of the blocks $(v_i^{GJ}, \omega_i^{GJ})$ producing 3 macroscopic out-of-plane rigid-body modes of the discrete cell \bar{A} of a periodic masonry wall (stack bond pattern). Top: 1 rigid translation V_3 . Bottom: 3 Cosserat rotations (Ω_1^c, Ω_2^c) .

and

$$\begin{aligned}
M_{11} &= \frac{1}{at} \left(\int_0^{\frac{a}{2}} \int_{-\frac{t}{2}}^{\frac{t}{2}} (r_3^{12} y_2 - r_2^{12} y_3) dy_3 dy_2 + \int_{-\frac{a}{2}}^0 \int_{-\frac{t}{2}}^{\frac{t}{2}} (r_3^{43} y_2 - r_2^{43} y_3) dy_3 dy_2 + \right. \\
&\quad \left. - \int_{\frac{b}{2}}^{\frac{b}{2}} \int_{-\frac{t}{2}}^{\frac{t}{2}} \eta r_2^{14} y_3 dy_3 dy_1 - \int_{-\frac{b}{2}}^{-\frac{b}{2}} \int_{-\frac{t}{2}}^{\frac{t}{2}} \eta r_2^{23} y_3 dy_3 dy_1 + \int_{-\frac{\eta b}{2}}^{\frac{\eta b}{2}} \int_{-\frac{t}{2}}^{\frac{t}{2}} (1 - \eta) r_2^{24} y_3 dy_3 dy_1 \right) \\
M_{12} &= -\frac{1}{bt} \left(\int_{\frac{b}{2}}^{\frac{b}{2}} \int_{-\frac{t}{2}}^{\frac{t}{2}} r_2^{14} y_3 dy_3 dy_1 + \int_{-\frac{b}{2}}^{-\frac{b}{2}} \int_{-\frac{t}{2}}^{\frac{t}{2}} r_2^{23} y_3 dy_3 dy_1 + \int_{-\frac{\eta b}{2}}^{\frac{\eta b}{2}} \int_{-\frac{t}{2}}^{\frac{t}{2}} r_2^{24} y_3 dy_3 dy_1 \right) \\
M_{21} &= \frac{1}{at} \left(\int_0^{\frac{a}{2}} \int_{-\frac{t}{2}}^{\frac{t}{2}} \frac{1}{2} (2r_1^{12} y_3 - \eta b r_3^{12}) dy_3 dy_2 + \int_{-\frac{a}{2}}^0 \int_{-\frac{t}{2}}^{\frac{t}{2}} \frac{1}{2} (2r_1^{43} y_3 + \eta b r_3^{43}) dy_3 dy_2 + \right. \\
&\quad \int_{\frac{b}{2}}^{\frac{b}{2}} \int_{-\frac{t}{2}}^{\frac{t}{2}} \eta (-r_3^{14} y_1 + r_1^{14} y_3) dy_3 dy_1 + \int_{-\frac{b}{2}}^{-\frac{b}{2}} \int_{-\frac{t}{2}}^{\frac{t}{2}} \eta (-r_3^{23} y_1 + r_1^{23} y_3) dy_3 dy_1 + \\
&\quad \left. \int_{-\frac{b\eta}{2}}^{\frac{b\eta}{2}} \int_{-\frac{t}{2}}^{\frac{t}{2}} (1 - \eta) (r_3^{24} y_1 - r_1^{24} y_3) dy_3 dy_1 \right) \\
M_{22} &= \frac{1}{bt} \left(\int_{\frac{b}{2}}^{\frac{b}{2}} \int_{-\frac{t}{2}}^{\frac{t}{2}} (-r_3^{14} y_1 + r_1^{14} y_3) dy_3 dy_1 + \int_{-\frac{b}{2}}^{-\frac{b}{2}} \int_{-\frac{t}{2}}^{\frac{t}{2}} (-r_3^{23} y_1 + r_1^{23} y_3) dy_3 dy_1 + \right. \\
&\quad \left. \int_{-\frac{b\eta}{2}}^{\frac{b\eta}{2}} \int_{-\frac{t}{2}}^{\frac{t}{2}} (-r_3^{24} y_1 + r_1^{24} y_3) dy_3 dy_1 \right). \quad (2.57)
\end{aligned}$$

Their expression for the stack bond and the classical running bond patterns is given in Appendix B.2.

The displacement jumps at the interfaces of the cell \bar{A} write:

$$\llbracket \mathbf{v} \rrbracket^{14} = \begin{bmatrix} \eta b (\Gamma_{11} + y_3 K_{21}) + a \left(\Gamma_{12} + y_3 K_{22} + \frac{b}{2} K_{31} \right) \\ \eta b (\Gamma_{21} - y_3 K_{11} + (-b + y_1) K_{31}) + a \left(\Gamma_{22} - y_3 K_{12} + \left(-\frac{b}{2} + y_1 \right) K_{32} \right) \\ \eta b (\Gamma_{31} + (b - y_1) K_{21}) + a \left(\Gamma_{32} - \frac{b}{2} K_{11} + \left(\frac{b}{2} - y_1 \right) K_{22} \right) \end{bmatrix}$$

$$\begin{aligned}
\llbracket \mathbf{v} \rrbracket^{23} &= \begin{bmatrix} \eta b (\Gamma_{11} + y_3 K_{21}) + a \left(\Gamma_{12} + y_3 K_{22} - \frac{b}{2} K_{31} \right) \\ \eta b (\Gamma_{21} - y_3 K_{11} + (b + y_1) K_{31}) + a \left(\Gamma_{22} - y_3 K_{12} + \left(\frac{b}{2} + y_1 \right) K_{32} \right) \\ \eta b (\Gamma_{31} + (-b - y_1) K_{21}) + a \left(\Gamma_{32} + \frac{b}{2} K_{11} + \left(-\frac{b}{2} - y_1 \right) K_{22} \right) \end{bmatrix} \\
\llbracket \mathbf{v} \rrbracket^{24} &= \begin{bmatrix} (-1 + \eta) b (\Gamma_{11} + y_3 K_{21}) + a (\Gamma_{12} + y_3 K_{22}) \\ (-1 + \eta) b (\Gamma_{21} - y_3 K_{11} + y_1 K_{31}) + a (\Gamma_{22} - y_3 K_{12} + y_1 K_{32}) \\ (-1 + \eta) b (\Gamma_{31} - y_1 K_{21}) + a (\Gamma_{32} - y_1 K_{22}) \end{bmatrix} \\
\llbracket \mathbf{v} \rrbracket^{12} &= \frac{1}{2} b \begin{bmatrix} 2\Gamma_{11} + 2y_3 K_{21} + (a - 2y_2) K_{31} \\ 2\Gamma_{21} - 2y_3 K_{11} - \eta b K_{31} - a K_{32} \\ 2\Gamma_{31} + (-a + 2y_2) K_{11} + \eta b K_{21} + a K_{22} \end{bmatrix} \\
\llbracket \mathbf{v} \rrbracket^{43} &= \frac{1}{2} b \begin{bmatrix} 2\Gamma_{11} + 2y_3 K_{21} + (-a - 2y_2) K_{31} \\ 2\Gamma_{21} - 2y_3 K_{11} + \eta b K_{31} + a K_{32} \\ 2\Gamma_{31} + (a + 2y_2) K_{11} - \eta b K_{21} - a K_{22} \end{bmatrix}. \quad (2.58)
\end{aligned}$$

2.6.3 Justification of the homogenisation procedure

Stefanou et al. (2008) has demonstrated that, when they are made of regular rigid blocks, single leaf masonry walls can be replaced by an equivalent Cosserat continuum model. The resulting model is specifically a Cosserat (or micropolar) plate (Eringen, 1967; Godio et al., 2015a), which accounts for both the in-plane and the out-of-plane interaction between the blocks by means of macroscopic deformations and curvatures of the type presented above, i.e. respectively $(\Gamma_{\alpha\beta}, K_{3\beta})$ and $(\Gamma_{3\beta}, K_{\alpha\beta})$. The reduction of problem dimension (from the 18 deformation measures of the 3D Cosserat continuum to the 12 of the micropolar plate model) is inherent to the homogenisation procedure presented by Stefanou et al. (2008), and then justify the map retrieved in this paper (Eq.(2.50)). In particular, the conditions for the blocks to be considered rigid and to have all the same shape and size are necessary in order to obtain a realistic description of the medium based on the Cosserat continuum. If one of these assumptions was not respected, new terms of generalized deformations and stresses would rise. In this case, a complete description of the masonry wall would be possible by recurring to a micromorphic continuum (Stefanou et al., 2010; Stefanou and Sulem, 2012).

It is worth mentioning that the Reissner-Mindlin plate model is often used for modelling the behaviour of masonry walls (Cecchi and Sab, 2004, 2007; Sab et al., 2007; Cecchi et al., 2007). The difference with the Cosserat model of the present approach concerns both the in-plane and the out-of-plane behaviour of the plate. Firstly, the in-plane kinematics of the micropolar model are enhanced by the Cosserat rotations. For this reason, the micropolar model takes into account the effect of the in-plane rotations of the blocks ω_3^{GJ} (Sulem and Mühlhaus, 1997; Godio et al., 2015d), which the aforementioned Reissner-Mindlin plate models do not. Secondly, it is clear from Eq.(2.4) how the Reissner-Mindlin model is different from the Cosserat model, since it considers only the symmetric part of the rotation gradient. Therefore, some differences arise when looking at the average out-of-plane curvatures (K_{11}, K_{22}) (Eq.(2.53)), representing, in the terminology used for plates, the deformations to torsion. In the Cosserat model, these curvatures are produced by distinct blocks' kinematics, respectively ω_1^{GJ} and ω_2^{GJ} (Eq.(2.53)-1,4). In the Reissner-Mindlin model, these curvatures are provided by the same set of rotations, but in a non-independent way (Cecchi and Sab, 2002b, 2006). On the contrary, both models have the same definitions for the curvatures (K_{12}, K_{21}) (Eq.(2.53)-2,3), representing the deformation to bending, and depend therefore on the same set of kinematics (Cecchi and Sab, 2002b, 2006).

2.6.4 Homogenisation

Similar to the case of the column (Section 2.5), blocks exhibit infinite strength and the interfaces resistance to slip and opening is described by means of a Coulomb failure criterion (Eq.(2.43)). In view of practical applications, it is useful to define different values for the cohesion and friction angle, depending on the interface orientation. Therefore, the dissipation function on the interfaces of the cell takes the following form (Godio et al., 2015d):

$$\pi^{IJ} \left(\llbracket v_i \rrbracket^{IJ}; \mathbf{n}_i^{IJ} \right) = \frac{c}{\text{Tan}[\phi]} \llbracket v_i \rrbracket^{IJ} \mathbf{n}_i^{IJ}, \text{ with } \begin{cases} (c, \phi) = (c^h, \phi^h), & \text{for } \Sigma^{14}, \Sigma^{23}, \Sigma^{24} \\ (c, \phi) = (c^v, \phi^v), & \text{for } \Sigma^{12}, \Sigma^{43}. \end{cases} \quad (2.59)$$

with $\pi^{IJ} < \infty$ provided that:

$$\begin{cases} \llbracket v_i \rrbracket^{IJ} \mathbf{n}_i^{IJ} \geq \left| \llbracket v_i \rrbracket^{IJ} \right| \text{Sin}[\phi^h], & \text{for } \Sigma^{14}, \Sigma^{23}, \Sigma^{24} \\ \llbracket v_i \rrbracket^{IJ} \mathbf{n}_i^{IJ} \geq \left| \llbracket v_i \rrbracket^{IJ} \right| \text{Sin}[\phi^v], & \text{for } \Sigma^{12}, \Sigma^{43}. \end{cases} \quad (2.60)$$

Superscripts h and v refer respectively to the horizontal (bed joints) and vertical (head joints) interfaces. With these notations, the plastic dissipation on the discrete cell \bar{A} is:

$$\begin{aligned} \pi^D \left(v_i^{GJ}, \omega_i^{GJ} \right) &= \frac{1}{abt} \left(\int_{-\frac{t}{2}}^{\frac{t}{2}} \int_{\eta_{\frac{b}{2}}}^{\frac{b}{2}} \pi^{14} \left(\llbracket \mathbf{v} \rrbracket^{14}; \mathbf{n}^{14} \right) dy_1 dy_3 \right. \\ &+ \int_{-\frac{t}{2}}^{\frac{t}{2}} \int_{-\frac{b}{2}}^{-\eta_{\frac{b}{2}}} \pi^{23} \left(\llbracket \mathbf{v} \rrbracket^{23}; \mathbf{n}^{23} \right) dy_1 dy_3 + \int_{-\frac{t}{2}}^{\frac{t}{2}} \int_{-\eta_{\frac{b}{2}}}^{\eta_{\frac{b}{2}}} \pi^{24} \left(\llbracket \mathbf{v} \rrbracket^{24}; \mathbf{n}^{24} \right) dy_1 dy_3 \\ &\left. + \int_{-\frac{t}{2}}^{\frac{t}{2}} \int_0^{\frac{a}{2}} \pi^{12} \left(\llbracket \mathbf{v} \rrbracket^{12}; \mathbf{n}^{12} \right) dy_2 dy_3 + \int_{-\frac{t}{2}}^{\frac{t}{2}} \int_{-\frac{a}{2}}^0 \pi^{43} \left(\llbracket \mathbf{v} \rrbracket^{43}; \mathbf{n}^{43} \right) dy_2 dy_3 \right) \\ &= \frac{c^v}{\text{Tan}[\phi^v]} \Gamma_{11} + \frac{c^h}{\text{Tan}[\phi^h]} \Gamma_{22}. \end{aligned} \quad (2.61)$$

By setting:

$$\Pi^{c, hom} = \pi^D,$$

and by using the kinematic definition of $G^{c, hom}$ (Eq.(2.24)), the macroscopic strength criterion for the masonry wall becomes:

$$\begin{aligned} G^{c, hom} &= \{ (T_{i\alpha}, M_{i\alpha}) \mid \left(T_{11} - \frac{c^v}{\text{Tan}[\phi^v]} \right) \Gamma_{11} + T_{12} \Gamma_{12} + T_{21} \Gamma_{21} \\ &+ \left(T_{22} - \frac{c^h}{\text{Tan}[\phi^h]} \right) \Gamma_{22} + T_{31} \Gamma_{31} + T_{32} \Gamma_{32} \\ &+ M_{11} K_{11} + M_{12} K_{12} + M_{21} K_{21} + M_{22} K_{22} \\ &+ M_{31} K_{31} + M_{32} K_{32} \leq 0, \forall (\Gamma_{i\alpha}, K_{i\alpha}) \}. \end{aligned} \quad (2.62)$$

The homogenised strength criterion is then computed by considering *all* the $KA(\Gamma_{i\alpha}, K_{i\alpha})$ set of kinematics $(v_i^{GJ}, \omega_i^{GJ})$ which are also plastically admissible. In the present case, this reduces to a set of 20 inequalities. These inequalities are the expression of the relevance conditions (2.60) at the extreme points of each interface of the cell (Figure 2.13). The first 12

conditions result from the horizontal interfaces $\Sigma^{14}, \Sigma^{23}, \Sigma^{24}$:

$$\begin{aligned}
& H^{1-8}(\Gamma_{i\alpha}, K_{i\alpha}) = \\
& -a \left(\Gamma_{22} - \epsilon_6 \frac{t}{2} K_{12} - \epsilon_1 (1 - \epsilon_2) \frac{b}{2} K_{32} \right) + \eta b \left(-\Gamma_{21} + \epsilon_6 \frac{t}{2} K_{11} + \epsilon_1 \left(1 - \frac{\epsilon_2}{2} \right) b K_{31} \right) \\
& + \text{Tan}[\phi^h] \left(\left[\eta b \left(\Gamma_{31} + \epsilon_1 \left(1 - \frac{\epsilon_2}{2} \right) b K_{21} \right) + a \left(\Gamma_{32} - \epsilon_1 \frac{b}{2} K_{11} + \epsilon_1 (1 - \epsilon_2) \frac{b}{2} K_{22} \right) \right]^2 \right. \\
& \quad \left. + \left[\eta b \left(\Gamma_{11} + \epsilon_6 \frac{t}{2} K_{21} \right) + a \left(\Gamma_{12} + \epsilon_6 \frac{t}{2} K_{22} + \epsilon_1 \frac{b}{2} K_{31} \right) \right]^2 \right)^{1/2} \leq 0 \quad (2.63)
\end{aligned}$$

$$\begin{aligned}
& H^{9-12}(\Gamma_{i\alpha}, K_{i\alpha}) = \\
& -a \left(\Gamma_{22} + \epsilon_3 \frac{\eta b}{2} K_{32} - \epsilon_6 \frac{t}{2} K_{12} \right) + (1 - \eta) b \left(\Gamma_{21} + \epsilon_3 \frac{\eta b}{2} K_{31} - \epsilon_6 \frac{t}{2} K_{11} \right) \\
& + \text{Tan}[\phi^h] \left(\left[-(1 - \eta) b \left(\Gamma_{31} - \epsilon_3 \frac{\eta b}{2} K_{21} \right) + a \left(\Gamma_{32} - \epsilon_3 \frac{\eta b}{2} K_{22} \right) \right]^2 \right. \\
& \quad \left. + \left[-(1 - \eta) b \left(\Gamma_{11} + \epsilon_6 \frac{t}{2} K_{21} \right) + a \left(\Gamma_{12} + \epsilon_6 \frac{t}{2} K_{22} \right) \right]^2 \right)^{1/2} \leq 0 \quad (2.64)
\end{aligned}$$

The remaining 8 conditions result from the vertical interfaces Σ^{12}, Σ^{43} :

$$\begin{aligned}
& H^{13-20}(\Gamma_{i\alpha}, K_{i\alpha}) = \\
& - \left(\Gamma_{11} + \epsilon_4 \frac{a}{2} K_{31} + \epsilon_6 \frac{t}{2} K_{21} \right) \\
& + \text{Tan}[\phi^v] \left(\left[\Gamma_{31} - \epsilon_4 \frac{a}{2} K_{11} - \epsilon_5 \frac{\eta b}{2} K_{21} - \epsilon_5 \frac{a}{2} K_{22} \right]^2 \right. \\
& \quad \left. + \left[\epsilon_5 \Gamma_{21} - \epsilon_5 \epsilon_6 \frac{t}{2} K_{11} + \frac{\eta b}{2} K_{31} + \frac{a}{2} K_{32} \right]^2 \right)^{1/2} \leq 0 \quad (2.65)
\end{aligned}$$

Table 2.1 shows the values taken by the coefficients $\epsilon_1, \dots, \epsilon_6$ in the above expressions. The conditions for the in-plane case (Godio et al., 2015d) are retrieved as special case, by imposing the out-of-plane Cosserat deformation measures $(\Gamma_{\alpha\beta}, K_{3\beta})$ to be zero. Notice that, with respect to the in-plane case, the inequalities presented herein are non-linear, since they capture both the in-plane and out-of-plane deformations of the cell, including their interaction. Similar to the case of the column, this prevents the derivation of the homogenised strength domain in terms of stresses and couple stresses following the optimization algorithm used in Godio et al. (2015d).

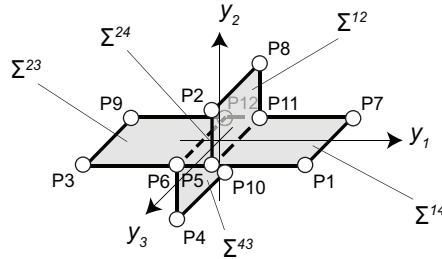


Figure 2.13: Points of the 3D elementary cell where the relevance condition (Eq.(2.44)) needs to be satisfied.

	Σ^{14}		Σ^{23}		Σ^{24}		Σ^{12}		Σ^{43}	
	P1	P5	P3	P6	P5	P6	P2	P5	P4	P6
ϵ_1	1	1	-1	-1						
ϵ_2	1	η	1	η						
ϵ_3					1	-1				
ϵ_4							0	1	0	-1
ϵ_5							-1	-1	1	1
ϵ_6	1	1	1	1	1	1	1	1	1	1

	Σ^{14}		Σ^{23}		Σ^{24}		Σ^{12}		Σ^{43}	
	P7	P11	P9	P12	P11	P12	P8	P11	P10	P12
ϵ_1	1	1	-1	-1						
ϵ_2	1	η	1	η						
ϵ_3					1	-1				
ϵ_4							0	1	0	-1
ϵ_5							-1	-1	1	1
ϵ_6	-1	-1	-1	-1	-1	-1	-1	-1	-1	-1

Table 2.1: Coefficients used in Eqs.(2.63)-(2.65).

2.7 Conclusions

The inner structure of discrete media may be very complex. In some cases, two-dimensional (or plane) descriptions of the medium prove inadequate and the use of three-dimensional (3D) models is required for the full assessment of their strength.

In this paper, a method for the evaluation of the homogenised strength of 3D periodic discrete media was developed. The presented method was the extension to the 3D case of a procedure initially formulated for the Cosserat continuum in two dimensions (Godio et al., 2015d). The homogenised strength domain was derived by application of the kinematic approach in the framework of limit analysis theory. In this way, a larger class of deformation modes and failure mechanisms involving not only the particles' relative translation but also the particles' relative rotation was taken into account in the macroscopic description of the medium.

The homogenisation procedure was illustrated in general manner, with regard to a 3D periodic collection of rigid blocks in contact (Section 2.3). The interaction between the blocks was established at their interfaces, where contact stresses were exchanged. The kinematic description of the discrete medium was then given by displacement velocity jumps produced at the interfaces between the blocks by their relative translations and rotations. Due to periodicity, all the computations were made on a preselected elementary cell. As result of homogenisation, the contact stress distributions gave rise to the macroscopic stresses and couple stresses of the 3D Cosserat continuum. Similarly, the Cosserat relative deformations and curvatures were produced by combinations of spatial rigid-body motions of the blocks that composed the discrete medium (Section 2.4).

The homogenisation method was applied to the case of masonry (Section 2.5 and Section 2.6).

Masonry was here considered as an assemblage of distinct blocks undergoing spatial translations and rotations. homogenised yield criteria were obtained by admitting that failure may take place at the joints only, the strength capacities of the joints being far lower than those of the blocks. In particular, masonry joints were considered as interfaces with Coulomb dissipative properties, given by the joint cohesion and friction angle.

The homogenised strength of masonry columns and walls was determined by deriving an equivalent 3D Cosserat continuum at the macroscopic scale. As a result of the homogenisation procedure, the number of macroscopic deformation measures was however reduced. This result was consistent with the geometry of columns and walls. The masonry column was so ascribed to a Cosserat (or Timoshenko) beam model. The masonry wall was assumed as a Cosserat (or micropolar) plate model. Both models were comprehensive of complete 3D kinematics, and shown an apparent interaction between the membrane (or in-plane) and flexural (or out-of-plane) actions in the assessment of masonry strength.

Chapter 3

Finite element formulation for Cosserat plates: elasticity

This Chapter describes the formulation and the validation of a finite element for Cosserat plate models. The element is formulated for elasticity and dynamics. It allows the implementation of an existing homogenisation model for masonry. The model is used to compute the natural flexural frequencies of a masonry panel modelled by discrete elements. It allows also to investigate the role of the in-plane rotations of the blocks, showing their participation to the inertial response of the panel against seismic excitations.

This Chapter is a published paper. Its reference is [Godio et al. \(2015a\)](#).

Contents

3.1	Introduction	81
3.2	3D Cosserat dynamics prerequisites	82
3.3	Equations of motion for Cosserat elastic plates	84
3.4	Element formulation	86
3.4.1	Stiffness matrix	87
3.4.2	Mass matrix	89
3.4.3	Element motion	89
3.5	The COSS8R element	90
3.5.1	Choice of the polynomial order of interpolation	90
3.5.2	Zero-energy modes investigation	91
3.5.3	Consistent mass matrix	94
3.6	Element validation	94
3.6.1	Patch test	94
3.6.2	Shear locking investigation	96
3.6.3	Dispersion functions	97
3.7	Application to masonry structures	99
3.7.1	Comparison with Discrete Elements solution	101
3.7.2	The role of drilling rotations	101
3.8	Conclusions	102

Summary

A displacement and rotation-based dynamic Finite Element formulation for Cosserat plates is discussed in detail in this paper. Special attention is given to the validation of the element through adequate benchmarks and patch tests. The choice of the interpolation functions and the order of integration of the stiffness and the mass matrices are extensively argued. The possibility of local system deficiencies is explored and a shear locking investigation specifically elaborated for Cosserat plates is carried out. It is shown how the present formulation has interesting computational properties, as compared to a classical continuum-based formulation, and how it can provide suitable results despite the use of reduced integration. An example of application of the finite element is given, in which the natural frequencies of a masonry panel modelled by means of Discrete Elements are computed and compared with the Finite Elements solution.

3.1 Introduction

Cosserat (or micropolar) continuum has recently attracted the attention of researchers from many different disciplines of Mechanics. Either facing it as an adequate mathematical framework for the regularization of ill-posed problems in the softening plasticity regime of classical (Cauchy) continua (Vardoulakis and Sulem, 1995), or as the starting point for the constitutive description of systems with internal lengths, or, again, as a medium with dispersive properties, the theory of Cosserat continuum has found numerous applications up to present.

Models based on Cosserat continuum have been employed, for instance, in the representation of granular media (Pasternak and Mühlhaus, 2005; Vardoulakis, 1989; Sulem et al., 2013), rock masses (de Buhan et al., 2002; Sulem et al., 2011), block (Sulem and Mühlhaus, 1997; Stefanou et al., 2008; Pau and Trovalusci, 2012) and layered structures (Forest and Sab, 1998), polycrystals and composites materials (Forest et al., 2001; Forest and Sab, 1998), structures of beams, nanostructures and continuous robotic systems (Dehghani and Moosavian, 2013; Robinson and Davies, 1999; Li and Xie, 2004). Other models have been formulated for the modelling of porous and multiphase materials (Tekoğlu and Onck, 2008), but also particle fluids and materials with electro- and ferromagnetic properties (Eringen, 1999, 2001). Micropolar descriptions are also used in biomechanics, for the mechanical behaviour of bones (Park and Lakes, 1986; Fatemi et al., 2002; Goda et al., 2014) and other biological tissues with microstructure (Sanchez-Molina et al., 2014; Sack et al., 2013). For a more comprehensive review of Cosserat (or micropolar) models for solids and plates, we refer to (Altenbach et al., 2009).

Problems involving boundary layer phenomena, localization of deformations and wave dispersion can be properly solved using Cosserat Finite Elements (FE). Sluys and de Borst presented a comprehensive study on the advantages of Cosserat FE compared to classical formulations based on Cauchy continuum, which suffer from the problem of mesh dependency when localization of shear strains takes place, see (de Borst and Sluys, 1991; de Borst, 1991; de Borst et al., 1993) among others. Interesting applications of Cosserat FE in modelling layered structures are given by (Riahi and Curran, 2009; Riahi et al., 2009; Dai et al., 1993). Cosserat FE for masonry structures are also formulated in (Cerrolaza et al., 1999; Addessi et al., 2010; Addessi and Sacco, 2012; Addessi, 2014). In modeling masonry, it is the non-symmetry of the stress tensor that makes Cosserat-continuum-based models preferable (Trovalusci and Pau, 2014) with respect to models based on other non-classical continua. Other more general FE formulations for micropolar plates and shells and for solids with microstructure are those recently proposed by (Chróścielewski and Witkowski, 2011) and (Nadler and Rubin, 2003; Jabareen and Rubin, 2014; Mtanes and Jabareen, 2014; Zervos, 2008).

However, even though many applications of Cosserat continuum using FE are found in the literature, the details of each FE formulation are partially exposed or not presented at all. Moreover, the performance of the element is seldom investigated, making hard to assess the chosen FE formulation and its applicability to other problems. The purpose of this paper is to propose a Cosserat finite element that may be used for different applications in structural and materials engineering.

The presented element is obtained by the superposition of a quadratic small-strains Cosserat membrane rectangle with a thick plate element with enriched kinematics. It results in a versatile shell-type flat element equipped with six degrees of freedom (DOF) per node, capable of modelling complex spatial structural configurations.

This Cosserat finite element has the advantage of providing accurate results even in the case of reduced integration, without using any hourglass control method. In classic FE formulations the hourglass control is frequently made by introducing an artificial stiffness to the in-plane rotations (Zienkiewicz and Taylor, 2005; Hughes and Brezzi, 1989; Chinosi et al., 1997;

Providas and Kattis, 2000; Kugler et al., 2010; Yang et al., 2000). In FE formulations based on Cosserat continuum, this stiffness is introduced in a physical way, because of the inherent drilling rotational DOF. The occurrence of zero-energy modes can be thus naturally avoided in the Cosserat FE formulations, and the element stiffness matrix is never deficient.

The paper has the following structure. In [Section 3.2](#) we outline the basic definitions and relations of a Cosserat continuum in three dimensions that are necessary for the rest of the paper. In [Section 3.3](#) we present a model for micropolar plates, through reduction of the three-dimensional problem. In [Section 3.4](#) we propose a general Cosserat dynamic formulation for the FE method. In [Section 3.5](#) we present a specific finite element: the choice of the interpolation order is discussed, the use of different integration techniques for the computation of the element stiffness and mass matrices are argued and the possibility of system deficiencies is explored. The validation of the element is made in [Section 3.6](#), where we investigate the shear locking phenomenon applied to micropolar plates. In [Section 3.7](#) we give an illustrative example of the use of the element in representing the modal response of a masonry structure consisted of discrete interacting building blocks.

Throughout the paper much attention is paid to the capacity of the formulation to predict the membrane (or in-plane) as well as the flexural (or out-of-plane) behaviour. Even though from a theoretical point of view they will be presented separately, only their superposition give the full, herein referred to as *plate*, structural response.

Common matrix notation is adopted. Upper case letters denote variables referring to the nodes of the element, while lower case letters refer to the local variables of the continuum field problem. It is implicitly assumed that the former are only time-dependent whereas the latter are space and time-dependent. Partial differentiation with respect to orthogonal coordinates is indicated by $[\]_{i,j} = \partial x_i / \partial x_j$. Time derivative is $[\]_{i,t} = [\]_i$.

3.2 3D Cosserat dynamics prerequisites

Following Germain's terminology ([Germain, 1973](#)), Cosserat continuum is a special case of a micromorphic continuum of first order ([Figure 3.1](#)). Therein, the particle (the material point in the sense of Germain) is considered rigid and, consequently, its kinematical description in the three-dimensional (3D) space is fulfilled by six DOF, i.e. three translations u_i and three rotations ω_i .

It results that the deformation measures of the medium, herein expressed in Cartesian coordinates and in the frame of a small strain theory, are given by two second order tensors, γ_{ij} and κ_{ij} , representing respectively the relative strains and the curvatures:

$$\gamma_{ij} = u_{i,j} + e_{ijk}\omega_k \quad (3.1)$$

$$\kappa_{ij} = \omega_{i,j} \quad (3.2)$$

with e_{ijk} the permutation symbol. The symmetric part of the strain tensor, denoted with $\gamma_{(ij)}$, coincides with the strain tensor of a classical (Cauchy) continuum, whereas its skew-symmetric part $\gamma_{[ij]}$ accounts for the relative deformations:

$$\gamma_{(ij)} = \frac{(u_{i,j} + u_{j,i})}{2} \quad (3.3)$$

$$\gamma_{[ij]} = e_{ijk}(\hat{\omega}_k - \omega_k) \quad (3.4)$$

where $e_{ijk}\hat{\omega}_k = (u_{j,i} - u_{i,j})/2$ is the infinitesimal rotation tensor.

The above deformation measures are energy conjugate with the non-symmetric stresses τ_{ij} and the couple stresses μ_{ij} . According to Boltzmann, the assumption of symmetry of the stress

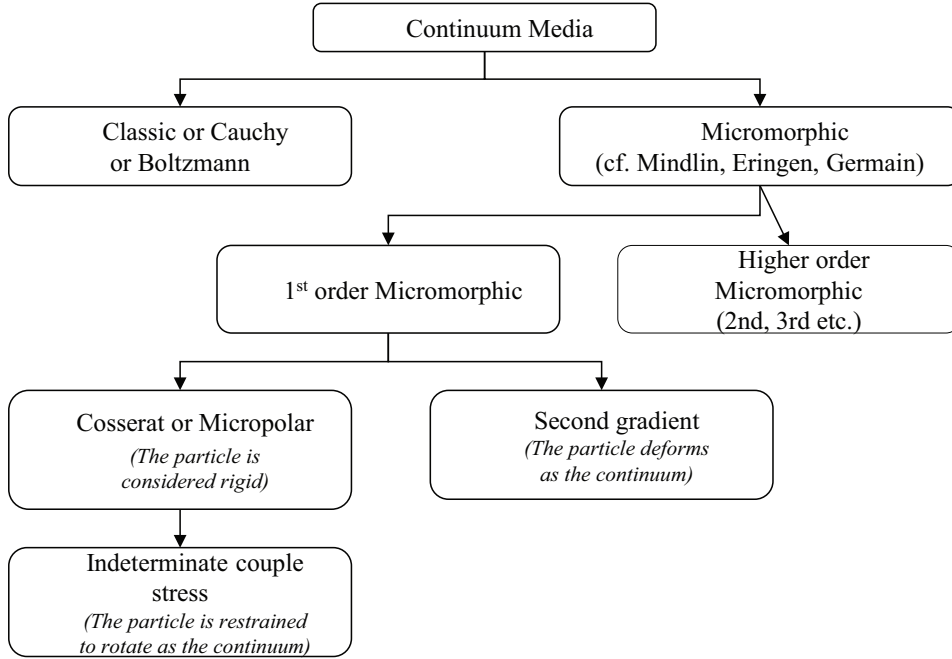


Figure 3.1: Higher order continuum theories according to [Germain \(1973\)](#) terminology. Cosserat continuum is a special case of a micromorphic continuum of first order.

tensor in classical continua has an axiomatic character (see [Schaefer \(1967\)](#); [Vardoulakis \(2009\)](#)). In the Cosserat medium, the loss of symmetry is due to the rotational DOF attached to the particle, as shown by Eq.(3.4), and the presence of the couple stresses (angular momentum). This makes rich the number of the material parameters to be identified within the constitutive relations, and makes Cosserat continuum suitable for the description of a great variety of problems. For instance, for a centro-symmetric material, a constitutive law can be defined in a general manner as:

$$\tau_{ij} = C_{ijkl}\gamma_{kl}, \quad \mu_{ij} = D_{ijkl}\kappa_{kl} \quad (3.5)$$

where C_{ijkl} and D_{ijkl} are fourth order tensors containing the material parameters. In this case, an isotropic micropolar material require the definition of six parameters, whereas a classical solid would only demand two moduli ([Altenbach et al., 2009](#)).

For a Cosserat continuum, the Cauchy tetrahedron can be generalized as follows ([Germain, 1973](#)):

$$T_i^d = \tau_{ij}n_j, \quad M_i^d = \mu_{ij}n_j \quad (3.6)$$

where T_i^d and M_i^d are the stress and the couple stress vectors applied on the boundary $\partial\Omega_\Sigma$ of a configuration Ω , and n_j is the normal outward unit vector at $\partial\Omega_\Sigma$. Moreover, both translations and rotations can be prescribed on the boundary $\partial\Omega_U$:

$$u_i = u_i^d, \quad \omega_i = \omega_i^d. \quad (3.7)$$

In Statics, the minimum of the Total Potential Energy gives the equilibrium equations in weak form. In Dynamics, the equations of motion can be derived by application of the Hamilton's variational Principle. For a virtual variation of the displacement δu_i and the rotational

field $\delta\omega_i$, the Principle reads, in case of a conservative holonomic continuum systems:

$$\delta \int_{t_1}^{t_2} [K^c - (V^c - W^c)] dt = 0. \quad (3.8)$$

In Eq.(3.8), we recognise the kinetic energy K^c , the deformation energy V^c , and the expression for the external works W^c . In terms of Cosserat kinematics, these quantities read:

$$V^c = \frac{1}{2} \int_{\Omega} (\tau_{ij} \gamma_{ij} + \mu_{ij} \kappa_{ij}) d\Omega \quad (3.9)$$

$$W^c = \int_{\Omega} (f_i u_i + m_i \omega_i) d\Omega + \int_{\partial\Omega_{\Sigma}} (T_i^d u_i + M_i^d \omega_i) dA \quad (3.10)$$

$$K^c = \frac{1}{2} \int_{\Omega} (\rho \dot{u}_i \dot{u}_i + \rho \dot{\omega}_i I_{ij} \dot{\omega}_j) d\Omega. \quad (3.11)$$

In the above, the body forces f_i and the body couples m_i represent long-range actions within the continuum. The material mass density is ρ , and the micro-inertia tensor is ρI_{ij} . The linear and angular momentum balance is then:

$$\begin{aligned} \tau_{ij,j} + f_i - \rho \ddot{u}_j &= 0 \\ \mu_{ij,j} - e_{ijk} \tau_{jk} + m_i - \rho I_{ij} \ddot{\omega}_j &= 0. \end{aligned} \quad (3.12)$$

3.3 Equations of motion for Cosserat elastic plates

The 3D Cosserat field's problem presented in Section 3.2 is governed by six partial differential equations (PDE) of second order, expressed in terms of the three unknown displacements and the three unknown rotations, see Eqs.(3.12). In the case of a plate, a homogeneous planar surface of unitary thickness $h = 1$ oriented in the 1-2 plane, the problem is invariant in the out-of-plane direction x_3 and so it can be consequently reduced (Figure 3.2). Regarding the curvatures, we have $\kappa_{13} = \kappa_{23} = \kappa_{33} = 0$, which annihilate the conjugate couple stress measures μ_{13} , μ_{23} and μ_{33} . Concerning the relative strains, γ_{33} vanishes due to the aforementioned hypothesis, and components γ_{13} and γ_{23} result in the simplified expressions:

$$\gamma_{13} = -\omega_2, \quad \gamma_{23} = \omega_1. \quad (3.13)$$

A typical assumption which is often taken in the construction of classical and micropolar plate theories and that we also adopt for our formulation, consists in neglecting the normal stress τ_{33} (see Eringen (1967) for a further discussion). However Eq.(3.13) preserves the stress components τ_{13} and τ_{23} . Although such components are absent in most of the models designed for Cosserat plates, see for instance those obtained by reduction of the 3D problem (Gevorkyan, 1967; Ambartsumian, 1996; Altenbach and Eremeyev, 2009), they are conserved in the present formulation. This allows for the implementation of more complete plate models, as the one proposed by Eringen (1967).

Dealing with plates, it is handy to separate the membrane (or in-plane) behaviour from the flexural (or out-of-plane) behaviour, see Figure 3.2. The static and kinematic remaining components are expressed in matrix notation in Table 3.1, where subscripts m and f refer respectively to the variables associated with the membrane and flexural behaviour. Regarding the membrane behaviour, we recognise the tractions $\tau_{\alpha\beta}$ ($\alpha = \beta$, with $\alpha, \beta = 1, 2$), the in-plane

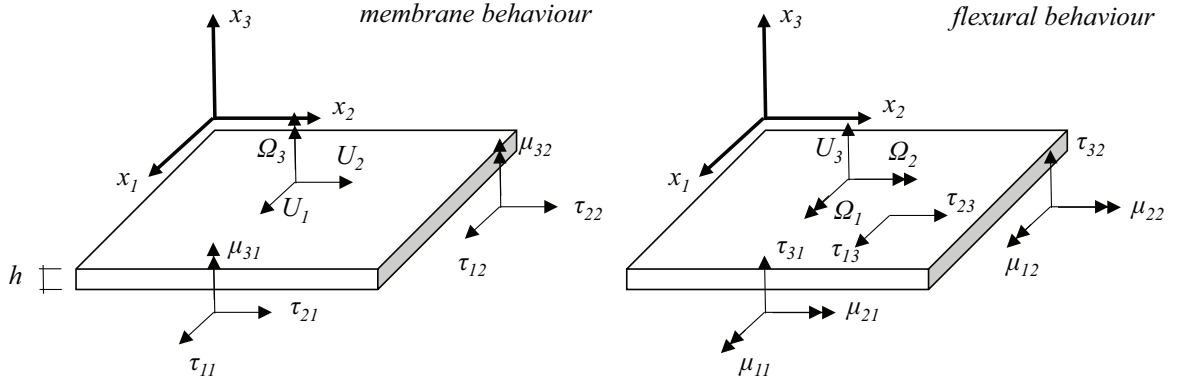


Figure 3.2: Stresses, couple stresses and degrees of freedom of a Cosserat plate: membrane (left) and flexural (right) behaviour.

shears $\tau_{\alpha\beta}$ ($\alpha \neq \beta$), and the in-plane couples $\mu_{3\alpha}$. Concerning the flexural behaviour, we identify the torsions $\mu_{\alpha\beta}$ ($\alpha = \beta$), the out-of-plane flexions $\mu_{\alpha\beta}$ ($\alpha \neq \beta$), the transverse shears $\tau_{3\alpha}$, and the longitudinal shears $\tau_{\alpha 3}$.

Following this notation, the PDE for the in- and out-of-plane motion of Cosserat plates read respectively, in compact form:

$$\begin{bmatrix} \mathbf{L}_{m1}[2 \times 4]^t & -\mathbf{L}_{m3}[2 \times 2]^t \\ -\mathbf{L}_{m2}[1 \times 4]^t & \mathbf{L}_{m4}[1 \times 2]^t \end{bmatrix} \begin{bmatrix} \boldsymbol{\tau}_m \\ \boldsymbol{\mu}_m \end{bmatrix} + \begin{bmatrix} \mathbf{f}_m \\ \mathbf{m}_m \end{bmatrix} - \begin{bmatrix} \mathbf{1}_m[2 \times 2] & \mathbf{0}[2 \times 1] \\ \mathbf{0}[1 \times 2] & I_m[1 \times 1] \end{bmatrix} \begin{bmatrix} \ddot{\mathbf{u}}_m \\ \ddot{\boldsymbol{\omega}}_m \end{bmatrix} = 0 \quad (3.14)$$

and

$$\begin{bmatrix} \mathbf{L}_{f1}[1 \times 4]^t & -\mathbf{L}_{f3}[1 \times 4]^t \\ -\mathbf{L}_{f2}[2 \times 4]^t & \mathbf{L}_{f4}[2 \times 4]^t \end{bmatrix} \begin{bmatrix} \boldsymbol{\tau}_f \\ \boldsymbol{\mu}_f \end{bmatrix} + \begin{bmatrix} \mathbf{f}_f \\ \mathbf{m}_f \end{bmatrix} - \begin{bmatrix} \mathbf{1}_f[1 \times 1] & \mathbf{0}[1 \times 2] \\ \mathbf{0}[2 \times 1] & \mathbf{I}_f[2 \times 2] \end{bmatrix} \begin{bmatrix} \ddot{u}_f \\ \ddot{\boldsymbol{\omega}}_f \end{bmatrix} = 0, \quad (3.15)$$

where the sub-matrices \mathbf{L}_{mi} and \mathbf{L}_{fi} (with $i = 1, \dots, 4$) are the operators giving the definition of the deformation measures of the plate (Eqs.(3.1)-(3.2)):

$$\begin{bmatrix} \boldsymbol{\gamma}_m \\ \boldsymbol{\kappa}_m \end{bmatrix} = \begin{bmatrix} \mathbf{L}_{m1}[4 \times 2] & \mathbf{L}_{m2}[4 \times 1] \\ \mathbf{L}_{m3}[2 \times 2] & \mathbf{L}_{m4}[2 \times 1] \end{bmatrix} \begin{bmatrix} \mathbf{u}_m \\ \boldsymbol{\omega}_m \end{bmatrix} \quad (3.16)$$

$$\begin{bmatrix} \boldsymbol{\gamma}_f \\ \boldsymbol{\kappa}_f \end{bmatrix} = \begin{bmatrix} \mathbf{L}_{f1}[4 \times 1] & \mathbf{L}_{f2}[4 \times 2] \\ \mathbf{L}_{f3}[4 \times 1] & \mathbf{L}_{f4}[4 \times 2] \end{bmatrix} \begin{bmatrix} u_f \\ \boldsymbol{\omega}_f \end{bmatrix}, \quad (3.17)$$

that is:

$$\begin{aligned} \mathbf{L}_{m1}[4 \times 2] &= \begin{bmatrix} [\]_{,1} & 0 \\ 0 & [\]_{,2} \\ [\]_{,2} & 0 \\ 0 & [\]_{,1} \end{bmatrix}, & \mathbf{L}_{m2}[4 \times 1] &= \begin{bmatrix} 0 \\ 0 \\ 1 \\ -1 \end{bmatrix}, & \mathbf{L}_{m3}[2 \times 2] &= \begin{bmatrix} 0 & 0 \\ 0 & 0 \end{bmatrix}, & \mathbf{L}_{m4}[2 \times 1] &= \begin{bmatrix} [\]_{,1} \\ [\]_{,2} \end{bmatrix} \\ \mathbf{L}_{f1}[4 \times 1] &= \begin{bmatrix} 0 \\ [\]_{,1} \\ 0 \\ [\]_{,2} \end{bmatrix}, & \mathbf{L}_{f2}[4 \times 2] &= \begin{bmatrix} 0 & -1 \\ 0 & 1 \\ 1 & 0 \\ -1 & 0 \end{bmatrix}, & \mathbf{L}_{f3}[4 \times 1] &= \begin{bmatrix} 0 \\ 0 \\ 0 \\ 0 \end{bmatrix}, & \mathbf{L}_{f4}[4 \times 2] &= \begin{bmatrix} [\]_{,1} & 0 \\ 0 & [\]_{,2} \\ [\]_{,2} & 0 \\ 0 & [\]_{,1} \end{bmatrix} \end{aligned} \quad (3.18)$$

In a plate, material symmetries can be defined only with respect to the normal axis x_3 (Eremeyev and Pietraszkiewicz, 2006; Eremeyev et al., 2013). Therefore, without losing generality

		membrane behaviour	flexural behaviour
statics	body forces	$\mathbf{f}_m = [f_1 \ f_2]^t$	$\mathbf{f}_f = [f_3]$
	body couples	$m_m = [m_3]$	$\mathbf{m}_f = [m_1 \ m_2]^t$
	stresses	$\boldsymbol{\tau}_m = [\tau_{11} \ \tau_{22} \ \tau_{12} \ \tau_{21}]^t$	$\boldsymbol{\tau}_f = [\tau_{13} \ \tau_{31} \ \tau_{23} \ \tau_{32}]^t$
	couple stresses	$\boldsymbol{\mu}_m = [\mu_{31} \ \mu_{32}]^t$	$\boldsymbol{\mu}_f = [\mu_{11} \ \mu_{22} \ \mu_{12} \ \mu_{21}]^t$
kinematics	displacements	$\mathbf{u}_m = [u_1 \ u_2]^t$	$u_f = [u_3]$
	rotations	$\omega_m = [\omega_3]$	$\boldsymbol{\omega}_f = [\omega_1 \ \omega_2]^t$
	strains	$\boldsymbol{\gamma}_m = [\gamma_{11} \ \gamma_{22} \ \gamma_{12} \ \gamma_{21}]^t$	$\boldsymbol{\gamma}_f = [\gamma_{13} \ \gamma_{31} \ \gamma_{23} \ \gamma_{32}]^t$
	curvatures	$\boldsymbol{\kappa}_m = [\kappa_{31} \ \kappa_{32}]^t$	$\boldsymbol{\kappa}_f = [\kappa_{11} \ \kappa_{22} \ \kappa_{12} \ \kappa_{21}]^t$
inertia terms	lateral inertia	$\mathbf{1}_m = \rho \begin{bmatrix} 1 & 0 \\ 0 & 1 \end{bmatrix}$	$1_f = \rho$
	rotary inertia	$I_m = \rho I_{33}$	$\mathbf{I}_f = \rho \begin{bmatrix} I_{11} & 0 \\ 0 & I_{22} \end{bmatrix}$

Table 3.1: Field variables of the Cosserat plate-type model in matrix notation. Membrane and flexural behaviour. The components of the inertia tensor are represented in the principal basis.

a constitutive law is introduced in the following form:

$$\begin{bmatrix} \boldsymbol{\tau}_m \\ \boldsymbol{\mu}_m \end{bmatrix} = \begin{bmatrix} \mathbf{A}_{[4 \times 4]} & \mathbf{G}_{[4 \times 2]} \\ \mathbf{H}_{[2 \times 4]} & \mathbf{D}_m_{[2 \times 2]} \end{bmatrix} \begin{bmatrix} \boldsymbol{\gamma}_m \\ \boldsymbol{\kappa}_m \end{bmatrix} \quad (3.19)$$

$$\begin{bmatrix} \boldsymbol{\tau}_f \\ \boldsymbol{\mu}_f \end{bmatrix} = \begin{bmatrix} \mathbf{F}_{[4 \times 4]} & \mathbf{0}_{[4 \times 4]} \\ \mathbf{0}_{[4 \times 4]} & \mathbf{D}_f_{[4 \times 4]} \end{bmatrix} \begin{bmatrix} \boldsymbol{\gamma}_f \\ \boldsymbol{\kappa}_f \end{bmatrix}. \quad (3.20)$$

In the above: \mathbf{A} governs the membrane behaviour; \mathbf{D}_f and \mathbf{D}_m control the in- and out-of-plane bending response; \mathbf{F} accounts for the transversal and the longitudinal shears. Matrices \mathbf{G} and \mathbf{H} are responsible for the coupling between the stress and couple stress components. Next, we will focus on the case of Cosserat materials possessing centrosymmetric properties. In such case, those matrices are considered zero. For a more complete FE formulation, the reader is referred to Appendix C.1.

3.4 Element formulation

In Cosserat FE, nodes are equipped with translational and rotational DOF. The number of nodes to which refer the translations and the rotations depends to the degree of interpolation attended for those fields. As it will be discussed in Section 3.5.1, many choices are possible in this sense. In order to keep the formulation general, we assume that the element translations are defined on N nodes, whereas element rotations are attached to M nodes. Therefore, the vectors containing the nodal variables of the element can be written as:

$$\begin{bmatrix} \mathbf{U}_m^t & \boldsymbol{\Omega}_m^t \end{bmatrix} = \begin{bmatrix} \mathbf{U}_m^1{}^t & \dots & \mathbf{U}_m^N{}^t & \boldsymbol{\Omega}_m^1 & \dots & \boldsymbol{\Omega}_m^M \end{bmatrix} \\ \begin{bmatrix} \mathbf{U}_f^t & \boldsymbol{\Omega}_f^t \end{bmatrix} = \begin{bmatrix} \mathbf{U}_f^1 & \dots & \mathbf{U}_f^N & \boldsymbol{\Omega}_m^1{}^t & \dots & \boldsymbol{\Omega}_m^M{}^t \end{bmatrix}. \quad (3.21)$$

The aforementioned N nodal displacements and the M nodal rotations are interpolated by means of general shape functions \mathbf{N} and Φ , respectively:

$$\begin{bmatrix} \mathbf{u}_m \\ \omega_m \end{bmatrix} = \begin{bmatrix} \mathbf{N}_m[2 \times 2N] & \mathbf{0}[2 \times M] \\ \mathbf{0}[1 \times 2N] & \Phi_m[1 \times M] \end{bmatrix} \begin{bmatrix} \mathbf{U}_m \\ \Omega_m \end{bmatrix} \quad (3.22)$$

$$\begin{bmatrix} u_f \\ \omega_f \end{bmatrix} = \begin{bmatrix} \mathbf{N}_f[1 \times N] & \mathbf{0}[1 \times 2M] \\ \mathbf{0}[2 \times N] & \Phi_f[2 \times 2M] \end{bmatrix} \begin{bmatrix} \mathbf{U}_f \\ \Omega_f \end{bmatrix}. \quad (3.23)$$

In particular, \mathbf{N}_m interpolate the in-plane displacements, \mathbf{N}_f the out-of-plane displacements, Φ_m the in-plane rotational field and Φ_f the out-of-plane rotational fields:

$$\begin{aligned} \mathbf{N}_m[2 \times 2N] &= \begin{bmatrix} N_1 & 0 & & N_N & 0 \\ 0 & N_1 & \dots & 0 & N_N \end{bmatrix}, \quad \mathbf{N}_f[1 \times N] = [N_1 \quad \dots \quad N_N] \\ \Phi_m[1 \times M] &= [\Phi_1 \quad \dots \quad \Phi_M], \quad \Phi_f[2 \times 2M] = \begin{bmatrix} \Phi_1 & 0 & & \Phi_M & 0 \\ 0 & \Phi_1 & \dots & 0 & \Phi_M \end{bmatrix}. \end{aligned} \quad (3.24)$$

It follows that the expressions of the deformation measures within the FE are:

$$\begin{bmatrix} \gamma_m \\ \kappa_m \end{bmatrix} = \begin{bmatrix} \mathbf{B}_{m1}[4 \times 2N] & \mathbf{B}_{m2}[4 \times M] \\ \mathbf{B}_{m3}[2 \times 2N] & \mathbf{B}_{m4}[2 \times M] \end{bmatrix} \begin{bmatrix} \mathbf{U}_m \\ \Omega_m \end{bmatrix} \quad (3.25)$$

$$\begin{bmatrix} \gamma_f \\ \kappa_f \end{bmatrix} = \begin{bmatrix} \mathbf{B}_{f1}[4 \times N] & \mathbf{B}_{f2}[4 \times 2M] \\ \mathbf{B}_{f3}[4 \times N] & \mathbf{B}_{f4}[4 \times 2M] \end{bmatrix} \begin{bmatrix} \mathbf{U}_f \\ \Omega_f \end{bmatrix}, \quad (3.26)$$

where the definition of compliant matrices $\mathbf{B}_{\alpha i}$ can be found by introducing Eq.(3.24) into Eqs.(3.16)-(3.17), and obtaining, in very compact form, the following relations:

$$\begin{cases} \mathbf{B}_{\alpha i} = \mathbf{L}_{\alpha i} \mathbf{N}_{\alpha}, & \text{for } i = 1, 3 \\ \mathbf{B}_{\alpha i} = \mathbf{L}_{\alpha i} \Phi_{\alpha}, & \text{for } i = 2, 4 \end{cases} \quad \text{with } \alpha = m, f. \quad (3.27)$$

Notice that matrices \mathbf{B}_{m2} and \mathbf{B}_{m4} are associated with the in-plane (or drilling) nodal rotations Ω_3 , which are absent in the classical engineering plate theories.

3.4.1 Stiffness matrix

The substitution of the relations (3.22)-(3.23) and (3.25)-(3.26) into the expressions of the deformation energy V^c (from Eq.(3.9)) and of the external works W^c (from Eq.(3.10)) for the plate, leads to the definitions of the element stiffness matrix and the nodal load vectors. Adopting the notation used by [Providas and Kattis \(2002\)](#) for the in-plane behaviour, it holds:

$$\begin{aligned} V_m^c &= \frac{1}{2} \begin{bmatrix} \mathbf{U}_m^t & \Omega_m^t \end{bmatrix} \begin{bmatrix} \mathbf{K}_{UU}^m & \mathbf{K}_{U\Omega}^m \\ \mathbf{K}_{\Omega U}^m & \mathbf{K}_{\Omega\Omega}^m \end{bmatrix} \begin{bmatrix} \mathbf{U}_m \\ \Omega_m \end{bmatrix} \\ W_m^c &= \begin{bmatrix} \mathbf{P}_m^t & \mathbf{Q}_m^t \end{bmatrix} \begin{bmatrix} \mathbf{U}_m \\ \Omega_m \end{bmatrix}, \end{aligned} \quad (3.28)$$

with the stiffness sub-matrices:

$$\mathbf{K}_{UU}^m = \int_{\Omega^e} \left(\mathbf{B}_{m1}[2N \times 4]^t \mathbf{A}_{[4 \times 4]} \mathbf{B}_{m1}[4 \times 2N] \right) dA \quad (3.29)$$

$$\mathbf{K}_{U\Omega}^m = \int_{\Omega^e} \left(\mathbf{B}_{m1}[2N \times 4]^t \mathbf{A}_{[4 \times 4]} \mathbf{B}_{m2}[4 \times M] \right) dA = \mathbf{K}_{\Omega U}^{m,t} \quad (3.30)$$

$$\mathbf{K}_{\Omega\Omega}^m = \int_{\Omega^e} \left(\mathbf{B}_{m2}[M \times 4]^t \mathbf{A}_{[4 \times 4]} \mathbf{B}_{m2}[4 \times M] + \mathbf{B}_{m4}[M \times 2]^t \mathbf{D}_m[2 \times 2] \mathbf{B}_{m4}[2 \times M] \right) dA, \quad (3.31)$$

and the nodal load vectors:

$$\begin{bmatrix} \mathbf{P}_m \\ \mathbf{Q}_m \end{bmatrix} = \int_{\Omega^e} \begin{bmatrix} \mathbf{N}_m[2N \times 2]^t & \mathbf{0}_{[2N \times 1]} \\ \mathbf{0}_{[M \times 2]} & \Phi_m[M \times 1]^t \end{bmatrix} \begin{bmatrix} \mathbf{f}_m \\ m_m \end{bmatrix} dA + \int_{\partial\Omega_\Sigma^e} \begin{bmatrix} \mathbf{N}_m[2N \times 2]^t & \mathbf{0}_{[2N \times 1]} \\ \mathbf{0}_{[M \times 2]} & \Phi_m[M \times 1]^t \end{bmatrix} \begin{bmatrix} \mathbf{T}_m^d \\ M_m^d \end{bmatrix} dS \quad (3.32)$$

defined on the element configuration Ω^e . The vectors \mathbf{T}_m^d, M_m^d represent the in-plane forces and moments prescribed on the boundary $\partial\Omega_\Sigma^e$ of the finite element. It is worth mentioning that the sub-matrix \mathbf{K}_{UU}^m represents the stiffness matrix of a classical membrane element, whereas $\mathbf{K}_{U\Omega}^m$ and $\mathbf{K}_{\Omega\Omega}^m$ are additional terms associated to the drilling rotations. This is the difference between the present Cosserat FE formulation and a classical Cauchy-continuum-based formulation, as far it concerns the in-plane behaviour. As it will be shown in [Section 3.5.2](#), the first term of $\mathbf{K}_{\Omega\Omega}^m$ alleviates the local stiffness matrix rank deficiency that occurs in case of reduced integration of classical elements against membrane actions.

The out-of-plane behaviour can be separated into pure bending (*b*) and shear (*s*) components. In this case the stiffness matrix is:

$$\mathbf{K}_f = \begin{bmatrix} \mathbf{K}_{UU}^s & \mathbf{K}_{U\Omega}^s \\ \mathbf{K}_{\Omega U}^s & \mathbf{K}_{\Omega\Omega}^s + \mathbf{K}_{\Omega\Omega}^b \end{bmatrix}, \quad (3.33)$$

with

$$\mathbf{K}_{UU}^s = \int_{\Omega^e} \left(\mathbf{B}_{f1}[N \times 4]^t \mathbf{F}_{[4 \times 4]} \mathbf{B}_{f1}[4 \times N] \right) dA \quad (3.34)$$

$$\mathbf{K}_{U\Omega}^s = \int_{\Omega^e} \left(\mathbf{B}_{f1}[N \times 4]^t \mathbf{F}_{[4 \times 4]} \mathbf{B}_{f2}[4 \times 2M] \right) dA = \mathbf{K}_{\Omega U}^{s\ t} \quad (3.35)$$

$$\mathbf{K}_{\Omega\Omega}^s = \int_{\Omega^e} \left(\mathbf{B}_{f2}[2M \times 4]^t \mathbf{F}_{[4 \times 4]} \mathbf{B}_{f2}[4 \times 2M] \right) dA \quad (3.36)$$

$$\mathbf{K}_{\Omega\Omega}^b = \int_{\Omega^e} \left(\mathbf{B}_{f4}[2M \times 4]^t \mathbf{D}_{f[4 \times 4]} \mathbf{B}_{f4}[4 \times 2M] \right) dA. \quad (3.37)$$

The nodal load vectors are:

$$\begin{bmatrix} \mathbf{P}_f \\ \mathbf{Q}_f \end{bmatrix} = \int_{\Omega^e} \begin{bmatrix} \mathbf{N}_f[N \times 1]^t & \mathbf{0}_{[N \times 2]} \\ \mathbf{0}_{[2M \times 1]} & \Phi_f[2M \times 2]^t \end{bmatrix} \begin{bmatrix} f_f \\ m_f \end{bmatrix} dA + \int_{\partial\Omega_\Sigma^e} \begin{bmatrix} \mathbf{N}_f[N \times 1]^t & \mathbf{0}_{[N \times 2]} \\ \mathbf{0}_{[2M \times 1]} & \Phi_f[2M \times 2]^t \end{bmatrix} \begin{bmatrix} T_f^d \\ M_f^d \end{bmatrix} dS \quad (3.38)$$

In Eq.(3.38), T_f^d and M_f^d represent the vertical force and out-of-plane moments prescribed on the boundary $\partial\Omega_\Sigma^e$. It is worth pointing out that, as far as it concerns the out-of-plane behaviour, the expressions of the stiffness matrix \mathbf{K}_f and of its sub-matrices obtained for the Cosserat plate element (Eq.(3.33)) have the same structure and form with those of a thick (Reissner-Mindlin) plate element. Indeed, the present Cosserat FE formulation is more general and encloses the Reissner-Mindlin FE formulation. This latter can be retrieved by a) neglecting the longitudinal shears τ_{13} and τ_{23} in the constitutive matrix \mathbf{F} (Eq.(3.20)) and b) by redefining of the operator \mathbf{L}_{f4} in Eq.(3.18), in order to take into account only the symmetric part of the rotation gradient into the definition of the out-of-plane curvatures κ_f (see [Table 3.1](#)). In this sense, the FE formulation provided for Reissner-Mindlin plates is a special case of the FE formulation for Cosserat plates presented herein. Due to this similarity, shear locking phenomenon is expected in the limit of very thin geometries in the present Cosserat formulation. This issue will be explored in [Section 3.6.2](#).

3.4.2 Mass matrix

The mass matrix can be computed by substituting Eq.(3.22)-(3.23) into the equation of the kinetic energy K^c (Eq.(3.11)) calculated for the plate. For the in-plane behaviour this results in the expression:

$$K_m^c = \frac{1}{2} \begin{bmatrix} \ddot{U}_m^t & \ddot{\Omega}_m^t \end{bmatrix} \begin{bmatrix} M^m & \mathbf{0} \\ \mathbf{0} & \Theta^m \end{bmatrix} \begin{bmatrix} \ddot{U}_m^t \\ \ddot{\Omega}_m^t \end{bmatrix}, \quad (3.39)$$

with the mass sub-matrices:

$$\begin{bmatrix} M^m & \mathbf{0} \\ \mathbf{0} & \Theta^m \end{bmatrix} = \int_{\Omega^e} \begin{bmatrix} N_m^{[2N \times 2]^t} & \mathbf{0}_{[2N \times 1]^t} \\ \mathbf{0}_{[M \times 2]} & \Phi_m^{[M \times 1]^t} \end{bmatrix} \begin{bmatrix} \mathbf{1}_m^{[2 \times 2]} & \mathbf{0}_{[2 \times 1]} \\ \mathbf{0}_{[1 \times 2]} & I_m^{[1 \times 1]} \end{bmatrix} \begin{bmatrix} N_m^{[2 \times 2N]} & \mathbf{0}_{[2 \times M]} \\ \mathbf{0}_{[1 \times 2N]} & \Phi_m^{[1 \times M]} \end{bmatrix} dA \quad (3.40)$$

For the out-of plane behaviour it holds:

$$\begin{bmatrix} M^f & \mathbf{0} \\ \mathbf{0} & \Theta^f \end{bmatrix} = \int_{\Omega^e} \begin{bmatrix} N_f^{[N \times 1]^t} & \mathbf{0}_{[N \times 2]} \\ \mathbf{0}_{[2M \times 1]} & \Phi_f^{[2M \times 2]^t} \end{bmatrix} \begin{bmatrix} \mathbf{1}_f^{[1 \times 1]} & \mathbf{0}_{[1 \times 2]} \\ \mathbf{0}_{[2 \times 1]} & I_f^{[2 \times 2]} \end{bmatrix} \begin{bmatrix} N_f^{[1 \times N]} & \mathbf{0}_{[1 \times 2M]} \\ \mathbf{0}_{[2 \times N]} & \Phi_f^{[2 \times 2M]} \end{bmatrix} dA \quad (3.41)$$

In the present formulation the micro-inertia tensor is considered isotropic. A rigorous way to determine the inertial terms of a Cosserat medium could be that dictated by Germain (1973) and Eringen (1999) (see also Stefanou et al. (2010)). The mass density ρ may be defined by identification of the rigid micro-structure with the material particle of the underlying continuum, as the integral of the mass density distribution ρ' over the volume of the particle V :

$$\rho dV = \int_V \rho' dV', \quad (3.42)$$

where $[\]'$ denotes that the variable is defined at the scale of the particle. Similarly, the micro-inertia tensor can be defined as the second order moment with respect to the position of the centre of the mass of the particle, i.e. (Eringen, 1999):

$$\rho I_{ij} dV = \int_V \rho' x'_i x'_j dV'. \quad (3.43)$$

3.4.3 Element motion

Following the definitions given in this Section, the PDE for a Cosserat plate FE are expressed in matrix form as:

$$\begin{bmatrix} K_{UU}^m & K_{U\Omega}^m \\ K_{\Omega U}^m & K_{\Omega\Omega}^m \end{bmatrix} \begin{bmatrix} U_m \\ \Omega_m \end{bmatrix} + \begin{bmatrix} M^m & \mathbf{0} \\ \mathbf{0} & \Theta^m \end{bmatrix} \begin{bmatrix} \ddot{U}_m \\ \ddot{\Omega}_m \end{bmatrix} = \begin{bmatrix} P_m \\ Q_m \end{bmatrix} \\ \begin{bmatrix} K_{UU}^s & K_{U\Omega}^s \\ K_{\Omega U}^s & K_{\Omega\Omega}^s + K_{\Omega\Omega}^b \end{bmatrix} \begin{bmatrix} U_f \\ \Omega_f \end{bmatrix} + \begin{bmatrix} M^f & \mathbf{0} \\ \mathbf{0} & \Theta^f \end{bmatrix} \begin{bmatrix} \ddot{U}_f \\ \ddot{\Omega}_f \end{bmatrix} = \begin{bmatrix} P_f \\ Q_f \end{bmatrix}. \quad (3.44)$$

Eq.(3.44) governs the motion of the element and is to be solved at each step of the analysis. To this purpose, a number of solution methods exist and some of them are exploited in the commercial code Abaqus (Simulia 2010), where the presented formulation has been implemented as a particular User Element (UEL) and employed within an implicit time-discretisation procedure. This makes possible to control the analysis at each step of a prescribed procedure, to compute the stress and deformation state at every Gauss point of the element and to combine the new element solution with that obtained by the pre-existing elements of the code.

3.5 The COSS8R element

The implemented element is an isoparametric quadratic plane rectangle with eight nodes and constant thickness (Figure 4.5). Reduced integration is made to avoid shear locking and therefore four Gauss points are used. Each node of the element is equipped with three translational and three rotational DOF. This results in a complete six-degree-of-freedom FE formulation, allowing to model shell structures as an assembly of these flat elements (Zienkiewicz and Taylor, 2005).

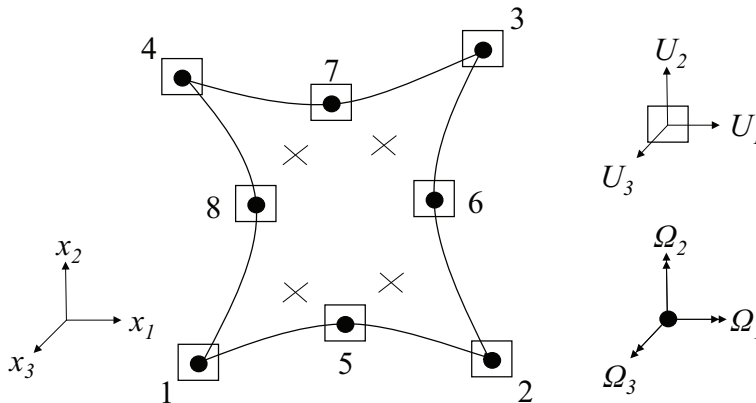


Figure 3.3: The COSS8R element, with 4 Gauss points (X), 8 nodes and 6 DOF per node: translations (square) and rotations (circle).

A similar FE formulation has been proposed in literature by Zhang et al. (2005), but, to the author's knowledge, its performance has not been yet explored.

3.5.1 Choice of the polynomial order of interpolation

The same quadratic shape functions \mathbf{N} and $\mathbf{\Phi}$ are used for the polynomial interpolation of the translational and the rotational kinematic fields. This choice is not the only one possible.

An alternative would be to consider Lagrangian elements with linear interpolations for both kinematic fields. However, in this case, Eqs.(3.3)-(3.4) indicate that some integral terms, as for example the product between the symmetric tensors $[\tau_{(ij)}\gamma_{(ij)}]$ and the product between the couple stresses and the curvatures $[\mu_{ij}\kappa_{ij}]$, would be of zero degree (constants). On the other hand, the product between the skew-symmetric tensors $[\tau_{[ij]}\gamma_{[ij]}]$ would be of second degree. In that case, a selective integration technique should be attempted in order to redress the same level of accuracy in the representation of both deformation measures, since, if only the lower order of interpolation was respected, it would result in a decrease of accuracy for coarse element discretisations.

Another approach could be to choose high precision Hermitian elements, as done by Unterreiner (1994). However, in spite of the higher accuracy reached by this approach, the plate formulation with Hermitian elements would be not trivial and more computationally intensive.

In Providas and Kattis (2002) it is demonstrated that, in the case of an explicitly derived formulation where no numerical integration is involved, a triangular Cosserat element for plane elasticity that uses quadratic shape functions for both displacements and rotations produces excellent results if compared to linear interpolations. Only marginally better would be the behavior of elements with quadratic (for translations) and linear (for rotations) approximations (Providas and Kattis, 2002). Indeed, the adoption of quadratic shape functions for the displacement field and of linear shape functions for the rotational field would assure the same order of

interpolation, as far as it concerns the in-plane strain vector $\boldsymbol{\gamma}_m$. This as consequence of its definition (Eq.(3.1)). Nevertheless, the adoption of linear functions for the rotations would lead, after Eq.(3.2), to constant in-plane $\boldsymbol{\kappa}_m$ and out-of-plane $\boldsymbol{\kappa}_f$ curvatures within the element. In view of the representation of flexural problems, this is considered as a limitation.

In order to overcome this problem, we make use of quadratic shape functions for both the translational and the rotational fields over the FE. Such a formulation allows to cover the interpolation order given by a linear/quadratic formulation and to increase the precision with respect to the curvatures. Aiming at modelling both the in-plane and the out-of-plane behaviour, this choice is expected to provide a good level of accuracy in case of coarse meshes and be still advantageous in view of the dynamic analyses, where the use of too refined formulations would increase excessively the computational cost.

3.5.2 Zero-energy modes investigation

Reduced integration comes with the price of introducing modes of deformation with zero energy, i.e. modes for which the element does not exhibit any stiffness (Hughes 1987). In the case of classical quadrilateral membrane elements such modes take the shape of an hourglass and they have to be controlled in order to assure accurate results. One way consists, for instance, in introducing an additional drilling rigidity into the element stiffness matrix ((Hughes and Brezzi, 1989; Chinosi et al., 1997; Zienkiewicz and Taylor, 2005)). This artificial stiffness does not have a particular physical meaning except in the framework of a Cosserat continuum, where it is provided by the in-plane particle rotations.

HOURGLASS MODES

In a general manner we consider the following standard eigenproblem:

$$[\mathbf{K} - \lambda \mathbf{1}] \bar{\mathbf{U}} = 0. \quad (3.45)$$

The solution of Eq.(3.45) gives L eigenvalues λ_l and L nodal eigenvectors $\bar{\mathbf{U}}^l$, with $l = 1, \dots, L$ and L being the dimension of the considered local stiffness matrix \mathbf{K} . It is known that every eigenvalue is equal to twice the strain energy due to the displacement field provided by the associated eigenvector (Hughes, 1987). As a consequence, one may expect from the solution of the eigenproblem as many null eigenvalues as the number of rigid motions and, for each additional null eigenvalue, an associated non-rigid motion with zero deformation energy can be found. In computational terms, this indicates a matrix rank deficiency. In mechanical terms, this shows that the formulation is affected by the presence of zero-energy modes.

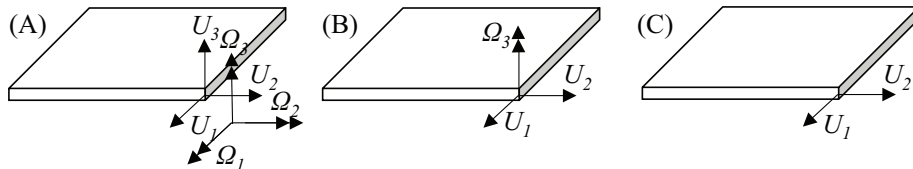


Figure 3.4: Elements tested for zero-energy modes investigation: (A) Cosserat element, plate configuration; (B) Cosserat element, membrane configuration; (C) classical Cauchy element, membrane part.

Starting from the present Cosserat formulation, we calculate the eigenvalues of the stiffness matrix \mathbf{K} for three different cases (Figure 3.4). First, the eigenproblem is solved for a complete six-degree-of-freedom Cosserat assembly (Figure 3.4-(A)). The same investigation is made

by considering only the membrane behaviour of the Cosserat element (Figure 3.4-(B)). Then, only the in-plane translations are kept, reducing the present formulation to a classical Cauchy membrane element (Figure 3.4-(C)). The stiffness matrix considered in each case is one (or an assembly) of the sub-matrices defined in Section 3.4.1. For the case (C) we also impose symmetry into the in-plane shear stress in order to retrieve Cauchy continuum. As shown in Appendix C.2, this can be accounted for in the construction of the material matrix \mathbf{A} , by respecting the following identities:

$$A_{1212} = A_{2121} = A_{1221} = A_{2112} \quad (3.46)$$

In Table 3.2, we give the comparison between the three aforementioned configurations, in terms of the number of computed zero-energy modes. Despite the reduced integration, the COSS8R element does not show any rank deficiency.

element formulation	\mathbf{K}	number of integration points	
		2x2	3x3
(A) Cosserat plate	Eqs.(3.29)-(3.31),(3.34)-(3.37)	0	0
(B) Cosserat membrane	Eqs.(3.29)-(3.31)	0	0
(C) Cauchy membrane	Eq.(3.29)	1	0

Table 3.2: Computed number of zero-energy modes other than those associated with rigid body modes.

SPURIOUS MODES

The origin of the zero-energy modes can be found in the difference between the number of local deformation variables of the continuum model that we intend to discretise and the number of deformation modes of the actual numerical model. Hence, given the continuum, it is sufficient to increase the number of degrees of freedom, for example through mesh refinement or by increasing the interpolation order, in order to alleviate the matrix deficiency and make the zero-energy mode *non-communicable* (Hughes, 1987). There exist, however, certain situations in which the problem still occurs.

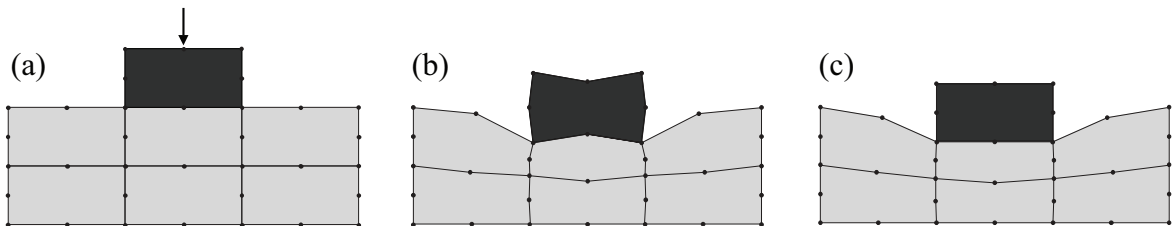


Figure 3.5: (a) a highly rigid element resting upon a layer of flexible elements with reduced integration; (b) propagating spurious mode in an assembly of Cauchy (S8R) elements; (c) accurate results from a COSS8R subdivision.

Herein we consider the well-discussed plane problem of Figure 3.5 (see Zienkiewicz and Taylor (2005)). Because of the reduced integration, an hourglass mode is activated in the rigid element as a result of the applied force, and it gives rise to a spurious (or *communicable*) mode which is able to propagate within a certain area in the elements below. In the case of the classical S8R element (Figure 3.5-(b)), only the use of a complete integration would allow to overcome

such problem and give accurate solutions, with the price of shear locking behaviour. On the contrary, the COSS8R element does not have this problem, as the rotational DOF perform an intrinsic action of hourglass control (Figure 3.5-(c)).

It is interesting to investigate how these spurious modes become manifest. To this end, we consider a homogeneous isotropic Cosserat centrosymmetric material. Matrices \mathbf{A} and \mathbf{D}_m in Eq.(3.19) are expressed as:

$$\mathbf{A} = \begin{bmatrix} K + G & K - G & 0 & 0 \\ K - G & K + G & 0 & 0 \\ 0 & 0 & G + G_c & G - G_c \\ 0 & 0 & G - G_c & G + G_c \end{bmatrix}, \quad \mathbf{D}_m = \begin{bmatrix} 2Gl_c & 0 \\ 0 & 2Gl_c \end{bmatrix} \quad (3.47)$$

where K is the compression modulus, G is the shear modulus, G_c is the Cosserat shear modulus and l_c denotes the internal length under shear. It is useful to define $\alpha = G_c/G$ as the coupling factor. As we show in Appendix C.2, this parameter allows to control the magnitude of the skew-symmetric term of the membrane strain vector, i.e. $\gamma_{[12]}$. For $\alpha = 0$, in-plane rotations are annihilated and the classical Cauchy element is retrieved through Eq.(3.46) (Figure 3.5-(b)). For $\alpha = 1$, the COSS8R element is recalled (Figure 3.5-(c)). Intermediate values of α allows to control the magnitude of, say, the Cosserat's term $\gamma_{[12]}$.

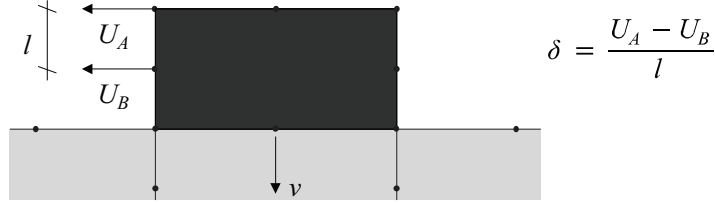


Figure 3.6: Definition of the distortion δ of the rigid element.

Always with reference to the above example (Figure 3.5), a parametric analysis is carried out on α . The results are presented in Figure 3.7, in terms of the distortion δ and the displacement v , which are defined in Figure 3.6 and normalized with the values calculated for $\alpha = 0$. Figure 3.7 shows an immediate decrease of distortion due to the introduction of the Cosserat's term (Figure 3.7-left). Moreover, the exact solution is reached rapidly by varying the coupling factor α from 0 to 1 (Figure 3.7-right). Therefore we can defend the idea that the non-symmetry of the stress tensor permits to avoid the rank deficiency into the element membrane stiffness in case of reduced integration. The non-symmetry of the stress tensor is a key feature of Cosserat continuum.

STIFFNESS MATRIX DEFICIENCIES IN MODELLING SHELL STRUCTURES

Regarding the complete plate formulation and the possibility to model shell spatial structures, we demonstrate in Appendix C.3 that the coupling factor α enters the definition of the first term of the stiffness sub-matrix (3.31). Such matrix, as it is indicated by Providas and Kattis (2000), has also a stabilization effect in the modelling of shell structures by assembling flat plate elements. We can thus conclude on the good computational performance of the present Cosserat plate element. The non-symmetry of the stress tensor has in fact a *general rank stabilization effect* versus the occurrence of hourglass modes in membrane behaviour, and matrix deficiencies in shell structures assemblies. This is a clear advantage as compared to classical-continuum-based FE formulations, where the use of artificial hourglass control techniques is inevitable.

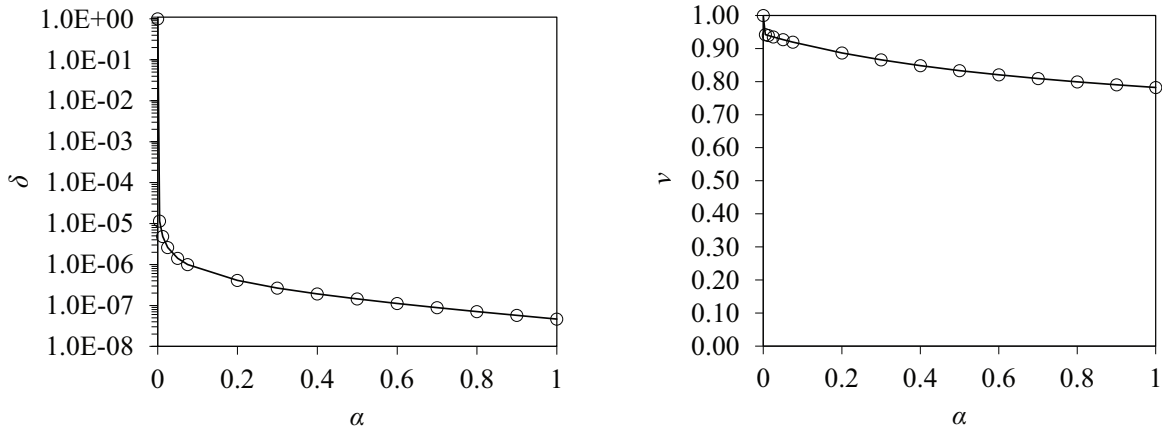


Figure 3.7: Normalised distortion factor (left) and normalised vertical displacement (right) versus the coupling factor α . The classical Cauchy (S8R) element is retrieved for $\alpha = 0$. The COSS8R element is for $\alpha = 1$.

3.5.3 Consistent mass matrix

The dynamic counterpart of Eq.(3.45) is the generalized eigenproblem:

$$[\mathbf{K} - \lambda\mathbf{M}] \bar{\mathbf{U}} = 0. \quad (3.48)$$

Always employing a reduced integration for the computation of the stiffness matrix \mathbf{K} (the case (A) of Figure 3.4 is herein referred to), reduced and complete integration are performed for the computation of the local mass matrix \mathbf{M} . Generalized eigenvalue analyses are carried on the aforementioned matrices and reveal the occurrence of infinite eigenvalues, in the case of reduced integration of the mass matrix. From a mechanical point of view, this corresponds to the presence of *massless degrees of freedom* (Bathe, 1996), for which the system exhibits infinite stiffness. A static condensation would then be necessary on such variables in order to give accurate results, and the element would result in lumped mass components. Therefore complete integration is used over the mass matrix, so as to keep an effectively consistent formulation.

Through this method we also confirm the absence of zero-energy modes in the dynamic regime.

3.6 Element validation

A number of numerical tests and examples are presented in this Section with the goal of assessing the performance of the present COSS8R element both in static and dynamic regime. In particular, a patch test specifically designed for Cosserat continua is made to prove the efficiency of the element in representing homogeneous in-plane relative strain and curvature states. Shear locking investigation is then carried out to attest the out-of-plane response of the element in the limit of thin geometries. The wave dispersion functions are finally calculated with reference to a one-dimensional problem and compared to the analytical solution.

3.6.1 Patch test

We consider the rectangular region of Figure 3.8, where an internal element is introduced within the patch in order to induce a geometric distortion to the whole discretisation.

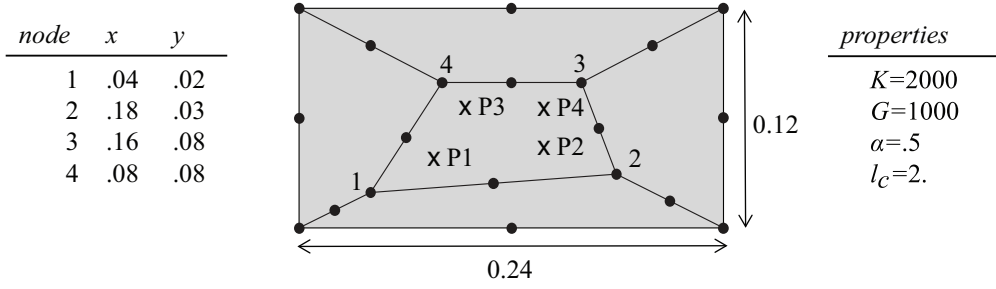


Figure 3.8: Element discretisation employed for the patch test.

The patch test used here is inspired by [Providas and Kattis \(2002\)](#), who used it for triangular elements, and it is adequately modified for rectangular FE. A homogeneous isotropic linear elastic Cosserat material is taken into account. The material matrix given by Eq.(46). Three tests are performed dealing with the membrane (or in-plane) behaviour ([Providas and Kattis, 2002](#)), see [Table 3.3](#). Test 1 verifies that the element is capable of reproducing constant symmetric shear components, as in a classical formulation. In Test 2, a non-symmetric constant shear is imposed through the application of external couples m_3 . For Test 3, the solution is such that the in-plane couple stresses are identical and constant.

The boundary conditions which allow the situations above to be achieved are applied to the external nodes of the patch and the solution is checked at Gauss point P1 of the internal element ([Figure 3.8](#)). As shown in [Table 3.4](#), good agreement with the theoretical solution is achieved in all tests. In Test 3, the level of accuracy reached by the formulation is comparable with that found by [Providas and Kattis \(2002\)](#) for their quadratic triangular element MQUAT.

In [Appendix C.4](#)¹, the presented patch test is extended and formulated for anisotropic Cosserat materials. This patch test is introduced and used in order to test the element in case of material anisotropy. In this case, the element satisfies the test showing the same accuracy level than in the classical test presented above.

Test 1			
$u_1 = 10^{-3}(x + 0.5y)$	$u_2 = 10^{-3}(x + y)$	$\omega_3 = 0.25 \times 10^{-3}$	$f_1 = f_2 = 0$
$\tau_{11} = \tau_{22} = 4$	$\tau_{12} = \tau_{21} = 1.5$	$\mu_{31} = \mu_{32} = 0$	$m_3 = 0$
Test 2			
$u_1 = 10^{-3}(x + 0.5y)$	$u_2 = 10^{-3}(x + y)$	$\omega_3 = 10^{-3}(0.25 + (4\alpha)^{-1})$	$f_1 = f_2 = 0$
$\tau_{11} = \tau_{22} = 4$	$\tau_{12} = 2\tau_{21} = 2$	$\mu_{31} = \mu_{32} = 0$	$m_3 = 1$
Test 3			
$u_1 = 10^{-3}(x + 0.5y)$	$u_2 = 10^{-3}(x + y)$	$\omega_3 = 10^{-3}(0.25 + (2\alpha)^{-1}(x - y))$	$f_1 = f_2 = 1$
$\tau_{11} = \tau_{22} = 4$	$\tau_{12} = 1.5 + (x - y)$	$\mu_{31} = -\mu_{32} = 4.$	$m_3 = 2(x - y)$
	$\tau_{21} = 1.5 - (x - y)$		

Table 3.3: Patch test for Cosserat plane elements: boundary conditions and expected solutions.

¹This is an additional Appendix that is absent from [Godio et al. \(2015a\)](#).

	τ_{11}	τ_{22}	τ_{12}	τ_{21}	μ_{31}	μ_{32}
Test 1	4.000	4.000	1.500	1.500	0.000	0.000
	[4.000]	[4.000]	[1.500]	[1.500]	[0.000]	[0.000]
Test 2	4.000	4.000	1.000	2.000	0.010	0.022
	[4.000]	[4.000]	[1.000]	[2.000]	[0.000]	[0.000]
Test 3	3.976	3.970	1.521	1.447	3.997	-4.001
	[4.000]	[4.000]	[1.537]	[1.462]	[4.000]	[-4.000]

Table 3.4: Results of patch tests at point P1. Exact results are reported in brackets.

3.6.2 Shear locking investigation

We consider the example of simply-supported and clamped-edge $L \times L$ square plates of constant thickness h , subjected to uniform distributed load p (Figure 3.9). In order to investigate the shear locking phenomenon, several analyses are carried out on these configurations by considering various FE subdivisions of increasing L/h ratios.

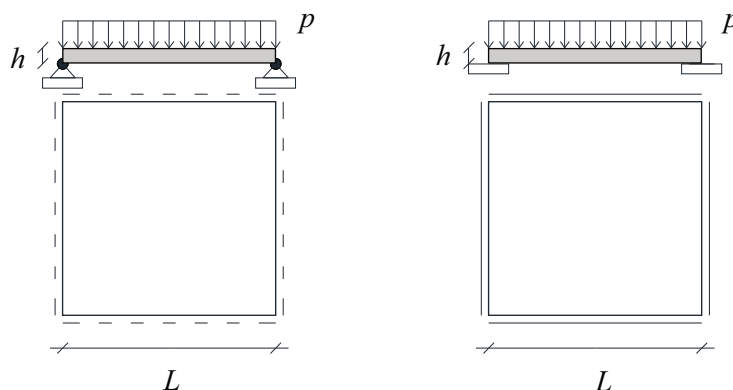


Figure 3.9: Bending-plate in two configurations: simply supported (left) and clamped edges (right).

To this purpose, we take into account the constitutive law proposed by [Altenbach and Eremeyev \(2009\)](#), who, starting from a Cosserat 3D flat configuration, deduce an isotropic relation for micropolar plates by integration in the thickness direction. Matrices \mathbf{F} and \mathbf{D}_f in Eq.(3.20) yield:

$$\mathbf{F} = \begin{bmatrix} 0 & 0 & 0 & 0 \\ 0 & \alpha_4 & 0 & 0 \\ 0 & 0 & 0 & 0 \\ 0 & 0 & 0 & \alpha_4 \end{bmatrix}, \quad \mathbf{D}_f = \begin{bmatrix} \beta_1 + \beta_2 + \beta_3 & & \beta_1 & 0 & 0 \\ & \beta_1 & \beta_1 + \beta_2 + \beta_3 & 0 & 0 \\ & 0 & & 0 & \beta_3 & \beta_2 \\ & 0 & & 0 & \beta_2 & \beta_3 \end{bmatrix} \quad (3.49)$$

where the parameters $\alpha_4, \beta_1, \beta_2, \beta_3$ are here retrieved from the works of Lakes made on high-density rigid polyurethane closed-cell foams (see Table 2-PU in [Altenbach and Eremeyev \(2009\)](#)).

In [Figure 3.10](#) we show the resultant deflection w_c , measured at the centre of the plate. The out-of-plane bending rigidity used for normalization is $D_f \equiv \beta_3$. The results are qualitatively similar to those found in literature for the thick (Reissner-Mindlin) plate elements (see [Zienkiewicz and Taylor \(2005\)](#)). In particular, the performance of the element reduces as the geometry of the plate becomes thin, and this phenomenon is more apparent for the plate with clamped edges than for the simply supported one. Nevertheless, in both cases convergence

is guaranteed upon mesh refinement. It is to note that, for high L/h ratios, the structural response reaches the solution predicted by the thin (Love-Kirchhoff) plate theory (see [Taylor and Govindjee \(2004\)](#)). This can be explained by the fact that, as for the Reissner-Mindlin formulation, the limit of thin geometries plays the role of an internal kinematical constraint, for which the transverse shear deformations tend to vanish. Moreover, due to the symmetry of the problem and the constitutive law considered, the torsional response is symmetric in the plate directions. These two conditions allow to retrieve the kinematics of a thin plate, in the limit of $L/h \rightarrow \infty$.

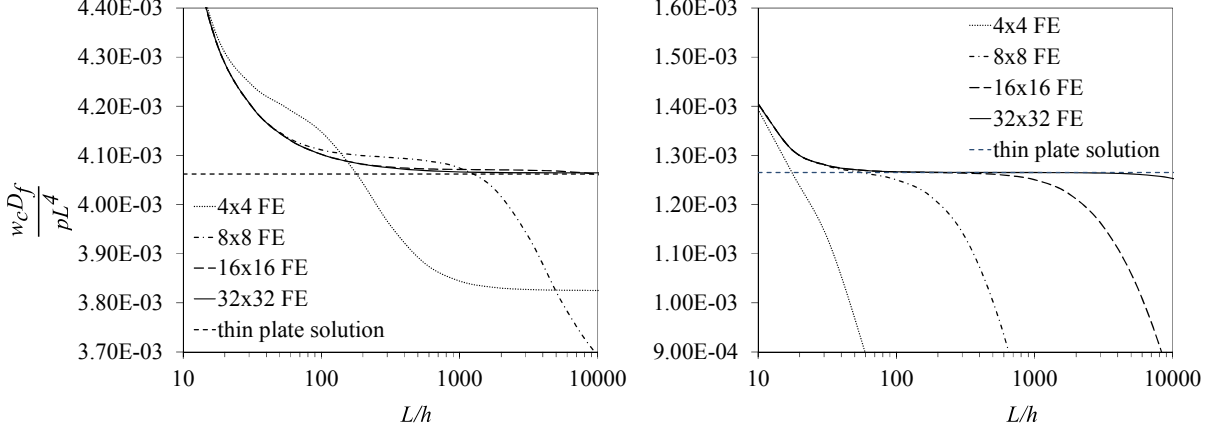


Figure 3.10: Normalised central deflection versus length-to-thickness ratio for given meshes. Left: simply supported plate. Right: clamped-edge plate.

In Appendix C.5² we perform an additional test in order to investigate the performance of the presented element in test configurations involving its response to bending and torsion. The test may be also found in [Jabareen and Rubin \(2008\)](#). It was suggested by Professor M. Rubin (private communication) as a valuable test in the validation of plate elements (see also [Babuška and Scapolla \(1989\)](#)).

3.6.3 Dispersion functions

We consider a narrow infinite strip of Cosserat material in the x_2 -direction, invariant in the x_1 and x_3 directions. The flexural problem of this one-dimensional configuration is governed by the following PDE (Eq.(3.12)):

$$\begin{aligned} \tau_{32,2} - \rho \ddot{u}_3 &= 0 \\ \mu_{12,2} + \tau_{32} - \rho I_1 \ddot{\omega}_1 &= 0. \end{aligned} \quad (3.50)$$

By using the definition of the deformation measures (Eqs.(3.1)-(3.2)) and the constitutive relations (Eq.(3.20)) one obtains:

$$\begin{aligned} F^{3232} [u_{3,2} - \omega_1]_{,2} - \rho \ddot{u}_3 &= 0 \\ D_f^{1212} \omega_{1,22} + F^{3232} [u_{3,2} - \omega_1] - \rho I_{11} \ddot{\omega}_1 &= 0. \end{aligned} \quad (3.51)$$

²This is an additional Appendix that is absent from [Godio et al. \(2015a\)](#).

which has indeed the same structure of that governing the free-vibrations of a Timoshenko beam. Setting:

$$\begin{aligned} u_3 &= Ae^{i(\kappa x_2 + \nu t)} \\ \omega_1 &= Be^{i(\kappa x_2 + \nu t)}, \end{aligned} \quad (3.52)$$

in which κ is the wave number, ν denotes the angular frequency, and A, B are imaginary constants and by substituting Eq.(3.52) into Eq.(3.51), we obtain, in matrix notation:

$$\begin{bmatrix} -F^{3232}\kappa^2 + \rho\nu^2 & -iF^{3232}\kappa \\ iF^{3232}\kappa & -F^{3232} - D_f^{1212}\kappa^2 + I_1\rho\nu^2 \end{bmatrix} \begin{bmatrix} A \\ B \end{bmatrix} = \begin{bmatrix} 0 \\ 0 \end{bmatrix} \quad (3.53)$$

The above system admits non-trivial solutions only when:

$$\kappa^4 - \left(\frac{\rho I_{11}}{D_f^{1212}} + \frac{\rho D_f^{1212}}{F^{3232}} \right) \kappa^2 \nu^2 - \frac{\rho}{D_f^{1212}} \nu^2 + \frac{\rho^2 I_{11}}{F^{3232} D_f^{1212}} \nu^4 = 0. \quad (3.54)$$

The roots of Eq.(3.54) are called dispersion relations and they can be expressed in a form similar to [de Borst and Sluys \(1991\)](#) as follows:

$$\nu_{1,2}(\kappa) = \sqrt{-\frac{\beta(\kappa)}{2\alpha(\kappa)} \pm \sqrt{\left[\frac{\beta(\kappa)}{2\alpha(\kappa)}\right]^2 - \frac{\gamma(\kappa)}{\alpha(\kappa)}}} \quad (3.55)$$

where

$$\begin{aligned} \alpha(\kappa) &= \rho^2 I_1 \\ \beta(\kappa) &= -\left(\rho \kappa^2 I_1 F^{3232} + D_f^{1212} \rho \kappa^2 + F^{3232} \rho \right) \\ \gamma(\kappa) &= D_f^{1212} F^{3232} \kappa^4 \end{aligned} \quad (3.56)$$

Similar to the Timoshenko beam theory, the dispersion relations reveal the two basic oscillation modes of the system. With reference to [Figure 3.11](#) we have: *mode 1*, the micro-rotation mode, describing the pure bending shape, and *mode 2*, the shear deformation mode, representing a shear strain state. The superposition of such modes gives the flexural response of the beam.

The membrane problem of the aforementioned one-dimensional Cosserat configuration is governed by the following PDE:

$$\tau_{22,2} - \rho \ddot{u}_2 = 0. \quad (3.57)$$

By using again Eqs.(3.1)-(3.2) and (3.19), one can rewrite the above equation as:

$$A^{2222} u_{2,22} - \rho \ddot{u}_2 = 0. \quad (3.58)$$

Looking for a solution of the form similar to Eq.(3.52), we obtain the following linear relation:

$$\nu_3(\kappa) = \sqrt{\frac{A^{2222}}{\rho}} \kappa, \quad (3.59)$$

which is associated to a *mode 3* of longitudinal waves.

For validation purposes, we consider as illustrative example a simply supported beam of length L . In such case, the resulting wave numbers are:

$$\kappa_n = \frac{n\pi}{L}, \quad \text{with } n = 1, 2, 3, \dots \quad (3.60)$$

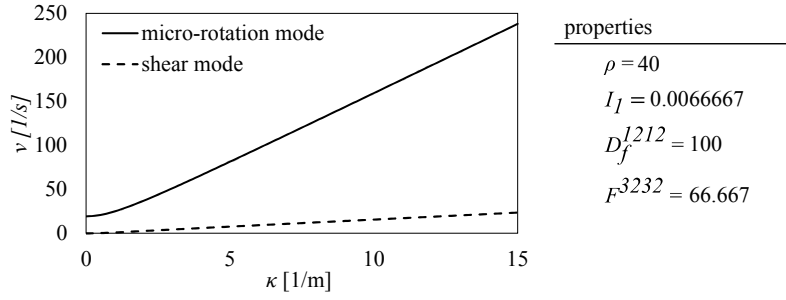


Figure 3.11: Dispersion relations for a one-dimensional Cosserat flexural problem: micro-rotation mode ν_1 and shear strain mode ν_2 .

corresponding to wave lengths:

$$\lambda_n = \frac{2\pi}{\kappa_n} = \frac{2L}{n}, \text{ with } n = 1, 2, 3, \dots \quad (3.61)$$

Once the modal wave numbers are calculated, it is necessary to pass by the dispersion relations (Figure 3.11) to obtain the corresponding natural frequencies.

The beam is discretised by a series of 20, 40, 80 and 160 FE over its length. Natural frequencies are computed by a modal analysis based on Lanczos method and compared with the analytical values indicated above. The relative error committed by the FE in representing the longitudinal vibrations is zero even with the coarsest discretisation. The relative error committed in the evaluation of the first eleven flexural oscillation modes is plotted in Figure 3.12, versus the normalised wave length λ_n/L . A 9-digit precision is used for the wave lengths. The relative error is defined as:

$$\epsilon_n^\lambda = 100 \times \frac{\lambda_n - \lambda_n^{FE}}{\lambda_n}. \quad (3.62)$$

In general, we may note how the convergence to the analytical values is achieved by the COSS8R element upon mesh refinement. As expected, we observe that, for a given discretisation, the relative error decreases for increasing wave lengths. Therefore, a quite fine mesh is needed to extract the highest frequencies from the FE model: a 40-element subdivision is considered acceptable.

3.7 Application to masonry structures

The purpose of this Section is to highlight the practical interest of the above Cosserat FE formulation in view of engineering applications. The case of masonry panels is selected, due to the apparent microstructure of such material. Through illustrative examples, we investigate the performance of the COSS8R element for the prediction of the modal response of masonry panels, considered as equivalent Cosserat plates. In particular, we focus on the specific role played by the drilling rotations.

For the analyses, we adopt the homogenised constitutive law for Cosserat plates proposed by Stefanou et al. (2008). This model is derived by identification of a periodic lattice made of regular rigid building blocks with an equivalent 3D Cosserat continuum. The resulting model is an equivalent micropolar plate with orthotropic properties, which accounts for both the in- and the out-of-plane deformation of masonry in the dynamic regime. For the expression of the

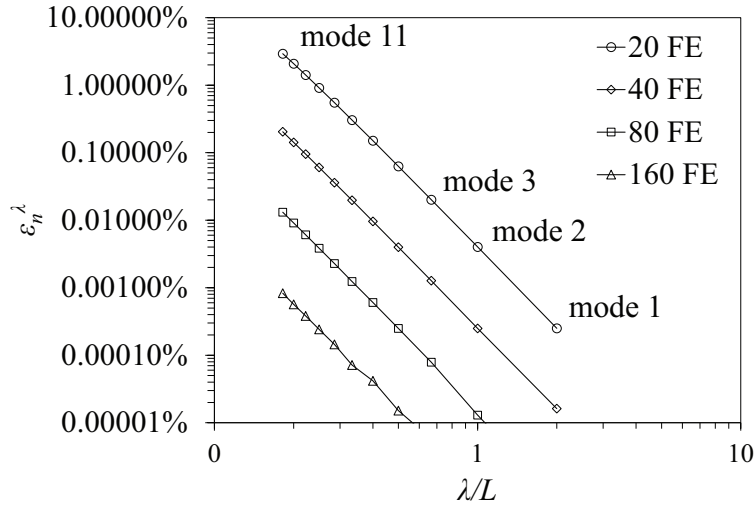


Figure 3.12: Relative error committed in the evaluation of the first eleven flexural wave lengths.

matrices for the constitutive laws and the inertial terms, the reader is referred to the original work (Stefanou et al., 2008).

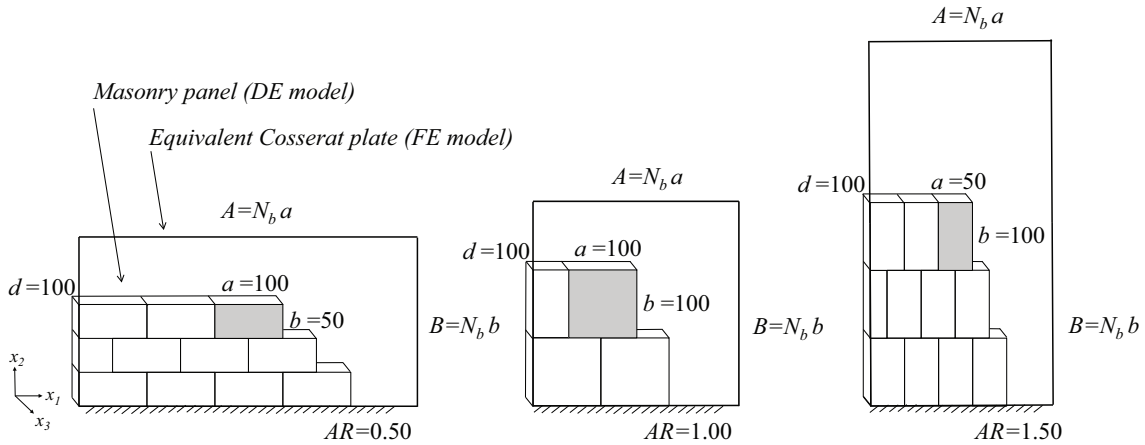


Figure 3.13: The three simulated masonry panels modelled with DE and with equivalent Cosserat plates by the COSS8R element: notation, boundary conditions and aspect ratios $AR = B/A$.

Modal analyses are carried out on plates having 3 different aspect ratios $AR = B/A$ (see Figure 3.13). For each of these three configurations, several simulations are launched by increasing the number of blocks N_b that compose the panels in both the horizontal and the vertical direction. This operation is done simultaneously, so that, for every given simulation, the panel's aspect ratio is kept constant and equal to the blocks' aspect ratio: $B/A = b/a$. The scale ratio, that is defined herein as the ratio between the size of the blocks and the size of the panel, decreases with the inverse of the number of blocks disposed in each direction, i.e. $a/A = b/B = 1/N_b$. On the contrary, the length-to-thickness ratio (representing the slenderness of the panel) increases as $B/d = N_b b/d$ (the thickness of the panel is kept constant). This is exactly equivalent with keeping fixed the overall size of the panel and reducing the size of the blocks, without varying their shape.

3.7.1 Comparison with Discrete Elements solution

The Cosserat homogenised constitutive law for masonry [Stefanou et al. \(2008\)](#) is implemented in the COSS8R element and incorporated in Abaqus through the subroutine UEL. The results produced by FE are compared with those obtained from the use a Discrete Elements (DE) analogue model. This latter is created by means of the numerical package 3DEC (Itasca Consulting Group 2013, [Cundall \(1988\)](#)). The analogue DE model consists in an assemblage of rigid blocks, which are disposed as presented in [Figure 3.13](#). The blocks interact with the adjacent blocks through linear elastic interfaces, that are governed by the same coefficients used in the homogenisation model considered in [Stefanou et al. \(2008\)](#). In this way, the same assumptions are made as far as it concerns the lattice studied by [Stefanou et al. \(2008\)](#), and, consequently, no calibration is needed between the DE and Cosserat FE model.

Modal analyses are carried out on the analogue DE model using the same strategy as described above for the FE model: the number of blocks is progressively increased, while the thickness of the assembled masonry panel is kept constant. It is worth mentioning that, according to [Lemos \(2007a\)](#), a large number of contact-points are required across the thickness of the panel in order to obtain an accurate representation of the out-of-plane behaviour with the DE model. This remarkably increases the calculation cost of the DE model, to FE's advantage, for which a 8x8-FE discretisation is considered sufficient after having performed a mesh convergence analysis (see [Section 3.6.3](#)).

The first in-plane and the first two out-of-plane modes, corresponding respectively to shear, bending and torsion oscillation modes are extracted from the COSS8R (Abaqus) and the DE analogue model (3DEC). The natural frequencies for each mode are compared in [Figure 3.14](#)-[Figure 3.16](#) in function of the number of bundling blocks N_b composing the panel in both directions ([Figure 3.13](#)). We observe that the frequencies provided by FE are slightly lower than those produced by DE, and that, for increasing number of blocks, DE and FE converge.

3.7.2 The role of drilling rotations

In [Fig. 17](#) we present the percentage of the modal effective mass related to the first in-plane deformation mode of the masonry panels. The modal effective mass associated to the horizontal and the vertical translations u_1, u_2 is computed over the element in the following manner ([Simulia 2010](#)):

$$\bar{M}_1 = \frac{(\bar{U}_m^t M^m \Delta_1)^2}{\bar{U}_m^t M^m \bar{U}_m}, \quad \bar{M}_2 = \frac{(\bar{U}_m^t M^m \Delta_2)^2}{\bar{U}_m^t M^m \bar{U}_m}. \quad (3.63)$$

The present Cosserat formulation also allows the calculation of the modal effective moment of inertia over each finite element. This effective inertia is associated to the drilling rotations of the plate ω_3 , through the expression:

$$\bar{J}_3 = \frac{(\bar{\Omega}_m^t \Theta^m \Delta_3)^2}{\bar{\Omega}_m^t \Theta^m \bar{\Omega}_m}. \quad (3.64)$$

In the above, \bar{U}_m and $\bar{\Omega}_m$ denote the in-plane nodal translations and rotations composing the eigenvector associated to the oscillation mode considered. The element mass sub-matrices are calculated according to [Eq.\(3.41\)](#). The vectors Δ_i give the response of every DOF of the element to a unitary motion applied in the i -th direction, which consists in a displacement (for $i = 1, 2$) and in an axis rotation (for $i = 3$). Note that the modal effective masses \bar{M}_1, \bar{M}_2 and the moment of inertia \bar{J}_3 are computed by Abaqus for the whole element discretisation. In

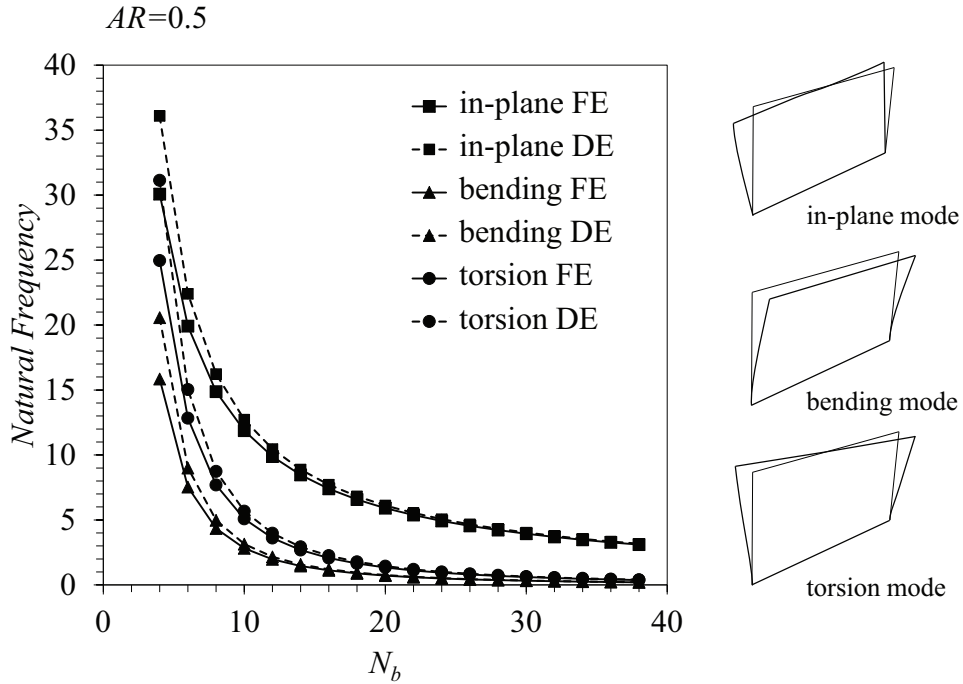


Figure 3.14: Modal frequencies of the masonry panel versus the number of building blocks composing the panel in both directions. Comparison between the results extracted by DE and by the use of the equivalent Cosserat plate model for masonry implemented in a COSS8R FE discretisation. Results for aspect ratio $AR = 0.50$.

Figure 3.17 we present the effective mass and inertia moment normalized, respectively, by the total mass M_{TOT} and the total in-plane moment of inertia J_{TOT} of the plate:

$$M_{TOT} = \rho A B d = \rho N_b^2 a b d$$

$$J_{TOT} = \frac{M_{TOT}}{12} \rho (A^2 + B^2) d = \frac{M_{TOT}}{12} \rho N_b^2 (a^2 + b^2) d.$$

We observe that the amount of the modal inertia that is taken by the drilling rotations for the first in-plane mode increases remarkably with the aspect ratio of the panel and with elongated blocks. In particular, for aspect ratios higher than the unit, this quantity amounts to approximately 50% of the total rotary inertia (see Fig. 17, $AR = 1.50$). The rest of the effective modal mass (until 100%) is covered by other higher frequency membrane modes that are not examined herein. This suggests that the drilling rotations can have a significant participation in the inertial response of masonry panels.

3.8 Conclusions

Nowadays Cosserat Finite Elements find numerous applications in mechanics and engineering. However, the details of the FE formulation are partially exposed in literature or not presented at all, and its performance is seldom investigated. Therefore, it is hard to assess the chosen formulation and to extend its applicability to other problems.

In this paper, a Cosserat dynamic Finite Element formulation for elastic plates has been presented and investigated in a detailed manner. In particular, a quadrilateral element with quadratic interpolation functions for both the displacement and the rotational fields has been

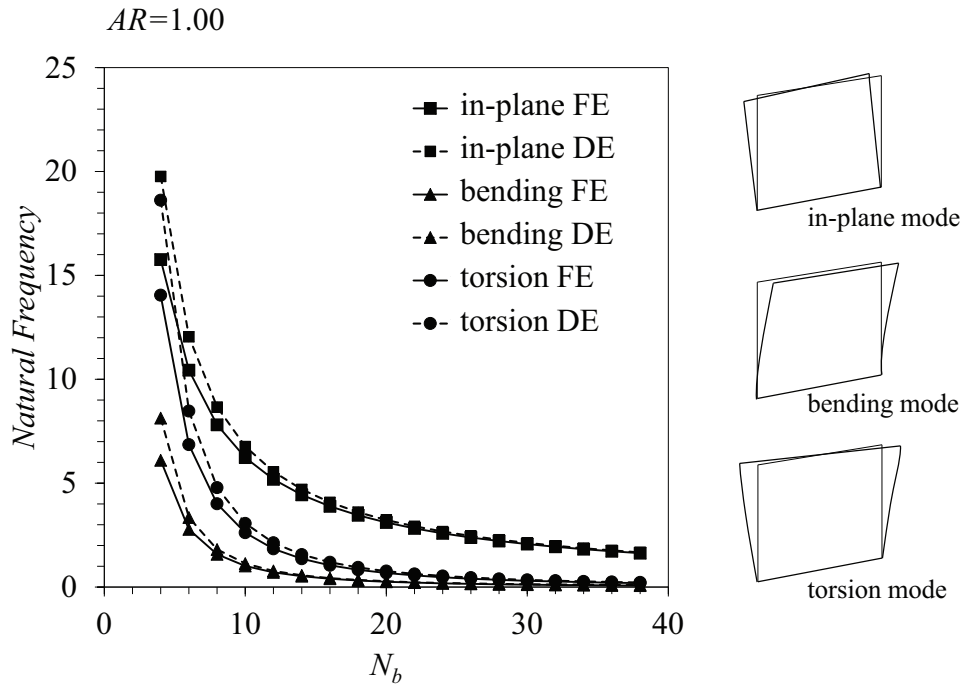


Figure 3.15: Modal frequencies of the masonry panel versus the number of building blocks composing the panel in both directions. Comparison between the results extracted by DE and by the use of the equivalent Cosserat plate model for masonry implemented in a COSS8R FE discretisation. Results for aspect ratio $AR = 1.00$.

proposed and validated through adequate patch tests and benchmarks. It has been demonstrated how, due to the non-symmetry of the stress tensor and the drilling rotation that is inherent to the micropolar continuum, this element has advantageous computational properties when compared to classical formulations. Local matrix deficiencies are not detected in the case of reduced integration, without the use of hourglass control techniques. Cosserat continuum introduces in a physical way the stiffness associated to the drilling rotations, which prevents the hourglass modes to occur and makes the presented formulation suitable for the assemblage of shell structures. The performance of the element in representing the bending behaviour in the limit of thin geometries has been also studied, showing a quite good performance against the shear locking phenomenon. The element has been then validated under dynamic conditions. Wave dispersion has been studied with respect to a Cosserat one-dimensional configuration. The comparison between the results of the numerical model against the theoretical solution has demonstrated the precision of the formulation in modelling in-plane and out-of-plane modal shapes with high frequencies.

The presented Cosserat Finite Element formulation is very general and allows various constitutive laws for materials with micro-structure to be implemented. In order to highlight the practical interest of the formulation, an application has been given, in which a masonry panel made of rigid building blocks with deformable interfaces has been modelled through the validated finite element. The in- and out-of-plane modal response of masonry has been considered, by focusing on the shearing, flexural and torsional oscillation modes of the panel. The role of the micro-structure has been also studied, by modelling panels with various aspect ratios and slenderness. The results from the homogenised Cosserat Finite Element analyses have been juxtaposed to those obtained by the use of an analogue Discrete Elements model, and a good agreement has been found. The role of the drilling rotations has been then assessed, showing

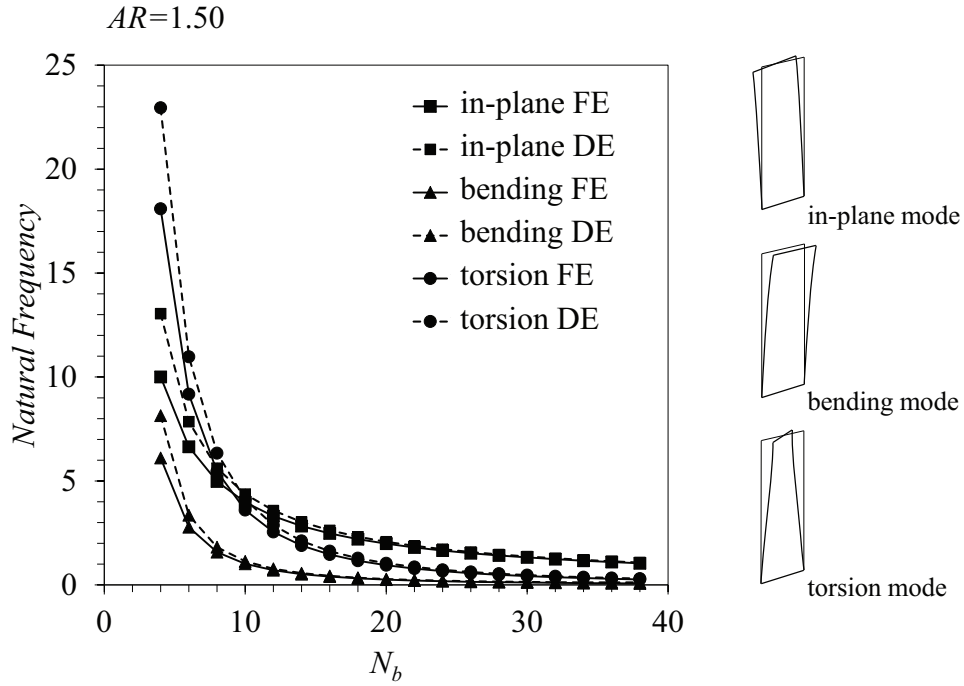


Figure 3.16: Modal frequencies of the masonry panel versus the number of building blocks composing the panel in both directions. Comparison between the results extracted by DE and by the use of the equivalent Cosserat plate model for masonry implemented in a COSS8R FE discretisation. Results for aspect ratio $AR = 1.50$.

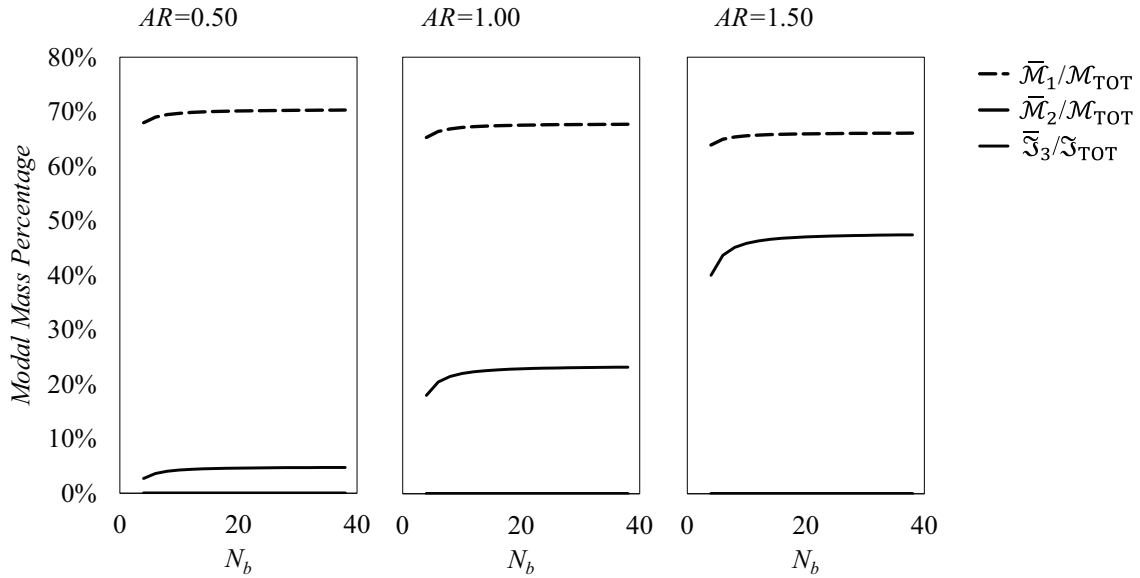


Figure 3.17: Percentage of modal effective masses and moment of inertia for the first in-plane mode of the masonry panel, versus the number of building blocks composing the panel in both directions. The modal masses \bar{M}_1 and \bar{M}_2 are associated to the horizontal and the vertical displacements. The modal moment of inertia \bar{J}_3 is associated to the drilling rotations.

their significant participation to the inertial response of the masonry panels against in-plane seismic excitations.

Chapter 4

Finite element formulation for Cosserat plates: plasticity

This Chapter reports the extension and the validation of the finite element presented in the previous Chapter to the elastoplastic framework. The theory of the multisurface plasticity is implemented for Cosserat plate models. The implementation of this theory is based on a projection algorithm. An important limitation of the classical implementation of the algorithm prevents its use in an efficient way. This limitation is discussed and a solution strategy is proposed. Numerous benchmarks show the element performance in problems involving multiple plastic surfaces, perfect plasticity and strain localisation.

This Chapter is a published paper. Its reference is [Godio et al. \(2016\)](#).

Contents

4.1	Introduction	111
4.2	The Cosserat (or micropolar) plate model	113
4.3	Multisurface plasticity theory for Cosserat materials	115
4.3.1	Further notations	117
4.4	Solution algorithm	118
4.4.1	Solution algorithm for multisurface plasticity	118
4.4.2	Implementation of the Newton-Raphson method in the CPP algorithm	119
4.5	Finite Element formulation	123
4.5.1	Element implementation	123
4.5.2	Derivation of the elastoplastic tangent stiffness matrix for multisurface plasticity	124
4.6	Element validation	126
4.6.1	The micropolar plate element COSS8R	127
4.6.2	Single element tests for multisurface plane plasticity	128
4.6.3	Structural benchmarks for micropolar plates	130
4.7	Conclusions	135

Summary

The macroscopic behaviour of materials is affected by their inner micro-structure. Elementary considerations based on the arrangement, and the physical and mechanical features of the micro-structure may lead to the formulation of elastoplastic constitutive laws, involving hardening/softening mechanisms and non-associative properties. In order to model the non-linear behaviour of micro-structured materials, the classical theory of time-independent multisurface plasticity is herein extended to Cosserat continua. The account for plastic relative strains and curvatures is made by means of a robust quadratic-convergent projection algorithm, specifically formulated for non-associative and hardening/softening plasticity. Some important limitations of the classical implementation of the algorithm for multisurface plasticity prevent its application for any plastic surfaces and loading conditions. These limitations are addressed in this paper, and a robust solution strategy based on the Singular Value Decomposition technique is proposed. The projection algorithm is then implemented into a finite element formulation for Cosserat continua. A specific finite element is considered, developed for micropolar plates. The element is validated through illustrative examples and applications, showing able performance.

4.1 Introduction

Trabecular bones, wood, soils, metals and many other materials existing in nature are provided with an internal micro-structure which is apparent at specific observation scales. The macroscopic response of these materials is therefore affected by the geometrical (characteristic length) and mechanical internal properties of their micro-structure. This holds true for man-made materials and structures such as composites, grid-works, masonry, etc.

An efficient and elegant way to model the overall response of such materials without the need to resort to non-local theories is represented by the Cosserat continuum. With respect to the classical (Cauchy) continuum, the Cosserat (or micropolar) continuum has independent rotational degrees of freedom attached to the material particle. This confers an internal length to the medium, and makes it suitable for the description of micro-structured materials. The additional degrees of freedom also provide a larger set of boundary conditions for the medium. It is well known how the presence of an internal length and the use of additional boundary conditions may affect the material response, especially in the non-linear range. Boundary layers and regions with concentrated irreversible deformation such as shear bands are controlled by internal material lengths (Muhlhaus and Vardoulakis, 1987; Vardoulakis and Sulem, 1995; Sulem et al., 2011). The use of the Cosserat continuum is hence crucial to model complex test configurations of micro-structured materials.

The use of Cosserat continua for representing the macroscopic behaviour of micro-structured materials is well assessed nowadays, at least for what concerns the elastic behaviour (Anderson and Lakes, 1994; Forest and Sab, 1998; Stefanou et al., 2008). Most of the models proposed in the literature are devoted to the formulation of homogenization schemes, i.e. mathematical or numerical procedures through which one can retrieve the micropolar properties of the material by starting from those of its micro-structure. However, there is still a lack of knowledge concerning the modeling of the inelastic behaviour of these materials. In the non-linear range, irreversible, dissipative, time-dependent phenomena relative to the evolution and damage of the material's inner structure occur. In this context, the formulation of models based on micropolar continua seems complicated, if not unfeasible. However, based on elementary considerations and often motivated by micromechanical observations (such as friction and interlocking phenomena in soils, or creep phenomena in cement materials), researchers may be led to the formulation of extended constitutive models for inelasticity. It has been the case, for instance, for the generalised J_2 -plasticity model for soils (Muhlhaus and Vardoulakis, 1987), which has made possible the study and the understanding of complex phenomena such as the localisation of deformation in micro-structured materials (Steinmann and Willam, 1991; de Borst and Sluys, 1991).

In this paper, a numerical solution procedure for the modeling of the elastoplastic behaviour of micro-structured materials is presented in the framework of the Cosserat continuum. Notice that problems related to the non-linear material behaviour always require the use of numerical tools. Concerning plasticity, some have gained recent attention. For instance, one may mention the use of mathematical programming techniques for the solution of incremental elastoplastic problems (Krabbenhøft et al., 2007a,b). Those techniques have been also employed for the solution of limit analysis problems (Makrodimopoulos and Martin, 2006; Bleyer and de Buhan, 2013). The numerical procedure adopted in this paper is based on a projection algorithm, originally formulated for classical hardening-plastic materials by Simo and Taylor (1985). The projection algorithm is a robust quadratic-convergent algorithm which is widely used in finite elements for the solution of elastoplastic boundary value problems. The algorithm is based on a return map, which solves the incremental elastoplastic problem at every increment of the load-path (and point of the model), by assuring the respect of the consistency requirement. The solution will be then found at the projection point of the given increment, falling on the

boundary of the elastic domain of the material (Simo and Taylor, 1985). Herein, we made use of the time-independent version of the projection algorithm. In other words, viscoplastic effects are not considered. In this setting, the most general version of the algorithm for the multisurface plasticity theory is adopted (Simo et al., 1988).

The theory of time-independent multisurface strain hardening plasticity is very general (Simo and Hughes, 1998). It allows to define multiple sets of plastic surfaces, non-associated plastic potentials, and softening/hardening laws of every kind. When interested in computing not only the ultimate (or limit) load, but the whole material response until failure, this theory gives great flexibility to the user in: a) prescribing failure criteria and b) choosing appropriate plastic evolution laws for the material. Nevertheless, the numerical implementation of the multisurface plasticity theory in finite elements suffers from important limitations, which prevent its application for any plastic surfaces and loading conditions. These limitations are explored in this paper, and a solution strategy based on the use of the Singular Value Decomposition (SVD) technique is proposed. This represents an important improvement in the numerical implementation of the algorithm for multisurface plasticity that can be used not only in the framework of the Cosserat continuum theory, but also in more classical finite element formulations.

In this paper, the theory of multisurface plasticity is adapted for Cosserat continua. The onset and the evolution of irreversible deformations within the micro-structured material is here detected in terms of plastic relative strains and curvatures. It is important to note that the use of projection algorithms for plasticity has been already encountered in the frame of the Cosserat continuum theory. Most of the existing works were devoted to the study of strain localisation. As known, the Cosserat continuum provides a natural regularization effect versus the pathological mesh-size-dependency intrinsic to classical numerical formulations. To this purpose, one can see the works of de Borst and co-workers (1991; 1991; 1991; 1993), but also Papanastasiou and Vardoulakis (1992); Li and Tang (2005); Neff et al. (2007), among others. Always in the frame of the Cosserat continuum theory, Addessi (2014) proposed a coupled damage-plastic model for micro-structured materials showing brittle macroscopic behaviour. In that case, a projection algorithm was used to integrate simultaneously the evolution of the plastic and damage variables, see also Steinmann (1995). Another use of the projection algorithm is found in Khoei and Karimi (2008), where an elastoplastic Cosserat model was incorporated into an extended finite element (X-FEM) formulation for the propagation of cracks. Nevertheless, in the aforementioned works it has always been considered a single plastic surface. In the present paper, the novelty is to consider a set of plastic surfaces which are multiple in number, of general form and intersecting. One example of Cosserat multisurface plasticity has been given by Godio et al. (2014), where an application to masonry structures is proposed as an extension to more classical approaches based on the Cauchy continuum (Stefanou et al., 2015).

The multisurface plasticity theory is here implemented into a Cosserat finite element and therefore incorporated within an implicit time-integration scheme for the non-linear analysis of micro-structured materials. A Newton-Raphson iterative method is employed for the solution of the elastoplastic problem both at the local level, i.e. on the integration point of the element, and at the global (element) level. At the local level, the Newton's method is used in conjunction with the SVD matrix inversion technique. This enables the projection algorithm to attain all the features of the multisurface plasticity theory, i.e. the definition of an unlimited number of plastic surfaces and potentials of general form. At the global level, the method requires the implementation of the algorithmic version of the elastoplastic stiffness tangent matrix in order to assess the full rate of convergence. The finite element that we use is a 8-node quadrilateral, that accommodates small displacements and small rotations at every node (Godio et al., 2015a). The element is formulated for a Cosserat (or micropolar) plate model (Eringen, 1967; Green et al., 1968). Such model enables the analysis of materials and structures with an inner

micro-structure mainly developed in two directions. Although this may certainly represent a simplification with respect to the three-dimensional case, a plate model allows the representation of complex spatial configurations in a quite refined way, with the advantage of being much less computational demanding. To this purpose, notice that the plate element is stress resultant, which means that no integration over the thickness is made. Moreover, small deflections and small angle approximations are involved in the formulation. In this sense, we are not dealing with a geometrically exact plate formulation.

The paper is structured as follows. [Section 4.2](#) provides basic background in Cosserat (or micropolar) plate models. In [Section 4.3](#) we present the multisurface plasticity theory for micro-structured materials within the frame of the Cosserat continuum. In this case, we will make use of general notations. In [Section 4.4](#) the projection algorithm is described, and details on the implementation of the plasticity theory in finite elements are provided in [Section 4.5](#). Finally in [Section 4.6](#) we focus more specifically on the micropolar plate element. We present numerical tests for the assessment of the projection algorithm accuracy and benchmarks for the validation and the actual use of the element. These benchmarks concern both the in-plane (or membrane) and the out-of-plane (or flexural) behaviour of the element. It is worth noticing that numerical benchmarks for Cosserat (multisurface) plasticity are nearly absent in literature. Those proposed in [Section 4.6](#) prove then useful for the validation of all kind of algorithms and finite elements formulated for micropolar plasticity. The benchmarks for the in-plane behaviour, in particular, apply for 2D Cosserat continua.

Matrix notation is adopted throughout the paper. We use symbol $d[\]$ to indicate an increment between two successive load steps, and $[\]^t$ to denote time derivative. Symbol $\partial_{\mathbf{v}}[\]$ is used for vector derivative.

4.2 The Cosserat (or micropolar) plate model

The Cosserat continuum (or micropolar) theory differs from the classical theory of the Cauchy continuum in two aspects ([Eringen, 1999](#)). First, the couple-stress is completely absent in the Cauchy continuum. Second, in the Cosserat continuum the stress tensor is not symmetric, as consequence of the couple-stresses. [Figure 4.1](#) shows the stresses and couple-stresses featuring in a micropolar plate model ([Godio et al., 2015a; Eringen, 1967](#)). The former are assembled in the vector $\boldsymbol{\tau}$ and the latter are contained into the polar vector $\boldsymbol{\mu}$:

$$\begin{aligned}\boldsymbol{\tau} &= \left[\tau_{11} \ \tau_{22} \ \tau_{12} \ \tau_{21} \ \tau_{13} \ \tau_{31} \ \tau_{23} \ \tau_{32} \right]^t \\ \boldsymbol{\mu} &= \left[\mu_{11} \ \mu_{22} \ \mu_{12} \ \mu_{21} \ \mu_{31} \ \mu_{32} \right]^t.\end{aligned}\tag{4.1}$$

As far as it concerns the membrane (or in-plane) behaviour ([Figure 4.1-left](#)), one recognizes: the in-plane tractions (τ_{11}, τ_{22}), the membrane shears (τ_{12}, τ_{21}) and the in-plane couple-stresses (μ_{31}, μ_{32}). These stress measures are those of 2D Cosserat continuum. In addition one has the components controlling the flexural (or out-of-plane) behaviour of the plate ([Figure 4.1-right](#)), namely: the torsions (μ_{11}, μ_{22}), the out-of-plane flexions (μ_{12}, μ_{21}), the transverse shears (τ_{31}, τ_{32}), and the longitudinal shears (τ_{13}, τ_{23}). Due to the presence of transverse shears, the micropolar plate model can be regarded as a thick plate theory. Its convergence towards the thin plate solution has been numerically assessed by [Godio et al. \(2015a\)](#).

The associated deformation measures of the plate are denoted with $\boldsymbol{\gamma}$ and $\boldsymbol{\kappa}$ and are:

$$\begin{aligned}\boldsymbol{\gamma} &= \left[\gamma_{11} \ \gamma_{22} \ \gamma_{12} \ \gamma_{21} \ \gamma_{13} \ \gamma_{31} \ \gamma_{23} \ \gamma_{32} \right]^t \\ \boldsymbol{\kappa} &= \left[\kappa_{11} \ \kappa_{22} \ \kappa_{12} \ \kappa_{21} \ \kappa_{31} \ \kappa_{32} \right]^t\end{aligned}\tag{4.2}$$

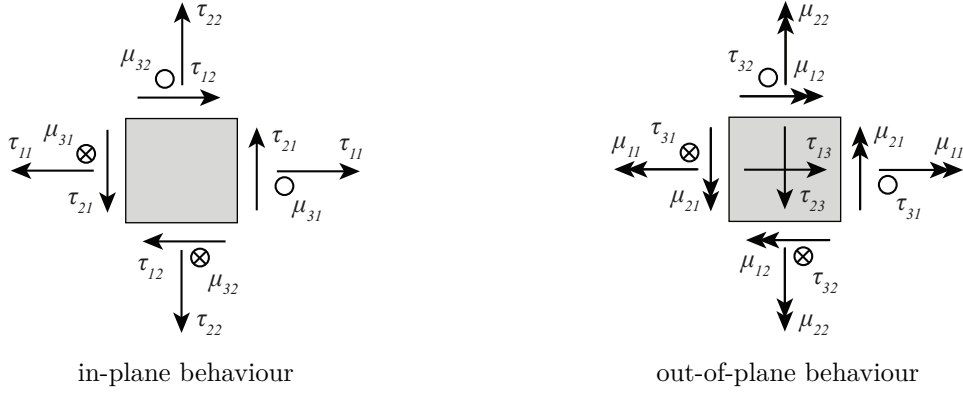


Figure 4.1: Stresses and couple-stresses of a Cosserat plate.

In particular one has: the in-plane extensions/compressions (γ_{11}, γ_{22}), the membrane shear strains (γ_{12}, γ_{21}) and the in-plane curvatures (κ_{31}, κ_{32}). Moreover, one has to take into account the out-of-plane curvatures, as the torsion deformations (κ_{11}, κ_{22}) and the bending deformations (κ_{12}, κ_{21}), together with the transverse and longitudinal shear strains, respectively (γ_{31}, γ_{32}) and (γ_{13}, γ_{23}).

The deformation measures are derived from the kinematics of the plate, which consists of 3 displacements, indicated with \mathbf{u} , and 3 rotations about the orthogonal axis, called Cosserat rotations $\boldsymbol{\omega}^c$:

$$\begin{aligned} \mathbf{u} &= [u_1 \quad u_2 \quad u_3]^t \\ \boldsymbol{\omega}^c &= [\omega_1^c \quad \omega_2^c \quad \omega_3^c]^t. \end{aligned} \quad (4.3)$$

For plates under small deflections and rotations, one defines the relative strain vector $\boldsymbol{\gamma}$ as (Steinmann and Willam, 1991):

$$\boldsymbol{\gamma} = \nabla \mathbf{u} + \mathbf{e} \cdot \boldsymbol{\omega}^c, \quad \gamma_{ij} = u_{i,j} + e_{ijk} \omega_k^c \quad (4.4)$$

and the curvature vector as:

$$\boldsymbol{\kappa} = \nabla \boldsymbol{\omega}^c, \quad \kappa_{ij} = \omega_{i,j}^c. \quad (4.5)$$

In these expressions, ∇ is the gradient operator and \mathbf{e} (or e_{ijk}) is the permutation symbol.

Dealing with finite elements, it is useful to express the balance equations in weak form. Herein, we make use of the virtual work principle on a region of the plate A and its boundary ∂A . Following the vector form introduced above and indicating a virtual variation by $\delta[\]$, the principle reads:

$$\mathbf{R} - \mathbf{P} - \mathbf{Q} = 0, \quad (4.6)$$

where:

$$\mathbf{R} = \int_A (\boldsymbol{\tau}^t \delta \boldsymbol{\gamma} + \boldsymbol{\mu}^t \delta \boldsymbol{\kappa}) \, dA \quad (4.7)$$

is the work of the stresses and couple-stresses,

$$\mathbf{P} = \int_A (\mathbf{b}^t \delta \mathbf{u} + \mathbf{l}^t \delta \boldsymbol{\omega}^c) \, dA + \int_{\partial A} (\mathbf{T}^t \delta \mathbf{u} + \mathbf{M}^t \delta \boldsymbol{\omega}^c) \, dA \quad (4.8)$$

is the work done respectively by the body forces \mathbf{b} and couples \mathbf{l} and the traction \mathbf{T} and moment \mathbf{M} on the boundary, and

$$Q = \int_A \left(\rho \dot{\mathbf{u}}^t \delta \mathbf{u} + \rho \ddot{\boldsymbol{\omega}}^{ct} \mathbf{I} \delta \boldsymbol{\omega}^c \right) dA \quad (4.9)$$

is the work due to the inertial mass ρ and second order moment \mathbf{I} .

4.3 Multisurface plasticity theory for Cosserat materials

The time-independent theory of non-smooth multisurface hardening plasticity is presented in this section. This theory, which was formerly formulated for simple (or Cauchy) materials in its original version (Vermeer and de Borst, 1984) and then extended for the computation of multiple yield surfaces (Simo et al., 1988; Simo and Hughes, 1998), is here used in the framework of the Cosserat continuum theory.

Proceeding in general fashion and adopting incremental notation, relative strains (4.4) and curvatures (4.5) can be assembled into a general total strain vector $d\boldsymbol{\varepsilon}$, defined as follows:

$$d\boldsymbol{\varepsilon} = \begin{bmatrix} d\boldsymbol{\gamma} & d\boldsymbol{\kappa} \end{bmatrix}^t. \quad (4.10)$$

Similarly, the stresses and the couple-stresses can be assembled into a general stress vector $d\boldsymbol{\sigma}$:

$$d\boldsymbol{\sigma} = \begin{bmatrix} d\boldsymbol{\tau} & d\boldsymbol{\mu} \end{bmatrix}^t. \quad (4.11)$$

The formulation (and the implementation) of the plasticity theory for Cosserat materials is obtained in a way similar to that followed for Cauchy materials (de Borst, 1991). By means of the additive decomposition, the vector of the total (small) strains is divided into the elastic $[\]^e$ and plastic $[\]^p$ parts:

$$d\boldsymbol{\varepsilon} = d\boldsymbol{\varepsilon}^e + d\boldsymbol{\varepsilon}^p. \quad (4.12)$$

The elastic response of the material is governed by the general linear constitutive law, relating stresses and couple-stresses to the elastic strain increment:

$$d\boldsymbol{\sigma} = \mathbf{C} [d\boldsymbol{\varepsilon} - d\boldsymbol{\varepsilon}^p], \quad (4.13)$$

where \mathbf{C} is the matrix of the elastic moduli. Dealing with an incremental problem, it is also useful to express the stresses as a function of the total strains:

$$d\boldsymbol{\sigma} = \mathbf{C}^{ep} d\boldsymbol{\varepsilon} \quad (4.14)$$

where \mathbf{C}^{ep} is now the matrix of the elastoplastic tangent moduli.

The hardening/softening variables are introduced in similar way. These are defined by $\boldsymbol{\alpha}$, and its dual \mathbf{q} . The former may be considered as a deformation measure, while the latter as a stress measure. Their relation is based on the definition of \mathbf{D} , the matrix of the hardening moduli:

$$d\mathbf{q} = -\mathbf{D}d\boldsymbol{\alpha}. \quad (4.15)$$

It follows the definition of generalised strains and stresses, useful for the sequel, respectively given by the couples $(\boldsymbol{\varepsilon}; \boldsymbol{\alpha})$ and $(\boldsymbol{\sigma}; \mathbf{q})$.

The salient feature of the multisurface plasticity theory lies on the definition of the elastic domain. Denoted with \mathbb{E}_σ , the elastic domain is defined as the convex region of the generalised stress space bounded by multiple N_F plastic surfaces $F^\beta(\boldsymbol{\sigma}; \mathbf{q})$ (Simo et al., 1988):

$$\mathbb{E}_\sigma = \left\{ (\boldsymbol{\sigma}; \mathbf{q}) \mid F^\beta(\boldsymbol{\sigma}; \mathbf{q}) \leq 0, \forall \beta \in [1, \dots, N_F] \right\} \quad (4.16)$$

These surfaces represent the prescribed material yield loci (or yield criteria). They are smooth, but intersect in *non-smooth* manner (Figure 4.2). The boundary of \mathbb{E}_σ is:

$$\partial\mathbb{E}_\sigma = \left\{ (\boldsymbol{\sigma}; \mathbf{q}) \mid F^\beta(\boldsymbol{\sigma}; \mathbf{q}) = 0, \forall \beta \in [1, \dots, N_F] \right\}. \quad (4.17)$$

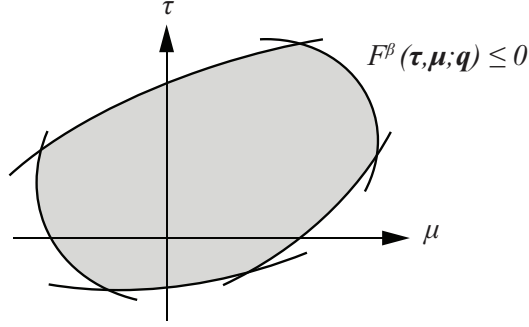


Figure 4.2: Schematic representation of the elastic domain of a Cosserat continuum. According to the multisurface plasticity theory, it is a convex region in the generalised stress space $(\boldsymbol{\tau}, \boldsymbol{\mu}; \mathbf{q})$ defined by multiple yield criteria.

Non-associative plasticity requires the definition of plastic potentials $G^\beta(\boldsymbol{\sigma}; \mathbf{q})$, and hardening/softening functions $H^\beta(\boldsymbol{\sigma}; \mathbf{q})$. Through these, one formulates the equations of evolution. On one hand, the flow rule defines the plastic strain increment:

$$d\boldsymbol{\varepsilon}^p = \sum_{\beta=1}^{N_F} \dot{\lambda}^\beta \partial_{\boldsymbol{\sigma}} G^\beta(\boldsymbol{\sigma}; \mathbf{q}). \quad (4.18)$$

On the other hand, the hardening law controls the increment of the hardening variables:

$$d\boldsymbol{\alpha} = \sum_{\beta=1}^{N_F} \dot{\lambda}^\beta \partial_{\mathbf{q}} H^\beta(\boldsymbol{\sigma}; \mathbf{q}). \quad (4.19)$$

The plastic multipliers $\dot{\lambda}^\beta$ give the magnitude of the plastic strain increment and, by extension, that of the hardening variables. They must respect the following restrictions, namely a) the complementary conditions:

$$F^\beta(\boldsymbol{\sigma}; \mathbf{q}) \leq 0, \quad \dot{\lambda}^\beta \geq 0, \quad \dot{\lambda}^\beta F^\beta(\boldsymbol{\sigma}; \mathbf{q}) = 0, \quad (4.20)$$

and b) the consistency requirement:

$$\dot{\lambda}^\beta dF^\beta(\boldsymbol{\sigma}; \mathbf{q}) = 0. \quad (4.21)$$

The above restrictions are written for the N_{act} activated surfaces, with $N_{act} \leq N_F$. They allow one to determine whether the material response to loading will be elastic or elastoplastic. In the presence of multiple surfaces, this is a central task in the formulation of the algorithm for plasticity. The unloading response is considered elastic, and not affected by damage (cf. Addessi (2014)).

4.3.1 Further notations

The multisurface plasticity theory requires, especially in its algorithmic version, a large number of variables and indices. When used in conjunction with the Cosserat continuum theory, notation may become quite complicated. Vector notation has already been introduced. From now on, it is convenient to introduce the following additional notations.

The set of plastic surfaces, plastic potential and hardening/softening functions will be indicated in the following vector form:

$$\mathbf{F} = \begin{bmatrix} F^1 \\ \vdots \\ F^{N_F} \end{bmatrix}, \quad \mathbf{G} = \begin{bmatrix} G^1 \\ \vdots \\ G^{N_F} \end{bmatrix}, \quad \mathbf{H} = \begin{bmatrix} H^1 \\ \vdots \\ H^{N_F} \end{bmatrix}. \quad (4.22)$$

In turn, functions \mathbf{F} , \mathbf{G} and \mathbf{H} will have gradients given by:

$$\nabla_{\boldsymbol{\sigma}} \mathbf{F} = \begin{bmatrix} \partial_{\boldsymbol{\sigma}} F^1 & \dots & \partial_{\boldsymbol{\sigma}} F^{N_F} \end{bmatrix} = \begin{bmatrix} \partial_{\tau_{11}} F^1 & \dots & \partial_{\tau_{11}} F^{N_F} \\ \vdots & & \vdots \\ \partial_{\mu_{32}} F^1 & \dots & \partial_{\mu_{32}} F^{N_F} \end{bmatrix} \quad (4.23)$$

$$\nabla_{\boldsymbol{\sigma}} \mathbf{G} = \begin{bmatrix} \partial_{\boldsymbol{\sigma}} G^1 & \dots & \partial_{\boldsymbol{\sigma}} G^{N_F} \end{bmatrix} = \begin{bmatrix} \partial_{\tau_{11}} G^1 & \dots & \partial_{\tau_{11}} G^{N_F} \\ \vdots & & \vdots \\ \partial_{\mu_{32}} G^1 & \dots & \partial_{\mu_{32}} G^{N_F} \end{bmatrix}, \quad (4.24)$$

and:

$$\nabla_{\mathbf{q}} \mathbf{F} = \begin{bmatrix} \partial_{\mathbf{q}} F^1 & \dots & \partial_{\mathbf{q}} F^{N_F} \end{bmatrix} = \begin{bmatrix} \partial_{q_1} F^1 & \dots & \partial_{q_1} F^{N_F} \\ \vdots & & \vdots \\ \partial_{q_{N_q}} F^1 & \dots & \partial_{q_{N_q}} F^{N_F} \end{bmatrix} \quad (4.25)$$

$$\nabla_{\mathbf{q}} \mathbf{H} = \begin{bmatrix} \partial_{\mathbf{q}} H^1 & \dots & \partial_{\mathbf{q}} H^{N_F} \end{bmatrix} = \begin{bmatrix} \partial_{q_1} H^1 & \dots & \partial_{q_1} H^{N_F} \\ \vdots & & \vdots \\ \partial_{q_{N_q}} H^1 & \dots & \partial_{q_{N_q}} H^{N_F} \end{bmatrix}. \quad (4.26)$$

Second derivatives of \mathbf{G} and \mathbf{H} will be the third-order tensors:

$$\begin{aligned} \nabla_{\boldsymbol{\sigma}\boldsymbol{\sigma}}^2 \mathbf{G} &= \begin{bmatrix} \nabla_{\boldsymbol{\sigma}\boldsymbol{\sigma}}^2 G^1 & \dots & \nabla_{\boldsymbol{\sigma}\boldsymbol{\sigma}}^2 G^{N_F} \end{bmatrix} \\ \nabla_{\mathbf{q}\mathbf{q}}^2 \mathbf{H} &= \begin{bmatrix} \nabla_{\mathbf{q}\mathbf{q}}^2 H^1 & \dots & \nabla_{\mathbf{q}\mathbf{q}}^2 H^{N_F} \end{bmatrix}. \end{aligned} \quad (4.27)$$

Similarly, the plastic multipliers will be assembled into the following vector:

$$\dot{\boldsymbol{\Lambda}} = \begin{bmatrix} \dot{\lambda}^1 \\ \vdots \\ \dot{\lambda}^{N_F} \end{bmatrix}. \quad (4.28)$$

With a notation of this type, expressions for multisurfaces plasticity can be recast in a simplified form. For example, the flow rule (Eq.(4.18)) reads:

$$d\boldsymbol{\varepsilon}^p = \nabla_{\boldsymbol{\sigma}} \mathbf{G} \cdot \dot{\boldsymbol{\Lambda}}.$$

4.4 Solution algorithm

4.4.1 Solution algorithm for multisurface plasticity

The elastoplastic problem is incremental, since the elastoplastic solution is in general stress-path dependent. Therefore an iterative solution scheme must be introduced. Herein, an implicit (backward-Euler) Closest-Point-Projection (CPP) solution algorithm is adopted.

The CPP algorithm (Simo and Taylor, 1985) is probably the most employed method in elastoplasticity. Its use for the multisurface plasticity (Simo et al., 1988) is based on a return map, which solves the incremental elastoplastic problem (given by Eqs.(4.12),(4.13),(4.15),(4.18) and (4.19)) and fulfills the restrictions (4.20)-(4.21). In this algorithm, the plastic multipliers play an essential role, since they control the loading/unloading conditions and allow to determine the set of activated plastic surfaces by means of a backward procedure. According to Simo et al. (1988), two procedures may be used for the determination of the set of active surfaces (see also Simo and Hughes (1998), Ch.V, p.212). *Procedure 1* consists in solving the incremental elastoplastic problem by holding fixed the set of active surfaces during the iterative process and checking Eq.(4.20) then. In *Procedure 2*, the set of active surfaces is updated during the iterative process, by enforcing Eq.(4.20) at every iteration. Herein we make use of the *Procedure 1*. It is in fact more robust than the *Procedure 2*, even though it is slightly more demanding from a computational point of view (Simo and Kennedy, 1992; Dujc and Brank, 2012).

The algorithm consists of the following steps (Figure 4.3):

- (1) Increments of the displacement $d\mathbf{u}_{n+1}$ and Cosserat rotation fields $d\boldsymbol{\omega}_{n+1}^c$ are given for the generic load step $(n+1)$. These fields are contained in a single vector $d\mathbf{s}_{n+1}$.
- (2) Total strain increments $d\boldsymbol{\varepsilon}_{n+1}$ (relative strains and curvatures) are computed through Eq.(4.4)-(4.5).
- (3) An elastic solution is predicted as trial $[]^T$ solution:

$$\begin{cases} \boldsymbol{\varepsilon}_{n+1}^{eT} = \boldsymbol{\varepsilon}_n^e + d\boldsymbol{\varepsilon}_{n+1} \\ \boldsymbol{\varepsilon}_{n+1}^{pT} = \boldsymbol{\varepsilon}_n^p \\ \boldsymbol{\alpha}_{n+1}^T = \boldsymbol{\alpha}_n \\ \boldsymbol{\sigma}_{n+1}^T = \mathbf{C}\boldsymbol{\varepsilon}_{n+1}^{eT} \\ \mathbf{q}_{n+1}^T = -\mathbf{D}\boldsymbol{\alpha}_{n+1}^T \\ \mathbf{F}_{n+1}^T = \mathbf{F}(\boldsymbol{\sigma}_{n+1}^T; \mathbf{q}_{n+1}^T). \end{cases} \quad (4.29)$$

In this phase all the N_F plastic surfaces F^β can be potentially activated ($N_{act} = N_F$).

- (4) Plastic surfaces are checked (yield criteria).
- (5) If the trial state $(\boldsymbol{\sigma}_{n+1}^T; \mathbf{q}_{n+1}^T)$ falls inside the elastic domain \mathbb{E}_σ , i.e.:

$$F^\beta \leq 0, \forall \beta \in [1, \dots, N_F], \quad (4.30)$$

then the trial solution is retained as the solution for the step (elastic increment).

- (6) If at least one of the surfaces is activated, i.e.:

$$F^\beta > 0, \forall \beta \in [1, \dots, N_{act}], \quad (4.31)$$

then an elastoplastic increment occurs, and the trial state needs to be corrected. A notable feature of the multisurface plasticity theory is that, when several surfaces are

activated, condition (4.31) does not necessarily imply that $\dot{\lambda}^\beta > 0$ for all the activated surfaces (Eq.(4.20)-2). *Procedure 1* consists then in a) solving the incremental elastoplastic problem, here reported as:

$$\begin{cases} \boldsymbol{\sigma}_{n+1} = \mathbf{C} [\boldsymbol{\varepsilon}_{n+1} - \boldsymbol{\varepsilon}_{n+1}^p] \\ \mathbf{q}_{n+1} = -\mathbf{D}\boldsymbol{\alpha}_{n+1} \\ \boldsymbol{\varepsilon}_{n+1}^p = \boldsymbol{\varepsilon}_n^p + \nabla_{\boldsymbol{\sigma}} \mathbf{G}_{n+1} \cdot \dot{\boldsymbol{\Lambda}}_{n+1} \\ \boldsymbol{\alpha}_{n+1} = \boldsymbol{\alpha}_n + \nabla_{\mathbf{q}} \mathbf{H}_{n+1} \cdot \dot{\boldsymbol{\Lambda}}_{n+1} \\ \mathbf{F}_{n+1} = 0, \end{cases} \quad (4.32)$$

by holding fixed the set of the activated surfaces, and b) checking the solution by testing condition (4.20)-2.

- (7) Surfaces for which condition (4.20)-2 is not satisfied (non-positive plastic multiplier) are dropped from the set of the activated plastic surfaces and a new trial solution is demanded:
(3) \leftarrow (7), with $N_{act} \leq N_F$.
- (8) If condition (4.20)-2 is satisfied for all the surfaces, the algorithm has converged to the elastoplastic solution.

4.4.2 Implementation of the Newton-Raphson method in the CPP algorithm

The elastoplastic problem (4.32) is solved at every increment (n) by employing a classical (or full) Newton-Raphson iterative method. Generally speaking, the method consists in, given a set of equations of the type $\mathbf{r}(\boldsymbol{\zeta}) - \mathbf{p} = 0$, solving the equations iteratively, by replacing them at every increment with the linear approximation:

$$\mathbf{r}^{(k+1)} - \mathbf{p} \approx \mathbf{r}^{(k)} + \partial_{\boldsymbol{\zeta}} \mathbf{r}^{(k)} (\boldsymbol{\zeta}^{(k+1)} - \boldsymbol{\zeta}^{(k)}) - \mathbf{p} = 0. \quad (4.33)$$

In the above, $\mathbf{r}^{(k)} = \mathbf{r}(\boldsymbol{\zeta}^{(k)})$ is the residual vector and $\partial_{\boldsymbol{\zeta}} \mathbf{r}^{(k)}$ is the Jacobian matrix of $\mathbf{r}^{(k)}$. Both quantities are known at the increment (k) and, since \mathbf{p} is constant, the solution for the increment (k + 1) is simply given by:

$$\boldsymbol{\zeta}^{(k+1)} = \boldsymbol{\zeta}^{(k)} - [\partial_{\boldsymbol{\zeta}} \mathbf{r}^{(k)}]^{-1} [\mathbf{r}^{(k)} - \mathbf{p}]. \quad (4.34)$$

Solution of the starting equations is then found when the norm of the updated residual becomes sufficiently small: $\|\mathbf{r}^{(k+1)} - \mathbf{p}\| < TOL_{NR}$. In general, the method converges after a number of iterations which depends on the type of equations being considered.

Referring to the CPP algorithm presented in Section 4.4.1, the residual vector for the incremental elastoplastic problem (4.32) writes:

$$\mathbf{r}^{(k)} = \begin{bmatrix} \mathbf{C}^{-1} \boldsymbol{\sigma}_{n+1}^{(k)} + \nabla_{\boldsymbol{\sigma}} \mathbf{G}_{n+1}^{(k)} \cdot \dot{\boldsymbol{\Lambda}}_{n+1}^{(k)} \\ \mathbf{F}_{n+1}^{(k)} \\ \mathbf{D}^{-1} \mathbf{q}_{n+1}^{(k)} + \nabla_{\mathbf{q}} \mathbf{H}_{n+1}^{(k)} \cdot \dot{\boldsymbol{\Lambda}}_{n+1}^{(k)} \end{bmatrix}, \quad (4.35)$$

where $\mathbf{G}_{n+1}^{(k)} = \mathbf{G}(\boldsymbol{\sigma}_{n+1}^{(k)}; \mathbf{q}_{n+1}^{(k)})$, while the constant vector \mathbf{p} is given by:

$$\mathbf{p} = \begin{bmatrix} \mathbf{C}^{-1} \boldsymbol{\sigma}_{n+1}^T \\ \mathbf{0} \\ \mathbf{D}^{-1} \mathbf{q}_{n+1}^T \end{bmatrix}. \quad (4.36)$$

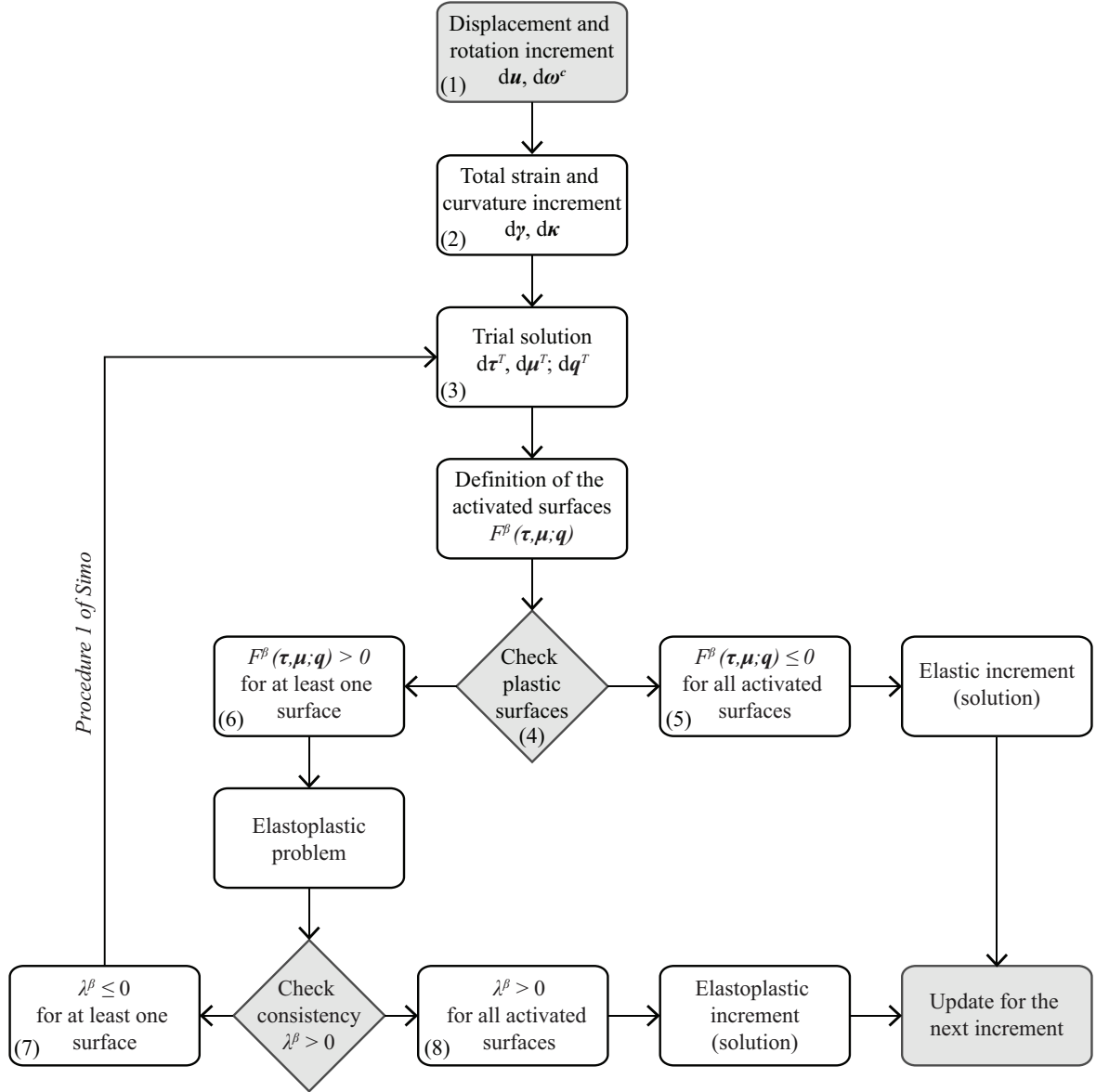


Figure 4.3: Illustration of the Closest-Point-Projection (CPP) algorithm adopted within the multisurface plasticity theory for Cosserat materials.

Notice that the equation $\mathbf{r}^{(k)} - \mathbf{p} = 0$ corresponds exactly with Eqs.(4.32). In particular, the first and the third term of Eq.(4.35)-(4.36) are obtained by replacing the set of generalised deformations $(\boldsymbol{\varepsilon}_{n+1}; \boldsymbol{\alpha}_{n+1})$ in the Eqs.(4.32) with the trial state of the generalised stresses $(\boldsymbol{\sigma}_{n+1}^T; \mathbf{q}_{n+1}^T)$ (Eq.(4.29)). The Jacobian matrix for the incremental elastoplastic problem then writes:

$$\partial_{\zeta} \mathbf{r}^{(k)} = \begin{bmatrix} \mathbf{C}^{-1} + \nabla_{\sigma\sigma}^2 \mathbf{G}_{n+1}^{(k)} \cdot \dot{\boldsymbol{\lambda}}_{n+1}^{(k)} & \nabla_{\sigma} \mathbf{G}_{n+1}^{(k)} & \nabla_{\sigma q}^2 \mathbf{G}_{n+1}^{(k)} \cdot \dot{\boldsymbol{\lambda}}_{n+1}^{(k)} \\ \nabla_{\sigma} \mathbf{F}_{n+1}^{(k)t} & \mathbf{0} & \nabla_q \mathbf{F}_{n+1}^{(k)t} \\ \nabla_{qq}^2 \mathbf{H}_{n+1}^{(k)} \cdot \dot{\boldsymbol{\lambda}}_{n+1}^{(k)} & \nabla_q \mathbf{H}_{n+1}^{(k)} & \mathbf{D}^{-1} + \nabla_{qq}^2 \mathbf{H}_{n+1}^{(k)} \cdot \dot{\boldsymbol{\lambda}}_{n+1}^{(k)} \end{bmatrix}. \quad (4.37)$$

It is important to note that in case of perfect plasticity one can to consider the submatrix formed by taking the block of the first two entries of the matrix (4.37). Similarly, the vectors

$\mathbf{r}^{(k)}$ and \mathbf{p} are reduced to their first two terms. The solution for the (k)-th iteration is given by:

$$\zeta^{(k+1)} = \begin{bmatrix} \boldsymbol{\sigma}_{n+1}^{(k+1)} \\ \dot{\boldsymbol{\lambda}}_{n+1}^{(k+1)} \\ \mathbf{q}_{n+1}^{(k+1)} \end{bmatrix}. \quad (4.38)$$

The Newton-Raphson method is the core of the CPP algorithm: it assures the existence and the accuracy of the elastoplastic solution at each increment (n). The Newton's scheme is initialized at $k = 0$ by injecting the trial state (4.29) into the linearized system (4.33), namely:

$$\zeta^{(0)} = \begin{bmatrix} \boldsymbol{\sigma}_{n+1}^T \\ \mathbf{0} \\ \mathbf{q}_{n+1}^T \end{bmatrix}, \quad (4.39)$$

and:

$$\left[\mathbf{r}^{(0)} - \mathbf{p} \right] = \begin{bmatrix} \mathbf{0} \\ \mathbf{F}_{n+1}^{(0)} \\ \mathbf{0} \end{bmatrix}, \quad (4.40)$$

with $\mathbf{F}_{n+1}^{(0)} > 0$ the vector of the activated surfaces. After this first iteration, the iterative process starts. At each iteration (k), the solution vector for the (k+1)-th iteration is computed according to Eq.(4.34). The residual vector (4.35) is next updated, and its norm is finally checked. Usual conditions for assessing method's convergence towards the elastoplastic solution are (Simo et al., 1988):

$$\begin{aligned} \|\mathbf{F}_{n+1}^{(k+1)}\| &< TOL_1 \\ \|\mathbf{r}^{(k+1)} - \mathbf{p}\| &< TOL_2. \end{aligned} \quad (4.41)$$

At that point, the solution of the elastoplastic problem (4.32) at the increment (n) is presumably found. According to the *Procedure 1* (Figure 4.3), the CPP algorithm requires the plastic multipliers to be *all* positive. If this condition is respected, the elastoplastic solution given by the Newton's method is retained and the iterative scheme is updated for the (n+1)-th successive increment. If not, the procedure is reinitialized within the same increment, but with a new, updated trial state (Figure 4.3).

It is to note that, generally, the convergence of this method to the solution is not always assured but if the first-iteration (or trial) vector $\zeta_{n+1}^{(0)}$ does not differ in norm from the expected solution. This could suggest the user to subdivide the analysis in a number of sufficiently small steps.

LIMITATIONS OF THE NEWTON-RAPHSON METHOD IN THE CPP ALGORITHM

When used within the CPP algorithm, the Newton-Raphson method has some limitations. The limitations derive from the definition of the elastic domain (Eq.(4.16)). According to Simo and Hughes (1998), this domain has finite dimension:

$$\dim \{\mathbb{E}_\sigma\} = N_\sigma + N_q < \infty. \quad (4.42)$$

It follows that each point of the generalised stress space $(\boldsymbol{\sigma}; \mathbf{q})$ belonging to the boundary of the elastic domain $\partial\mathbb{E}_\sigma$ can be intercepted by at most $(N_\sigma + N_q)$ *independent* plastic surfaces,

i.e. surfaces leading to non-redundant constraints (Simo and Hughes, 1998). In fact, if one of these surfaces was not *independent* with the others, the normal vectors $\partial_{\sigma} F^{\beta}$ and $\partial_q F^{\beta}$ would become linearly dependent. The consequence thereof is that matrices $\nabla_{\sigma} \mathbf{F}$ and $\nabla_q \mathbf{F}$ and the Jacobian matrix (4.37) would become singular. In this case, the use of standard matrix inversion techniques in Eq.(4.34) would be ineffective and convergence of the Newton's iterative process would not be achieved.

Figure 4.4 shows two distinct configurations leading to singular Jacobian matrix. For illustration purposes, perfect plasticity is chosen and only two components of the stress tensor are kept, i.e. $(\sigma_{11}, \sigma_{22})$. In this case, $N_{\sigma} = 2, N_q = 0$. In the first example (Figure 4.4-left), 3 surfaces enclose the elastic domain. Therefore $N_F > (N_{\sigma} + N_q)$. Consequently, the projection of the trial stress $d\sigma^T$ at the point of intersection would cause Jacobian matrix singularity at the first Newton's iteration. In the second example (Figure 4.4-right), only 2 surfaces are defined ($N_F = 2$), but the normals to the surfaces are pointwise coincident. In this case the criteria are clearly redundant. The Jacobian matrix would be then rank deficient, and the Newton's process would newly stop.

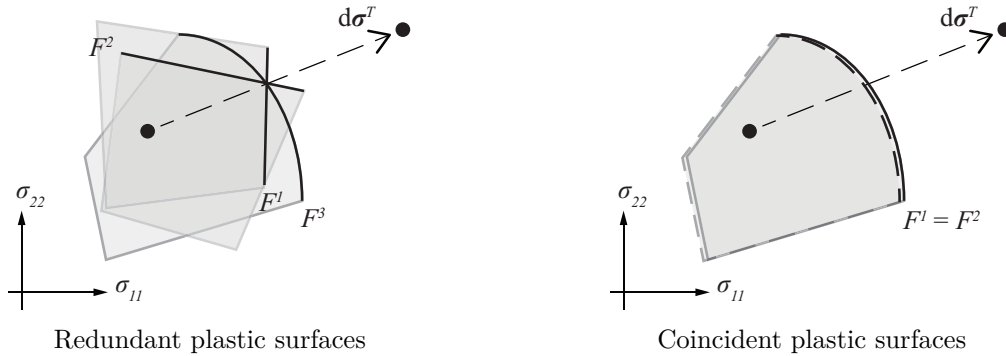


Figure 4.4: Two possible configurations for which Jacobian matrix is singular for perfect plasticity.

Both examples are admissible from a physical point of view, and the CPP algorithm should not fail in cases like these. In order to overcome this numerical inefficiency intrinsic to the Newton-Raphson method, and to enable the projection algorithm to fully attain all the features of the multisurface plasticity theory, the Singular Value Decomposition (SVD) technique is adopted in the present formulation for the inversion of the Jacobian matrix in Eq.(4.34). This technique is general and robust. In this context, it allows the definition of a theoretically unlimited number of yield criteria, plastic potentials and hardening/softening laws of every form. The next Section briefly outlines the SVD technique.

IMPLEMENTATION OF THE SINGULAR VALUE DECOMPOSITION TECHNIQUE IN THE NETWTON-RAPHSON METHOD FOR THE CCP ALGORITHM

The Singular Value Decomposition (or SVD) is a technique allowing to compute the pseudo-inverse of a rectangular matrix. Here we use the algorithm based on this technique, presented in Press et al. (1992).

The method consists in factorizing a generic rectangular $[M \times N]$ matrix \mathbf{A} as the inner product between three matrices, namely \mathbf{U} , \mathbf{V} and $\mathbf{\Lambda}$, as follows:

$$\mathbf{A} = \mathbf{U} \mathbf{\Lambda} \mathbf{V}^t. \quad (4.43)$$

\mathbf{U} and \mathbf{V} are two orthogonal $[M \times M]$ and $[N \times N]$ square matrices, respectively. The columns of \mathbf{U} are computed as the eigenvectors of the inner product $\mathbf{A}\mathbf{A}^t$, whereas the columns of \mathbf{V} are computed as the eigenvectors of the product $\mathbf{A}^t\mathbf{A}$. $\mathbf{\Lambda}$ is a $[M \times N]$ diagonal, positive definite matrix containing a_i , the non-negative singular values of \mathbf{A} (the singular values are the square root of the eigenvalues). Under this form, the computation of the inverse of \mathbf{A} reduces to:

$$\mathbf{A}^{-1} = \mathbf{V}\mathbf{\Lambda}^{-1}\mathbf{U}^t. \quad (4.44)$$

When \mathbf{A} is non singular, i.e. its singular values are all positive, the SVD technique allows to compute the inverse matrix \mathbf{A}^{-1} as other methods do (notice however that \mathbf{A} is rectangular). When \mathbf{A} is singular (or badly conditioned), some of its singular values a_i^0 are null (or very close to zero). This would make the inversion of $\mathbf{\Lambda}$ (and \mathbf{A}) impossible. In that case, the SVD technique consists in constructing the inverse matrix $\hat{\mathbf{\Lambda}}^{-1}$, by imposing the following condition:

$$\text{if } a_i^0 < \text{TOL}_{SVD}, \text{ then } (1/a_i^0) = 0. \quad (4.45)$$

The resultant matrix \mathbf{A}^+ , indicated as the *pseudo-inverse* of \mathbf{A} , represents the the closest matrix approximation of \mathbf{A}^{-1} :

$$\mathbf{A}^+ = \mathbf{V}\hat{\mathbf{\Lambda}}^{-1}\mathbf{U}^t. \quad (4.46)$$

The SVD technique has been implemented within the Newton's iterative process for the inversion of the Jacobian matrix (Eq.(4.34)). Cases as those depicted in Figure 4.4 can be properly treated through this method. When the Jacobian matrix is singular, the SVD gives its pseudo-inverse. When no singularity occurs, the SVD technique always provides an accurate alternative to other classical inversion methods. The effect of the application of the SVD technique on elastoplastic problems is shown in Section 4.6, by means of specific benchmarks.

4.5 Finite Element formulation

4.5.1 Element implementation

The theory of multisurface plasticity for Cosserat materials is herein incorporated into a displacement and rotation-based finite element formulation. For further details on the formulation of Cosserat finite elements of this type, the reader is referred to Providas and Kattis (2002); Zervos (2008); Godio et al. (2015a). The account for plastic strains is made through the adoption of the implicit (backward-Euler) Closest-Point-Projection algorithm and the related solution strategies presented in Section 4.4.

Dealing with irreducible finite elements, approximations of the kinematic fields are first needed. In the case of Cosserat element, displacement and rotational fields are interpolated with respect to nodal translations \mathbf{U} and Cosserat nodal rotations $\mathbf{\Omega}^c$. This can be made, for instance, by means of specific shape functions \mathbf{N} and $\mathbf{\Phi}$, associated respectively to the displacements and the rotations (Godio et al., 2015a). However, in order to keep the formulation simple and general, and being in analogy to other more conventional theories, here we express the element interpolation as:

$$d\mathbf{s} = \mathbf{N}d\mathbf{S}, \quad (4.47)$$

where \mathbf{s} contains both the displacement \mathbf{u} and the rotational fields $\boldsymbol{\omega}^c$, and \mathbf{S} is the vector of the nodal degrees-of-freedom. Its increment writes:

$$d\mathbf{S} = \begin{bmatrix} d\mathbf{U} & d\mathbf{\Omega}^c \end{bmatrix}^t. \quad (4.48)$$

Similarly, the increment of the total strain vector $\boldsymbol{\varepsilon}$ (Eq.(4.11)) of the element is:

$$d\boldsymbol{\varepsilon} = \mathbf{B}d\mathbf{S}, \quad (4.49)$$

with \mathbf{B} the element compliant matrix. With this notation, the principle of virtual work (Eq.(4.6)) on the element of area A^e holds at the increment $(n+1)$:

$$[\mathbf{R}(\mathbf{S}_{n+1}) - \mathbf{P}_{n+1}]^t \delta\mathbf{S} = 0, \quad (4.50)$$

where:

$$\mathbf{R}(\mathbf{S}_{n+1}) = \int_{A^e} \mathbf{B}^t \boldsymbol{\sigma}(\mathbf{S}_{n+1}) dA, \quad \mathbf{P}_{n+1} = \int_{A^e} \mathbf{N}^t \mathbf{f}_{n+1} dA \quad (4.51)$$

are respectively the resultant vectors of the internal and the external forces $\mathbf{f} = [\mathbf{b} \quad \mathbf{l}]^t$ acting on the element. The dynamic part of Eq.(4.6) and the work done by the tractions and moments on the boundary are omitted.

Solution to Eq.(4.50) can be obtained for every $\delta\mathbf{S}$ and at every increment (n) through an iterative solution procedure. This procedure is controlled at the *global* level, i.e. for the whole element discretisation, and encloses that adopted for the material (Section 4.4.2), which is now solved at the *local* level, i.e. at the quadrature points of the element. The majority of the commercial codes implementing the finite element method employ for this purpose a classical Newton-Raphson scheme. Therefore, from the knowledge of the iteration (h) , by using Eq.(4.34) one obtains the solution vector $\mathbf{S}_{n+1}^{(h+1)}$ at the iteration $(h+1)$:

$$\mathbf{S}_{n+1}^{(h+1)} = \mathbf{S}_{n+1}^{(h)} - [\partial_{\mathbf{S}} \mathbf{R}_{n+1}^{(h)}]^{-1} [\mathbf{R}_{n+1}^{(h)} - \mathbf{P}_{n+1}]. \quad (4.52)$$

Once the solution vector $\mathbf{S}_{n+1}^{(h+1)}$ is known, the residual vector $\mathbf{R}_{n+1}^{(h)}$ is also updated to $(h+1)$ -th iteration, and (after the assembly operation) convergence is checked at the global level. In order to avoid confusion, in Eq.(4.52) the index (h) is used to distinguish the global Newton's iteration from the local one, denoted with (k) (Section 4.4.2), made at the quadrature point.

By using the chain rule along with Eqs.(4.14),(4.49) and (4.51), the Jacobian matrix in Eq.(4.52) takes the following form:

$$\begin{aligned} \partial_{\mathbf{S}} \mathbf{R}_{n+1}^{(h)} &= [\partial_{\boldsymbol{\sigma}_{n+1}} \mathbf{R}_{n+1}^{(h)}] \cdot [\partial_{\boldsymbol{\varepsilon}_{n+1}} \boldsymbol{\sigma}_{n+1}^{(h)}] \cdot [\partial_{\mathbf{S}_{n+1}} \boldsymbol{\varepsilon}_{n+1}^{(h)}] \\ &= \int_{A^e} (\mathbf{B}^t \mathbf{C}_{n+1}^{(h)} \mathbf{B}) dA = \mathbf{K}_{n+1}^{(h)}, \end{aligned} \quad (4.53)$$

where $\mathbf{C}_{n+1}^{(h)}$ is the matrix of the elastoplastic tangent moduli (Eq.(4.14)), computed at the time step $(n+1)$ and updated at the h -th global iteration. $\mathbf{K}_{n+1}^{(h)}$ is the corresponding element's elastoplastic tangent stiffness matrix. Its expression proves crucial in preserving the rate of quadratic convergence that distinguishes the full Newton-Raphson method from its modified version (Hughes, 1987; Simo and Hughes, 1998). The explicit expression of the elastoplastic element stiffness matrix is derived in the next Section, in the framework of the Cosserat multisurface plasticity theory.

4.5.2 Derivation of the elastoplastic tangent stiffness matrix for multisurface plasticity

The peculiar aspect of finite elements based on Cosserat continuum is that both the terms associated with the nodal translations and the nodal rotations confer rigidity to the element.

However, in order to avoid further complexity in notation, here the derivation of the stiffness matrix $\mathbf{K}_{n+1}^{(h)}$ is carried out in general form. This can make the derivation similar to that made in other elastoplastic theories, as in the classical continuum theory (Simo and Hughes, 1998) or in the generalised theories of beams and plates (Zienkiewicz and Taylor, 2005). However, one must have in mind the complex structure of the Cosserat continuum in the context of the multisurface plasticity theory. For instance, due to plasticity, coupling between the terms related to the stresses and the couple-stresses may occur, even when dealing with centro-symmetric materials.

For completeness, we derive below two versions of the tangent moduli $\mathbf{C}_{n+1}^{(h)}$ entering Eq.(4.53): the *continuum* and the *algorithmic*. The continuum version refers directly to the theory of multisurface plasticity developed in Section 4.3. The algorithmic version refers specifically to the iterative solution scheme presented in Section 4.4. It is important to note that only the use of the algorithmic moduli in the expression of the element stiffness matrix (4.53) preserves, whatever the increment size, the quadratic convergence of the Newton's method. The continuum moduli reaches this rate only in the limit of very small step increments (Hughes, 1987; Simo and Hughes, 1998).

CONTINUUM TANGENT MODULUS

Eqs.(4.12),(4.13),(4.15),(4.18),(4.19) and (4.21) are recast in the following system of matrix equations:

$$\begin{cases} d\boldsymbol{\sigma} = \mathbf{C} [d\boldsymbol{\varepsilon} - d\boldsymbol{\varepsilon}^p] \\ dq = -\mathbf{D}d\alpha \\ d\boldsymbol{\varepsilon}^p = \nabla_{\boldsymbol{\sigma}}\mathbf{G} \cdot \dot{\boldsymbol{\Lambda}} \\ d\alpha = \nabla_q\mathbf{H} \cdot \dot{\boldsymbol{\Lambda}} \\ \nabla_{\boldsymbol{\sigma}}\mathbf{F}^t \cdot d\boldsymbol{\sigma} + \nabla_q\mathbf{F}^t \cdot dq = 0. \end{cases} \quad (4.54)$$

Combining Eqs.(4.54)-1 and (4.54)-3 one obtains:

$$d\boldsymbol{\sigma} = \mathbf{C} [d\boldsymbol{\varepsilon} - \nabla_{\boldsymbol{\sigma}}\mathbf{G} \cdot \dot{\boldsymbol{\Lambda}}]. \quad (4.55)$$

The above equation, substituted into Eq.(4.54)-5 together with Eq.(4.54)-2,4, yields:

$$\dot{\boldsymbol{\Lambda}} = \mathbf{M}^{-1} \cdot \nabla_{\boldsymbol{\sigma}}\mathbf{F}^t \cdot \mathbf{C} \cdot d\boldsymbol{\varepsilon} \quad (4.56)$$

with:

$$\mathbf{M} = \nabla_{\boldsymbol{\sigma}}\mathbf{F}^t \cdot \mathbf{C} \cdot \nabla_{\boldsymbol{\sigma}}\mathbf{G} + \nabla_q\mathbf{F}^t \cdot \mathbf{D} \cdot \nabla_q\mathbf{H} \quad (4.57)$$

The substitution of Eq.(4.56) into Eq.(4.55) leads to the expression for the matrix of the elastoplastic tangent moduli \mathbf{C}^{ep} :

$$\begin{aligned} d\boldsymbol{\sigma} &= \mathbf{C}^{ep}d\boldsymbol{\varepsilon} \\ \mathbf{C}^{ep} &= \left[\mathbf{C} - \mathbf{C} \cdot \nabla_{\boldsymbol{\sigma}}\mathbf{G} \cdot \mathbf{M}^{-1} \cdot \nabla_{\boldsymbol{\sigma}}\mathbf{F}^t \cdot \mathbf{C} \right]. \end{aligned} \quad (4.58)$$

It is important to note that the \mathbf{M} matrix and the matrix of the elastoplastic tangent modulus \mathbf{C}^{ep} are not necessarily symmetric. Both matrices would become symmetric only in the case of associative plasticity, namely:

$$\nabla_{\boldsymbol{\sigma}}\mathbf{G} \equiv \nabla_{\boldsymbol{\sigma}}\mathbf{F}, \quad \nabla_q\mathbf{H} \equiv \nabla_q\mathbf{F}. \quad (4.59)$$

ALGORITHMIC TANGENT MODULUS

The algorithmic, or *consistent* (Simo and Hughes, 1998; Zienkiewicz and Taylor, 2005), version of the elastoplastic tangent matrix, namely $\mathbf{C}_{n+1}^{(h)}$, is retrieved in similar way with its continuum version \mathbf{C}^{ep} (Eq.(4.58)). For clarity we omit the index (h). One can rewrite system (4.32) in the following algorithmic form:

$$\begin{cases} d\boldsymbol{\sigma}_{n+1} = \mathbf{C} [d\boldsymbol{\varepsilon}_{n+1} - d\boldsymbol{\varepsilon}_{n+1}^p] \\ dq_{n+1} = -\mathbf{D}d\alpha_{n+1} \\ d\boldsymbol{\varepsilon}_{n+1}^p = \nabla_{\sigma\sigma}^2 \mathbf{G}_{n+1} \cdot \dot{\boldsymbol{\Lambda}}_{n+1} \cdot d\boldsymbol{\sigma}_{n+1} + \nabla_{\sigma} \mathbf{G}_{n+1} \cdot d\dot{\boldsymbol{\Lambda}}_{n+1} \\ d\alpha_{n+1} = \nabla_{qq}^2 \mathbf{H}_{n+1} \cdot \dot{\boldsymbol{\Lambda}}_{n+1} \cdot dq_{n+1} + \nabla_q \mathbf{H}_{n+1} \cdot d\dot{\boldsymbol{\Lambda}}_{n+1} \\ \nabla_{\sigma} \mathbf{F}_{n+1}^t \cdot d\boldsymbol{\sigma}_{n+1} + \nabla_q \mathbf{F}_{n+1}^t \cdot dq_{n+1} = 0 \end{cases}, \quad (4.60)$$

where the increment $d\dot{\boldsymbol{\Lambda}}_{n+1}$ is introduced. Eqs.(4.60)-1,3 are then combined, in order to give:

$$d\boldsymbol{\sigma}_{n+1} = \boldsymbol{\Theta}_{n+1} \left[d\boldsymbol{\varepsilon}_{n+1} - \nabla_{\sigma} \mathbf{G}_{n+1} \cdot d\dot{\boldsymbol{\Lambda}}_{n+1} \right], \quad (4.61)$$

where $\boldsymbol{\Theta}_{n+1}$ is the matrix of the *elastic algorithmic moduli* (Simo and Hughes, 1998). Its definition is (cf. Eq.(4.37)):

$$\boldsymbol{\Theta}_{n+1} = \left[\mathbf{C}^{-1} + \nabla_{\sigma\sigma}^2 \mathbf{G}_{n+1} \cdot \dot{\boldsymbol{\Lambda}}_{n+1} \right]^{-1}. \quad (4.62)$$

In addition, Eqs.(4.60)-2,4 give:

$$dq_{n+1} = \boldsymbol{\Psi}_{n+1} \left[-\nabla_q \mathbf{H}_{n+1} \cdot d\dot{\boldsymbol{\Lambda}}_{n+1} \right], \quad (4.63)$$

where $\boldsymbol{\Psi}_{n+1}$ writes:

$$\boldsymbol{\Psi}_{n+1} = \left[\mathbf{D}^{-1} + \nabla_{qq}^2 \mathbf{H}_{n+1} \cdot \dot{\boldsymbol{\Lambda}}_{n+1} \right]^{-1}. \quad (4.64)$$

Due to the similarity with $\boldsymbol{\Theta}_{n+1}$, matrix $\boldsymbol{\Psi}_{n+1}$ could be defined as the matrix of the *hardening algorithmic moduli*. Substituted into Eq.(4.60)-5, Eqs.(4.61) and (4.63) hold:

$$d\dot{\boldsymbol{\Lambda}}_{n+1} = \tilde{\mathbf{M}}_{n+1}^{-1} \cdot \nabla_{\sigma} \mathbf{F}_{n+1}^t \cdot \boldsymbol{\Theta}_{n+1} \cdot d\boldsymbol{\varepsilon}_{n+1}, \quad (4.65)$$

and consequently Eq.(4.61) becomes:

$$\mathbf{C}_{n+1} = \left[\boldsymbol{\Theta}_{n+1} - \boldsymbol{\Theta}_{n+1} \cdot \nabla_{\sigma} \mathbf{G}_{n+1} \cdot \tilde{\mathbf{M}}_{n+1}^{-1} \cdot \nabla_{\sigma} \mathbf{F}_{n+1}^t \cdot \boldsymbol{\Theta}_{n+1} \right]. \quad (4.66)$$

In Eq.(4.58), matrix $\tilde{\mathbf{M}}_{n+1}$ is defined as in Eq.(4.57), with the exception that matrices \mathbf{C} and \mathbf{D} must be replaced here with their algorithmic versions $\boldsymbol{\Theta}_{n+1}$ and $\boldsymbol{\Psi}_{n+1}$. Notice, in conclusion, how the matrix of the algorithmic moduli (4.66) reduces to that of the continuum moduli (4.58), as the step increment is small. This shows that problem (4.60) is consistent with problem (4.54).

4.6 Element validation

In Section 4.4 and 4.5, the theory, the solution algorithm and the element implementation of multisurface plasticity for Cosserat materials have been presented in general manner. In this Section attention is focused on a specific finite element, formulated for micropolar plate models. The element is briefly introduced and its validation in the framework of multisurface plasticity is then carried out in two steps. Firstly, the accuracy of the CPP algorithm is tested locally, i.e. at the integration point level, through simple element tests. Secondly, the efficiency of the algorithm is assessed at the global (or element) level, based on more complex discretisations related to structural problems.

4.6.1 The micropolar plate element COSS8R

The element called COSS8R (Godio et al., 2015a) is a quadratic micropolar plate element (Figure 4.5). It possesses 8 nodes, all situated on the element sides. Each node is equipped with 6 degrees-of-freedom, i.e. 3 translations and 3 Cosserat rotations. In this element, the shape functions \mathbf{N} and $\mathbf{\Phi}$, used respectively for the interpolation of the displacement and the rotational fields, are the same. The integration of the element stiffness matrix is made on 4 quadrature points (reduced integration), whereas the integration of the element mass matrix requires 9 quadrature points (full integration). This avoids the shear locking phenomenon (in statics) and the occurrence of massless degrees-of-freedom (in dynamics). For further details, the reader is referred to Godio et al. (2015a). It is important to note that, in the extension to plasticity, the presence of multiple quadrature points requires the independent solution of the elastoplastic problem at each of these points ¹.

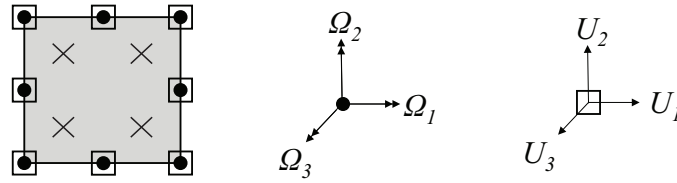


Figure 4.5: The quadratic micropolar plate element COSS8R (Godio et al., 2015a).

membrane behaviour	flexural behaviour
$\mathbf{u}_m = [u_1 \quad u_2]^t$	$u_f = [u_3]$
$\omega_m^c = [\omega_3]$	$\omega_f^c = [\omega_1 \quad \omega_2]^t$
$\boldsymbol{\gamma}_m = [\gamma_{11} \quad \gamma_{22} \quad \gamma_{12} \quad \gamma_{21}]^t$	$\boldsymbol{\gamma}_f = [\gamma_{13} \quad \gamma_{31} \quad \gamma_{23} \quad \gamma_{32}]^t$
$\boldsymbol{\kappa}_m = [\kappa_{31} \quad \kappa_{32}]^t$	$\boldsymbol{\kappa}_f = [\kappa_{11} \quad \kappa_{22} \quad \kappa_{12} \quad \kappa_{21}]^t$
$\mathbf{b}_m = [b_1 \quad b_2]^t$	$\mathbf{b}_f = [b_3]$
$l_m = [l_3]$	$\mathbf{l}_f = [l_1 \quad l_2]^t$
$\boldsymbol{\tau}_m = [\tau_{11} \quad \tau_{22} \quad \tau_{12} \quad \tau_{21}]^t$	$\boldsymbol{\tau}_f = [\tau_{13} \quad \tau_{31} \quad \tau_{23} \quad \tau_{32}]^t$
$\boldsymbol{\mu}_m = [\mu_{31} \quad \mu_{32}]^t$	$\boldsymbol{\mu}_f = [\mu_{11} \quad \mu_{22} \quad \mu_{12} \quad \mu_{21}]^t$

Table 4.1: Membrane and flexural static and kinematics of a Cosserat plate element.

For the sequel of this Section, it is useful to distinguish the variables describing the membrane response from the variables describing the flexural response of the plate element (Table 4.1). Accordingly, the membrane elastic response is controlled by matrices \mathbf{A} and \mathbf{D}_m , expressed as (Papanastasiou and Vardoulakis, 1992; Godio et al., 2015a):

$$\boldsymbol{\tau}_m = \mathbf{A}\boldsymbol{\gamma}_m, \quad \boldsymbol{\mu}_m = \mathbf{D}_m\boldsymbol{\kappa}_m$$

$$\mathbf{A} = \begin{bmatrix} K + G & K - G & 0 & 0 \\ K - G & K + G & 0 & 0 \\ 0 & 0 & G + G_c & G - G_c \\ 0 & 0 & G - G_c & G + G_c \end{bmatrix}, \quad \mathbf{D}_m = \begin{bmatrix} 2Gl_c & 0 \\ 0 & 2Gl_c \end{bmatrix} \quad (4.67)$$

¹Appendix D.1 provides further details on the implementation of the COSS8R element as Abaqus User Element. This Appendix is absent from Godio et al. (2016).

with K the compression modulus, G the shear modulus, G_c the Cosserat shear modulus and l_c the characteristic length of the micro-structured material. The flexural elastic response is controlled by matrices \mathbf{Q} and \mathbf{D}_f , reading (Altenbach and Eremeyev, 2009; Godio et al., 2015a):

$$\mathbf{Q} = \begin{bmatrix} 0 & 0 & 0 & 0 \\ 0 & \alpha_4 & 0 & 0 \\ 0 & 0 & 0 & 0 \\ 0 & 0 & 0 & \alpha_4 \end{bmatrix}, \quad \mathbf{D}_f = \begin{bmatrix} \beta_1 + \beta_2 + \beta_3 & & \beta_1 & 0 & 0 \\ & \beta_1 & \beta_1 + \beta_2 + \beta_3 & 0 & 0 \\ & 0 & & 0 & \beta_3 & \beta_2 \\ & 0 & & 0 & \beta_2 & \beta_3 \end{bmatrix} \quad (4.68)$$

with α_4 the material parameter related to the transverse shears, and $\beta_1, \beta_2, \beta_3$ those related to the torsions and the out-of-plane flexions of the plate.

4.6.2 Single element tests for multisurface plane plasticity

The scope of single element tests is twofold. On one hand, the algorithm accuracy is assessed not only pointwise, but also at the element level, i.e. after integration of the element's stiffness matrix. This guarantees the good response of the element and the convergence of the iterative scheme at the global level. On the other hand, with tests of this kind the performance of the element can be shown in special configurations, as for states of non-homogeneous deformation or in presence of multiple plastic surfaces. In this setting, the use of the SVD technique within the Newton-Raphson process is investigated.

Herein we carry out two series of tests based on two basic configurations (Figure 4.6): one involving uni-axial loading/unloading cycles, and one involving the use of multiple plastic surfaces for bi-axial stress states. All tests are displacement-controlled.



Figure 4.6: Configurations used for the single element tests in multisurface plasticity.

UNI-AXIAL LOADING/UNLOADING CYCLES

The application of the displacement increment Δu_1 leads to a homogeneous state of tension/compression/tension on the element (Figure 4.6-left). The uni-axial constitutive law is given by:

$$\tau_{11} = E\gamma_{11}, \quad (4.69)$$

with E the elastic modulus. The plastic surface with linear isotropic hardening is given in the form:

$$\begin{aligned} |\tau_{11}| - \tau_y + q_1 &\leq 0 \\ q_1 &= h\alpha_1 \end{aligned} \quad (4.70)$$

with τ_y the uni-axial limit stress. Figure 4.7 illustrates the stress path followed during the test and the stress-strain relation curves. The evolution of the elastic domain during the elastoplastic loading phases (a-b) and (c-d) is apparent.

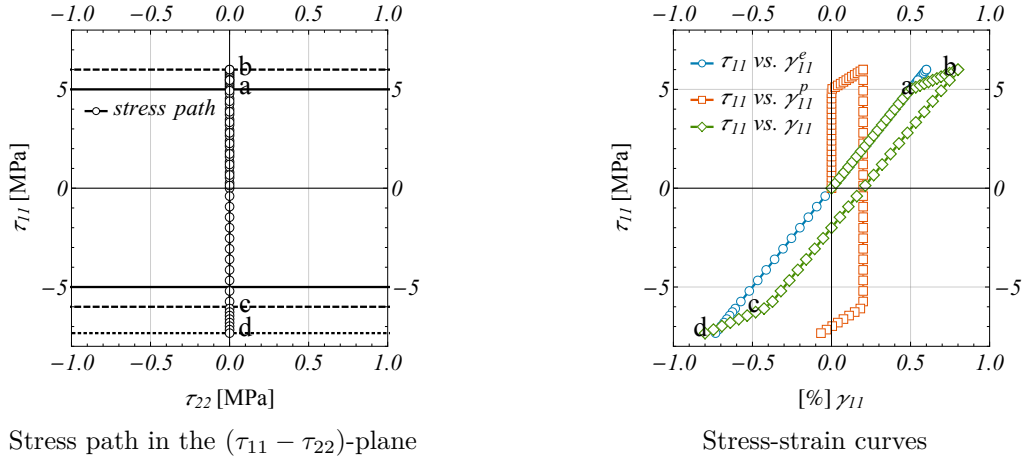


Figure 4.7: Element response to uni-axial cyclic loading. Elastic modulus $E = 10\text{MPa}$, hardening modulus $h = 10\text{MPa}$, yield stress $\tau_y = 5\text{MPa}$.

BI-AXIAL LOAD TESTS FOR MULTISURFACE PLASTICITY

Five tests, indicated with B1 to B5, are carried out. In these tests, displacement increments are applied in x_1 and x_2 directions (Figure 4.6-right), leading the element to homogeneous bi-axial stress states. Different sets of plastic surfaces are considered for each test. In particular, we consider five plastic surfaces together with a linear isotropic hardening/softening function:

$$\begin{aligned}
 F^1 &= \tau_{22}/\tau_y - 1 + q_1 \\
 F^2 &= \tau_{11}/\tau_y - 1 + q_1 \\
 F^3 &= (\tau_{11} + \tau_{22})/(2\tau_y) - 1 + q_1 \\
 F^4 &= (\tau_{11}/\tau_y)^2 + (\tau_{22}/\tau_y)^2 - 1 + q_1 \\
 F^5 &= (\tau_{11}/(1.4 \tau_y))^2 + (\tau_{22}/(0.6 \tau_y))^2 - 1 + q_1 \\
 q_1 &= h\alpha_1.
 \end{aligned} \tag{4.71}$$

Moreover, we consider a material with isotropic elastic constitutive law, given by Eq.(4.67). All tests except Test B5 are carried out by using the same elastic properties (Figure 4.8), and the same number of equally spaced increments (30). This allows the convergence to be reached in Tests B1, B2 and to provide high level of accuracy in Test B3, B4. For Test B5, the total number of increments is doubled and the hardening modulus is $0.1h$.

In Test B1 (Figure 4.8) surfaces F^1, F^2 are used. These two intersecting plastic surfaces are activated during the monotonic bi-axial loading. For perfect plasticity (Figure 4.8-left), the stress path is limited by the boundary of the elastic domain. In case of isotropic hardening (Figure 4.8-right), both surfaces evolve towards the new stress state of the element. Notice that the symmetry of the problem is reflected in the symmetry of the solution, which is the same in x_1 - and x_2 -directions. Moreover, the same solution is reached at all integration points of the element. For brevity, only τ_{11} as function of the total γ_{11} , elastic γ_{11}^e and plastic deformation γ_{11}^p , and of the hardening parameter α is presented.

In Test B2 (Figure 4.9) surface F^3 is added to F^1, F^2 and in Test B3 (Figure 4.10) surface F^4 and an identical surface denoted F^6 are employed. These two tests follow the examples of Figure 4.4, since they allow to consider redundant and coincident plastic surfaces respectively. If the SVD technique was not employed for the solution of the incremental elastoplastic problem (Section 4.4.2), the inversion of the Jacobian matrix would not be possible in these cases and the test would fail once the surfaces reached. This would hold for Test B2 in the case of perfect

plasticity ($N_F = N_\sigma$) and for Test B3 in both cases, since the same hardening variable is used for the two surfaces F^4, F^6 . Nevertheless, these tests are handled by the element, thanks to the proposed solution strategy that involves the SVD technique. On one hand (Figure 4.9), the element is able to activate all the necessary surfaces. Since surface F^3 is redundant with F^1 and F^2 , the resulting deformations are actually the same with those of Test B1. On the other hand (Figure 4.10), both surfaces evolve in identical manner.

Test B4 (Figure 4.11) makes use of F^4 and F^6 . It consists of two successive monotonic load steps. First $\Delta u_1 > 0$ and then $\Delta u_2 > 0$ are applied. As a result of the form of the elastic domain, the second load step results in a loading step in direction x_2 and an unloading step in direction x_1 . This occurs both in case of hardening and of perfect plasticity, where the stress state is constrained to move along the boundary of the elastic domain. Also in this test, the SVD technique enables the element to follow exactly the stress path imposed, F^4 and F^6 being coincident.

In Test B5 (Figure 4.12) surfaces F^4 and F^5 are used. The test consists in five successive load steps, namely: a) $\Delta u_1 > 0, \Delta u_2 = 0$; b) $\Delta u_1 = 0, \Delta u_2 > 0$; c) $\Delta u_1 < 0, \Delta u_2 = 0$; d) $\Delta u_1 = 0, \Delta u_2 < 0$; e) $\Delta u_1 > 0, \Delta u_2 = 0$. Following these steps, the element carries out a complete loading/unloading cycle in x_1 and x_2 directions simultaneously. Accordingly, the stress path activates different plastic surfaces at each load step. Notice how the activation of the surfaces occurs precisely at their points of intersection. Moreover, in case of hardening plasticity the accumulated plastic strains induces the general expansion of the elastic domain.

4.6.3 Structural benchmarks for micropolar plates

Structural benchmarks are made to test (and suggest) the use of the algorithm of multisurface plasticity for Cosserat materials and the developed plate element in cases of practical interest. Herein we carry out three benchmarks. In all the examples we consider 3D structural problems. The first benchmark is concerned with the development of in-plane strain localisation in hollow cylinders with micropolar properties. With the second benchmark we model the behaviour of micropolar square plates undergoing out-of-plane macroscopic plastic curvatures. The third benchmark aims at studying the load-bearing capacity of a shallow foundation resting upon a micropolar soil under plane strain conditions.

STRAIN LOCALISATION IN HOLLOW CYLINDERS

We consider a hollow cylinder of height $H = 60\text{mm}$, radius $R = 15\text{mm}$ and constant thickness $t = 1\text{mm}$. The cylinder is subjected to torsion (Figure 4.13). In particular, the top and the bottom sides of the cylinder have all the degrees-of-freedom prevented except the axial rotation, denoted with Ω_3 , which is controlled. The lateral surface of the cylinder is free of stresses and couple-stresses.

The cylinder is made of a micro-structured material. Its macroscopic behaviour is described by a Cosserat continuum with homogeneous isotropic centro-symmetric elastic properties (Eq.(4.67)-(4.68)). The in-plane response of the material follows here the tangential (θ) and longitudinal (z) directions of the cylinder. The out-of-plane direction is on the radial (r) direction (Figure 4.13). The elastic parameters of the material are: $K = 4000\text{MPa}$, $G = 4000\text{MPa}$, $G_c = 2000\text{MPa}$, and $\alpha_4 = 1500\text{MPa}$, $\beta_1 = 2000\text{MPa} \times \text{mm}$, $\beta_2 = 0\text{MPa} \times \text{mm}$, $\beta_3 = 4000\text{MPa} \times \text{mm}$. The characteristic (or inner) length of the micro-structured material is $l_c = 2.5\text{mm}$ (Eq.(4.67)).

The elastoplastic response of the material is described by means of the $J2$ (or Von-Mises) plasticity model formulated for Cosserat continua. The yield criterion for the generalised $J2$ -

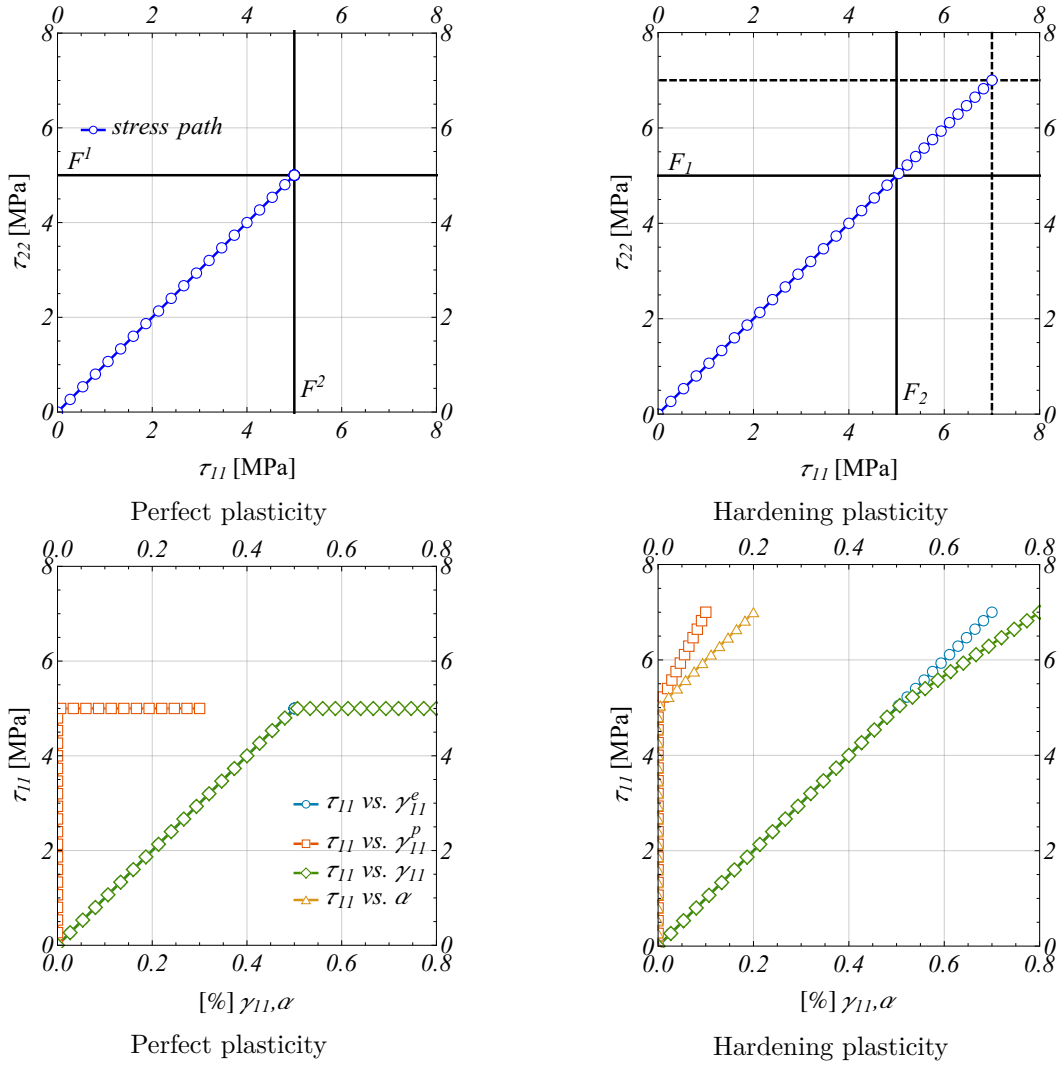


Figure 4.8: Element response to bi-axial test B1. Top: stress path in the $(\tau_{11} - \tau_{22})$ -plane. Bottom: stress-strain curve. In-plane elastic properties: $K = 5\text{MPa}$, $G = 5\text{MPa}$, $G_c = 0\text{MPa}$, $l_c = 0$. Hardening modulus $h = 10\text{MPa}$, yield stress $\tau_y = 5\text{MPa}$.

hardening-plasticity relies on the following single plastic surface (de Borst, 1991):

$$F = \sqrt{3J_2} - \sigma(\gamma_2^p) \quad (4.72)$$

where σ represents the equivalent yield stress, J_2 is the second invariant of the deviatoric stress tensor and γ_2^p is the second invariant of the deviatoric plastic strain tensor. For the Cosserat continuum, J_2 and γ_2^p write respectively:

$$J_2 = \frac{1}{2} \begin{bmatrix} \boldsymbol{\tau}_m^t & \boldsymbol{\mu}_m^t \end{bmatrix} \mathbf{P} \begin{bmatrix} \boldsymbol{\tau}_m \\ \boldsymbol{\mu}_m \end{bmatrix}, \quad (4.73)$$

and:

$$\gamma_2^p = \sqrt{\frac{2}{3} \begin{bmatrix} \boldsymbol{\gamma}_m^t & \boldsymbol{\kappa}_m^t \end{bmatrix} \tilde{\mathbf{P}} \begin{bmatrix} \boldsymbol{\gamma}_m \\ \boldsymbol{\kappa}_m \end{bmatrix}}, \quad (4.74)$$

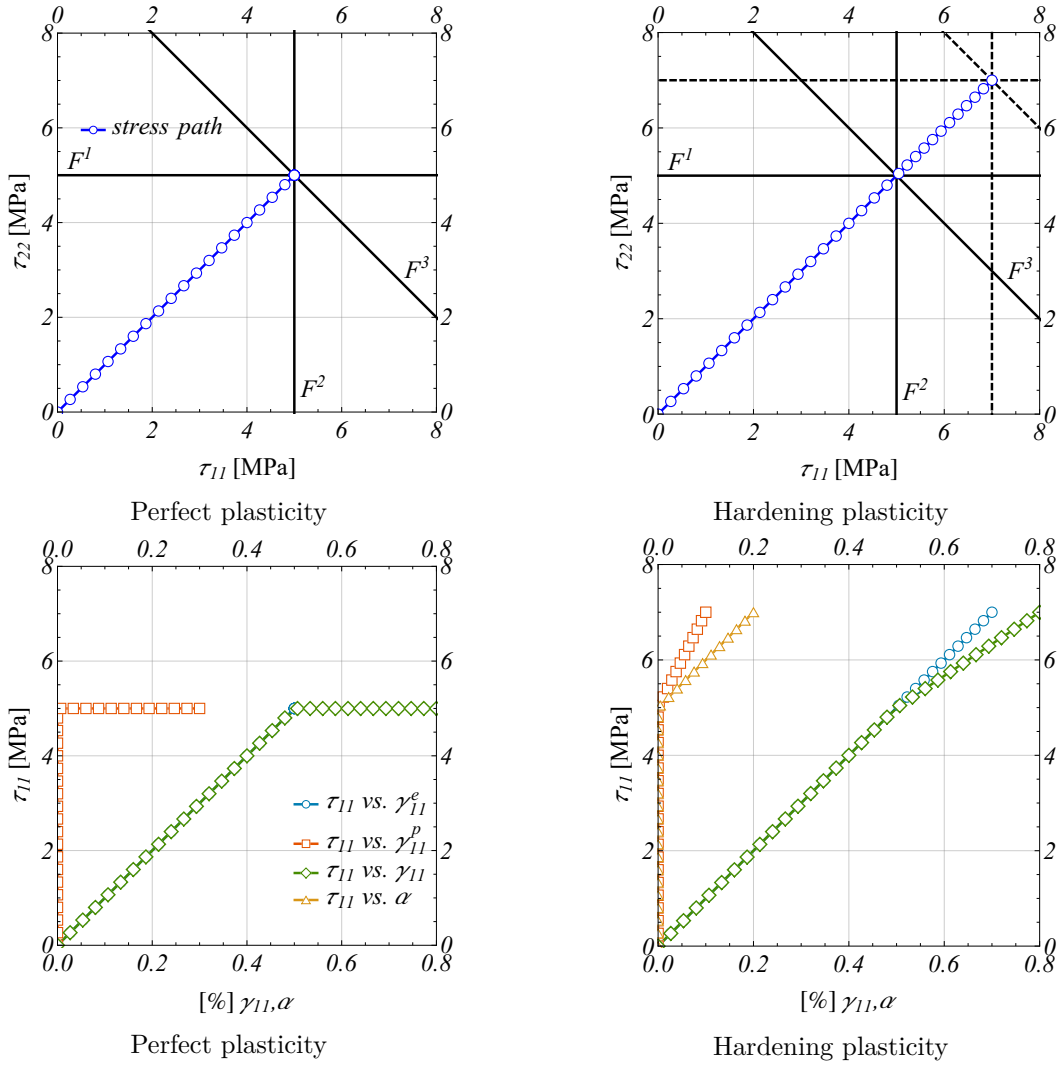


Figure 4.9: Element response to bi-axial test B2. Top: stress path in the $(\tau_{11} - \tau_{22})$ -plane. Bottom: stress-strain curve.

with matrices \mathbf{P} and $\tilde{\mathbf{P}}$ defined as:

$$\mathbf{P} = \begin{bmatrix} \frac{4}{3}(a_1 + a_2) & -\frac{2}{3}(a_1 + a_2) & 0 & 0 & 0 & 0 \\ -\frac{2}{3}(a_1 + a_2) & \frac{4}{3}(a_1 + a_2) & 0 & 0 & 0 & 0 \\ 0 & 0 & 2a_1 & 2a_2 & 0 & 0 \\ 0 & 0 & 2a_2 & 2a_1 & 0 & 0 \\ 0 & 0 & 0 & 0 & 2a_3/l_c^2 & 0 \\ 0 & 0 & 0 & 0 & 0 & 2a_3/l_c^2 \end{bmatrix}$$

$$\tilde{\mathbf{P}} = \begin{bmatrix} \frac{4}{3}(b_1 + b_2) & -\frac{2}{3}(b_1 + b_2) & 0 & 0 & 0 & 0 \\ -\frac{2}{3}(b_1 + b_2) & \frac{4}{3}(b_1 + b_2) & 0 & 0 & 0 & 0 \\ 0 & 0 & 2b_1 & 2b_2 & 0 & 0 \\ 0 & 0 & 2b_2 & 2b_1 & 0 & 0 \\ 0 & 0 & 0 & 0 & 2l_c^2 b_3 & 0 \\ 0 & 0 & 0 & 0 & 0 & 2l_c^2 b_3 \end{bmatrix}. \quad (4.75)$$

Scalars a_1, a_2, a_3 and b_1, b_2, b_3 are the plastic parameters of the material. Following [de Borst \(1991\)](#), we use $a_1 = 1/4, a_2 = 1/4, a_3 = 1/2$ and $b_1 = 1/3, b_2 = 1/3, b_3 = 2/3$. Herein,

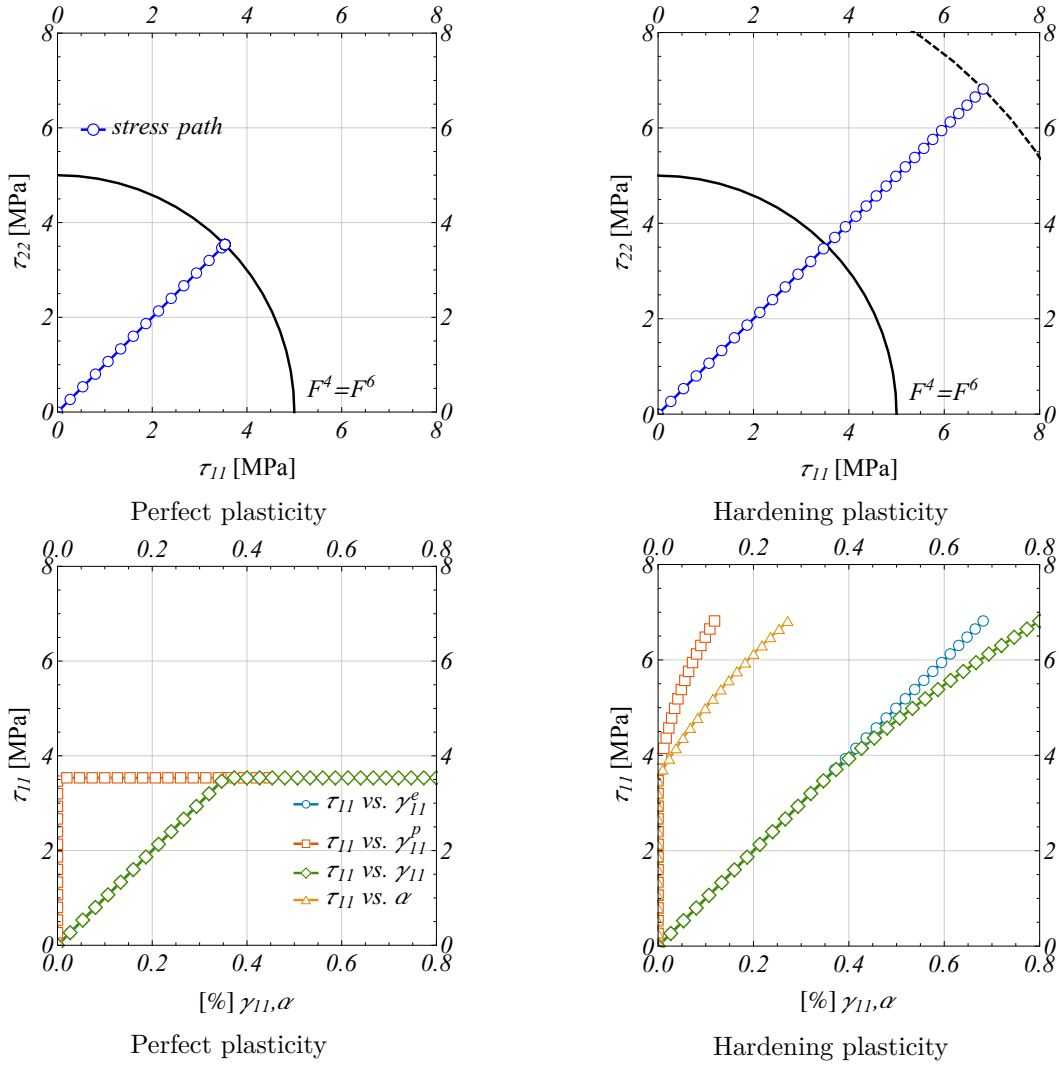


Figure 4.10: Element response to bi-axial test B3. Top: stress path in the $(\tau_{11} - \tau_{22})$ -plane. Bottom: stress-strain curve.

strain-softening plasticity is simulated through a linear softening rule, with hardening modulus $h = -400\text{MPa}$ and yield stress $\sigma = 100\text{MPa}$.

Simulations are carried out with three different finite element discretisations. The COSS8R being a flat element, it is suitable to choose a larger number along the tangential direction of the cylinder. Therefore, assemblies of 16×8 , 24×16 and 32×24 elements are used. Analyses are run by updating the reference system at every load step. In this way large axial rotations are avoided. Moreover, an automatic step increment control technique is used throughout the analyses.

The resulting macroscopic behaviour of the cylinders is shown in [Figure 4.14](#)-left, in terms of normalized reaction moment M_z and differential axial rotation $\Delta\Omega_z = \Omega_z^t - \Omega_z^b$. The onset of plastic deformations (on the first branch) rapidly culminates with a softening branch, which is accompanied by strain localisation ([Figure 4.14](#)-right). The deformation pattern of the cylinders beyond the moment peak value is shown in [Figure 4.15](#) for the different discretisations adopted. This result is expected since, due to the axial symmetry of the problem, the deformation is the same with that of other 2D structural problems ([de Borst, 1991](#); [Sharbati and Naghdabadi,](#)

2006). Accordingly, the linear elastic branch is well captured even by the coarsest discretisation, and the softening branch is reached by adopting slightly finer discretisations. Strain localisation occurs exactly as in the shear layers studied by de Borst (1991). The strain localisation shows then an apparent mesh-independency (Figure 4.14-right), i.e. the width of the localisation region does not depend on the number of elements falling inside this region. This is a fundamental feature of finite elements based on the Cosserat continuum (de Borst et al., 1993; Papanastasiou and Vardoulakis, 1992; Neff et al., 2007).

TORSION OF SQUARE PLATES

As second example we consider a square plate, of span $L = 10\text{mm}$ and thickness $t = 1\text{mm}$ (Figure 4.16). The plate has two opposite free edges and two opposite clamped edges, with all the degrees-of-freedom prevented. A rotation Ω_2 is imposed at one of the clamped edges. The rotation produces a macroscopic deformation that involves the out-of-plane behaviour of the plate. We are here interested in the assessment of the ultimate (or limit) resulting moment M_2 supported by the plate, under multiple intersecting plastic surfaces.

The plate is made of a micro-structured material which has the same elastic micropolar properties with that composing the hollow cylinders considered in Section 4.6.3. However, criteria for the out-of-plane behaviour of a Cosserat plate are absent in the literature. One criterion which is often used in practice is the Nielsen's criterion, formulated for reinforced concrete plates (Makrodimopoulos and Martin, 2006; Krabbenhøft et al., 2007a). This criterion is usually expressed for conventional (or engineering) plate theories. Herein, it is formulated in order to take into account the out-of-plane statics of the micropolar plate model (Figure 4.1). It consists of six distinct and intersecting plastic surfaces:

$$\begin{aligned}
 F^1 &= (\mu_{11} - \mu_{22})^2/4 - (M_{21}^+ - \mu_{21})(M_{12}^+ - \mu_{12}) \\
 F^2 &= (\mu_{11} - \mu_{22})^2/4 - (M_{21}^- + \mu_{21})(M_{12}^- + \mu_{12}) \\
 F^3 &= \mu_{21} - M_{21}^+ \\
 F^4 &= \mu_{12} - M_{12}^+ \\
 F^5 &= -\mu_{21} - M_{21}^- \\
 F^6 &= -\mu_{12} - M_{12}^-.
 \end{aligned} \tag{4.76}$$

Parameters $M_{21}^+, M_{21}^-, M_{12}^+, M_{12}^-$ are the (non-negative) out-of-plane yield flexions μ_{12} and μ_{21} of the reinforced concrete plate. M^+ and M^- represent the ultimate moment leading respectively the upper and the lower side fiber of the plate to failure. For simplicity, these parameters are all considered equal to $m = 5\text{MPa} \times \text{mm}$. For illustration purposes, simulations are carried out in the frame of perfect and associative plasticity. It is worth mentioning that the conventional torsional moment of the engineering theory of plates, M_t , is here expressed in terms of the Cosserat torsions μ_{11} and μ_{22} by imposing: $M_t = (\mu_{11} - \mu_{22})/2$. In this way the Nielsen's criterion may be extended to Cosserat plate models.

The plate is modeled by means of three different finite element discretisations. Figure 4.17 shows that, even with the coarsest 2×2 discretisation, the macroscopic response of the plate is captured accurately by the COSS8R element. At the beginning the plate behaves elastically, but as far as some of the plastic surfaces are activated (Eq.(4.76)), plastic curvatures are developed until the formation of a macroscopic failure mechanism. This corresponds to the ultimate resulting moment M_2 . Figure 4.18 displays the number of activated surfaces once the limit moment is reached. It is found that, for the problem considered, only the first two plastic surfaces F^1, F^2 are activated throughout the analyses. It is apparent how the algorithm of multisurface plasticity is able to select different sets of plastic surfaces at each integration point

of the finite element. This confers high flexibility to the element and may increase the accuracy in problems characterised by states of non-homogeneous deformations.

SHALLOW FOUNDATION ON MICROPOLAR SOIL

In the third benchmark we consider a shallow foundation supported by a homogeneous layer of soil (Figure 4.19). The foundation has a width $B = 33.34\text{m}$ and is subjected to a distributed pressure T_2 . The layer of soil has dimensions $L \times H = 200\text{m} \times 50\text{m}$. Classical *smooth* conditions are applied to the boundaries of the layer. The geometry of the problem allows then to consider only half of the model. This is made by preventing the horizontal translations U_2 and the in-plane rotations Ω_3 along the symmetry plane. It is worth noting that plane strain conditions, for which the out-of-plane component τ_{33} is non-null (de Borst et al., 1993), are formulated for this benchmark.

The foundation is considered as rigid and the interface with the soil perfectly cohesive. The soil is an isotropic material with micropolar elastic properties given by $K = 34000\text{kPa}$, $G = 18000\text{kPa}$ and $G_c = 0.7G$ (Eq.(4.67)). The elastoplastic response of the soil is described by means of the following set of plastic surfaces (Figure 4.20):

$$\begin{aligned} F^1 &= \sqrt{3J_2} + Ap - \sigma \\ F^2 &= \sqrt{3J_2} - Cp - Cp_c. \end{aligned} \quad (4.77)$$

The first surface is the generalisation of the Drucker-Prager plasticity model for Cosserat continua (de Borst et al., 1993; Papanastasiou and Vardoulakis, 1992; Li and Tang, 2005), for which p is the mean pressure and $A = 0.39$. The second surface introduces a generalised compression cap to the model, with $p_c = 2496\text{kPa} = 3\sigma$ the yield stress in compression and $C = 0.81$. No hardening is considered.

The aim of the benchmark is twofold. On one hand, the variation of the load-bearing capacity of the foundation is assessed for soils with different internal lengths l_c (scale effect). The effect of different yield criteria is also studied (Eq.(4.77)). On the other hand, the ultimate load is computed in the limit of small lengths in order to obtain the solution for the Cauchy continuum.

Figure 4.21 shows the macroscopic response of the foundation in terms of normalized pressure T_2 and vertical displacement δ_2 . The scale effect is apparent on Figure 4.21-left: a larger internal length yields to a stiffer elastoplastic response and a higher load-bearing capacity. On the contrary, the activation of a compression cap leads to a consistent reduction of the ultimate load. The macroscopic response for the Cauchy continuum (Figure 4.21-right) is obtained by imposing an internal length which is very small as compared to the size of the foundation. Moreover, the conditions $G_c = 0$ and $a_3 = 0$ allow respectively to retrieve the symmetry of the elastic response (Eq.(4.67)) and the classical J_2 -plasticity model (Eq.(4.72)). For validation purposes, the macroscopic response given by the COSS8R element is compared with that obtained by a finite element formulated for classical continua. To this end, a 6-noded Gauss-type mixed triangular element (Krabbenhøft et al., 2007a,b) contained in the commercial code OptumG2 is used. The solution algorithm used in OptumG2 differs from that presented herein, since based on optimization methods (Krabbenhøft et al., 2007b). The comparison shows how the COSS8R element is able to cover the solution for the Cauchy continuum, with an error less than 1%.

4.7 Conclusions

The development of robust and efficient numerical procedures is a principal task prior to modeling materials with complex micro-structure. In the attempt of describing the macroscopic

behaviour of such materials, this aspect is even more pronounced. Particularly important is in fact the determination of the overall response of the material, as function of the properties and the spatial arrangement of its micro-structure. Especially in the inelastic range, this is not a trivial task, since even when the macroscopic properties are established, one needs to resort to numerical tools for the assessment of the material response.

The use of the Cosserat continuum has gained much interest in this field, by virtue of its relatively simple formulation (limited number of variables and clear physical meaning) which yet allows to handle quite complex configurations of materials with pronounced micro-structure (masonry, soils, rocks, grid-works, etc.).

This paper was devoted to the development and validation of a numerical procedure for the analysis of micro-structured materials with macroscopic non-linear behaviour. For this purpose, the time-independent multisurface plasticity theory was extended to the Cosserat continuum. Multisurface plasticity theory allows the description of a large class of mechanisms, such as strain hardening and softening mechanisms, and the definition of both associative and non-associative properties for the material. Moreover, through this theory the elastic domain may be constructed by using a set of multiple plastic, intersecting surfaces of general form. When referred to the macroscopic description of the material, this may prove particularly useful, as each plastic surface may be related to distinct failure mechanisms at the micro-structure level.

The implementation of the multisurface plasticity theory into a Cosserat finite element formulation was presented in general manner. The implementation of the theory was based on a projection algorithm formulated for implicit time-integration schemes. The same algorithm may be encountered in more classical formulations, as the theory of classical (Cauchy) continua and the generalised theories of beams and shells. The paper focused on several numerical aspects concerning the element implementation, in relation with the iterative solution schemes used at the local (integration point) and global (element) level. A full Newton-Raphson method was used at both levels. At the local level, the projection algorithm required the use of a non conventional matrix-inversion technique (SVD). This technique was introduced in order to fully exploit all the salient features of the multisurface plasticity theory and to avoid some important limitations that were explored in details. It allowed the definition of plastic surfaces which are (hypothetically) unlimited in number and of the most general form. At the global level, the full rate of convergence was assured by the use of the elastoplastic stiffness tangent matrix of the Cosserat element. This matrix was herein derived explicitly in algorithmic form and for the very general multisurface and non-associative case.

A specific Cosserat finite element developed for micropolar plate models was finally presented. The element considered was already developed and tested in elasticity and dynamics. This paper was concerned with its extension and validation to the multisurface plasticity. Numerical tests assessed the (high) level of accuracy reached by the projection algorithm in case of multisurface Cosserat plasticity. Several benchmarks showed that the element provides accurate results under non-conventional loading and boundary conditions, involving strain softening, multiple plastic surfaces and strain localisation.

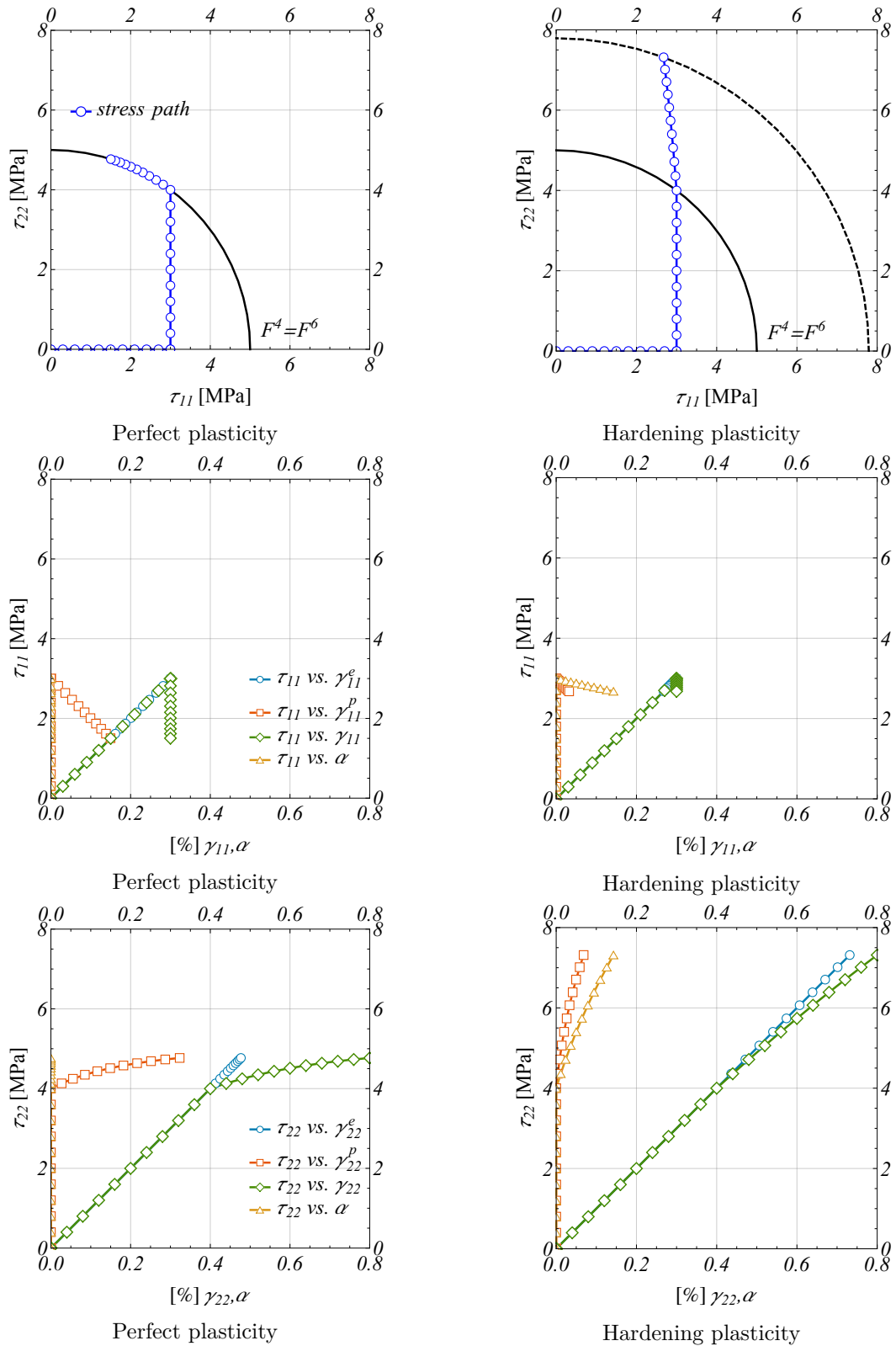


Figure 4.11: Element response to bi-axial test B4. Top: stress path in the $(\tau_{11} - \tau_{22})$ -plane. Center and bottom: stress-strain curve.

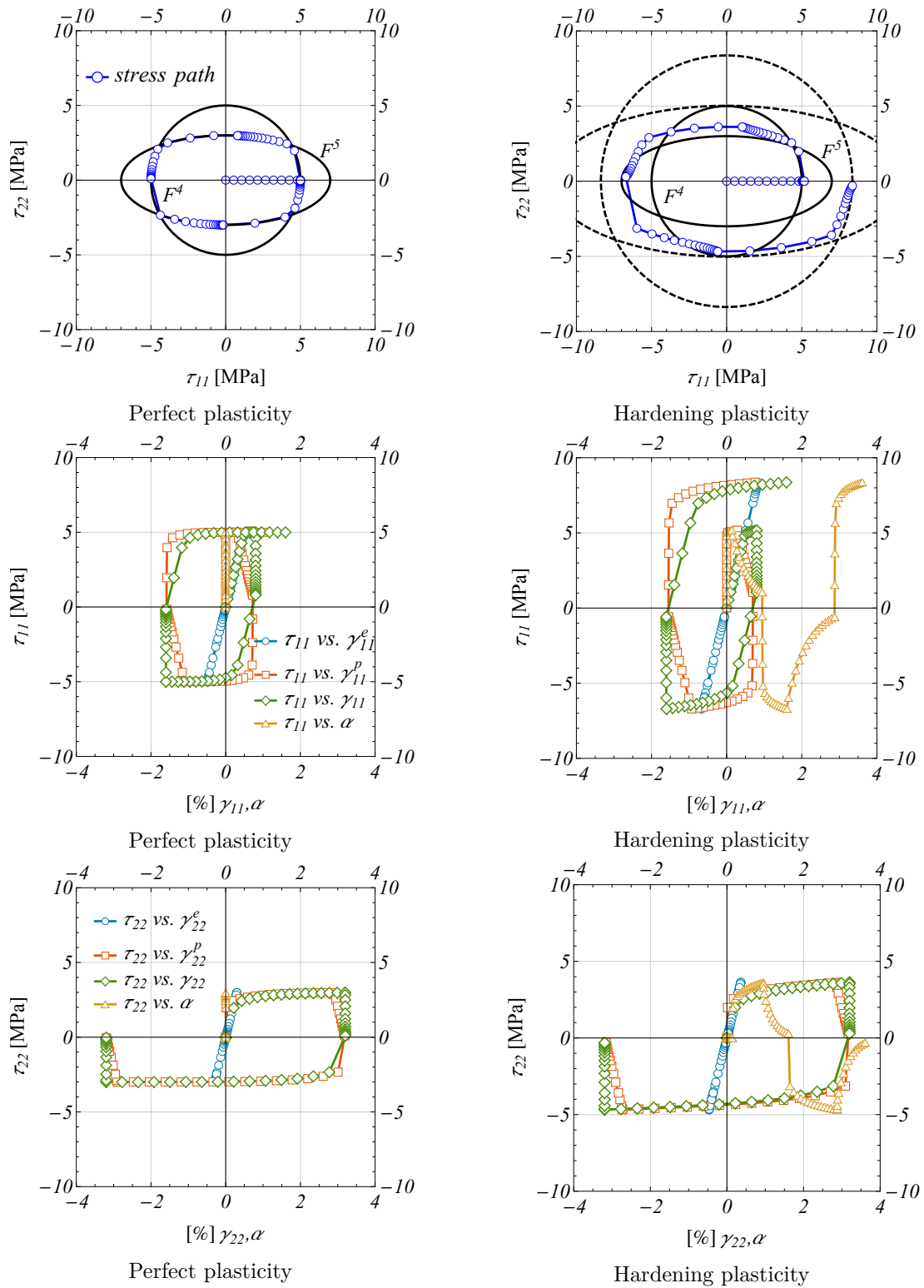


Figure 4.12: Element response to bi-axial test B5. Top: stress path in the $(\tau_{11} - \tau_{22})$ -plane. Center and bottom: stress-strain curve.

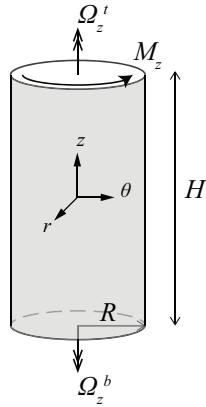


Figure 4.13: Hollow cylinder under axial rotation. Notations and boundary conditions.

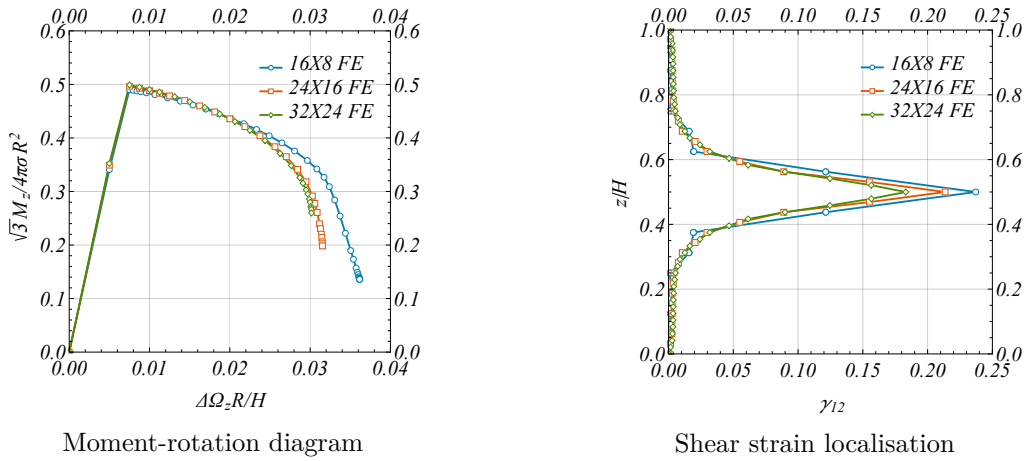


Figure 4.14: Macroscopic behaviour of the hollow cylinder (left) and localisation of the in-plane shear strain γ_{12} (right) for different discretisations with the COSS8R finite element (FE).

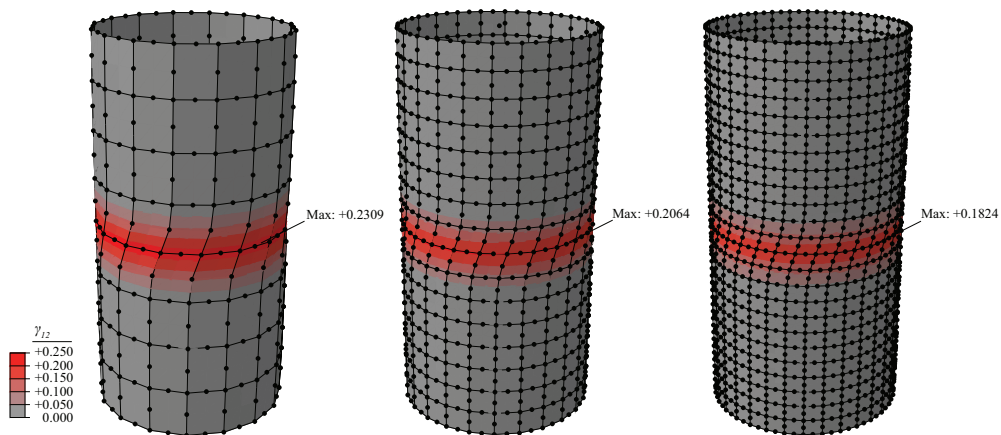


Figure 4.15: Deformation pattern and iso-contour of in-plane shear strain distribution for different discretisations of the hollow cylinder: left 16×8 FE, centre 24×16 FE, right 32×24 FE. Values for the ultimate resulting moment beyond the peak level.

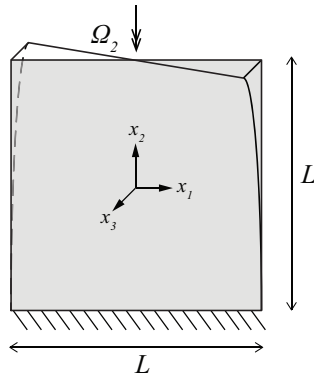


Figure 4.16: Square plate under torsion. Illustration of the boundary conditions and of the expected deformation pattern.

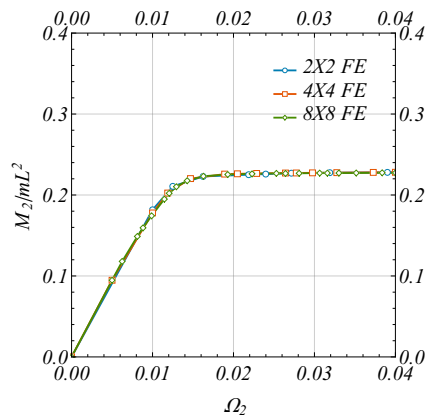


Figure 4.17: Macroscopic behaviour of the square plate under torsion for different finite element discretisations.

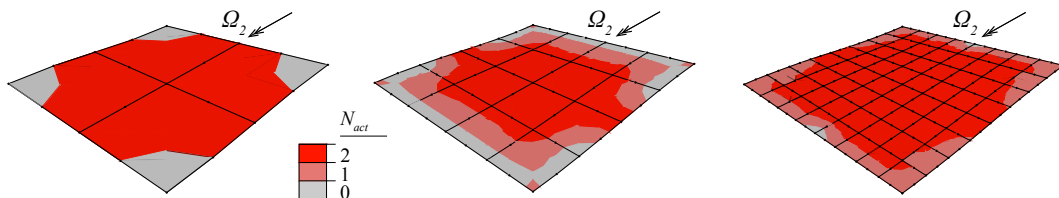


Figure 4.18: Deformation pattern and iso-contour of the number of activated plastic surfaces for different discretisations of the square plate: left 2×2 FE, centre 4×4 FE, right 8×8 FE.

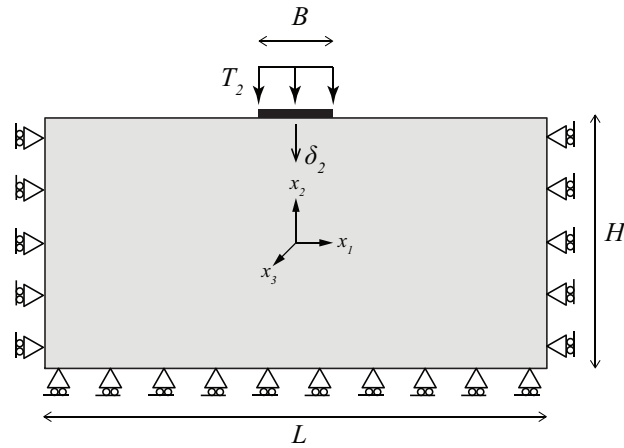


Figure 4.19: Shallow foundation under distributed pressure supported by a soil with micropolar properties. Geometry and boundary conditions.

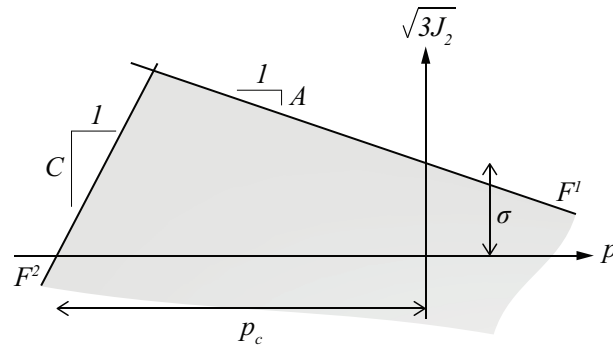


Figure 4.20: Illustration of the set of plastic surfaces describing the elastoplastic response of the soil.

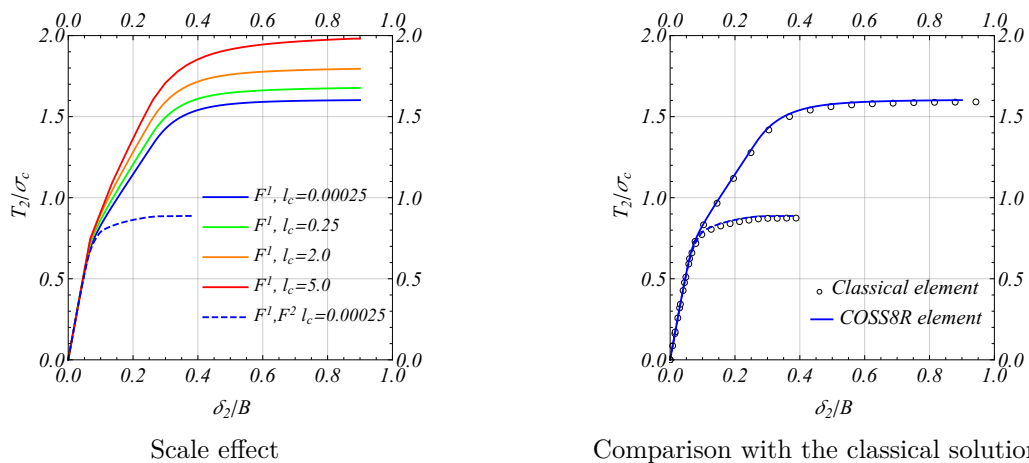


Figure 4.21: Left: macroscopic response of the shallow foundation for soils with different internal lengths. Right: response for small internal lengths ($l_c = 0.00025\text{m}$) and comparison with finite elements based on the Cauchy continuum (Krabbenhøft et al., 2007b).

Chapter 5

Scale effect in masonry failure: a numerical investigation by finite and discrete elements

This conclusive Chapter investigates the scale effect in the formation of failure mechanisms in masonry structures. Three different modelling strategies for masonry are proposed and compared. 1) A homogenisation model based on the Cosserat continuum; this model is constructed by implementing the homogenised yield criteria formulated in the previous Chapters into the developed Cosserat finite element. 2) A homogenisation model based on the Cauchy continuum; this model is constructed by selecting constitutive laws and yield criteria from the literature. 3) A discrete elements model. The performance of the three models in representing the elastoplastic response of a masonry panel is discussed. The capability of the homogenisation models in predicting the scale effect is investigated.

Contents

5.1	Modelling strategies for masonry	149
5.2	The elastoplastic Cosserat continuum model	149
5.2.1	The Cosserat medium	149
5.2.2	A Cosserat model for masonry	151
5.3	The elastoplastic Cauchy continuum model	151
5.3.1	The Cauchy medium	151
5.3.2	A Cauchy model for masonry	152
5.4	The discrete elements model	152
5.4.1	A discrete elements model for masonry	153
5.5	Modelling of a simple shear wall	153
5.5.1	Geometry, material properties and boundary conditions	153
5.5.2	Scale effect	154
5.5.3	Prediction of the wall response	155
5.5.4	Failure mechanisms and local deformations	155
5.6	Conclusions	156

Summary

Homogenisation models based on Cosserat continuum allow to model the mechanical behaviour of discrete media, with the account of their inner micro-structure. This applies both for the elastic and the inelastic properties of the medium, as for for example its strength. As shown in the previous Chapters, masonry can be considered as a discrete medium, due to its apparent periodic micro-structure.

In this short conclusive Chapter, three different modelling strategies for masonry are compared. A homogenisation model based on Cosserat continuum is first presented. The model is constructed by taking into account an existing homogenised constitutive law for elasticity and dynamics, and a set of homogenised yield criteria computed by following the procedure presented in Chapter 2. Such constitutive laws and yield criteria are introduced into the finite element formulation for Cosserat media presented in Chapter 4 and 5, allowing to carry out the analysis of masonry structures. Another homogenisation model based on Cauchy continuum is then presented. This model is constructed by introducing appropriate homogenised constitutive laws and yield criteria selected from the literature into a classical finite element formulation. The performance of the Cosserat continuum model is compared to that of the Cauchy continuum model, and the applicability of both models in representing masonry is discussed based on the comparison with a third analogue discrete elements model. The comparison is carried out in the elastoplastic static regime. With respect to the homogenisation models, the discrete elements model allows to represent masonry by respecting the actual arrangement, shape and size of the blocks. The relative size of the blocks with respect that of the structure determines then the scale ratio of masonry. The comparison between the three models reveals that the characteristic length inherent to the Cosserat medium enables to capture this scale ratio in the formation of failure mechanisms in masonry, in which the model based on the Cauchy medium does not succeed. The homogenisation model based on the Cosserat continuum proves therefore to be an appropriate and relevant modelling strategy for masonry structures.

5.1 Modelling strategies for masonry

Discrete elements and finite elements methods are two of the most widespread employed numerical procedures in mechanics for the analysis of materials and structures. Applied to masonry structures, these methods are used mainly to provide a *fine* and a *coarse* description of the structural behaviour (Trovalusci and Masiani, 1999), through the formulation of respectively *discrete* and *continuum* models. Discrete models are idealizations in which material particles are modelled separately and their interaction is represented explicitly. In continuum models, the particles constituting the material are smeared into an equivalent medium. Their interaction is described on the average sense only, by means of equivalent constitutive laws.

The finite element formulation presented in Chapter 3 and Chapter 4 allows the implementation of Cosserat continuum models of the type of a plate. Herein, it is in our purpose to evaluate the applicability (and demonstrate the advantages) of such continuum models against the use of more refined descriptions. A Cosserat continuum model is constructed by selecting as constitutive law for elasticity and dynamics, a homogenisation model already existing in the literature. The homogenised strength domains computed in Chapter 1 are then introduced as yield criteria, determining the elastoplastic response of masonry. The solution obtained by the continuum model is so compared to that given by the use of an analogue discrete elements model. Especially regarding masonry structures, such a comparison is of great importance, since some of the requisites demanded by practitioners can be tested in this way. In particular, it is our intent to investigate: a) the representation of the in-plane behaviour of masonry in the static elastoplastic regime, b) the evaluation of the scale ratio for which the applicability of the continuum model reaches its limits with respect to the discrete model and c) the solution accuracy provided by the two adopted modelling strategies. For further investigations on the in-plane response of masonry between linear and non-linear homogenised Cosserat continuum and discrete models, we refer respectively to Stefanou et al. (2008); Baraldi et al. (2015) and Cerrolaza et al. (1999); Trovalusci and Masiani (2003, 2005), among others.

A continuum model based on the classical (or Cauchy) medium is also considered in the comparison. This model is constructed by choosing both the elastic constitutive law and the yield criteria from those available in the literature. Its comparison with the continuum model based on the Cosserat medium and the discrete model has clearly a twofold character. On one hand, the performance of the Cauchy continuum model are explored with respect to the discrete model, in terms of solution accuracy. On the other hand, the definition of more appropriate yield criteria lead the Cosserat continuum model to prevail on the Cauchy model in the prediction of the scale effect associated to masonry failure.

A brief description of the continuum and the discrete models is given in the next three Sections. Notice that only basic notations will be provided for the continuum models and details on their numerical implementation will be skipped. For further details, the reader is referred to the previous Chapters.

5.2 The elastoplastic Cosserat continuum model

5.2.1 The Cosserat medium

In the Cosserat continuum, the material particle experiences displacements V_α (or translations) and angular displacements Ω^c (or rotations). The tensor $\Gamma_{\alpha\beta}$ accounts for the relative deformation occurring between the displacement gradient $D_{\alpha\beta}$ and the Cosserat (or particle) rotation Ω^c :

$$\Gamma_{\alpha\beta} = D_{\alpha\beta} + e_{\alpha\beta 3} \Omega_3^c, \quad (5.1)$$

with $D_{\alpha\beta} = V_{\alpha,\beta}$ and $e_{\alpha\beta\gamma}$ the Levi-Civita's symbol. $\Gamma_{\alpha\beta}$ is a non-symmetric tensor, and is decomposed into its symmetric $\Gamma_{(\alpha\beta)}$ and skew-symmetric $\Gamma_{[\alpha\beta]}$ parts reading:

$$\Gamma_{(\alpha\beta)} = D_{(\alpha\beta)}, \quad \Gamma_{[\alpha\beta]} = D_{[\alpha\beta]} + e_{\alpha\beta\gamma}\Omega_3^c. \quad (5.2)$$

The tensor $K_{3\beta}$ accounts for the rotation gradient (or curvature) of the medium, which writes:

$$K_{3\beta} = \Omega_{3,\beta}^c. \quad (5.3)$$

The equations governing the in-plane dynamic behaviour of a Cosserat medium are:

$$\begin{aligned} T_{\alpha\beta,\beta} + \rho (B_\alpha - \ddot{V}_\alpha) &= 0 \\ M_{3\beta,\beta} + e_{\alpha\beta\gamma}T_{\alpha\beta} + \rho (L_3 - I_3\ddot{\Omega}_3^c) &= 0, \end{aligned} \quad (5.4)$$

where B_α and L_3 are respectively the intensity of the external in-plane body forces and body couples acting on the medium, ρ the mass density of the medium, and I_3 its micro-inertia, which represents the rotary inertia of the particle. $T_{\alpha\beta}$ and $M_{3\beta}$ denote respectively the in-plane components of the non-symmetric stress tensor and of the couple stress tensor (Figure 5.1-left).

The deformation measures are split into an elastic $[\]^e$ and plastic $[\]^p$ part. The elastic constitutive law is:

$$T_{\alpha\beta} = A_{\alpha\beta\gamma\delta}\Gamma_{\gamma\delta}^e, \quad M_{3\beta} = D_{3\beta\gamma\delta}K_{3\delta}^e. \quad (5.5)$$

According to the multisurface plasticity theory (Chapter 4), the increments of plastic deformation are derived from the plastic potentials $P^j = P^j(T_{\alpha\beta}, M_\beta)$ as:

$$d\Gamma_{\alpha\beta}^p = \sum_{j=1}^{N_F} \lambda^j \partial_{T_{\alpha\beta}} P^j, \quad dK_{3\beta}^p = \sum_{j=1}^{N_F} \lambda^j \partial_{M_\beta} P^j, \quad (5.6)$$

with $\lambda^j \geq 0$ the consistency parameters. The elastic domain of the Cosserat medium \mathbb{E}_σ^c is herein denoted with G^c and is defined as:

$$G^c = \{(T_{\alpha\beta}, M_\beta) \mid F^j(T_{\alpha\beta}, M_\beta) \leq 0, \forall j = 1, \dots, N_F\}, \quad (5.7)$$

where the plastic surfaces $F^j = F^j(T_{\alpha\beta}, M_\beta)$ represent the yield criteria (Figure 5.1-right).

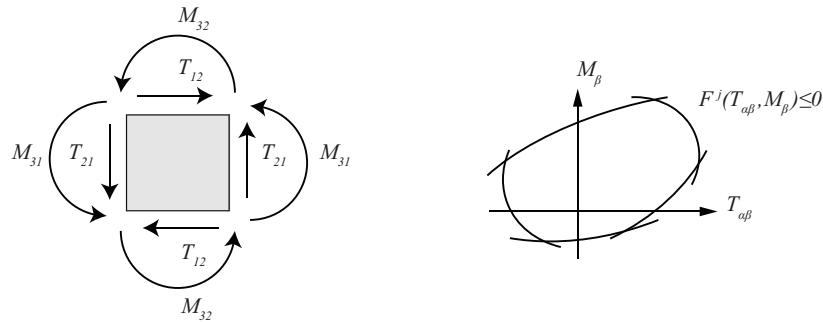


Figure 5.1: Notations used for the Cosserat medium (in-plane behaviour). Shear stresses and couple stresses (left) and elastic domain (right).

5.2.2 A Cosserat model for masonry

In view of the comparison between the Cosserat continuum and the discrete model, some existing homogenisation models can be selected from the literature. Concerning elasticity we have the works of Mühlhaus et al. (1997), Stefanou et al. (2008) and Salerno and de Felice (2009). Concerning plasticity we recall the yield criteria proposed by Mühlhaus et al. (1997) and those presented in Chapter 1 of the present thesis.

As far as it concerns the elastic and dynamic behaviour of masonry, we implement the continuum model proposed by Stefanou et al. (2008). This homogenisation model has been derived by identification of a running-bond masonry wall made of rigid blocks with an equivalent 3D Cosserat elastic continuum. The resulting model is an orthotropic Cosserat plate that is comprehensive of in- and out-of-plane elastic constitutive laws and inertial terms. The parameters entering the continuum model are the dimensions of the building blocks a, b and t (Figure 5.2), the normal and shear joint stiffness C_N, C_Q , and the mass density of the blocks ρ .

The elastoplastic behaviour of masonry is described through a set of multiple yield criteria. These criteria correspond to the strength domains computed through the homogenisation method presented in Chapter 1 and Chapter 2, by application of the kinematic approach of limit analysis. It is worth remarking that, based on this method, yield criteria may be computed for a running-bond masonry pattern with generic blocks overlap η and interfaces obeying a Coulomb slip criterion with properties c and ϕ that depend on their orientation. However, in order to be consistent with the elastic counterpart of the continuum model, the aforementioned criteria are computed with respect to the same diamond-shaped elementary cell considered by Stefanou et al. (2008) of a classical (1/2) running-bond pattern (Figure 5.2-right).

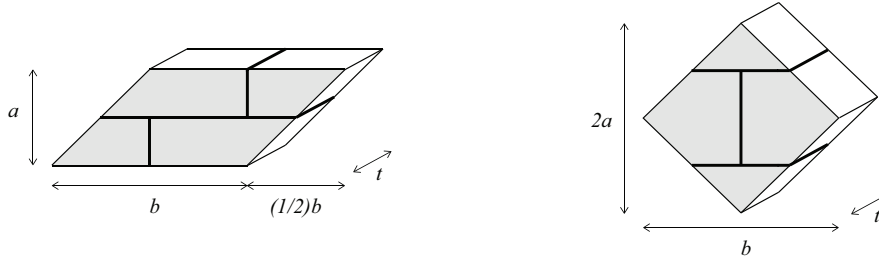


Figure 5.2: Two different elementary cells of a classical 1/2 running-bond masonry wall. Left: the cell with the form of a parallelogram considered for homogenisation in Chapter 1. Right: the diamond-shaped cell considered by Stefanou et al. (2008); de Buhan and de Felice (1997) and in the present Chapter.

5.3 The elastoplastic Cauchy continuum model

5.3.1 The Cauchy medium

In the Cauchy medium the kinematics of the material particle is described by the translations V_α only. The deformation measures of the medium reduce then to the symmetric tensor $D_{(\alpha\beta)}$ (Eq.(5.2)-1). The associated stress tensor is the symmetric tensor $T_{(\alpha\beta)}$ (Figure 5.3-left). The equations of motion are then given by Eq.(5.4)-1. Furthermore, in this case, the elastic domain is denoted with \mathbb{E}_σ (or G) and is defined as:

$$G = \{(T_{(\alpha\beta)}) | F^j(T_{(\alpha\beta)}) \leq 0, \forall j = 1, \dots, N_F\}, \quad (5.8)$$

where the plastic surfaces $F^j = F^j(T_{(\alpha\beta)})$ prescribe the N_F yield criteria for the Cauchy medium (Figure 5.3-right).

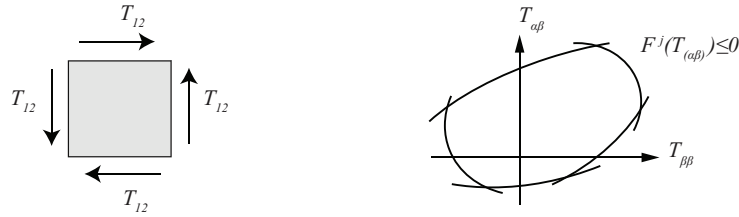


Figure 5.3: Notations used for the Cauchy medium (in-plane behaviour). Shear stresses (left) and elastic domain (right).

5.3.2 A Cauchy model for masonry

Many models existing in the literature are devoted to the description of masonry by means of homogenisation methods based on the Cauchy continuum. The number of models is far larger than those based on the Cosserat continuum. However, only few of them provide the expressions of the obtained constitutive laws in analytical form, making hard their use in further practical applications. Among those studying the elastic behaviour of masonry, one may cite [Cecchi and Di Marco \(2000\)](#); [Cecchi and Sab \(2002a\)](#); [Zucchini and Lourenço \(2002\)](#); [Salerno and de Felice \(2009\)](#). Among those studying the elastoplastic behaviour, we cite the works of [Alpa and Monetto \(1994\)](#); [de Buhan and de Felice \(1997\)](#).

Following the procedure depicted by [Salerno and de Felice \(2009\)](#), the homogenised elastic coefficients for masonry entering in the Cauchy continuum model can be derived as function of the coefficients of the Cosserat model, i.e.:

$$A_{Cauchy}^{1111} = A^{1111}, \quad A_{Cauchy}^{2222} = A^{2222}, \quad A_{Cauchy}^{1212} = 2 \frac{A^{1212} A^{2121}}{A^{1212} + A^{2121}}. \quad (5.9)$$

When based on the above relations, the Cauchy continuum model stocks the same amount of elastic strain energy density than the Cosserat one. This is satisfied under states of periodic deformation and provided that the Cosserat model is constructed by kinematic identification ([Salerno and de Felice, 2009](#)), as actually done by [Stefanou et al. \(2008\)](#). This legitimate the use of the above relations for the determination of the elastic coefficients of the present Cauchy model.

As far as it concerns the elastoplastic behaviour of masonry, we implement the homogenised yield criteria provided by [de Buhan and de Felice \(1997\)](#). These criteria are referred to the Cauchy continuum. As shown in [Chapter 1](#), they are a special case of the yield criteria computed for the Cosserat continuum model. They do not consider the effect of the relative rotations of the blocks in the formation of failure mechanisms. For this reason, they provide a coarser estimation of the plastic dissipation produced by masonry during the deformation process.

5.4 The discrete elements model

For the construction of the discrete elements model, we employ the commercial code 3DEC ([Itasca Consulting Group, 2013](#)). This program falls within the class of the discontinuous analysis procedures. Each block, that in our specific case is considered rigid, possesses 6 degrees-of-freedom and interacts with the adjacent blocks through a number of contact-points detected at the interfaces by means of an automatic detection algorithm ([Cundall, 1988](#); [Hart et al., 1988](#)). Contact forces are exchanged at these points. The code makes use of an explicit (or forward-Euler) time-integration scheme and takes into account large strains by updating at every load step the contact pairs detected at the interface of the blocks. Furthermore, the

occurrence of plastic deformations is computed within 3DEC by a classical projection algorithm similar to that discussed in [Chapter 4](#).

5.4.1 A discrete elements model for masonry

The discrete elements model allows to represent masonry by reflecting the actual blocks' arrangement, shape and size, and the actual interface properties. Consequently, the contact models on which the homogenisation models studied in elasticity and dynamics by [Stefanou et al. \(2008\)](#) and in elastoplasticity by [de Buhan and de Felice \(1997\)](#) and in [Chapter 1](#) and [Chapter 2](#) of the present work can be properly reproduced by 3DEC. Indeed, in all the aforementioned works masonry is regarded at the microscopic level as a discrete medium, in which blocks undergo rigid-body motions and with deformable interfaces. No calibration of the elastic stiffness parameters C_N and C_Q is thus necessary between the contact models considered in the homogenisation procedures and the discrete elements model. Moreover, the elastoplastic behaviour of the interfaces is accounted for by considering a Coulomb slip criterion with cohesion c , friction angle ϕ and associative properties. The fact that all geometric and material parameters of the discrete model are in agreement with those on which the continuum model is based, leads to (and justifies) the comparison between the three modelling approaches proposed in this Chapter.

5.5 Modelling of a simple shear wall

5.5.1 Geometry, material properties and boundary conditions

We consider a single-leaf masonry wall with height H , width L and thickness t ([Figure 5.4](#)). The wall is made of regular rigid blocks, disposed following a classical (1/2) running-bond pattern. The geometric and material properties used for the construction of the continuum ([Section 5.2](#), [Section 5.3](#)) and discrete ([Section 5.4](#)) models are given in [Table 5.1](#). In particular, the block aspect ratio is denoted with $m = 2a/b$.

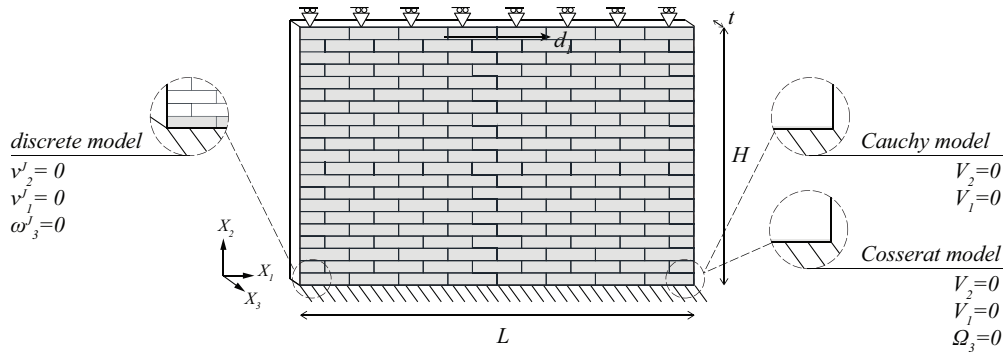


Figure 5.4: Masonry shear wall. Illustration of the geometry and boundary conditions adopted for the discrete and the continuum models.

[Figure 5.5](#) shows the resulting set of homogenised yield criteria for the Cosserat and the Cauchy continuum models. These criteria are plotted in the space of the Cauchy stress space, namely $(T_{11}, T_{22}, T_{(12)})$. For illustration purposes, the remaining stress components of the Cosserat continuum model have been fixed to $M_{31} = M_{32} = 0$ and $T_{[12]} = (1/3)T_{(12)}$ ([Figure 5.5-left](#)). It is worth emphasizing how, due to the non symmetry of the stress tensor, the homogenised elastic domain of the Cosserat continuum model is reduced with respect to that of

blocks	
m	0.4952 ($a = 52\text{mm}, b = 210\text{mm}$)
t	100mm
ρ	1.5kg/dm ³
joints	
C_N	80N/mm ³
C_Q	60N/mm ³
ϕ	30°
c	1.2N/mm ²

Table 5.1: Geometric and material properties of discrete and continuum models adopted for the masonry shear wall.

the Cauchy model. The domains are equivalent only when the stress state becomes symmetric (Figure 5.5-right).

The numerical benchmark carried out in this Section consists in modelling the behaviour of a shear wall. This consists of two steps: in step 1 a vertical load $q = 0.6\text{N/mm}^2$ is applied at the top side of the wall; in step 2, the vertical displacement and in-plane rotation are prevented and the horizontal displacement d_1 is controlled at the blocks belonging to the top side of the wall. This configuration is representative of infill masonry. Throughout the simulations, the following set of boundary conditions is applied (Figure 5.4): in the discrete elements model, blocks belonging to the lower course of the wall have their translations v_1^{GJ}, v_2^{GJ} and rotations ω_3^{GJ} prevented. The same conditions, but in terms of continuous kinematics V_1, V_2, Ω_3 , are applied to the Cosserat continuum model. The Cauchy continuum model allows then boundary conditions on the translations V_1, V_2 only.

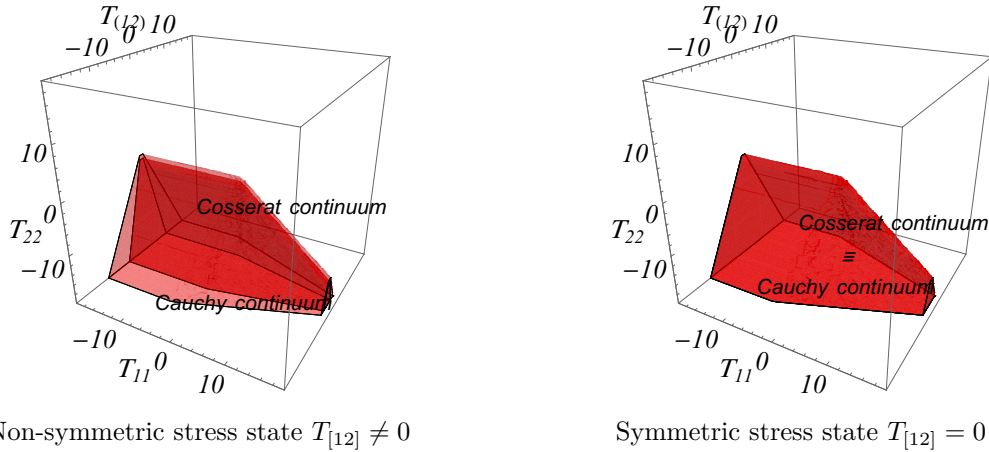


Figure 5.5: Set of homogenised yield criteria for 1/2 running-bond masonry, enclosing the elastic domains of the Cosserat (dark red) and the Cauchy (light red) elastoplastic continuum models (Table 5.1). Domains for non-symmetric (left) and symmetric (right) stress states.

5.5.2 Scale effect

The comparison between the discrete and the homogenised continuum models is carried out on walls with increasing number of blocks. In particular, we consider walls composed by $2 \times 5, 4 \times$

10, 8×20 , 12×30 and 16×40 blocks (Figure 5.6). The thickness of the wall t is kept constant and the wall aspect ratio is $L/H = 0.619$. Based on this strategy, elastoplastic analyses are carried out with the intent of comparing the response of masonry when the relative size of the blocks to the size of the structure becomes smaller and smaller.

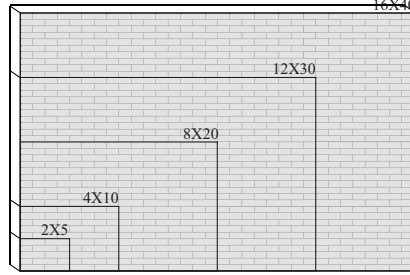


Figure 5.6: Walls made up of different number of blocks considered for the study of the scale effect in masonry.

Figure 5.7 shows the response of the wall captured by the three models in terms of normalized force-displacement diagrams. In these curves, F_1 is the horizontal reaction force computed at the base of the wall and δ_1 is the normalized displacement (or *drift*) controlled at the top of the wall: $\delta_1 = (d_1/H) \times 100$. Normalization enables to investigate the scale effect. The curves are in fact equivalent to those obtained if wall's dimensions were kept constant and blocks' size decreased. A considerable scale effect is observed from the discrete model. When walls are composed by a smaller number of blocks, the wall response shows clearly a steeper slope in the elastic and the elastoplastic branch. The Cosserat continuum model also captures this scale effect (even if in a less marked manner), while the Cauchy model does not.

5.5.3 Prediction of the wall response

Figure 5.8 compares the solution provided by the continuum models versus the discrete elements solution, the number of blocks being fixed. We notice how, for walls composed by few blocks (5×2), the difference between the three models is large. In this case, boundary conditions play a fundamental role, which have not been taken into account in the formulation of the homogenisation models considered (Stefanou et al., 2008; Salerno and de Felice, 2009; de Buhan and de Felice, 1997, and Chapter 1). However, as far as the number of blocks increases, this difference between the discrete and the Cosserat continuum models tends to vanish, disclosing an expected trend towards a unique *homogenised* response. The Cauchy continuum model is, on the contrary, less representative of response of the wall than the Cosserat continuum model, even in the limit of small scale ratios (large number of blocks).

5.5.4 Failure mechanisms and local deformations

The force-displacement diagrams discussed above are representative of the overall response of the walls. In order to investigate the validity of the continuum models with respect to the discrete one, it is also interesting to compare the finite and discrete elements solutions in terms of a) the formation of failure mechanisms, and b) the development of local irreversible deformations.

Figure 5.9-Figure 5.11 show how the regions of the wall in which the stress state activates the homogenised yield criteria in the continuum models correspond to the regions the discrete elements model where plastic deformations (in terms of slips between the blocks) are initiated into. The Figures are referred to the wall made of 12×30 but similar patterns are observed in walls made of fewer blocks. This makes evident that the failure mechanisms described by the

three modelling approaches are, at least qualitatively, in accordance. However, the Cosserat continuum model seems to better capture the failure pattern in its final configuration.

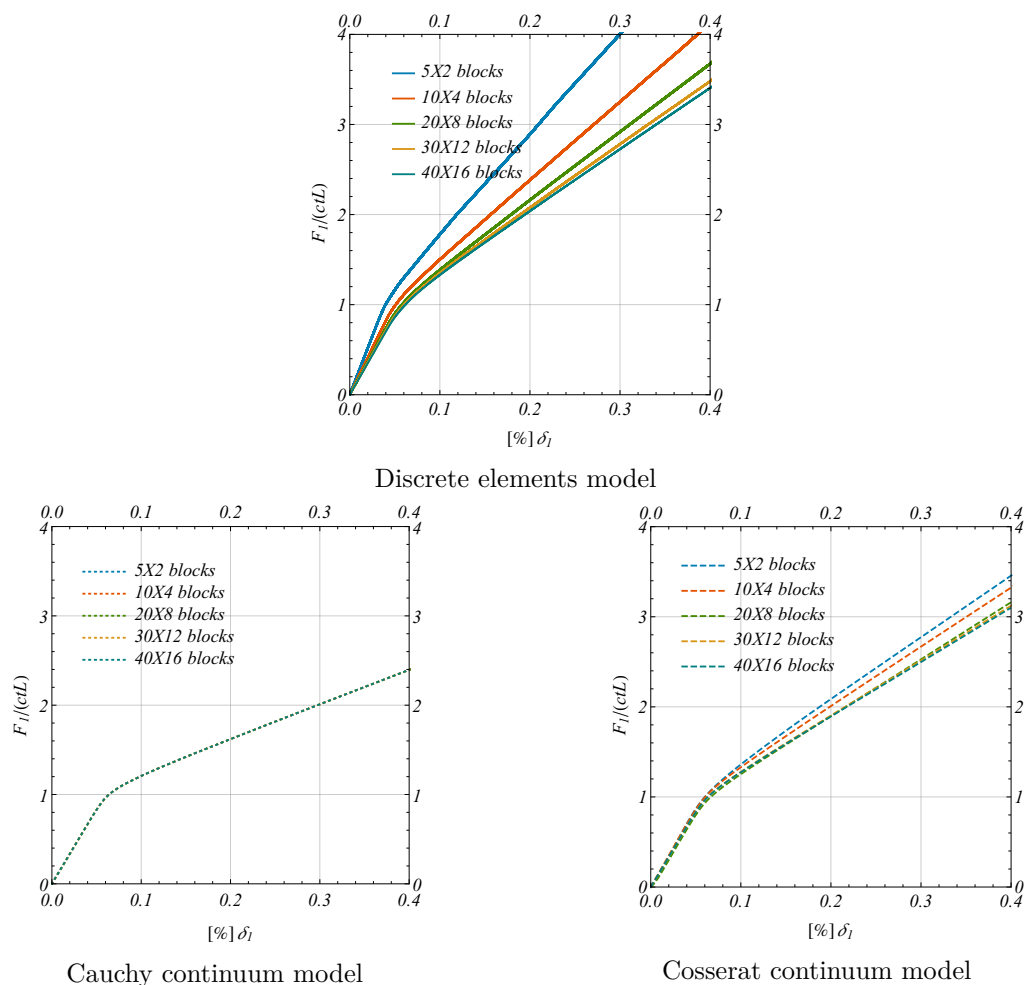


Figure 5.7: Scale effect in a confined masonry wall under shear. Normalized force-displacement diagrams from the discrete (top) and the homogenised continuum models (bottom), for walls composed by different number of blocks. The response given by the Cauchy model is invariant of the number of blocks.

5.6 Conclusions

In this conclusive Chapter, a homogenisation model based on Cosserat continuum was proposed as modelling strategy for masonry structures. The model was constructed by selecting from the literature an already existing constitutive law for masonry in elasticity. Besides, a set of multiple homogenised yield criteria were computed in rigorous manner, based on the analytical approach presented in Chapter 1 and Chapter 2. The homogenised elastic coefficients and plastic surfaces were next implemented into the finite element formulation for Cosserat plate models developed in Chapter 3 and Chapter 4, making possible to carry out the analysis of structural elements.

A homogenisation model based on the Cauchy medium was also considered. In this case, the elastoplastic behaviour was controlled by elastic constitutive laws and yield criteria entirely taken from the literature and consistent with those used for the construction of the Cosserat

continuum model. The response of the Cosserat and Cauchy continuum models was compared to that of an analogue discrete elements model, in which blocks were modelled as rigid bodies and their interaction was represented explicitly by means of contact laws.

A masonry wall under shear loading was taken as example for the numerical simulations and the comparisons between the three models. The results obtained demonstrated the efficiency of the homogenisation models in modelling the formation of failure mechanisms within masonry. However, only the Cosserat continuum model proved capable to predict the scale effect in masonry failure, which was illustrated by the discrete elements model.

This short conclusive Chapter made possible to show an application of the modelling approach presented in this thesis to masonry structures. At first approach, the presented *elasto-plastic Cosserat continuum model* shows able performance in the prediction of the overall response of masonry, both considering its elastic and inelastic behaviour. Moreover, a phenomenon rarely considered in the technical literature as the scale effect (Salerno and de Felice, 2009; Trovalusci and Masiani, 2003, 2005) is efficiently taken into account by the Cosserat model, unlike the classical approaches based on the Cauchy medium.

Of course, at this stage many other examples should be provided in order to gain a deeper insight on the subject. For instance, the scale effect can be even more pronounced when openings such as doors and windows are present into the wall. The presented model constitutes, however, the basis for the creation of a more sophisticated numerical tool for the seismic analysis of masonry structures. In this perspective, the implementation of a complete set of yield criteria as those presented in Chapter 2 for the coupled in-plane and out-of-plane behaviour of masonry must be considered in future works. The model should then be extended to block crushing (Stefanou et al., 2015). The introduction of specific evolutions laws for the softening and damage behaviour of masonry is then a task to be envisaged.

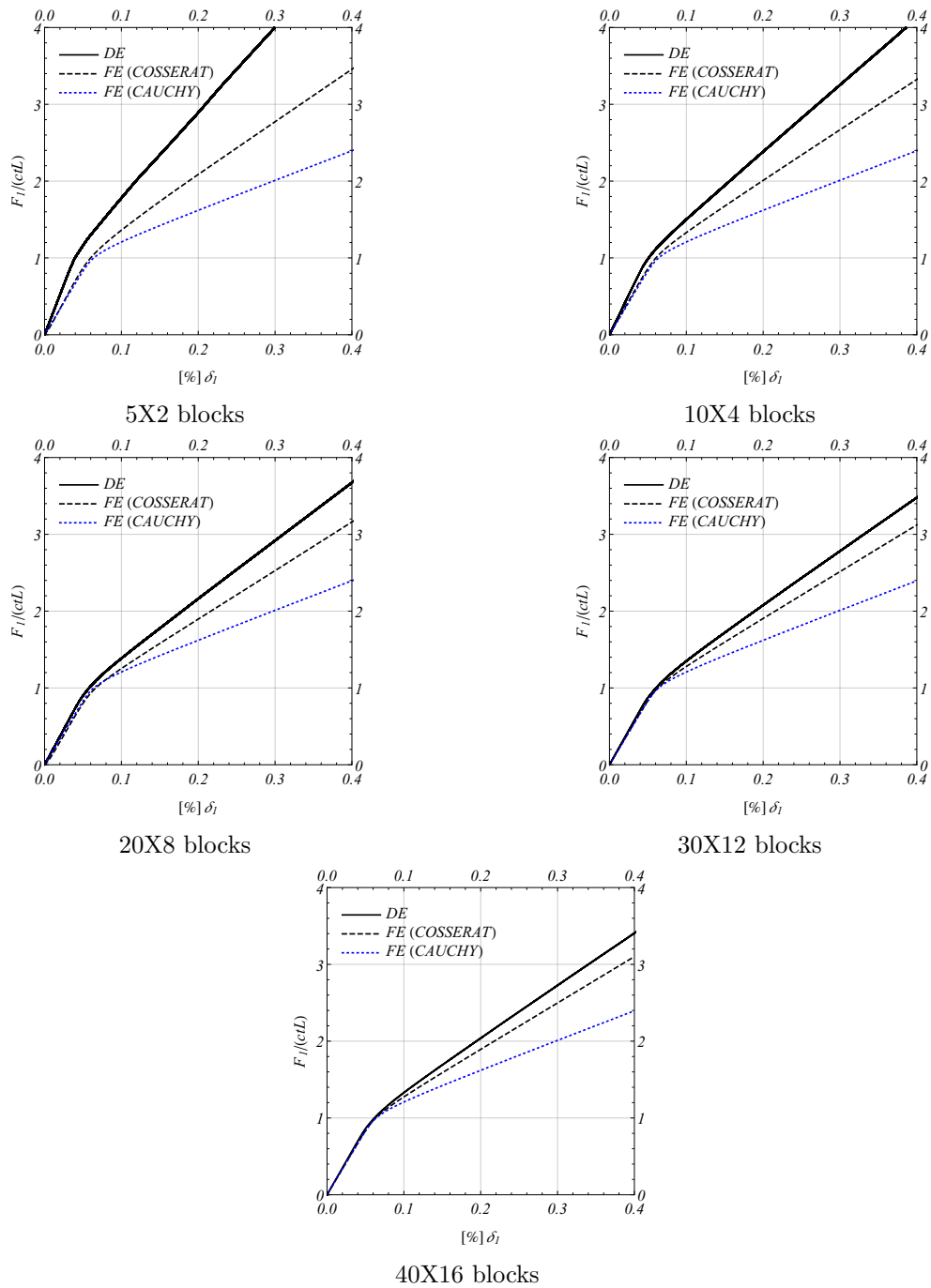
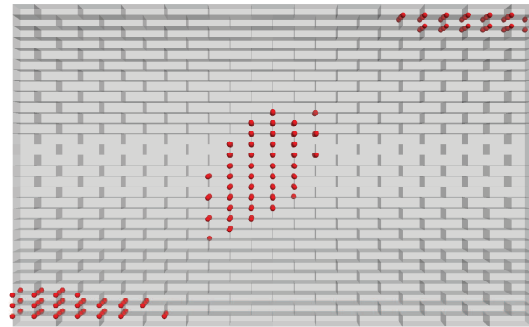
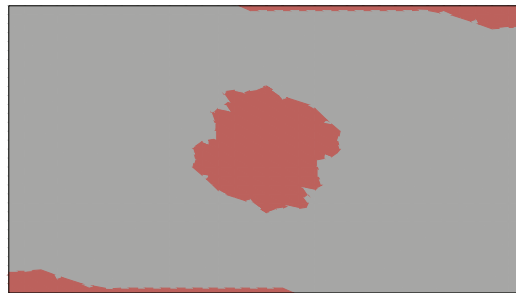


Figure 5.8: Comparison between the discrete elements (DE) and the homogenised continuum finite element (FE) models in modelling a masonry shear wall, in terms of normalized force-displacement diagrams. Results are presented from the top to the bottom for walls composed by an increasing number of blocks.



Discrete elements model



Cauchy continuum model

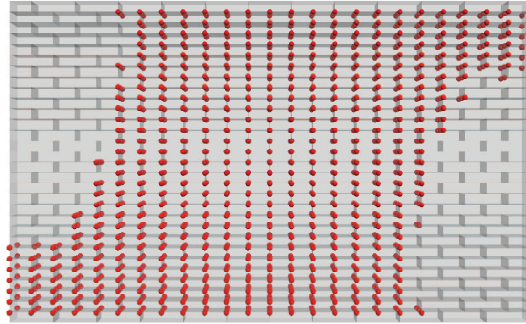


Cosserat continuum model

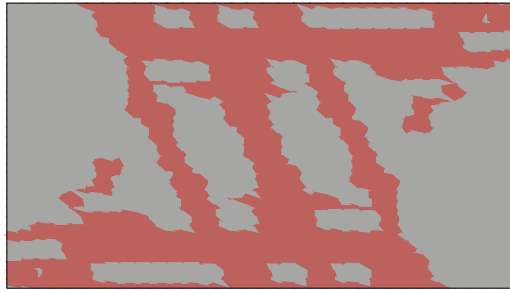


$$\delta_1 \approx 0.05$$

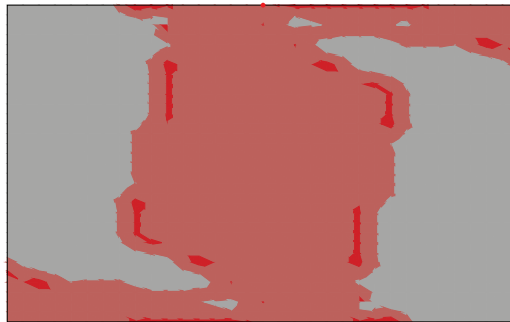
Figure 5.9: Development of the inter-block slip in the discrete elements model when $\delta_1 \approx 0.05$ (top - red dots) versus activation of the multiple homogenised yield criteria in the Cauchy (red region - centre) and Cosserat continuum model (bottom). Wall made of 12×30 blocks.



Discrete elements model



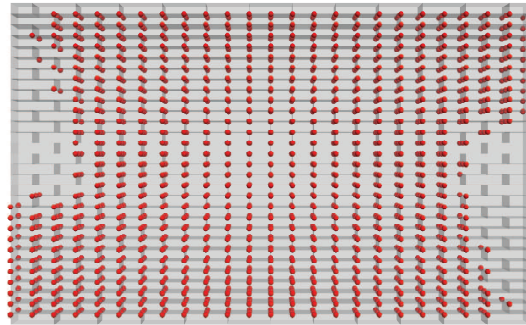
Cauchy continuum model



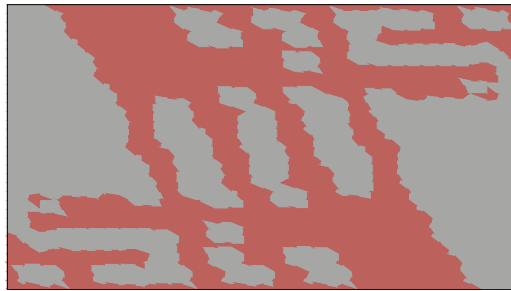
Cosserat continuum model

$$\delta_1 \approx 0.1$$

Figure 5.10: Development of the inter-block slip in the discrete elements model when $\delta_1 \approx 0.1$ (top - red dots) versus activation of the multiple homogenised yield criteria in the Cauchy (red region - centre) and Cosserat continuum model (bottom). Wall made of 12×30 blocks.



Discrete elements model



Cauchy continuum model



Cosserat continuum model

$$\delta_1 \approx 0.2$$

Figure 5.11: Development of the inter-block slip in the discrete elements model when $\delta_1 \approx 0.2$ (top - red dots) versus activation of the multiple homogenised yield criteria in the Cauchy (red region - centre) and Cosserat continuum model (bottom). Wall made of 12×30 blocks.

Conclusions

Summary of the main contributions

Analytical work

The analytical work carried out in this thesis is mainly found in [Chapter 1](#) and [Chapter 2](#). In these Chapters, the development of an analytical method for the estimation of the homogenised in-plane and out-of-plane strength of masonry was carried out.

- In [Chapter 1](#) the method was formulated for the assessment of the in-plane strength of masonry. In particular, the question of the influence of the relative rotation of the blocks on the strength capacity of masonry was addressed. It is clear that the relative rotation of the blocks contribute to the relative displacement across the joints and consequently promote the formation of irreversible deformations and failure mechanisms within masonry. This aspect is visible from the majority of the experimental tests carried out on masonry walls, either in the form of local rotations or of veritable flexural modes. However, it was seldom explored in the literature. The homogenisation method introduced in [Chapter 1](#) provided further development to the current state-of-the-art methodology for calculating the strength of masonry, by introducing in rigorous manner the influence of blocks' rotations.

The homogenisation method was based on the Cosserat continuum theory. The enhanced kinematics of the Cosserat continuum allowed a more efficient description of masonry with respect to that already given in the literature by the use of the Cauchy continuum. The improvements referred, first, to a finer reproduction of the deformation modes of masonry. Relative blocks' rotations were in fact related to the macroscopic in-plane curvatures and the non-symmetric strains of the Cosserat medium, which are absent in the classical continuum theory. Furthermore, the Cosserat continuum provided an improved estimation of the power dissipated during failure. For these reasons, the yield criteria computed for the Cosserat continuum are better estimates of the actual strength capacity of masonry, as compared to those computed for the Cauchy continuum.

The use of the Cosserat continuum in the evaluation of masonry strength has already been encountered in the literature. The novelty of the presented analytical method was given by the fact that no a priori assumptions were made on the most relevant failure mechanisms that may occur within masonry. On the contrary, failure mechanisms were researched among all the possible mechanisms involving the relative translations and rotations of the blocks. The examples of the masonry column and wall showed that, whatever the blocks disposition and joints properties, their overall strength capacity were reduced due to the relative rotation of the blocks. It was shown how this effect was correctly captured by the Cosserat continuum, which, unlike the Cauchy continuum, admits in-plane moments and non-symmetric shear forces.

It is worth mentioning that the presence of moments acting in the plane of the walls is intrinsic in structural problems related to masonry, especially in those related to seismic analyses. Aiming at formulating a modelling strategy for masonry in this field, the contribution given by the Cosserat continuum in modelling its strength is therefore of great importance.

- The homogenisation method presented in [Chapter 1](#) focused on the in-plane strength of masonry. In [Chapter 2](#) the method was extended for the assessment of the coupled in-plane and out-of-plane strength of masonry. In that case, the overall strength of masonry columns and walls was determined by deriving an equivalent Cosserat continuum with complete three-dimensional kinematics. As a result of the homogenisation procedure, the

number of macroscopic deformation measures was reduced. This result was consistent with the geometry of the column and wall. The masonry column was so ascribed to a Cosserat beam model. The masonry wall was then assumed as a Cosserat (or micropolar) plate model. Both models were comprehensive of complete three-dimensional kinematics, and showed an apparent interaction between the in-plane and the out-of-plane actions in the assessment of masonry strength. The relative rotation of the blocks accentuated this effect and diminished the in-plane strength. The use of three-dimensional with respect to two-dimensional models for masonry was therefore encouraged.

Numerical work

The numerical work carried out in this thesis is mainly found in [Chapter 3](#) and [Chapter 4](#). In these Chapters, the development of an elastoplastic finite element formulation for Cosserat plate models was carried out.

- In [Chapter 3](#), a specific quadratic element with reduced integration was presented. The interesting aspect emerging from the formulation of the element was that the terms of the stiffness matrix associated with the displacement and the rotational fields both conferred rigidity to the element. On one hand, this enabled the element to control in direct manner the occurrence of spurious and hourglass modes versus forces and moments acting on its plane. On the other hand, it made the element suitable for the assemblage of spatial shell structures. This aspect represents an important (and yet not well known) advantage that should encourage and privilege the use of finite elements based on the Cosserat continuum theory versus more classical formulations based on the Cauchy continuum, for which the use of artificial hourglass-control techniques is always needed.

The presented element was tested in predicting the in-plane and the out-of-plane static and modal response of various structural configurations. The choice of a quadratic interpolation order allowed the element to attain a good level of accuracy in representing the out-of-plane behaviour of the plate, even in the limit of thin geometries. Moreover, the element showed high precision in representing the modal frequencies in simple structural configurations. The use of the presented element in dynamic simulations based on direct integration techniques is therefore expected to be advantageous. Its relatively simple formulation makes it preferable to other elements based on higher order or selective interpolations. The limited computational cost due to the reduced integration of the stiffness matrix makes it still competitive in non-linear problems as compared to elements based on linear interpolation orders.

- The finite element formulation for Cosserat plate models was developed in [Chapter 3](#) in elasticity and dynamics. In [Chapter 4](#), the formulation was extended to the elastoplastic framework. Material non-linearities were taken into account in the formulation through the implementation of the multisurface plasticity theory. The implementation of this theory for the Cosserat medium was based on a projection algorithm formulated for implicit (backward-Euler) time-integration schemes. The same algorithm may be found in more classical formulations, as those of the classical (Cauchy) continua or those for the generalized theories of beams and shells. In this case, an important correction was made in the implementation of the algorithm. The correction consisted in the use of a non conventional matrix-inversion technique, based on the singular value decomposition (SVD) method. The introduction of this technique allowed the presented finite element formulation to attain all the salient features of the multisurface plasticity theory and to overcome some important limitations that are present in its classical implementation. In particular,

it enabled the definition of plastic surfaces and evolution laws that are unlimited in number and of the most general form. It was found that many (basic) configurations limiting the use of the projection algorithm for multisurface plasticity can be avoided through this method. Its use in more classical theories and models is therefore recommended.

The finite element presented in [Chapter 3](#) was also tested in the framework of multisurface plasticity in [Chapter 4](#), by means of several numerical benchmarks. In general, the element showed high level of accuracy and able performance in the solution of elastoplastic problems involving multiple plastic surfaces, strain-hardening mechanisms and strain localisation phenomena. The full rate of convergence was preserved in the simulations by the use of the actual elastoplastic tangent stiffness matrix of the element. This matrix was derived explicitly in its algorithmic form, for the most general multisurface, strain-hardening and non-associative case. This form is hardly found in the literature. Herein it was given in matrix notation, making straightforward its further implementation in numerical codes using the Newton-Raphson and the arc-length methods.

Modelling of masonry structures

The analytical and the numerical parts of the thesis contributed to the development of a homogenisation continuum model for masonry, which is the primary objective of the present research work. The formulation and the use of this continuum model are found in [Chapter 3](#) and the conclusive [Chapter 5](#).

- In [Chapter 3](#), a homogenisation model for masonry existing in the literature was implemented into the developed finite element formulation, with the aim of reproducing the three-dimensional behaviour of masonry in elasticity and dynamics. The model was based on the Cosserat continuum and was tested in reproducing the modal response of a masonry panel made of rigid blocks and deformable interfaces. Its validity was discussed based on the comparison with an analogue discrete elements model. The convergence of the homogenisation and the discrete elements model in the limit of small blocks was assessed. This was made by regarding the principal deformation modes of the panel, related to the in-plane shear, out-of-plane flexion and torsion of the panel. The role of the in-plane blocks rotations in the inertial response of the panels was also investigated. In this case, the in-plane shear deformation mode of the panel was selected. The modal effective mass associated to in-plane rotations of the blocks was computed by the Cosserat homogenisation model. This quantity is representative of the modal inertia related to those specific kinematics. Therefore, it cannot be represented by models based on the Cauchy continuum. Simulations revealed an important participation of the in-plane rotations of the blocks to the inertial response of the panel, encouraging the use of models based on the Cosserat continuum for the seismic analysis of masonry structures.
- In [Chapter 5](#), the elastoplastic behaviour of a masonry panel acting as shear wall was modelled. This was made possible by enriching the homogenisation model for elasticity considered in [Chapter 3](#) with the homogenised yield criteria computed based on the procedure developed in [Chapter 1](#) and [Chapter 2](#). The comparison with the analogue discrete elements model was made by modelling explicitly, in this latter, the elastoplastic behaviour of the joints. The results obtained from the comparison demonstrated the efficiency of the homogenisation model in representing the discrete elements response in the limit of small blocks. In this case, attention was focused on the capacity of the continuum model in representing the formation of failure mechanisms within masonry and in predicting its overall non-linear response.

The comparison with a homogenisation model based on the Cauchy continuum illustrated then how the Cosserat continuum model is capable to predict the apparent scale effect observed in masonry failure, while the model based on the Cauchy medium did not. In conclusion, the internal length inherent to the Cosserat medium enables to introduce the characteristic length related to masonry micro-structure. In this way, the scale effect and the influence of the relative rotation of the blocks are efficiently taken into account by the continuum model. This concerns the elastic, modal and the elastoplastic behaviour of masonry. Its implication in the seismic analysis of masonry structures proves then crucial.

Perspectives

This thesis contributed to the development of a robust continuum model for masonry structures. The model was based on rigorous homogenisation methods and was formulated in the framework of the Cosserat continuum theory. Homogenisation yields a limited number of parameters in the model. Cosserat continuum is the first of the enhanced continuous media, for which the internal length related to masonry micro-structure can be properly introduced and modelled.

In the formulation of continuum models for masonry, the study of the following topics by means of homogenization methods still remains challenging:

- the effect of boundary conditions, as the presence of boundary layers and the interaction with other building materials such as reinforced-concrete, steel, wood, etc.
- the effect of large deformations and large deflections
- the modelling of damage and softening behaviour (post-peak response)
- the modelling of the finite strength of the blocks
- the response to creep
- the modelling of more complex masonry patterns, i.e. brickworks made of two or multiple types of blocks, or voids.

Appendices

Appendix A

A.1 Average Cosserat deformations of the discrete cell

The expression of the average cell translation V_α can be demonstrated by introducing Eq.(1.28)-1 into the form:

$$\begin{aligned}
& \frac{1}{|D|} \left(\sum_{J=1}^{N_D} \int_{B^J} v_\alpha^J dS \right) = \\
& = \frac{1}{|D|} \left(\sum_{J=1}^{N_D} \int_{B^J} \left(\Gamma_{\alpha\beta} y_\beta^{GJ} + V_\alpha - e_{\alpha\beta} \left[K_\gamma y_\gamma^{GJ} (y_\beta - y_\beta^{GJ}) + \Omega^c y_\beta \right] \right) dS \right) \\
& = V_\alpha + \frac{1}{|D|} \Gamma_{\alpha\beta} \left(\sum_{J=1}^{N_D} y_\beta^{GJ} |B^J| \right) - \frac{1}{|D|} e_{\alpha\beta} K_\gamma \left(\sum_{J=1}^{N_D} y_\gamma^{GJ} \int_{B^J} (y_\beta - y_\beta^{GJ}) dS \right) \\
& \quad - \frac{1}{|D|} e_{\alpha\beta} \Omega^c \left(\sum_{J=1}^{N_D} \int_{B^J} y_\beta dS \right) \\
& = V_\alpha + \Gamma_{\alpha\beta} y_\beta^{G0} - e_{\alpha\beta} \Omega^c y_\beta^{G0}. \tag{A.1}
\end{aligned}$$

When the local reference system is taken at the centre of mass of the elementary cell, the expression reduces to V_α (Eq.(1.33)). Note that one could obtain the same result also by considering:

$$\frac{1}{|D|} \left(\sum_{J=1}^{N_D} \int_{B^J} v_\alpha^{GJ} dS \right) = V_\alpha \tag{A.2}$$

A proof similar to that shown above for V_α applies for the expression of Ω^c (Eq.(1.32)). The only difference is that, in this case, Eq.(1.28)-2 must be considered instead of Eq.(1.28)-1.

For the demonstration of $D_{\alpha\beta}$ (Eq.(1.31)) one can write:

$$\begin{aligned}
& \frac{1}{|D|} \left(\sum_{IJ} \int_{\Sigma^{IJ}} \llbracket v_\alpha^G \rrbracket^{IJ} n_\beta^{IJ} dL \right) = \\
& = \frac{1}{|D|} \left(\sum_{IJ} \int_{\Sigma^{IJ}} \left(v_\alpha^{GI} n_\beta^{IJ} + v_\alpha^{GJ} n_\beta^{JI} \right) dL \right),
\end{aligned}$$

$$\begin{aligned}
&= \frac{1}{|D|} \left(\sum_{J=1}^{N_D} \int_{\partial B^{J,i}} v_{\alpha}^{GJ} n_{\beta}^J dL \right) \\
&= \frac{1}{|D|} \left(\sum_{J=1}^{N_D} \int_{\partial B^J} v_{\alpha}^{GJ} n_{\beta}^J dL \right) - \frac{1}{|D|} \left(\sum_{J=1}^{N_D} \int_{\partial B^{J,e}} v_{\alpha}^{GJ} n_{\beta}^J dL \right), \tag{A.3}
\end{aligned}$$

where the boundary of every block ∂B^J is split into the part belonging to the cell interfaces $\partial B^{J,i}$ and the part belonging to the external boundary of the cell: $\partial D = \bigcup_{J=1}^{N_D} \partial B^{J,e}$ and $\partial B^J = \partial B^{J,i} \cup \partial B^{J,e}$. After the divergence theorem and by using Eq.(1.28)-1, the first term gives:

$$\begin{aligned}
&\frac{1}{|D|} \left(\sum_{J=1}^{N_D} \int_{\partial B^J} v_{\alpha}^{GJ} n_{\beta}^J dL \right) = \\
&= \frac{1}{|D|} \left(\sum_{J=1}^{N_D} \int_{B^J} v_{\alpha,\beta}^{GJ} dL \right) = 0, \tag{A.4}
\end{aligned}$$

while the second term yields:

$$\begin{aligned}
&-\frac{1}{|D|} \left(\sum_{J=1}^{N_D} \int_{\partial B^{J,e}} v_{\alpha}^{GJ} n_{\beta}^J dL \right) = \\
&= -\frac{1}{|D|} \left(\sum_{J=1}^{N_D} \int_{\partial B^{J,e}} (D_{\alpha\gamma} y_{\gamma}^{GJ} + V_{\alpha}) n_{\beta}^J dL \right) \\
&= -\frac{1}{|D|} D_{\alpha\gamma} \left(\sum_{J=1}^{N_D} y_{\gamma}^{GJ} \int_{\partial B^{J,e}} n_{\beta}^J dL \right) - \frac{1}{|D|} \left(\sum_{J=1}^{N_D} V_{\alpha} \int_{\partial B^{J,e}} n_{\beta}^J dL \right) = D_{\alpha\beta}. \tag{A.5}
\end{aligned}$$

The last passage in Eq.(A.5) is proved by the fact that the elementary the cell is enclosed by the periodicity vectors $\boldsymbol{\alpha}^1, \boldsymbol{\alpha}^2$. Therefore, the two outward unit normal vectors of the boundary of the cell ∂D are the covariant vectors of $\boldsymbol{\alpha}^1, \boldsymbol{\alpha}^2$. The same considerations apply for the demonstration of K_{β} (Eq.(1.30)), which is not reported here. The demonstration of Eq.(1.29) for the marcoscopic relative deformation $\Gamma_{\alpha\beta}$ is also similar, and leads to long expressions. For brevity, it will be avoided in the text.

A.2 Macroscopic relative deformations and curvatures on the elementary cell A

By making use of Eqs.(1.29)-(1.30), and taking into account the rigid-body kinematics of the blocks (Eq.(1.15)), it is possible to compute the macroscopic Cosserat deformations and curvatures of the cell A in terms of the translational and rotational kinematics of the blocks. As the stack bond and the running bond are common in applications, we give here their expressions.

For the stack bond pattern ($\eta = 0$), the average relative deformations hold:

$$\begin{aligned}\Gamma_{11} &= \frac{v_1^{G1} - v_1^{G2} - v_1^{G3} + v_1^{G4}}{2b} + \frac{a(\omega^{G1} - \omega^{G2} + \omega^{G3} - \omega^{G4})}{8b} \\ \Gamma_{12} &= \frac{v_1^{G1} + v_1^{G2} - v_1^{G3} - v_1^{G4}}{2a} + \Omega^c \\ \Gamma_{21} &= \frac{v_2^{G1} - v_2^{G2} - v_2^{G3} + v_2^{G4}}{2b} - \Omega^c \\ \Gamma_{22} &= \frac{v_2^{G1} + v_2^{G2} - v_2^{G3} - v_2^{G4}}{2a} - \frac{b(\omega^{G1} - \omega^{G2} + \omega^{G3} - \omega^{G4})}{8a},\end{aligned}\tag{A.6}$$

and the average curvatures read:

$$\begin{aligned}K_1 &= \frac{\omega^{G1} - \omega^{G2} - \omega^{G3} + \omega^{G4}}{2b} \\ K_2 &= \frac{\omega^{G1} + \omega^{G2} - \omega^{G3} - \omega^{G4}}{2a}.\end{aligned}\tag{A.7}$$

For the running bond pattern ($\eta = 1/2$), Eqs.(1.29)-(1.30) become:

$$\begin{aligned}\Gamma_{11} &= \frac{v_1^{G1} - v_1^{G2} - v_1^{G3} + v_1^{G4}}{2b} + \frac{a(\omega^{G1} - \omega^{G2} + \omega^{G3} - \omega^{G4})}{8b} \\ \Gamma_{12} &= \frac{v_1^{G1} + 3v_1^{G2} - v_1^{G3} - 3v_1^{G4}}{4a} - \frac{\omega^{G1} - \omega^{G2} + \omega^{G3} - \omega^{G4}}{8} + \Omega^c \\ \Gamma_{21} &= \frac{v_2^{G1} - v_2^{G2} - v_2^{G3} + v_2^{G4}}{2b} - \Omega^c \\ \Gamma_{22} &= \frac{v_2^{G1} + 3v_2^{G2} - v_2^{G3} - 3v_2^{G4}}{4a} - \frac{3b(\omega^{G1} - \omega^{G2} + \omega^{G3} - \omega^{G4})}{32a},\end{aligned}\tag{A.8}$$

and

$$\begin{aligned}K_1 &= \frac{\omega^{G1} - \omega^{G2} - \omega^{G3} + \omega^{G4}}{2b} \\ K_2 &= \frac{\omega^{G1} + 3\omega^{G2} - \omega^{G3} - 3\omega^{G4}}{4a}.\end{aligned}\tag{A.9}$$

The various deformation modes for the stack bond pattern (Eqs.(A.6)-(A.7)) are illustrated in [Figure 1.19](#). For both block patterns, the contribution of the blocks' rotations in the average curvatures (A.7) and (A.9), and in the average deformations (A.6) and (A.8) is apparent. In each case it depends on the aspect ratio of the blocks, a/b .

A.3 Macroscopic stresses and couple stresses on the elementary cell A

The expression for the macroscopic stresses and couples stresses as functions of the contact stress distributions on the elementary cell A (Section 1.6), are retrieved through Eqs.(1.36)-(1.37). The equations for the generic running bond pattern are presented in the text (Eqs.(1.72)-(1.73)).

For the stack bond pattern ($\eta = 0$) the macroscopic stresses are:

$$\begin{aligned} T_{\alpha 1} &= \frac{1}{a} \left(\int_0^{\frac{a}{2}} r_{\alpha}^{12} dy_2 + \int_{-\frac{a}{2}}^0 r_{\alpha}^{43} dy_2 \right) \\ T_{\alpha 2} &= \frac{1}{a} \left(\int_0^{\frac{b}{2}} r_{\alpha}^{14} dy_1 + \int_{-\frac{b}{2}}^0 r_{\alpha}^{23} dy_1 \right), \end{aligned} \quad (\text{A.10})$$

and the macroscopic couple stresses are:

$$\begin{aligned} M_1 &= \frac{1}{a} \left(\int_0^{\frac{a}{2}} -r_1^{12} y_2 dy_2 + \int_{-\frac{a}{2}}^0 -r_1^{43} y_2 dy_2 \right) \\ M_2 &= \frac{1}{b} \left(\int_0^{\frac{b}{2}} r_2^{14} y_1 dy_1 + \int_{-\frac{b}{2}}^0 r_2^{23} y_1 dy_1 \right). \end{aligned} \quad (\text{A.11})$$

For the classical classical running bond pattern ($\eta = 1/2$) they are:

$$\begin{aligned} T_{\alpha 1} &= \frac{1}{a} \left(\int_0^{\frac{a}{2}} r_{\alpha}^{12} dy_2 + \int_{-\frac{a}{2}}^0 r_{\alpha}^{43} dy_2 \right. \\ &\quad \left. + \int_{\frac{b}{4}}^{\frac{b}{2}} \frac{1}{2} r_{\alpha}^{14} dy_1 + \int_{-\frac{b}{2}}^{-\frac{b}{4}} \frac{1}{2} r_{\alpha}^{23} dy_1 + \int_{-\frac{b}{4}}^{\frac{b}{4}} -\frac{1}{2} r_{\alpha}^{24} dy_1 \right) \\ T_{\alpha 2} &= \frac{1}{b} \left(\int_{\frac{b}{4}}^{\frac{b}{2}} r_{\alpha}^{14} dy_1 + \int_{-\frac{b}{2}}^{-\frac{b}{4}} r_{\alpha}^{23} dy_1 + \int_{-\frac{b}{4}}^{\frac{b}{4}} r_{\alpha}^{24} dy_1 \right), \end{aligned} \quad (\text{A.12})$$

and:

$$\begin{aligned} M_1 &= \frac{1}{ab} \left(\int_0^{\frac{a}{2}} \frac{1}{4} (-4r_1^{12} y_2 + br_2^{12}) dy_2 + \int_{-\frac{a}{2}}^0 -\frac{1}{4} (4r_1^{43} y_2 + br_2^{43}) dy_2 \right. \\ &\quad \left. + \int_{\frac{b}{4}}^{\frac{b}{2}} \frac{1}{2} r_2^{14} y_1 dy_1 + \int_{-\frac{b}{2}}^{-\frac{b}{4}} \frac{1}{2} r_2^{23} y_1 dy_1 + \int_{-\frac{b}{4}}^{\frac{b}{4}} -\frac{1}{2} r_2^{24} y_1 dy_1 \right) \\ M_2 &= \frac{1}{b} \left(\int_{\frac{b}{4}}^{\frac{b}{2}} r_2^{14} y_1 dy_1 + \int_{-\frac{b}{2}}^{-\frac{b}{4}} r_2^{23} y_1 dy_1 + \int_{-\frac{b}{4}}^{\frac{b}{4}} r_2^{24} y_1 dy_1 \right). \end{aligned} \quad (\text{A.13})$$

Appendix B

B.1 Out-of-plane components of the macroscopic Cosserat deformation measures of the cell \bar{A}

For the stack bond pattern ($\eta = 0$), the average out-of-plane relative deformations of the cell A are, after Eq.(2.52):

$$\begin{aligned}\Gamma_{31} &= \frac{v_3^{G1} - v_3^{G2} - v_3^{G3} + v_3^{G4}}{2b} - \frac{a(\omega_3^{G1} - \omega_3^{G2} + \omega_3^{G3} - \omega_3^{G4})}{8b} + \Omega_2^c \\ \Gamma_{32} &= \frac{v_3^{G1} + v_3^{G2} - v_3^{G3} - v_3^{G4}}{2a} + \frac{b(\omega_2^{G1} - \omega_2^{G2} + \omega_2^{G3} - \omega_2^{G4})}{8a} - \Omega_1^c,\end{aligned}\quad (\text{B.1})$$

and the average out-of-plane curvature hold (Eq.(2.53)):

$$\begin{aligned}K_{11} &= \frac{\omega_1^{G1} - \omega_1^{G2} - \omega_1^{G3} + \omega_1^{G4}}{2b} \\ K_{12} &= \frac{\omega_1^{G1} + \omega_1^{G2} - \omega_1^{G3} - \omega_1^{G4}}{2a} \\ K_{21} &= \frac{\omega_2^{G1} - \omega_2^{G2} - \omega_2^{G3} + \omega_2^{G4}}{2b} \\ K_{22} &= \frac{\omega_2^{G1} + \omega_2^{G2} - \omega_2^{G3} - \omega_2^{G4}}{2a}.\end{aligned}\quad (\text{B.2})$$

For the classical running bond pattern ($\eta = 1/2$), the above quantities read, respectively:

$$\begin{aligned}\Gamma_{31} &= \frac{v_3^{G1} - v_3^{G2} - v_3^{G3} + v_3^{G4}}{2b} - \frac{a(\omega_3^{G1} - \omega_3^{G2} + \omega_3^{G3} - \omega_3^{G4})}{8b} + \Omega_2^c \\ \Gamma_{32} &= \frac{v_3^{G1} + 3v_3^{G2} - v_3^{G3} - 3v_3^{G4}}{4a} + \\ &\frac{3b(\omega_2^{G1} - \omega_2^{G2} + \omega_2^{G3} - \omega_2^{G4})}{32a} + \frac{(\omega_1^{G1} - \omega_1^{G2} + \omega_1^{G3} - \omega_1^{G4})}{8} - \Omega_1^c.\end{aligned}\quad (\text{B.3})$$

and:

$$\begin{aligned}K_{11} &= \frac{\omega_1^{G1} - \omega_1^{G2} - \omega_1^{G3} + \omega_1^{G4}}{2b} \\ K_{12} &= \frac{\omega_1^{G1} + 3\omega_1^{G2} - \omega_1^{G3} - 3\omega_1^{G4}}{4a} \\ K_{21} &= \frac{\omega_2^{G1} - \omega_2^{G2} - \omega_2^{G3} + \omega_2^{G4}}{2b} \\ K_{22} &= \frac{\omega_2^{G1} + 3\omega_2^{G2} - \omega_2^{G3} - 3\omega_2^{G4}}{4a}.\end{aligned}\quad (\text{B.4})$$

An illustration of the Cosserat deformation measures when the cell A shows a stack bond pattern (Eqs.(B.5)-(B.2)) is given in [Figure 2.11](#).

B.2 Out-of-plane components of the macroscopic Cosserat stresses and couple stresses of the cell \bar{A}

The macroscopic Cosserat stresses and couple stresses (Eqs.(2.56)-(2.57)) corresponding to the stack bond pattern ($\eta = 0$) of the cell A are:

$$\begin{aligned} T_{31} &= \frac{1}{at} \left(\int_{-\frac{t}{2}}^{\frac{t}{2}} \int_0^{\frac{a}{2}} r_3^{12} dy_2 dy_3 + \int_{-\frac{t}{2}}^{\frac{t}{2}} \int_{-\frac{a}{2}}^0 r_3^{43} dy_2 dy_3 \right) \\ T_{32} &= \frac{1}{bt} \left(\int_{-\frac{t}{2}}^{\frac{t}{2}} \int_0^{\frac{b}{2}} r_3^{14} dy_1 dy_3 + \int_{-\frac{t}{2}}^{\frac{t}{2}} \int_{-\frac{b}{2}}^0 r_3^{23} dy_1 dy_3 \right), \end{aligned} \quad (\text{B.5})$$

and:

$$\begin{aligned} M_{11} &= \frac{1}{at} \left(\int_0^{\frac{a}{2}} \int_{-\frac{t}{2}}^{\frac{t}{2}} (r_3^{12} y_2 - r_2^{12} y_3) dy_3 dy_2 + \int_{-\frac{a}{2}}^0 \int_{-\frac{t}{2}}^{\frac{t}{2}} (r_3^{43} y_2 - r_2^{43} y_3) dy_3 dy_2 \right) \\ M_{12} &= -\frac{1}{bt} \left(\int_0^{\frac{b}{2}} \int_{-\frac{t}{2}}^{\frac{t}{2}} r_2^{14} y_3 dy_3 dy_1 + \int_{-\frac{b}{2}}^0 \int_{-\frac{t}{2}}^{\frac{t}{2}} r_2^{23} y_3 dy_3 dy_1 \right) \\ M_{21} &= \frac{1}{at} \left(\int_0^{\frac{a}{2}} \int_{-\frac{t}{2}}^{\frac{t}{2}} r_1^{12} y_3 dy_3 dy_2 + \int_{-\frac{a}{2}}^0 \int_{-\frac{t}{2}}^{\frac{t}{2}} r_1^{43} y_3 + dy_3 dy_2 \right) \\ M_{22} &= \frac{1}{bt} \left(\int_0^{\frac{b}{2}} \int_{-\frac{t}{2}}^{\frac{t}{2}} (-r_3^{14} y_1 + r_1^{14} y_3) dy_3 dy_1 + \int_{-\frac{b}{2}}^0 \int_{-\frac{t}{2}}^{\frac{t}{2}} (-r_3^{23} y_1 + r_1^{23} y_3) dy_3 dy_1 \right). \end{aligned} \quad (\text{B.6})$$

For the 1/2 running bond pattern they become:

$$\begin{aligned} T_{31} &= \frac{1}{at} \left(\int_{-\frac{t}{2}}^{\frac{t}{2}} \int_0^{\frac{a}{2}} r_3^{12} dy_2 dy_3 + \int_{-\frac{t}{2}}^{\frac{t}{2}} \int_{-\frac{a}{2}}^0 r_3^{43} dy_2 dy_3 \right. \\ &\quad \left. + \int_{-\frac{t}{2}}^{\frac{t}{2}} \int_{\frac{b}{4}}^{\frac{b}{2}} \frac{1}{2} r_3^{14} dy_1 dy_3 + \int_{-\frac{t}{2}}^{\frac{t}{2}} \int_{-\frac{b}{2}}^{-\frac{b}{4}} \frac{1}{2} r_3^{23} dy_1 dy_3 - \int_{-\frac{t}{2}}^{\frac{t}{2}} \int_{-\frac{b}{4}}^{\frac{b}{4}} \frac{1}{2} r_3^{24} dy_1 dy_3 \right) \\ T_{32} &= \frac{1}{bt} \left(\int_{-\frac{t}{2}}^{\frac{t}{2}} \int_{\frac{b}{4}}^{\frac{b}{2}} r_3^{14} dy_1 dy_3 + \int_{-\frac{t}{2}}^{\frac{t}{2}} \int_{-\frac{b}{2}}^{-\frac{b}{4}} r_3^{23} dy_1 dy_3 + \int_{-\frac{t}{2}}^{\frac{t}{2}} \int_{-\frac{b}{4}}^{\frac{b}{4}} r_3^{24} dy_1 dy_3 \right), \end{aligned} \quad (\text{B.7})$$

and:

$$\begin{aligned} M_{11} &= \frac{1}{at} \left(\int_0^{\frac{a}{2}} \int_{-\frac{t}{2}}^{\frac{t}{2}} (r_3^{12} y_2 - r_2^{12} y_3) dy_3 dy_2 + \int_{-\frac{a}{2}}^0 \int_{-\frac{t}{2}}^{\frac{t}{2}} (r_3^{43} y_2 - r_2^{43} y_3) dy_3 dy_2 + \right. \\ &\quad \left. - \int_{\frac{b}{4}}^{\frac{b}{2}} \int_{-\frac{t}{2}}^{\frac{t}{2}} \frac{1}{2} r_2^{14} y_3 dy_3 dy_1 - \int_{-\frac{b}{2}}^{-\frac{b}{4}} \int_{-\frac{t}{2}}^{\frac{t}{2}} \frac{1}{2} r_2^{23} y_3 dy_3 dy_1 + \int_{-\frac{b}{4}}^{\frac{b}{4}} \int_{-\frac{t}{2}}^{\frac{t}{2}} \frac{1}{2} r_2^{24} y_3 dy_3 dy_1 \right) \\ M_{12} &= -\frac{1}{bt} \left(\int_{\frac{b}{4}}^{\frac{b}{2}} \int_{-\frac{t}{2}}^{\frac{t}{2}} r_2^{14} y_3 dy_3 dy_1 + \int_{-\frac{b}{2}}^{-\frac{b}{4}} \int_{-\frac{t}{2}}^{\frac{t}{2}} r_2^{23} y_3 dy_3 dy_1 + \int_{-\frac{b}{4}}^{\frac{b}{4}} \int_{-\frac{t}{2}}^{\frac{t}{2}} r_2^{24} y_3 dy_3 dy_1 \right) \\ M_{21} &= \frac{1}{at} \left(\int_0^{\frac{a}{2}} \int_{-\frac{t}{2}}^{\frac{t}{2}} \frac{1}{2} \left(2r_1^{12} y_3 - \frac{1}{2} b r_3^{12} \right) dy_3 dy_2 + \int_{-\frac{a}{2}}^0 \int_{-\frac{t}{2}}^{\frac{t}{2}} \frac{1}{2} \left(2r_1^{43} y_3 + \frac{1}{2} b r_3^{43} \right) dy_3 dy_2 + \right. \\ &\quad \left. \int_{\frac{b}{4}}^{\frac{b}{2}} \int_{-\frac{t}{2}}^{\frac{t}{2}} \frac{1}{2} (-r_3^{14} y_1 + r_1^{14} y_3) dy_3 dy_1 + \int_{-\frac{b}{2}}^{-\frac{b}{4}} \int_{-\frac{t}{2}}^{\frac{t}{2}} \frac{1}{2} (-r_3^{23} y_1 + r_1^{23} y_3) dy_3 dy_1 + \right. \\ &\quad \left. \int_{-\frac{b}{4}}^{\frac{b}{4}} \int_{-\frac{t}{2}}^{\frac{t}{2}} \frac{1}{2} (r_3^{24} y_1 - r_1^{24} y_3) dy_3 dy_1 \right) \end{aligned}$$

$$M_{22} = \frac{1}{bt} \left(\int_{\frac{b}{4}}^{\frac{b}{2}} \int_{-\frac{t}{2}}^{\frac{t}{2}} (-r_3^{14} y_1 + r_1^{14} y_3) dy_3 dy_1 + \int_{-\frac{b}{2}}^{-\frac{b}{4}} \int_{-\frac{t}{2}}^{\frac{t}{2}} (-r_3^{23} y_1 + r_1^{23} y_3) dy_3 dy_1 + \int_{-\frac{b}{4}}^{\frac{b}{4}} \int_{-\frac{t}{2}}^{\frac{t}{2}} (-r_3^{24} y_1 + r_1^{24} y_3) dy_3 dy_1 \right). \quad (\text{B.8})$$

Appendix C

C.1 Stiffness matrix for materials with in-plane centro-symmetry

Considering a Cosserat material without specific centrosymmetric properties and always supposing uncoupled in-plane and out-of-plane behavior, Eq.(3.9) reads:

$$V_m^c = \frac{1}{2} \begin{bmatrix} U_m^t & \Omega_m^t \end{bmatrix} \begin{bmatrix} K_{UU}^m & K_{U\Omega}^m + \tilde{K}_{U\Omega}^m \\ K_{\Omega U}^m + \tilde{K}_{\Omega U}^m & K_{\Omega\Omega}^m + \tilde{K}_{\Omega\Omega}^m \end{bmatrix} \begin{bmatrix} U_m \\ \Omega_m \end{bmatrix}. \quad (\text{C.1})$$

The additional terms are indicated with $[\tilde{\quad}]$ and are:

$$\begin{aligned} \tilde{K}_{U\Omega}^m &= \int_{\Omega^e} \left[B_{m1[2N \times 4]}^t G_{[4 \times 2]} B_{m4[2 \times M]} \right] dA \\ \tilde{K}_{\Omega U}^m &= \int_{\Omega^e} \left[B_{m4[M \times 2]}^t H_{[2 \times 4]} B_{m1[4 \times 2N]} \right] dA \\ \tilde{K}_{\Omega\Omega}^m &= \int_{\Omega^e} \left[B_{m4[M \times 2]}^t H_{[2 \times 4]} B_{m2[4 \times M]} + B_{m2[M \times 4]}^t G_{[4 \times 2]} B_{m4[2 \times M]} \right] dA. \end{aligned} \quad (\text{C.2})$$

C.2 Coupling factor

Let us consider the elastic deformation energy associated to the present Cosserat plate model due to the in-plane deformations:

$$V_m^c = \frac{1}{2} \int_{\Omega^e} [\boldsymbol{\tau}_m^t \boldsymbol{\gamma}_m + \boldsymbol{\mu}_m^t \boldsymbol{\kappa}_m] dA. \quad (\text{C.3})$$

Taking into account the constitutive law (18), we obtain:

$$V_m^c = \frac{1}{2} \int_{\Omega^e} [\boldsymbol{\gamma}_m^t \mathbf{A} \boldsymbol{\gamma}_m + \boldsymbol{\kappa}_m^t \mathbf{D}_m \boldsymbol{\kappa}_m] dA. \quad (\text{C.4})$$

The derivation of the skew-symmetric part from the element formulation is made possible by separating every term of the strain vector into its symmetric and skew-symmetric part and by reordering the resulting components in a new vectorial form:

$$\tilde{\boldsymbol{\gamma}}_m = [\gamma_{11} \quad \gamma_{22} \quad \gamma_{(12)} \quad \gamma_{[12]}]^t, \quad \tilde{\boldsymbol{\kappa}}_m = [\kappa_{31} \quad \kappa_{32}]^t = \boldsymbol{\kappa}_m. \quad (\text{C.5})$$

The stress components can be also separated into their symmetric and skew-symmetric parts:

$$\tilde{\boldsymbol{\tau}}_m = [\tau_{11} \quad \tau_{22} \quad \tau_{(12)} \quad \tau_{[12]}]^t, \quad \tilde{\boldsymbol{\mu}}_m = [[\mu_{31} \quad \mu_{32}]]^t = \boldsymbol{\mu}_m. \quad (\text{C.6})$$

A new constitutive law between (C.5) and (C.6) can be expressed through the basic linear relation

$$\tilde{\mathbf{A}} = \frac{\partial^2 \tilde{V}_m^c}{\partial \tilde{\boldsymbol{\gamma}}_m \partial \tilde{\boldsymbol{\gamma}}_m}, \quad (\text{C.7})$$

where \tilde{V}_m^c takes the form:

$$\tilde{V}_m^c = \frac{1}{2} \int_{\Omega^e} [\tilde{\boldsymbol{\gamma}}_m^t \tilde{\mathbf{A}} \tilde{\boldsymbol{\gamma}}_m + \boldsymbol{\kappa}_m^t \mathbf{D}_m \boldsymbol{\kappa}_m] dA. \quad (\text{C.8})$$

Thus, starting from matrix

$$\mathbf{A} = \begin{bmatrix} A^{1111} & A^{1122} & & \\ A^{2211} & A^{2222} & & \\ & & A^{1212} & A^{1221} \\ & & A^{2112} & A^{2121} \end{bmatrix}, \quad (\text{C.9})$$

we obtain:

$$\tilde{\mathbf{A}} = \begin{bmatrix} A^{1111} & A^{1122} & & \\ A^{2211} & A^{2222} & & \\ & & A^{(12)(12)} & A^{(12)[12]} \\ & & A^{12} & A^{[12][12]} \end{bmatrix}, \quad (\text{C.10})$$

with

$$\begin{aligned} A^{(12)(12)} &= [A^{1212} + A^{1221} + A^{2121} + A^{2112}] / 2 \\ A^{(12)[12]} &= [A^{1212} - A^{1221} - A^{2121} + A^{2112}] / 2 \\ A^{12} &= [A^{1212} + A^{1221} - A^{2121} - A^{2112}] / 2 \\ A^{[12][12]} &= [A^{1212} - A^{1221} + A^{2121} - A^{2112}] / 2. \end{aligned} \quad (\text{C.11})$$

Cauchy continuum can be retrieved by annihilating the skew-symmetric terms contained in Eqs.(C.11), which automatically guarantees the self-satisfaction of the balance equations, without the necessity of any couple stress addition. In the case that \mathbf{A} is given by the first sub-matrix of Eq.(3.47), we have:

$$A^{[12][12]} = 2G_c = 2G\alpha = 2A^{(12)(12)}\alpha, \quad A^{(12)[12]} = A^{12} = 0. \quad (\text{C.12})$$

Therefore the term α controls in magnitude the skew-symmetric part of the shear stress within the constitutive law.

C.3 Drilling rigidity

Given \mathbf{A} by Eq.(C.9) and \mathbf{B}_{m2} by Eq.(3.27), the first term of the stiffness matrix in Eq.(3.31) reads:

$$\mathbf{K}_{\Omega\Omega}^m{}^{(1)} = \int_{\Omega^e} \begin{bmatrix} 0 & 0 \\ 0 & 0 \\ \Phi_1 & \Phi_N \\ -\Phi_1 & \dots & -\Phi_N \end{bmatrix}^t \begin{bmatrix} A^{1111} & A^{1122} \\ A^{2211} & A^{2222} \\ & A^{1212} & A^{1221} \\ & A^{2112} & A^{2121} \end{bmatrix} \begin{bmatrix} 0 & 0 \\ 0 & 0 \\ \Phi_1 & \Phi_N \\ -\Phi_1 & \dots & -\Phi_N \end{bmatrix} dA \quad (\text{C.13})$$

Recalling the definitions (3.18) and (C.11)-4, the above matrix is:

$$\mathbf{K}_{\Omega\Omega}^m{}^{(1)} = \int_{\Omega^e} 2A^{[12][12]} \Phi_m \otimes \Phi_m dA = \int_{\Omega^e} 2A^{[12][12]} \Phi_m^t \Phi_m dA, \quad (\text{C.14})$$

where the outer product \otimes has been expressed as a scalar product, with Φ_m from Eq.(3.24). We note that only the matrix $\mathbf{K}_{\Omega\Omega}^m{}^{(1)}$ contains the elastic modulus $A^{[12][12]}$ associated to the Cosserat's term responsible for the hourglass control, i.e. $\gamma_{[12]}$. Writing the elastic potential associated to that matrix as:

$$V_{m,\Omega\Omega}^c{}^{(1)} = \frac{1}{2} \Omega_m^t \mathbf{K}_{\Omega\Omega}^m{}^{(1)} \Omega_m \quad (\text{C.15})$$

and by introducing Eq.(C.14), we have:

$$V_{m,\Omega\Omega}^c{}^{(1)} = \frac{1}{2} \int_{\Omega^e} [\Phi_m \Omega_m]^t 2A^{[12][12]} [\Phi_m \Omega_m] dA. \quad (\text{C.16})$$

In the above we recognize the second expression of Eq.(3.22). It results in:

$$V_{m,\Omega\Omega}^c{}^{(1)} = \frac{1}{2} \int_{\Omega^e} 2A^{[12][12]} \omega_3^2 dA. \quad (\text{C.17})$$

So $\mathbf{K}_{\Omega\Omega}^m{}^{(1)}$ depends on the drilling rotations ω_3 and if $A^{[12][12]} = 2G\alpha$ (Eq. (C.12)), then α gives a weight to the drilling rotations in the assemblage of the element membrane stiffness matrix.

The above potential is similar to that generally proposed by [Providas and Kattis \(2000\)](#) for the construction of shell structures by assemblage of flat FE. This latter can be expressed as:

$$V_{m,\Omega\Omega}^{PK}{}^{(1)} = \beta\gamma \int_{\Omega^e} (\hat{\omega}_{30} - \omega_3)^2 dA \approx \beta\gamma \int_{\Omega^e} \gamma_{[12]}^2 dA, \quad (\text{C.18})$$

where $\hat{\omega}_{30}$ the average infinitesimal rotation (Eq.(3.4)) of the element, β depends on the material and γ is an arbitrary parameter through which one makes the stiffness matrix non-singular, against possible membrane actions.

C.4 Patch test for anisotropic Cosserat materials

For anisotropic Cosserat material, matrices \mathbf{A} and \mathbf{D}_m governing the in-plane behaviour (Eq.(3.47)) take the following form (Sulem and Mühlhaus, 1997):

$$\mathbf{A} = \begin{bmatrix} K+G & K-G & & 0 & & 0 \\ K-G & K+G & & 0 & & 0 \\ & 0 & 0 & G+\alpha(1-\beta)G & & G-\alpha G \\ & 0 & 0 & G-\alpha G & G+\alpha(1+\beta)G & \end{bmatrix}, \quad \mathbf{D}_m = \begin{bmatrix} 2Gl_c & 0 \\ 0 & 2Gl_c \end{bmatrix} \quad (\text{C.19})$$

where β is a coefficient controlling the anisotropy of the material to shear.

The generalization of the patch test formulated by Providas and Kattis (2002) for anisotropic Cosserat materials is given in general form in Table C.2. Notice that the patch test of Providas and Kattis (2002) is retrieved by imposing $\beta = 0$ (isotropic material). On the contrary, due to the anisotropy of the material (for $\beta \neq 0$), symmetry of the in-plane shear stress τ_m is lost in Test 1. Therefore, the application of the body couple m_3 is needed. In this case Test 1 becomes redundant with respect to Test 2 and can be avoided.

The present formulation satisfy the patch test for anisotropic materials. Table C.1 shows that the error committed by the formulation in predicting the stresses and couple stresses in case of anisotropy is of the same order than the error committed for an isotropic material. In this example, we have used $\beta = 0.5$. The other material parameters are contained in Figure 3.8.

	τ_{11}	τ_{22}	τ_{12}	τ_{21}	μ_{31}	μ_{32}
Test 1	4.000	4.000	1.3125	1.6875	0.000	0.000
	[4.000]	[4.000]	[1.3125]	[1.6875]	[0.000]	[0.000]
Test 2	4.000	4.000	1.6875	1.0625	0.000	0.000
	[4.000]	[4.000]	[1.6875]	[1.0625]	[0.000]	[0.000]
Test 3	3.986	3.996	1.330	1.631	4.001	-3.991
	[4.000]	[4.000]	[1.341]	[1.641]	[4.000]	[-4.000]

Table C.1: Results of patch tests for anisotropic Cosserat material. Stresses and couple stresses at point P1. Exact results are reported in brackets.

Test 1		
$u_1 = 10^{-3}(x + 0.5y)$	$u_2 = 10^{-3}(x + y)$	$\omega_3 = 0.25 \times 10^{-3}$
$f_1 = 0$	$f_2 = 0$	$m_3 = -0.0015\alpha\beta G$
$\tau_{11} = \tau_{22} = 0.002K$	$\tau_{12} = (0.0015 - 0.00075\alpha\beta)G$	$\mu_{31} = \mu_{32} = 0$
$\tau_{21} = (0.0015 + 0.00075\alpha\beta)G$		
Test 2		
$u_1 = 10^{-3}(x + 0.5y)$	$u_2 = 10^{-3}(x + y)$	$\omega_3 = 10^{-3} \left(0.25 + (4\alpha)^{-1} \right)$
$f_1 = 0$	$f_2 = 0$	$m_3 = (0.001 - 0.0015\alpha\beta)G$
$\tau_{11} = \tau_{22} = 0.002K$	$\tau_{12} = (0.002 + (-0.00025 - 0.00075\alpha)\beta)G$	$\mu_{31} = \mu_{32} = 0$
$\tau_{21} = (0.001 + (-0.00025 + 0.00075\alpha)\beta)G$		
Test 3		
$u_1 = 10^{-3}(x + 0.5y)$	$u_2 = 10^{-3}(x + y)$	$\omega_3 = 10^{-3} \left(0.25 + (2\alpha)^{-1}(x - y) \right)$
$f_1 = (0.001 - 0.0005\beta)G$	$f_2 = (0.001 + 0.0005\beta)G$	$m_3 = (0.002x - 0.002y - 0.0015\alpha\beta)G$
$\tau_{11} = \tau_{22} = 0.002K$	$\tau_{12} = ((0.001 - 0.0005\beta)x + (0.0005\beta - 0.001)y - 0.00075\alpha\beta + 0.0015)G$	$\mu_{31} = -\mu_{32} = \frac{0.001}{\alpha} G l_c$
$\tau_{21} = ((-0.0005\beta - 0.001)x + (0.0005\beta + 0.001)y + 0.00075\alpha\beta + 0.0015)G$		

Table C.2: Generalization of the patch test of [Providas and Kattis \(2002\)](#) for anisotropic Cosserat materials: boundary conditions and expected solutions.

C.5 Advanced test to torsion for Cosserat plates

The test is performed on a rhombic plate. Depending on the configuration considered (Figure C.1-left), the plate has one or two adjacent clamped edges, where all the degrees-of-freedom are prevented. The free-end of the plate is subjected to a local (nodal) out-of-plane force F_3 . The plate has an orthotropic behaviour to bending, for which the material matrix \mathbf{D}_f takes the following form (Eq.(3.49)):

$$\mathbf{D}_f = \begin{bmatrix} \beta_1 + \beta_2 + \beta_3 & & \beta_1 & & 0 & & 0 \\ & \beta_1 & \beta_1 + \beta_2 + \beta_3 & & 0 & & 0 \\ & 0 & & 0 & \beta_3(1 - \delta) & & \beta_2 \\ & 0 & & 0 & & \beta_2 & \beta_3(1 + \delta) \end{bmatrix}, \quad (\text{C.20})$$

where δ controls the anisotropy of the plate to bending.

The aim of the test is to assess the numerical convergence of the formulation upon mesh refinement. This is made for: a) increasing element distortion θ , b) increasing degree of anisotropy δ and c) different boundary conditions. For the simulations, regular discretisations of $2 \times 2, 4 \times 4, 8 \times 8$ up to 64×64 elements are used. It is worth remarking that the orthotropy directions are always kept coincident with the x_1, x_2 axis, whereas the element discretisation follows the shape of the plate (Figure C.1-right).

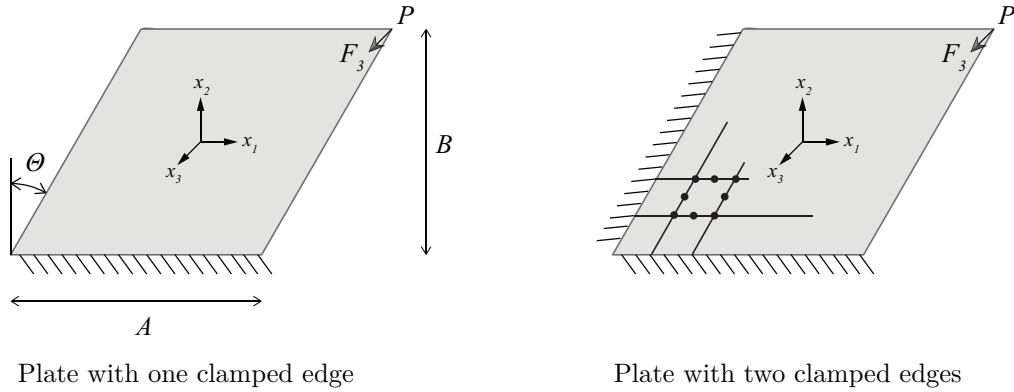


Figure C.1: Rhombic plate subjected to local out-of-plane force F_3 . Notations, boundary conditions and element discretisation.

Figure C.2 shows the relative error ε committed by the element in predicting the out-of-plane displacement at point P of the plate versus the number of finite elements N_{FE} used per side. To this purpose, the numerical solution U_3^h is compared with the *exact* solution U_3^{ex} , obtained with the finest 64×64 -element discretisation:

$$\varepsilon = 100 \times \frac{U_3^h - U_3^{\text{ex}}}{U_3^{\text{ex}}}. \quad (\text{C.21})$$

It is shown how the geometrical distortion of the elements, the application of additional constraints and the introduction of an orthotropic behaviour with respect to bending lead, in general, to a reduction of the performance of the element. It is apparent how this latter is highly affected when considering highly distorted elements, i.e. for $\theta = 60^\circ$. On the contrary, the effect of additional boundary conditions and material anisotropy is much less pronounced.

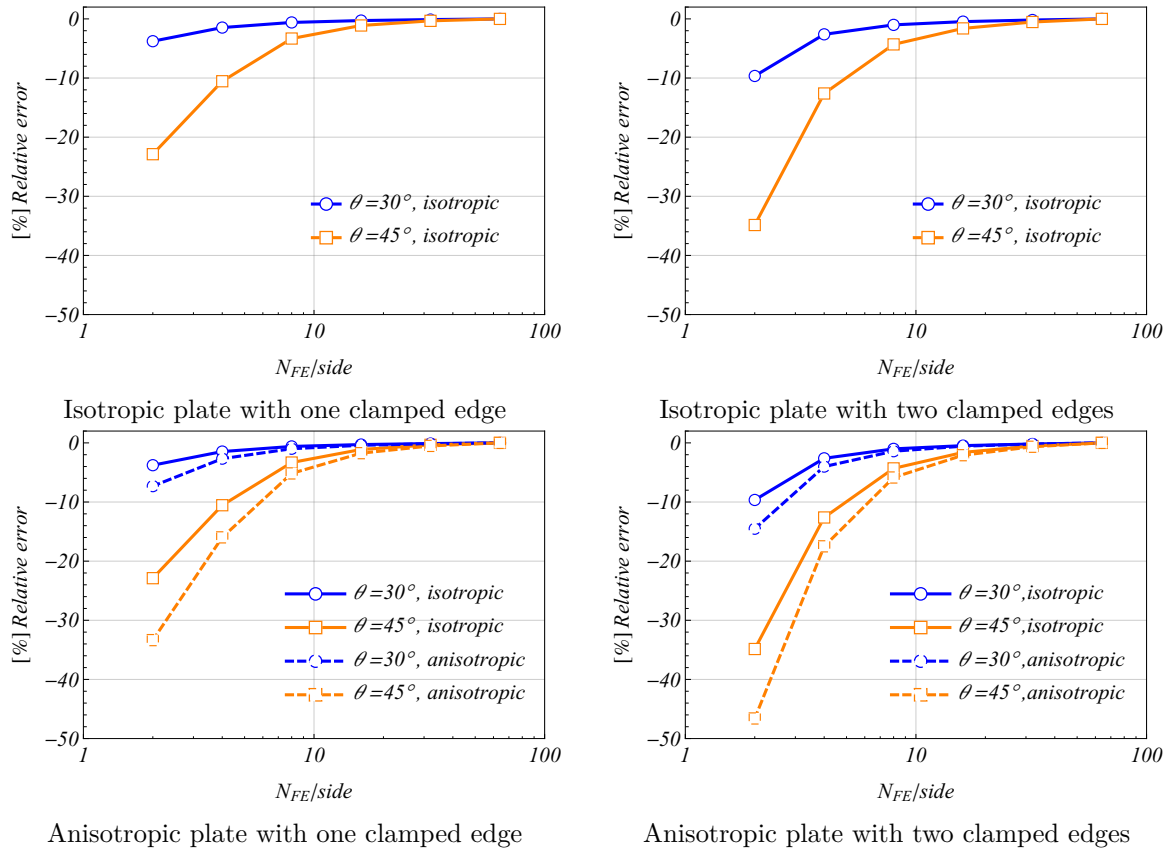


Figure C.2: Relative error committed in the evaluation of the out-of-plane displacement of point P of the plate. Top: response for isotropic plates. Bottom: comparison with anisotropic plates. Geometry: $A = 50\text{mm}$, $B = 45\text{mm}$, $F_3 = 1\text{N}$. Out-of-plane properties: $\alpha_4 = 1500\text{MPa}$, $\beta_1 = 2000\text{MPa} \times \text{mm}$, $\beta_2 = 0\text{MPa} \times \text{mm}$, $\beta_3 = 4000\text{MPa} \times \text{mm}$. Anisotropic plates are for $\delta = 0.5$.

Appendix D

D.1 Implementation of the COSS8R element in Abaqus

Abaqus (Simulia, 2010) is one of the main commercial software packages that implement the finite element method. As in the majority of the commercial software packages dedicated to finite elements, in Abaqus the user defines an analysis (or load case) history. This mainly consists in (Simulia, 2010):

- Dividing the job into different *steps*. A step is a convenient phase of the analysis history. In its simplest form, a step can be just a static analysis of a load change from one magnitude to another.
- Defining the analysis procedure to be followed for each step. Choosing the type of analysis to be performed during each step results in good flexibility when programming complex load case histories. In the present case, static and modal analyses can be performed by the implemented finite element formulation.
- Prescribing loads, boundary conditions and output requests for the step. The loads and the boundary conditions can be changed, together with the analysis procedures, from step to step. Since the state variables of the model (in this case the stresses, the elastic and plastic deformations, the hardening variables) are updated throughout the load case history, the effects of a step can be included in each new subsequent step.

During the execution of the analysis history, each step is divided into multiple *increments*, corresponding to load (or time) increments. Step increments can be explicitly demanded by the user (for example for output request) or automatically required by the program in order to respect convergence conditions on the expected step solution.

The COSS8R element described in Chapter 3 and Chapter 4 is introduced in Abaqus as *user-defined element*. The subroutine provided by Abaqus allowing to define a user-defined element is called UEL (Simulia, 2010). The user subroutine UEL operates in Abaqus at the increment level. It performs all the calculations assigned to the finite element, and is called by Abaqus each time element calculations are required. This subroutine is very general and can result very efficient in solving equations in terms of non-standard degrees of freedom. In the present case, it allows to consider the nodal rotations $\mathbf{\Omega}$ as the Cosserat rotations $\mathbf{\Omega}^c$ (including the drilling rotations $\mathbf{\Omega}_3^c$) in the finite element formulation. Figure D.1 illustrates how Abaqus calls the user subroutine UEL and operates on the user-defined elements. Notice that the user-defined elements are invoked by Abaqus in the same manner as the native Abaqus elements. The layout is as follows (Figure D.1):

- (1) A generic step is executed, as prescribed by the analysis history defined by the user.

- (2) The step is first initialized throughout all the elements of the model, which corresponds to step increment $n = 0$. The user subroutine UEL is called for the first time in the step, but no calculations are required on the user-defined elements at this stage.
- (3) Starting from the first increment ($n = 1$) and until convergence is reached (stage (6)), a step increment $n + 1$ is predicted by Abaqus and given to the user-defined elements in terms of nodal degrees of freedom $d\mathbf{S}_{n+1}$. In the present case, nodal displacements $d\mathbf{U}_{n+1}$ and nodal rotations $d\mathbf{\Omega}_{n+1}^c$ are assigned to the COSS8R elements.
- (4) Given the increment, the UEL subroutine solves for every finite element the partial differential equations governing the prescribed incremental problem. In this case, solution to the elasto-plastic problem described in Chapter 4 is computed at every Gauss point of the COSS8R elements. The solution is given in terms of generalized deformation and stress increments $d\boldsymbol{\varepsilon}_{n+1}, d\boldsymbol{\sigma}_{n+1}$ and hardening variables $d\boldsymbol{\alpha}_{n+1}, d\mathbf{q}_{n+1}$. The Closest Point Projection (CPP) algorithm is applied at this stage.
- (5) Within the same increment, the internal and external residual vectors, respectively \mathbf{R}_{n+1} and \mathbf{P}_{n+1} (Chapter 4), the tangent stiffness matrix \mathbf{K}_{n+1} and the mass matrix \mathbf{M}_{n+1} (Chapter 3) are also integrated over the finite elements. Notice that only these quantities are returned to Abaqus.
- (6) The assembly of the global residual vectors $\bar{\mathbf{R}}_{n+1}$ and $\bar{\mathbf{P}}_{n+1}$ and the global tangent stiffness and mass matrices $\bar{\mathbf{K}}_{n+1}$ and $\bar{\mathbf{M}}_{n+1}$ is made by Abaqus, starting from the local quantities computed in (5). Solution convergence is checked by Abaqus at this stage. If convergence is not reached, a new (and smaller) step increment is predicted and the UEL subroutine is recalled (stage (3)).
- (7) If convergence is reached, Abaqus updates the global solution with that for the given increment $d\mathbf{S}_{n+1}$, and recalls the UEL subroutine for the next step: (3) \leftarrow (7).

As it is apparent from the above layout, the assembly of the global matrices and the computation of the global solution are entirely carried out by Abaqus during the job processing. Moreover, the pre-processing and post-processing are also provided by Abaqus. They can be controlled through the tools that Abaqus classically places at user's disposal, i.e. the Abaqus graphical interface (Abaqus/CAE), the submission of input files, and the use of specific scripts written in Python language (Simulia, 2010). To this purpose notice that, in general, plotting of user-defined elements is not supported by Abaqus/CAE. However, if these elements contain, as in the present case, translational and rotational degrees of freedom, they can be overlaid with the native Abaqus elements. This is made by tying the nodes of the user-defined elements with the nodes of the standard elements. Moreover, the nodal degrees of freedom of both elements must correspond (Simulia, 2010). If one follows this strategy, model plots of the user-defined elements are displayed in the post-processing. This allows the user to see the undeformed and deformed shape of the structure. User-defined variables (like the generalized stress and deformation measures, the labels of the activated criteria, etc.) can also be visualized on the structure in the form of plot contours. In this case, the use of another specific user subroutine called UVARM (Simulia, 2010) is necessary.

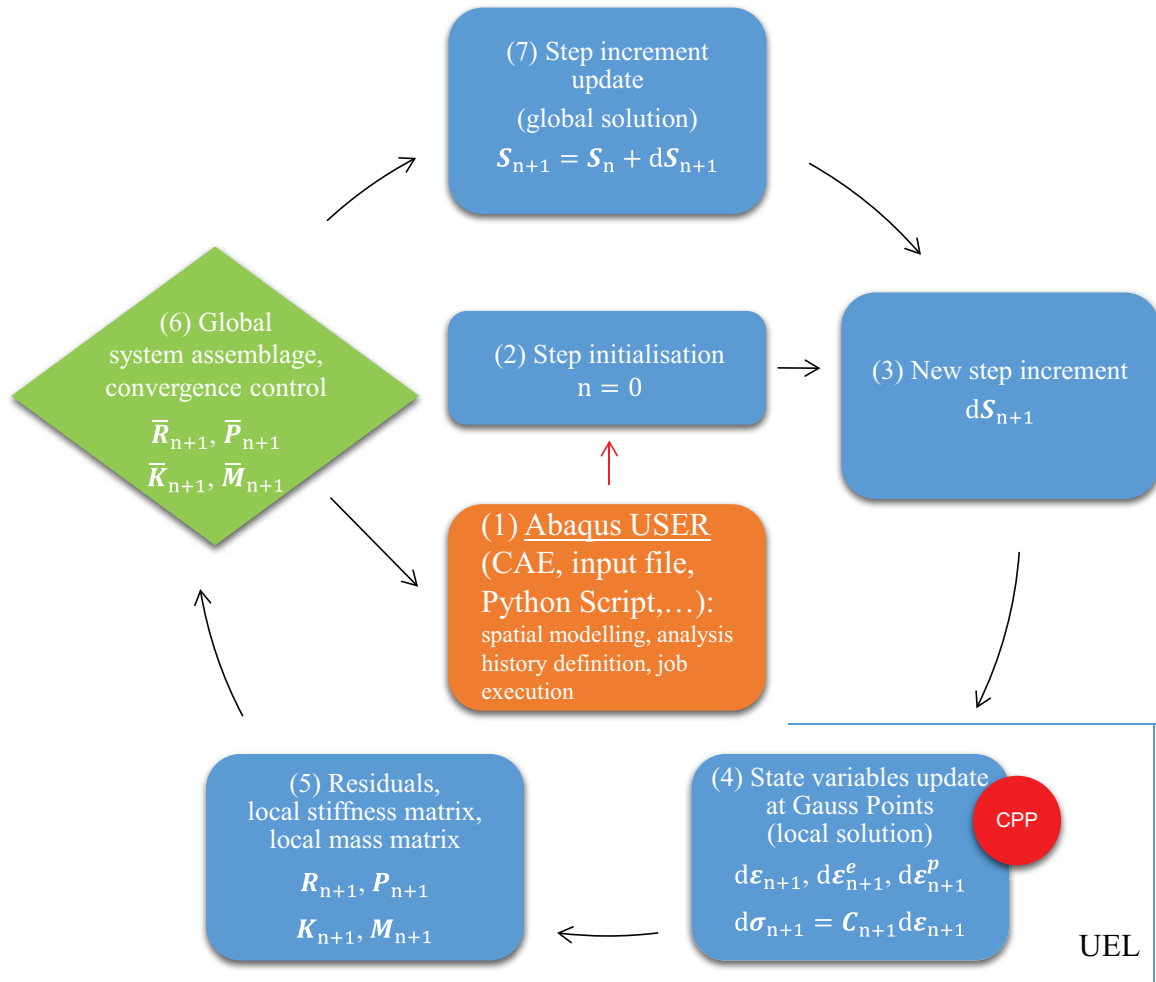


Figure D.1: The algorithm through which Abaqus calls the user subroutine UEL and operates on the user-defined elements. CPP indicates the Closest-Point-Projection algorithm used for the solution of the elastoplastic problem (Chapter 4).

Bibliography

- Addressi, D., Apr. 2014. A 2D Cosserat finite element based on a damage-plastic model for brittle materials. *Computers & Structures* 135, 20–31.
URL <http://linkinghub.elsevier.com/retrieve/pii/S0045794914000145><http://www.sciencedirect.com/science/article/pii/S0045794914000145>
- Addressi, D., Marfia, S., Sacco, E., Toti, J., 2014. Modeling Approaches for Masonry Structures. *The Open Civil Engineering Journal* (2), 288–300.
- Addressi, D., Sacco, E., Mar. 2012. A multi-scale enriched model for the analysis of masonry panels. *International Journal of Solids and Structures* 49 (6), 865–880.
URL <http://linkinghub.elsevier.com/retrieve/pii/S0020768311004069>
- Addressi, D., Sacco, E., Paolone, A., Jul. 2010. Cosserat model for periodic masonry deduced by nonlinear homogenization. *European Journal of Mechanics - A/Solids* 29 (4), 724–737.
URL <http://linkinghub.elsevier.com/retrieve/pii/S0997753810000410>
- Alpa, G., Monetto, I., 1994. Microstructural masonry model with for dry in-plane loading. *Journal of the Mechanics and Physics of Solids* 42 (7), 1159–1175.
- Altenbach, H., Eremeyev, V., Apr. 2009. On the linear theory of micropolar plates. *ZAMM - Journal of Applied Mathematics and Mechanics / Zeitschrift für Angewandte Mathematik und Mechanik* 89 (4), 242–256.
URL <http://doi.wiley.com/10.1002/zamm.200800207>
- Altenbach, J., Altenbach, H., Eremeyev, V. a., Sep. 2009. On generalized Cosserat-type theories of plates and shells: a short review and bibliography. *Archive of Applied Mechanics* 80 (1), 73–92.
URL <http://link.springer.com/10.1007/s00419-009-0365-3>
- Ambartsumian, S., 1996. The theory of transverse bending of plates with asymmetric elasticity. *Mechanics of composite materials* 32 (1), 30–38.
URL <http://link.springer.com/article/10.1007/BF02254645>
- Anderson, W. B., Lakes, R. S., 1994. Size effects due to Cosserat elasticity and surface damage in closed-cell polymethacrylimide foam. *Journal of Materials Science* 29, 6413–6419.
- Anthoine, A., 1995. Derivation of the in-plane elastic characteristics of masonry through homogenization theory. *International Journal of Solids and Structures* 32 (2), 137–163.
- Anthoine, A., 1997. Homogenization of periodic masonry: plane stress, generalized plane strain or 3D modelling? *Communications in Numerical Methods in Engineering* 13 (November 1995), 319–326.
URL [http://onlinelibrary.wiley.com/doi/10.1002/\(SICI\)1099-0887\(199705\)13:5<319::AID-CN55>3.0.CO;2-S/abstract](http://onlinelibrary.wiley.com/doi/10.1002/(SICI)1099-0887(199705)13:5<319::AID-CN55>3.0.CO;2-S/abstract)

- Babuška, I., Scapolla, T., 1989. Benchmark computation and performance evaluation for a rhombic plate bending problem. *International Journal for Numerical Methods in Engineering* 28 (1), 155–179.
- Bacigalupo, A., Gambarotta, L., 2012. Computational two-scale homogenization of periodic masonry: Characteristic lengths and dispersive waves. *Computer Methods in Applied Mechanics and Engineering* 213-216, 16–28.
URL <http://dx.doi.org/10.1016/j.cma.2011.11.020>
- Baggio, C., Trovalusci, P., 1998. Limit analysis for no-tension and frictional three-dimensional discrete systems. *Journal of Structural Mechanics*.
URL <http://www.tandfonline.com/doi/abs/10.1080/08905459708945496>
- Baraldi, D., Cecchi, A., Tralli, A., 2015. Continuous and discrete models for masonry like material: A critical comparative study. *European Journal of Mechanics - A/Solids* 50, 39–58.
URL <http://linkinghub.elsevier.com/retrieve/pii/S0997753814001521>
- Bardet, J. P., Vardoulakis, I., Jan. 2001. The asymmetry of stress in granular media. *International Journal of Solids and Structures* 38 (2), 353–367.
- Barth, M., Marti, P., 1997. Tests on Clay Brick Masonry with Dry Head Joints (in German). Report No. 230.
- Bathe, K., 1996. Finite element procedures. Prentice Hall, New Jersey.
- Beall, C., Jul. 2000. New masonry products and materials. *Progress in Structural Engineering and Materials* 2 (3), 296–303.
URL <http://doi.wiley.com/10.1002/1528-2716%28200007%2F09%292%3A3%3C296%3A%3AAID-PSE38%3E3.0.CO%3B2-6>
- Besdo, D., 1985. Inelastic behavior of plane frictionless block-systems described as Cosserat media. *Archives of Mechanics*.
URL <http://scholar.google.com/scholar?hl=en&btnG=Search&q=intitle:Inelastic+behaviour+of+plane+frictionless+block+systems+described+as+Cosserat+media#0>
- Bleyer, J., de Buhan, P., 2013. On the performance of non-conforming finite elements for the upper bound limit analysis of plates. *International Journal for Numerical Methods in Engineering* 94 (3), 308–330.
- Casolo, S., Jun. 2004. Modelling in-plane micro-structure of masonry walls by rigid elements. *International Journal of Solids and Structures* 41 (13), 3625–3641.
URL <http://linkinghub.elsevier.com/retrieve/pii/S0020768304000484>
- Cecchi, A., Di Marco, R., May 2000. Homogenization of masonry walls with a computational oriented procedure. Rigid or elastic block? *European Journal of Mechanics - A/Solids* 19 (3), 535–546.
URL <http://linkinghub.elsevier.com/retrieve/pii/S0997753800001595>
- Cecchi, A., Milani, G., Mar. 2008. A kinematic FE limit analysis model for thick English bond masonry walls. *International Journal of Solids and Structures* 45 (5), 1302–1331.
URL <http://linkinghub.elsevier.com/retrieve/pii/S0020768307003848>
- Cecchi, A., Milani, G., Tralli, A., 2007. A Reissner-Mindlin limit analysis model for out-of-plane loaded running bond masonry walls. *International Journal of Solids and Structures* 44, 1438–1460.

- Cecchi, A., Sab, K., Jan. 2002a. A multi-parameter homogenization study for modeling elastic masonry. *European Journal of Mechanics - A/Solids* 21 (2), 249–268.
URL <http://linkinghub.elsevier.com/retrieve/pii/S0997753801011950>
- Cecchi, A., Sab, K., Jan. 2002b. Out of plane model for heterogeneous periodic materials: the case of masonry. *European Journal of Mechanics - A/Solids* 21 (5), 715–746.
URL <http://linkinghub.elsevier.com/retrieve/pii/S0997753802012433>
- Cecchi, A., Sab, K., May 2004. A comparison between a 3D discrete model and two homogenised plate models for periodic elastic brickwork. *International Journal of Solids and Structures* 41 (9-10), 2259–2276.
URL <http://linkinghub.elsevier.com/retrieve/pii/S0020768303007224>
- Cecchi, A., Sab, K., 2006. A corrigendum to "A comparison between a 3D discrete model and two homogenised plate models for periodic elastic brickwork". *International Journal of Solids and Structures* 43, 390–392.
- Cecchi, A., Sab, K., Sep. 2007. A homogenized Reissner–Mindlin model for orthotropic periodic plates: Application to brickwork panels. *International Journal of Solids and Structures* 44 (18-19), 6055–6079.
URL <http://linkinghub.elsevier.com/retrieve/pii/S0020768307000777>
- Cerrolaza, M., Sulem, J., Elbied, A., 1999. A Cosserat non-linear finite element analysis software for blocky structures. *Advances in Engineering Software* 30 (1), 69–83.
URL <http://www.sciencedirect.com/science/article/pii/S0965997898000593>
- Chettah, A., Mercatoris, B., Sacco, E., Massart, T., Sep. 2013. Localisation analysis in masonry using transformation field analysis. *Engineering Fracture Mechanics* 110, 166–188.
URL <http://linkinghub.elsevier.com/retrieve/pii/S0013794413002555>
- Chinosi, C., Comodi, M., Sacchi, G., Apr. 1997. A new finite element with ‘drilling’ D.O.F. *Computer Methods in Applied Mechanics and Engineering* 143 (1-2), 1–11.
URL <http://www.sciencedirect.com/science/article/pii/S0045782596011486>
<http://linkinghub.elsevier.com/retrieve/pii/S0045782596011486>
- Chróscielewski, J., Witkowski, W., May 2011. FEM analysis of Cosserat plates and shells based on some constitutive relations. *ZAMM - Journal of Applied Mathematics and Mechanics / Zeitschrift für Angewandte Mathematik und Mechanik* 91 (5), 400–412.
URL <http://doi.wiley.com/10.1002/zamm.201000090>
- Como, M., 2013. *Statics of Historic Masonry Constructions*. Springer Berlin Heidelberg.
URL <http://www.springer.com/materials/mechanics/book/978-3-642-30131-5>
- Cundall, P., Jun. 1988. Formulation of a three-dimensional distinct element model—Part I. A scheme to detect and represent contacts in a system composed of many polyhedral blocks. *International Journal of Rock Mechanics and Mining Sciences & Geomechanics Abstracts* 25 (3), 107–116.
URL <http://www.sciencedirect.com/science/article/pii/0148906288922930>
<http://linkinghub.elsevier.com/retrieve/pii/0148906288922930>
- Dai, C., Muhlhaus, H., Duncan Fama, M., Meek, J., Jan. 1993. Finite element analysis of Cosserat Theory for layered rock masses. *Computers and Geotechnics* 15 (3), 145–162.
URL <http://linkinghub.elsevier.com/retrieve/pii/0266352X93900105>

- Dai, C., Mühlhaus, H.-B., Meek, J., Duncan Fama, M., Jun. 1996. Modelling of blocky rock masses using the Cosserat method. *International Journal of Rock Mechanics and Mining Sciences & Geomechanics Abstracts* 33 (4), 425–432.
URL <http://linkinghub.elsevier.com/retrieve/pii/0148906295000712>
- de Bellis, M. L., Addessi, D., 2011. A Cosserat based multi-scale model for masonry structures. *International Journal for Multiscale Computational Engineering* 9 (5), 543–563.
- de Borst, R., 1991. Simulation of strain localisation: a reappraisal of the Cosserat continuum. *Engineering Computations* 8 (4), 317–332.
URL <http://www.emeraldinsight.com/10.1108/eb023842>
- de Borst, R., Mühlhaus, H.-B., 1991. Continuum models for discontinuous media.
URL <http://www.narcis.nl/publication/RecordID/oai:tudelft.nl:uuid:f6615aa2-abca-4e09-81fa-846713cd4e1b>
- de Borst, R., Sluys, L., Sep. 1991. Localisation in a Cosserat continuum under static and dynamic loading conditions. *Computer Methods in Applied Mechanics and Engineering* 90 (1-3), 805–827.
URL <http://linkinghub.elsevier.com/retrieve/pii/0045782591901859>
- de Borst, R., Sluys, L., Mühlhaus, H., Pamin, J., 1993. Fundamental issues in finite element analyses of localization of deformation. *Engineering Computations* 10 (2), 99–121.
URL <http://www.emeraldinsight.com/journals.htm?articleid=1662802&show=abstract>
- de Buhan, P., de Felice, G., 1997. A homogenization approach to the ultimate strength of brick masonry. *Journal of the Mechanics and Physics of Solids* 45 (7), 1085–1104.
URL <http://www.sciencedirect.com/science/article/pii/S0022509697000021>
- de Buhan, P., Dormieux, L., Salençon, J., 1998. Modélisation micropolaire de la résistance d'un milieu renforcé par inclusions. *Comptes Rendus de l'Académie des ...*
URL <http://www.sciencedirect.com/science/article/pii/S1251806999890034>
- de Buhan, P., Fréard, J., Garnier, D., Maghous, S., Aug. 2002. Failure Properties of Fractured Rock Masses as Anisotropic Homogenized Media. *Journal of Engineering Mechanics* 128 (8), 869–875.
URL [http://ascelibrary.org/doi/pdf/10.1061/\(ASCE\)0733-9399\(2002\)128:8\(869\)http://ascelibrary.org/doi/abs/10.1061/%28ASCE%290733-9399%282002%29128%3A8%28869%29](http://ascelibrary.org/doi/pdf/10.1061/(ASCE)0733-9399(2002)128:8(869)http://ascelibrary.org/doi/abs/10.1061/%28ASCE%290733-9399%282002%29128%3A8%28869%29)
- de Felice, G., Amorosi, A., Malena, M., 2010. Elasto-plastic analysis of block structures through a homogenization method. *International Journal for Numerical and Analytical Methods in Geomechanics* 34 (3), 221–247.
- Dehghani, M., Moosavian, S. A. A., May 2013. Static modeling of continuum robots by circular elements. In: 2013 21st Iranian Conference on Electrical Engineering (ICEE). IEEE, Mashhad, pp. 1–6.
URL <http://www.scopus.com/inward/record.url?eid=2-s2.0-84886907798&partnerID=tZ0tx3y1>
- DeJong, M., 2009. Seismic assessment strategies for masonry structures. Ph.D. thesis, Massachusetts Institute of Technology.
URL <http://dspace.mit.edu/handle/1721.1/49538>

- DeJong, M. J., Vibert, C., 2012. Seismic response of stone masonry spires: Computational and experimental modeling. *Engineering Structures* 40, 566–574.
URL <http://linkinghub.elsevier.com/retrieve/pii/S0141029612001186>
- Doherty, K., Griffith, M. C., Lam, N., Wilson, J., Apr. 2002. Displacement-based seismic analysis for out-of-plane bending of unreinforced masonry walls. *Earthquake Engineering & Structural Dynamics* 31, 833–850.
URL <http://doi.wiley.com/10.1002/eqe.126>
- Dujc, J., Brank, B., 2012. Stress resultant plasticity for shells revisited. *Computer Methods in Applied Mechanics and Engineering* 247-248, 146–165.
URL <http://dx.doi.org/10.1016/j.cma.2012.07.012>
- Eremeyev, V. a., Lebedev, L. P., Altenbach, H., 2013. *Foundations of Micropolar Mechanics*. SpringerBriefs in Applied Sciences and Technology. Springer Berlin Heidelberg, Berlin, Heidelberg.
URL <http://link.springer.com/10.1007/978-3-642-28353-6>
- Eremeyev, V. A., Pietraszkiewicz, W., Aug. 2006. Local Symmetry Group in the General Theory of Elastic Shells. *Journal of Elasticity* 85 (2), 125–152.
URL <http://link.springer.com/10.1007/s10659-006-9075-z>
- Eringen, A. C., Jan. 1967. Theory of micropolar plates. *ZAMP - Zeitschrift für angewandte Mathematik und Physik* 18 (1), 12–30.
URL <http://link.springer.com/article/10.1007/BF01593891><http://link.springer.com/10.1007/BF01593891>
- Eringen, A. C., 1999. *Microcontinuum field theories. I: Foundations and solids*. Springer, New York.
URL <http://www.citeulike.org/group/13900/article/8270507>
- Eringen, A. C., 2001. *Microcontinuum field theories. II: Fluent media*. Springer, New York.
URL http://books.google.com/books?hl=en&lr=&id=LQtmv_uiY5QC&oi=fnd&pg=PR7&dq=Microcontinuum+Field+Theories+II+Fluent+Media&ots=fes9Nc0xMj&sig=-mSFb5NGfJ8IrqWBGcDvE08gUXA
- Eurocode 6, 2006. *Eurocode 6: Design of Masonry Structures*.
- Eurocode 8, 2003. *Eurocode 8: Design of structures for earthquake resistance*.
- Fatemi, J., Van Keulen, F., Onck, P. R., 2002. Generalized continuum theories: Application to stress analysis in bone. In: *Meccanica*. Vol. 37. pp. 385–396.
URL <http://www.scopus.com/inward/record.url?eid=2-s2.0-0036441138&partnerID=tZ0tx3y1>
- Florence, C., Sab, K., Jan. 2006. A rigorous homogenization method for the determination of the overall ultimate strength of periodic discrete media and an application to general hexagonal lattices of beams. *European Journal of Mechanics - A/Solids* 25 (1), 72–97.
URL <http://linkinghub.elsevier.com/retrieve/pii/S0997753805000847>
- Forest, S., Pradel, F., Sab, K., Jun. 2001. Asymptotic analysis of heterogeneous Cosserat media. *International Journal of Solids and Structures* 38 (26-27), 4585–4608.
URL <http://linkinghub.elsevier.com/retrieve/pii/S002076830000295X>

- Forest, S., Sab, K., Jul. 1998. Cosserat overall modeling of heterogeneous materials. *Mechanics Research Communications* 25 (4), 449–454.
 URL <http://scholar.google.com/scholar?hl=en&btnG=Search&q=intitle:Cosserat+overall+modelling+of+heterogeneous+materials#0http://linkinghub.elsevier.com/retrieve/pii/S0093641398000597>
- Germain, P., 1973. The method of virtual power in continuum mechanics. Part 2: Microstructure. *SIAM Journal on Applied Mathematics* 25 (3), 556–575.
 URL <http://epubs.siam.org/doi/abs/10.1137/0125053>
- Gevorkyan, G. A., Nov. 1967. The basic equations of flexible plates for a medium of cosserat. *Soviet Applied Mechanics* 3 (11), 41–45.
 URL <http://www.springerlink.com/index/R50287J732040T29.pdfhttp://link.springer.com/10.1007/BF00896787>
- Goda, I., Assidi, M., Ganghoffer, J. F., Jan. 2014. A 3D elastic micropolar model of vertebral trabecular bone from lattice homogenization of the bone microstructure. *Biomechanics and modeling in mechanobiology* 13 (1), 53–83.
 URL <http://www.ncbi.nlm.nih.gov/pubmed/23579636>
- Godio, M., Stefanou, I., Sab, K., Sulem, J., Sep. 2014. Cosserat Elastoplastic Finite Elements for Masonry Structures. *Key Engineering Materials* 624, 131–138.
 URL <http://www.scientific.net/KEM.624.131>
- Godio, M., Stefanou, I., Sab, K., Sulem, J., 2015a. Dynamic finite element formulation for Cosserat elastic plates. *International Journal for Numerical Methods in Engineering* 101 (13), 992–1018.
 URL <http://doi.wiley.com/10.1002/nme.4833>
- Godio, M., Stefanou, I., Sab, K., Sulem, J., 2016. Multisurface plasticity for Cosserat materials: plate element implementation and validation. *International Journal for Numerical Methods in Engineering*. Published online.
 URL <http://doi.wiley.com/10.1002/nme.5219>
- Godio, M., Stefanou, I., Sab, K., Sulem, J., Sakji, S., 2015d. A limit analysis approach based on Cosserat continuum for the evaluation of the homogenized in-plane strength of discrete media: application to masonry. Submitted.
- Grande, E., Imbimbo, M., Sacco, E., 2011. A Beam Finite Element for Nonlinear Analysis of Masonry Elements With or Without Fiber-Reinforced Plastic (FRP) Reinforcements. *International Journal of Architectural Heritage* 5 (6), 693–716.
 URL <http://www.tandfonline.com/doi/abs/10.1080/15583058.2010.490616>
- Green, A., Naghdi, P., Osborn, R., 1968. Theory of an elastic-plastic Cosserat surface. *International Journal of Solids and Structures* 4, 907–927.
- Griffith, M., Vaculik, J., Lam, N., 2007. Cyclic testing of unreinforced masonry walls in two-way bending. *Earthquake Engineering & Structural Dynamics* 36, 801–821.
 URL <http://onlinelibrary.wiley.com/doi/10.1002/eqe.654/abstract>
- Hart, R., Cundall, P. A., Lemos, J. V., 1988. Formulation of a three-dimensional distinct element model—Part II. Mechanical calculations for motion and interaction of a system composed of many polyhedral blocks. *International Journal of Rock Mechanics and Mining Sciences &*

- Geomechanics Abstracts 25, 117–125.
URL <http://linkinghub.elsevier.com/retrieve/pii/0148906288922942>
- Hendry, A. W., Sinha, B. P., Davies, S. R., 1997. Design of Masonry Structures, Third Edition of Load Bearing Brickwork Design. Taylor & Francis, London.
URL [file:///Volumes/750G/#setting/#Papers2Library/Papers2/Files/DesignofMasonryStructures,ThirdEditionofLoadBearingBrickworkDesign-A.W.Hendry,B.P.Sinha&S.R.Davies.pdf%delimit%026E30F\\$npapers2://publication/uuid/C614F8B9-3427-4B9C-9D42-F2BBDB1A75E5](file:///Volumes/750G/#setting/#Papers2Library/Papers2/Files/DesignofMasonryStructures,ThirdEditionofLoadBearingBrickworkDesign-A.W.Hendry,B.P.Sinha&S.R.Davies.pdf%delimit%026E30F$npapers2://publication/uuid/C614F8B9-3427-4B9C-9D42-F2BBDB1A75E5)
- Hendry, E. A. W., 2001. Masonry walls: Materials and construction. Construction and Building Materials 15, 323–330.
- Heyman, J., 1997. The Stone Skeleton: Structural Engineering of Masonry Architecture. Cambridge University Press.
URL <https://books.google.fr/books?id=IvuIvzwGClwC>
- Hiriart-Urruty, J., Lemaréchal, C., 1993. Convex Analysis and Minimization Algorithms I.
URL <http://scholar.google.com/scholar?hl=en&btnG=Search&q=intitle:Convex+Analysis+and+Minimization+Algorithms+I#2>
- Hughes, T., 1987. The finite element method: linear static and dynamic finite element analysis. Prentice-Hall, New Jersey.
URL <http://www.dandelon.com/servlet/download/attachments/dandelon/ids/DE001C964953B446034A0C1257276003D0A31.pdfhttp://scholar.google.com/scholar?hl=en&btnG=Search&q=intitle:The+finite+element+method+Linear+static+and+dynamic+finite+element+analysis#0http://scholar.google.com/scholar?hl=en&btnG=Search&q=intitle:The+finite+element+method:+linear+static+and+dynamic+finite+element+analysis#0>
- Hughes, T. J., Brezzi, F., Jan. 1989. On drilling degrees of freedom. Computer Methods in Applied Mechanics and Engineering 72 (1), 105–121.
URL <http://cat.inist.fr/?aModele=afficheN&cpsid=164587http://www.sciencedirect.com/science/article/pii/0045782589901242http://linkinghub.elsevier.com/retrieve/pii/0045782589901242>
- Itasca Consulting Group, 2013. 3DEC 5.0.
- Jabareen, M., Rubin, M., 2008. A generalized Cosserat point element (CPE) for isotropic nonlinear elastic materials including irregular 3-D brick and thin structures. Journal of Mechanics of Materials and Structures 3 (8).
- Jabareen, M., Rubin, M., Jan. 2014. A six node plane strain triangular Cosserat Point Element (CPE) for nonlinear elasticity. International Journal of Engineering Science 74, 118–142.
URL <http://linkinghub.elsevier.com/retrieve/pii/S0020722513001249>
- Khoei, A., Karimi, K., Dec. 2008. An enriched-FEM model for simulation of localization phenomenon in Cosserat continuum theory. Computational Materials Science 44 (2), 733–749.
URL <http://linkinghub.elsevier.com/retrieve/pii/S0927025608002541>
- Kittel, C., 1996. Introduction to Solid State Physics, 7th Edition. John Wiley & Sons, Inc., New York.

- Krabbenhøft, K., Lyamin, A. V., Sloan, S. W., 2007a. Formulation and solution of some plasticity problems as conic programs. *International Journal of Solids and Structures* 44 (5), 1533–1549.
- Krabbenhøft, K., Lyamin, A. V., Sloan, S. W., Wriggers, P., Jan. 2007b. An interior-point algorithm for elastoplasticity. *International Journal for Numerical Methods in Engineering* 69 (3), 592–626.
URL <http://doi.wiley.com/10.1002/nme.1771>
- Kugler, S., Fotiu, P. a., Murin, J., Feb. 2010. A highly efficient membrane finite element with drilling degrees of freedom. *Acta Mechanica* 213 (3-4), 323–348.
URL <http://link.springer.com/10.1007/s00707-009-0279-8>
- Kumar, R. S., McDowell, D. L., Dec. 2004. Generalized continuum modeling of 2-D periodic cellular solids. *International Journal of Solids and Structures* 41 (26), 7399–7422.
URL <http://linkinghub.elsevier.com/retrieve/pii/S0020768304003658>
- Lee, J., 1995. Advantages of strain-space formulation in computational plasticity. *Computers & structures* 54 (3), 515–520.
URL <http://www.sciencedirect.com/science/article/pii/0045794994003498>
- Lemos, J. V., May 2007a. Discrete Element Modeling of Masonry Structures. *International Journal of Architectural Heritage* 1 (2), 190–213.
URL <http://www.tandfonline.com/doi/abs/10.1080/15583050601176868>
- Lemos, J. V., 2007b. Numerical issues in the representation of masonry structural dynamics with discrete elements. *Compdyn* (June), 13–16.
URL <http://scholar.google.com/scholar?hl=en&btnG=Search&q=intitle:NUMERICAL+ISSUES+IN+THE+REPRESENTATION+OF+MASONRY+structural+dynamics+with+discrete+elements#2>
- Li, L., Xie, S., Nov. 2004. Finite element method for linear micropolar elasticity and numerical study of some scale effects phenomena in MEMS. *International Journal of Mechanical Sciences* 46 (11), 1571–1587.
URL <http://linkinghub.elsevier.com/retrieve/pii/S0020740304002590>
- Li, X., Tang, H., 2005. A consistent return mapping algorithm for pressure-dependent elastoplastic Cosserat continua and modelling of strain localisation. *Computers and Structures* 83 (1), 1–10.
- Liberatore, D., Addessi, D., 2015. Strength domains and return algorithm for the lumped plasticity equivalent frame model of masonry structures. *Engineering Structures* 91, 167–181.
URL <http://linkinghub.elsevier.com/retrieve/pii/S0141029615001248>
- Lippmann, H., 1969. Eine Cosserat-Theorie des plastischen Fließens. *Acta Mechanica* 284, 255–284.
URL <http://link.springer.com/article/10.1007/BF01182264>
- Lourenço, P. B., 1996. Computational strategies for masonry structures. Ph.D. thesis, Delft University of Technology.
- Lourenço, P. B., Milani, G., Tralli, A., Zucchini, A., 2007. Analysis of masonry structures: review of and recent trends in homogenization techniques This article is one of a selection of papers published in this Special Issue on Masonry. *Canadian Journal of Civil Engineering*

- 34 (11), 1443–1457.
URL <http://www.nrcresearchpress.com/doi/abs/10.1139/L07-097>
- Makrodimopoulos, A., Martin, C. M., 2006. Lower bound limit analysis of cohesive-frictional materials using second-order cone programming. *International Journal for Numerical Methods in Engineering* 66 (4), 604–634.
URL <http://dx.doi.org/10.1002/nme.1567>
- Masiani, R., Rizzi, N., Trovalusci, P., Dec. 1995. Masonry as structured continuum. *Meccanica* 30 (6), 673–683.
URL <http://link.springer.com/article/10.1007/BF00986573><http://link.springer.com/10.1007/BF00986573>
- Massart, T., Peerlings, R., Geers, M., Sep. 2004. Mesoscopic modeling of failure and damage-induced anisotropy in brick masonry. *European Journal of Mechanics - A/Solids* 23 (5), 719–735.
URL <http://linkinghub.elsevier.com/retrieve/pii/S0997753804000713>
- Massart, T., Peerlings, R., Geers, M., Gottcheiner, S., May 2005. Mesoscopic modeling of failure in brick masonry accounting for three-dimensional effects. *Engineering Fracture Mechanics* 72 (8), 1238–1253.
URL <http://linkinghub.elsevier.com/retrieve/pii/S0013794404002024>
- Milani, E., Milani, G., Tralli, A., Oct. 2008. Limit analysis of masonry vaults by means of curved shell finite elements and homogenization. *International Journal of Solids and Structures* 45 (20), 5258–5288.
URL <http://linkinghub.elsevier.com/retrieve/pii/S0020768308002217>
- Milani, G., Lourenço, P., Tralli, A., Jan. 2006a. Homogenised limit analysis of masonry walls, Part II: Structural examples. *Computers & Structures* 84 (3-4), 181–195.
URL <http://linkinghub.elsevier.com/retrieve/pii/S0045794905003147>
- Milani, G., Lourenço, P. B., Tralli, A., Jan. 2006b. Homogenised limit analysis of masonry walls, Part I: Failure surfaces. *Computers & Structures* 84 (3-4), 166–180.
- Milani, G., Lourenço, P. B., Tralli, A., Oct. 2006c. Homogenization approach for the limit analysis of out-of-plane loaded masonry walls. *Journal of structural engineering* 132 (October), 1650–1663.
URL [http://ascelibrary.org/doi/abs/10.1061/\(ASCE\)0733-9445\(2006\)132:10\(1650\)](http://ascelibrary.org/doi/abs/10.1061/(ASCE)0733-9445(2006)132:10(1650))
- Milani, G., Taliercio, A., Apr. 2015. In-plane failure surfaces for masonry with joints of finite thickness estimated by a Method of Cells-type approach. *Computers & Structures* 150, 34–51.
URL <http://linkinghub.elsevier.com/retrieve/pii/S0045794914002910>
- Mindlin, R., 1964. Micro-structure in linear elasticity. *Archive for Rational Mechanics and Analysis*.
URL <http://www.springerlink.com/index/N7078N1674172013.pdf>
- Mistler, M., Anthoine, A., Butenweg, C., Sep. 2007. In-plane and out-of-plane homogenisation of masonry. *Computers & Structures* 85 (17-18), 1321–1330.
URL <http://linkinghub.elsevier.com/retrieve/pii/S0045794906003609>
- Mojsilović, N., 2011. Strength of masonry subjected to in-plane loading: A contribution. *International Journal of Solids and Structures* 48, 865–873.

- Mtanes, E., Jabareen, M., Sep. 2014. A plane strain quadrilateral Cosserat point element (CPE) for nonlinear orthotropic elastic materials — An extension to initially distorted geometry and general orthotropic directions. *Finite Elements in Analysis and Design* 87, 10–21.
URL <http://linkinghub.elsevier.com/retrieve/pii/S0168874X14000614>
- Mühlhaus, H. B., 1989. Application of Cosserat theory in numerical solutions of limit load problems. *Ingenieur-Archiv* 59 (2), 124–137.
URL <http://www.springerlink.com/index/n212407710322312.pdf><http://link.springer.com/10.1007/BF00538366>
- Mühlhaus, H.-B., Sulem, J., Unterreiner, P., 1997. *Discrete and Continuous Models for Dry Masonry Columns*.
URL [http://ascelibrary.org/doi/abs/10.1061/\(ASCE\)0733-9399\(1997\)123:4\(399\)](http://ascelibrary.org/doi/abs/10.1061/(ASCE)0733-9399(1997)123:4(399))
- Mühlhaus, H. B., Vardoulakis, I., 1987. The thickness of shear bands in granular materials. *Geotechnique* 37 (3), 271–283.
- Nadler, B., Rubin, M., Nov. 2003. Determination of hourglass coefficients in the theory of a Cosserat point for nonlinear elastic beams. *International Journal of Solids and Structures* 40 (22), 6163–6188.
URL <http://linkinghub.elsevier.com/retrieve/pii/S0020768303003652>
- Naghdi, P., Trapp, J., Sep. 1975. The significance of formulating plasticity theory with reference to loading surfaces in strain space. *International Journal of Engineering Science* 13 (9-10), 785–797.
URL <http://linkinghub.elsevier.com/retrieve/pii/0020722575900804><http://www.sciencedirect.com/science/article/pii/0020722575900804>
- Neff, P., Chelmiński, K., Müller, W., Wiens, C., 2007. a Numerical Solution Method for an Infinitesimal Elasto-Plastic Cosserat Model. *Mathematical Models and Methods in Applied Sciences* 17 (08), 1211–1239.
- Pain, H., 2005. *The physics of vibrations and waves*.
URL http://books.google.com/books?hl=en&lr=&id=g__6DX33JWUC&oi=fnd&pg=PR5&dq=THE+PHYSICS+OF+VIBRATIONS+and+waves&ots=89i8nzPy8d&sig=Qi8XVYwXzyctZfryRl-FMgjJhDchhttp://books.google.com/books?hl=en&lr=&id=g__6DX33JWUC&oi=fnd&pg=PR5&dq=The+physics+of+vibrations+and+waves&ots=89j5nrOG77&sig=7VTN_pXYu_kNT0zGe5wJKN51AB8
- Papanastasiou, P. C., Vardoulakis, I., 1992. Numerical treatment of progressive localization in relation to borehole stability. *International Journal for Numerical and Analytical Methods in Geomechanics* 16 (6), 389–424.
URL <http://doi.wiley.com/10.1002/nag.1610160602>
- Park, H. C., Lakes, R. S., 1986. Cosserat micromechanics of human bone: Strain redistribution by a hydration sensitive constituent. *Journal of Biomechanics* 19 (5), 385–397.
URL <http://www.scopus.com/inward/record.url?eid=2-s2.0-0022580563&partnerID=tZ0tx3y1>
- Pasternak, E., Mühlhaus, H.-B., Jul. 2005. Generalised homogenisation procedures for granular materials. *Journal of Engineering Mathematics* 52 (1), 199–229.
URL <http://link.springer.com/10.1007/s10665-004-3950-z>

- Pau, A., Trovalusci, P., May 2012. Block masonry as equivalent micropolar continua: the role of relative rotations. *Acta Mechanica* 223 (7), 1455–1471.
URL <http://link.springer.com/10.1007/s00707-012-0662-8>
- Penna, A., Lagomarsino, S., Galasco, A., 2014. A nonlinear macroelement model for the seismic analysis of masonry buildings. *Earthquake Engineering and Structural Dynamics* 43 (2), 159–179.
- Petry, S., Beyer, K., 2014a. Cyclic test data of six unreinforced masonry walls with different boundary conditions. *Earthquake Spectra*.
URL <http://dx.doi.org/10.1193/101513EQS269><http://earthquakespectra.org/doi/abs/10.1193/101513EQS269>
- Petry, S., Beyer, K., 2014b. Influence of boundary conditions and size effect on the drift capacity of URM walls. *Engineering Structures* 65, 76–88.
URL <http://dx.doi.org/10.1016/j.engstruct.2014.01.048>
- Pietruszczak, S., Ushaksaraei, R., Jul. 2003. Description of inelastic behaviour of structural masonry. *International Journal of Solids and Structures* 40 (15), 4003–4019.
URL <http://linkinghub.elsevier.com/retrieve/pii/S0020768303001744>
- Pradel, F., Sab, K., 1998. Cosserat modelling of elastic periodic lattice structures. *Comptes Rendus de l'Académie des Sciences-Series ...*, 699–704.
URL <http://www.sciencedirect.com/science/article/pii/S125180699880002X>
- Press, W. H., Teukolsky, S., Vetterling, W. T., Flannery, B. P., Nov. 1992. *Numerical recipes in Fortran 77: the art of scientific computing*. Cambridge University Press, Cambridge.
URL <http://linkinghub.elsevier.com/retrieve/pii/037847549390043T>
- Providas, E., Kattis, M., Jun. 2000. An assessment of two fundamental flat triangular shell elements with drilling rotations. *Computers & Structures* 77 (2), 129–139.
URL <http://linkinghub.elsevier.com/retrieve/pii/S0045794999002151>
- Providas, E., Kattis, M., Nov. 2002. Finite element method in plane Cosserat elasticity. *Computers & Structures* 80 (27-30), 2059–2069.
URL <http://linkinghub.elsevier.com/retrieve/pii/S0045794902002626>
- Riahi, A., Curran, J. H., Aug. 2009. Full 3D finite element Cosserat formulation with application in layered structures. *Applied Mathematical Modelling* 33 (8), 3450–3464.
URL <http://linkinghub.elsevier.com/retrieve/pii/S0307904X08003090>
- Riahi, A., Curran, J. H., Bidhendi, H., Sep. 2009. Buckling analysis of 3D layered structures using a Cosserat continuum approach. *Computers and Geotechnics* 36 (7), 1101–1112.
URL <http://linkinghub.elsevier.com/retrieve/pii/S0266352X09000585>
- Robinson, G., Davies, J. B. C., 1999. Continuum robots - a state of the art. *Proceedings - IEEE International Conference on Robotics and Automation* 4, 2849–2854.
URL <http://www.scopus.com/inward/record.url?eid=2-s2.0-0032668064&partnerID=tZ0tx3y1>
- Sab, K., Sep. 2003. Yield design of thin periodic plates by a homogenization technique and an application to masonry walls. *Comptes Rendus Mécanique* 331 (9), 641–646.
URL <http://linkinghub.elsevier.com/retrieve/pii/S163107210300144X>

- Sab, K., Cecchi, A., Dallot, J., 2007. Determination of the overall yield strength domain of out-of-plane loaded brick masonry. *International Journal for Multiscale Computational Engineering* 5 (2), 83–92.
 URL <http://www.dl.begellhouse.com/journals/61fd1b191cf7e96f,25cc62a120ff4480,7e369b2422df452a.html>
- Sack, K., Skatulla, S., Sansour, C., Aug. 2013. Research and Applications in Structural Engineering, Mechanics and Computation. In: Zingoni, A. (Ed.), *Proceedings of the 5th International Conference on Structural Engineering, Mechanics and Computation (SEMC)*, 2013. CRC Press, Cape Town, pp. 423–427.
 URL <http://www.scopus.com/inward/record.url?eid=2-s2.0-84889018835&partnerID=tZ0tx3y1><http://www.crcnetbase.com/doi/book/10.1201/b15963>
- Salençon, J., May 2013. *Yield Design*. John Wiley & Sons, Inc., Hoboken, NJ USA.
 URL <http://doi.wiley.com/10.1002/9781118648988>
- Salerno, G., de Felice, G., Mar. 2009. Continuum modeling of periodic brickwork. *International Journal of Solids and Structures* 46 (5), 1251–1267.
 URL <http://linkinghub.elsevier.com/retrieve/pii/S0020768308004642>
- Sanchez-Molina, D., Velazquez-Ameijide, J., Arregui-Dalmases, C., Rodríguez, D., Quintana, V., Shafieian, M., Crandall, J. R., Jan. 2014. A microcontinuum model for mechanical properties of esophageal tissue: experimental methodology and constitutive analysis. *Annals of biomedical engineering* 42 (1), 62–72.
 URL <http://www.scopus.com/inward/record.url?eid=2-s2.0-84896700706&partnerID=tZ0tx3y1><http://www.ncbi.nlm.nih.gov/pubmed/23975385>
- Schaefer, H., 1967. Analysis der Motorfelder im Cosserat-Kontinuum. *ZAMM - Journal of Applied Mathematics and Mechanics / Zeitschrift für Angewandte Mathematik und Mechanik* 47, 319–328.
 URL http://www.neo-classical-physics.info/uploads/3/0/6/5/3065888/schaefer_-_motor_fields_in_cosserat_continua.pdf
- Sharbati, E., Naghdabadi, R., Dec. 2006. Computational aspects of the Cosserat finite element analysis of localization phenomena. *Computational Materials Science* 38 (2), 303–315.
 URL <http://linkinghub.elsevier.com/retrieve/pii/S0927025606000541>
- Simo, J., Hughes, T., 1998. *Computational inelasticity*.
 URL <http://www.ulb.tu-darmstadt.de/tocs/127987207.pdf>
- Simo, J., Kennedy, J., Gonvondjee, S., 1988. Non-smooth multisurface plasticity and viscoplasticity. Loading/unloading conditions and numerical algorithms. *International Journal for Numerical Methods in Engineering* 26 (June 1987), 2161–2185.
 URL <http://onlinelibrary.wiley.com/doi/10.1002/nme.1620261003/abstract>
- Simo, J., Taylor, R., 1985. Consistent tangent operators for rate-independent elastoplasticity. *Computer Methods in Applied Mechanics and Engineering* 48 (1), 101–118.
- Simo, J. C., Kennedy, J. G., Apr. 1992. On a Stress Resultant Geometrically Exact Shell Model. Part V: Nonlinear Plasticity: Formulation and Integration Algorithms. *Comput. Methods Appl. Mech. Eng.* 96 (2), 133–171.
 URL [http://dx.doi.org/10.1016/0045-7825\(92\)90129-8](http://dx.doi.org/10.1016/0045-7825(92)90129-8)

- Simon, J., Bagi, K., Dec. 2014. Discrete element analysis of the minimum thickness of oval masonry domes. *International Journal of Architectural Heritage*.
URL <http://dx.doi.org/10.1080/15583058.2014.996921>
- Simulia, 2010. Abaqus 6.10.
- Stefanou, I., Sab, K., Heck, J.-V., 2015. Three dimensional homogenization of masonry structures with building blocks of finite strength: A closed form strength domain. *International Journal of Solids and Structures* 54, 258–270.
URL <http://dx.doi.org/10.1016/j.ijsolstr.2014.10.007>
- Stefanou, I., Sulem, J., 2012. Micromorphic Continua: Application To the Homogenization of Diatomic Masonry Columns. *International Journal for Multiscale Computational Engineering* 10 (6), 599–613.
URL <http://www.dl.begellhouse.com/journals/61fd1b191cf7e96f,3089bea11cd334bd,506f8a524b9d39d0.html>
- Stefanou, I., Sulem, J., Vardoulakis, I., Feb. 2008. Three-dimensional Cosserat homogenization of masonry structures: Elasticity. *Acta Geotechnica* 3 (1), 71–83.
URL <http://link.springer.com/10.1007/s11440-007-0051-y>
- Stefanou, I., Sulem, J., Vardoulakis, I., Jun. 2010. Homogenization of interlocking masonry structures using a generalized differential expansion technique. *International Journal of Solids and Structures* 47 (11-12), 1522–1536.
URL <http://linkinghub.elsevier.com/retrieve/pii/S0020768310000533>
- Steinmann, P., 1994. Theory of finite deformation and finite rotation multiplicative elastoplasticity. *International Journal of Solids and Structures* 31 (8), 1063–1084.
- Steinmann, P., 1995. Theory and numerics of ductile micropolar elastoplastic damage. *International Journal for Numerical Methods in Engineering* 38 (4), 583–606.
URL <http://dx.doi.org/10.1002/nme.1620380406>
- Steinmann, P., Willam, K., 1991. Localization within the Framework of Micropolar Elastoplasticity. In: Brüller, O., Mannl, V., Najjar, J. (Eds.), *Advances in Continuum Mechanics*. Springer Berlin Heidelberg, pp. 296–313.
URL http://dx.doi.org/10.1007/978-3-642-48890-0_24
- Sulem, J., Mühlhaus, H.-B., Jan. 1997. A continuum model for periodic two-dimensional block structures. *Mechanics of Cohesive-frictional Materials* 2 (1), 31–46.
URL [http://onlinelibrary.wiley.com/doi/10.1002/\(SICI\)1099-1484\(199701\)2:1<31::AID-CFM24>3.0.CO;2-0/abstracthttp://doi.wiley.com/10.1002/%28SICI%291099-1484%28199701%292%3A1%3C31%3A%3AAID-CFM24%3E3.0.CO%3B2-0](http://onlinelibrary.wiley.com/doi/10.1002/(SICI)1099-1484(199701)2:1<31::AID-CFM24>3.0.CO;2-0/abstracthttp://doi.wiley.com/10.1002/%28SICI%291099-1484%28199701%292%3A1%3C31%3A%3AAID-CFM24%3E3.0.CO%3B2-0)
- Sulem, J., Stefanou, I., Veveakis, E., Feb. 2011. Stability analysis of undrained adiabatic shearing of a rock layer with Cosserat microstructure. *Granular Matter* 13 (3), 261–268.
URL <http://link.springer.com/10.1007/s10035-010-0244-1>
- Sulem, J., Veveakis, M., Stefanou, I., May 2013. Failure in shear bands for granular materials: thermo-hydro-chemo-mechanical effects. *Géotechnique Letters* 3 (April-June), 31–36.
URL <http://www.icevirtuallibrary.com/content/article/10.1680/geolett.12.00063http://hal.archives-ouvertes.fr/hal-00862508/>

- Suquet, P., 1983. Limit Analysis and Homogenisation. *Comptes Rendus Mécanique* 296 (5), 1355–1358.
- Taylor, R. L., Govindjee, S., Jul. 2004. Solution of clamped rectangular plate problems. *Communications in Numerical Methods in Engineering* 20 (10), 757–765.
URL <http://onlinelibrary.wiley.com/doi/10.1002/cnm.652/abstract>
<http://doi.wiley.com/10.1002/cnm.652>
- Tekoğlu, C., Onck, P., Dec. 2008. Size effects in two-dimensional Voronoi foams: A comparison between generalized continua and discrete models. *Journal of the Mechanics and Physics of Solids* 56 (12), 3541–3564.
URL <http://linkinghub.elsevier.com/retrieve/pii/S0022509608001142>
- Tomazevic, M., Klemenc, I., 1997. Seismic behaviour of confined masonry walls. *Earthquake Engineering & Structural Dynamics* 26 (November 1996), 1059–1071.
- Trovalusci, P., Masiani, R., 1999. Material symmetries of micropolar continua equivalent to lattices. *International journal of solids and structures*.
URL <http://www.sciencedirect.com/science/article/pii/S0020768398000730>
- Trovalusci, P., Masiani, R., Mar. 2003. Non-linear micropolar and classical continua for anisotropic discontinuous materials. *International Journal of Solids and Structures* 40 (5), 1281–1297.
URL <http://linkinghub.elsevier.com/retrieve/pii/S002076830200584X>
- Trovalusci, P., Masiani, R., Oct. 2005. A multifield model for blocky materials based on multi-scale description. *International Journal of Solids and Structures* 42 (21-22), 5778–5794.
URL <http://linkinghub.elsevier.com/retrieve/pii/S0020768305001381>
- Trovalusci, P., Pau, A., Aug. 2014. Derivation of microstructured continua from lattice systems via principle of virtual works: the case of masonry-like materials as micropolar, second gradient and classical continua. *Acta Mechanica* 225 (1), 157–177.
URL <http://link.springer.com/10.1007/s00707-013-0936-9>
- Tu, Y.-H., Chuang, T.-H., Liu, P.-M., Yang, Y.-S., Dec. 2010. Out-of-plane shaking table tests on unreinforced masonry panels in RC frames. *Engineering Structures* 32 (12), 3925–3935.
URL <http://www.sciencedirect.com/science/article/pii/S014102961000341X>
- Unterreiner, P., 1994. Contribution à l'étude et à la modélisation numérique des sols cloués: application au calcul en déformation des ouvrages de soutènement. Ph.D. thesis, Ecole des Ponts et Chaussées.
URL <http://cat.inist.fr/?aModele=afficheN&cpsidt=164587>
- Vardoulakis, I., 1989. Shear-banding and liquefaction in granular materials on the basis of a Cosserat continuum theory. *Ingenieur-Archiv* 59 (2), 106–113.
URL <http://link.springer.com/article/10.1007/BF00538364>
<http://link.springer.com/10.1007/BF00538364>
- Vardoulakis, I., 2009. Lecture notes on Cosserat continuum mechanics with application to the mechanics of granular media.
URL <http://geolab.mechan.ntua.gr/teaching/lectnotes/CCM2009.pdf>

- Vardoulakis, I., Sulem, J., 1995. Bifurcation analysis in geomechanics. Blackie Academic and Professional, Glasgow.
 URL <http://books.google.com/books?hl=en&lr=&id=W8K79FaiQTwC&oi=fnd&pg=PP1&dq=Bifurcation+analysis+in+geomechanics&ots=nyVBR5mlFs&sig=2QjiIdEIUW9IgobkygrQ4qxHv8U>
- Vermeer, P., de Borst, R., 1984. Non-associated plasticity for soils, concrete and rock. *HERON* 29 (3), 1–64.
 URL <http://www.narcis.nl/publication/RecordID/oai:tudelft.nl:uuid:4ee188ab-8ce0-4df3-adf5-9010ebfaabf0>
- Yang, H. T. Y., Saigal, S., Masud, A., Kapania, R. K., Jan. 2000. A survey of recent shell finite elements. *International Journal for Numerical Methods in Engineering* 47 (1-3), 101–127.
 URL [http://onlinelibrary.wiley.com/doi/10.1002/\(SICI\)1097-0207\(20000110/30\)47:1/3<101::AID-NME763>3.0.CO;2-C/abstracthttp://doi.wiley.com/10.1002/%28SICI%291097-0207%2820000110/30%2947%3A1/3%3C101%3A%3AAID-NME763%3E3.0.CO%3B2-C](http://onlinelibrary.wiley.com/doi/10.1002/(SICI)1097-0207(20000110/30)47:1/3<101::AID-NME763>3.0.CO;2-C/abstracthttp://doi.wiley.com/10.1002/%28SICI%291097-0207%2820000110/30%2947%3A1/3%3C101%3A%3AAID-NME763%3E3.0.CO%3B2-C)
- Zervos, A., 2008. Finite elements for elasticity with microstructure and gradient elasticity. *International Journal for Numerical Methods in Engineering* 73 (4), 564–595.
 URL <http://onlinelibrary.wiley.com/doi/10.1002/nme.2093/abstract>
- Zhang, H., Wang, H., Liu, G., Jun. 2005. Quadrilateral isoparametric finite elements for plane elastic Cosserat bodies. *Acta Mechanica Sinica* 21 (4), 388–394.
 URL <http://link.springer.com/10.1007/s10409-005-0041-y>
- Zienkiewicz, O., Taylor, R., 2005. *The finite element method for solid and structural mechanics*, sixth Edition. Elsevier Butterworth-Heinemann, Oxford.
 URL <http://books.google.com/books?hl=en&lr=&id=VvpU3zssD0wC&oi=fnd&pg=PP1&dq=The+Finite+element+method+for+solid+and+structural+mechanics&ots=f122jTFE56&sig=oL3WUvQEcwndSoXEJGaxdVfR9tQ>
- Zucchini, A., Lourenço, P., Jun. 2002. A micro-mechanical model for the homogenisation of masonry. *International Journal of Solids and Structures* 39 (12), 3233–3255.
 URL <http://linkinghub.elsevier.com/retrieve/pii/S0020768302002305>